# FUNCTIONAL RENORMALIZATION GROUP APPROACH TO CORRELATED QUANTUM SYSTEMS FAR FROM EQUILIBRIUM


DISSERTATION

zur Erlangung des Grades eines
Doktors der Physik
am Fachbereich Physik
der Freien Universität Berlin

vorgelegt von

CHRISTIAN KLÖCKNER

Berlin, 2019

Christian Klöckner: *Functional Renormalization Group Approach to Correlated Quantum Systems Far from Equilibrium,* © 2019

ERSTGUTACHTER: Prof. Dr. Christoph Karrasch
ZWEITGUTACHTER: Prof. Felix von Oppen, PhD
TAG DER DISPUTATION: 11.07.2019

## SELBSTÄNDIGKEITSERKLÄRUNG

Hiermit versichere ich, dass ich in meiner Dissertation alle Hilfsmittel und Hilfen angegeben habe, und auf dieser Grundlage die Arbeit selbstständig verfasst habe. Diese Arbeit habe ich nicht schon einmal in einem früheren Promotionsverfahren eingereicht.

*Berlin, 2019*

Christian Klöckner

## ABSTRACT

The experimental progress in cold atomic gases and mesoscopic systems has allowed unprecedented access to low dimensional correlated quantum systems far from equilibrium. This has revealed a variety of novel phenomena such as many-body localization, time crystals and dynamical phase transitions.

The theoretical description of such systems has remained a challenge: The numerically exact solution of generic, correlated quantum systems requires computational effort that scales exponentially in the number of fermions, rendering larger systems and therefore collective behavior inaccessible. This necessitates approximations. In low dimensions, infrared divergences prohibit the use of a purely perturbative approach. Renormalization group based techniques, where energy scales are treated successively remedy some of these shortcomings. We therefore propose the use of the functional renormalization group to access correlation functions far from equilibrium in large, interacting systems. Such techniques were previously successfully applied in the investigation of quantum impurity problems and quenches in tight-binding chains and are widely used in the study of equilibrium phase diagrams.

After a presentation of the Keldysh formalism, that constitutes a natural language out of equilibrium, we present perturbation theory and the functional renormalization group approach in a diagrammatic language. We then develop, optimize and apply flexible fRG techniques to four different problems in one-dimensional tight-binding chains with short-ranged two-particle interaction.

First, we discuss the emergence of anomalous transport in the presence of a quasiperiodic potential by analyzing linear response and a far-from-equilibrium quench protocol. We then develop a variant of the fRG to access pure excited eigenstates. We use this algorithm to investigate many-body states in large tight-binding chains and show that generic excitations appear thermal while some states show unique spectral properties. To study the influence of inelastic scattering on the transport properties in such a chain we then go beyond an effective single-particle picture; to that end, we present an algorithm, that includes scattering in long chains. Finally, we discuss infinite chains coupled to a substrate while driven out of equilibrium by an electric field. Exploiting the inherent symmetries, we develop efficient algorithms and apply them to a simple tight-binding chain with nearest-neighbor interaction to explore the interplay of spontaneous symmetry breaking and driving. We demonstrate, that ordering is suppressed and provide results that indicate unconventional transport in the driven system.

# KURZFASSUNG

Durch die Erforschung kalter Atomgase und mesoskopischer Systeme wurden niedrigdimensionale, korrelierte Quantensysteme entfernt von thermischen Gleichgewicht erstmals experimentell zugänglich. Dies führte zur Entdeckung einer Vielzahl neuer, physikalischer Phänomene wie der Vielteilchenlokalisierung, Zeitkristalle und dynamischer Phasenübergänge. Die theoretische Beschreibung solcher Systeme stellt jedoch weiterhin eine Herausforderung dar, da exaktes Lösen generischer, korrelierter Quantensysteme einen exponentiell von der Systemgröße abhängigen, numerischen Aufwand erfordert. Die Anwendung rein pertubativer Methoden ist wegen Divergenzen im Infrarotbereich problematisch. Auf der Renormierungsgruppenidee basierende Methoden lösen jedoch einige dieser Probleme. Daher konzentrieren wir uns auf die funktionale Renormierungsgruppe (fRG) um Korrelationsfunktionen großer, wechselwirkender Systeme weit entfernt vom Gleichgewicht zu betrachten. Ähnliche Methoden wurden bereits erfolgreich zur Untersuchung von Quantenpunkten sowie Tight-Binding-Modellen verwendet und finden breite Anwendung bei der Untersuchung von Phasendiagrammen.

Eingangs stellen wir den Keldysh-Formalismus dar, der eine natürliche Sprache zur Beschreibung von Systemen außerhalb des Gleichgewicht ist. Dann werden zentrale Konzepte der Störungstheorie und der fRG in diagrammatischer Sprache präsentiert. Schließlich befassen wir uns mit der Entwicklung und Anwendung fRG-basierter Methoden zur Behandlung verschiedener, eindimensionaler, wechselwirkender Tight-Binding-Modelle.

Als erste Anwendung diskutieren wir das Auftreten anormalen Transports in quasiperiodischen Potenzialen, die wir mithilfe linearer Antwortfunktionen und einem Quenchprotokoll untersuchen. Es folgt die Entwicklung einer fRG-Variante, die einen direkten Zugang zu angeregten Eigenzuständen ermöglicht. Anschließend wird diese auf lange, wechselwirkende Ketten angewendet und wir demonstrieren, dass generische Zustände thermische Charakteristiken aufweisen, während andere auffällige spektrale Signaturen zeigen. Um den Einfluss unelastischer Streuung auf den Transport zu untersuchen, präsentieren wir ein vereinfachtes fRG-Verfahren zweiter Ordnung. Schließlich diskutieren wir unendliche Ketten auf einem Substrat, die von einem elektrischen Feld aus dem Gleichgewicht gebracht werden. Unter Ausnutzung ihrer Symmetrien entwickeln wir eine effiziente Methode und untersuchen in einem einfachen Modell das Wechselspiel zwischen spontaner Symmetriebrechung und dem elektrischen Feld. Wir zeigen, dass hierbei Ordnung unterdrückt wird und finden Indizien für unkonventionellen Transport.

# CONTENTS

# 1 INTRODUCTION

## 1.1 MOTIVATION

In the last decades, great experimental progress has been made in the preparation and control of correlated low-dimensional quantum systems out of equilibrium. Two noteworthy techniques are cold atomic gases and mesoscopic systems.

Cold atomic gases have allowed for a wide variety of non-equilibrium experiments with unprecedented control and remarkable coherence [BDZ08; Sch+15b; GB17; LGS15]. To effectively simulate low-dimensional Hamiltonian dynamics, atoms are trapped in interfering, coherent laser beams. Two-particle interaction between these atoms can be tuned from the non-interacting to the strongly correlated regime via Feshbach resonances [Chi+10]. Through sudden changes in the trapping potential various quench protocols can be realized. The high level of control and coherence allows to access the physics of an isolated system on long time-scales. This allows for the investigation of transient dynamics as well as the decay to a quasi-stationary state on intermediate time-scales, before residual coupling thermalize the system.

Another field, that has seen large progress is the fabrication of mesoscopic systems. A variety of geometries can be realized and phase coherence throughout the system allows direct access to many quantum-mechanical phenomena [LAG04]. By gates attached to the system, the stationary state far from equilibrium can be explored.

More and more, we come to understand, that systems far from equilibrium are not just a mere extension of equilibrium and linear-response physics but feature their own set of exciting phenomena like transient superconductivity [Mit+16; Ken+17], time crystals [Wil12; Zha+17; Cho+17], prethermalization [Gri+12; Ney+17], many-body localization [Sch+15b; Cho+16; SPL10] and dynamical phase transitions [Hey18].

Beyond a fundamental interest, these experimental advances are responsible for a newly invigorated desire to better understand such systems. However, on the theoretical side, there are two distinct challenges:

The first one is the crucial role of correlations in low dimensions. In three dimensional systems, much of the phenomenology can be understood on a single-particle level. Fermi-liquid theory [Gia03] shows that in 3D metals two-particle interactions lead to the emergence of quasiparticles with a renormalized dispersion. Close to the Fermi-

edge these quasiparticles are long lived. In contrast, in lower dimensions scattering of quasiparticles is enhanced and the system is not well described by a renormalization of the non-interacting theory. In one dimension for instance, collective modes form the fundamental excitation and lead to the emergence of power-law behavior in transport properties at low energies.

The second challenge is the treatment of transport. A large number of theoretical methods was developed based on the peculiar properties of ground states. Among other features, ground-states display comparably low entanglement and are therefore more readily represented as matrix product states. Many of the formerly very successful numerical tools like the density matrix renormalization group or quantum Monte Carlo can only be extended beyond equilibrium at exponential computational cost.

To set the stage for this work, we will briefly introduce the models considered and the ideas behind some of the widely employed methods to treat such systems.

## 1.2 MODELS

At the heart of condensed matter physics lies the problem of electrons propagating in a periodic potential formed by regularly arranged ions. While Bloch's theorem tells us, that the eigenstates of such a problem are delocalized, it is convenient to express the Hamiltonian in localized basis states (called the *Wannier basis*), that reflect the original localized eigenstates of the individual electron-core pairs [Ash76]. Throughout, we will denote the second-quantization annihilation (creation) operators of a Wannier state localized at site $i$ by $c_i^{(\dagger)}$. In this basis, spatially separated Wannier states are only weakly coupled; therefore often it is sufficient to consider a free Hamiltonian of the form

$$H_0 = \sum_{\langle i,j \rangle} t_{i,j} c_i^\dagger c_j + \text{h.c.}, \tag{1.2.1}$$

where $\langle \cdot, \cdot \rangle$ denotes nearest neighbors. For simplicity, we will restrict ourselves to spinless fermions with time-reversal symmetry and only consider a single band. As this rules out local interactions, the most short-ranged and therefore parametrically largest interaction is a density-density interaction,

$$H_{\text{int}} = \sum_{\langle i,j \rangle} U_{i,j} c_i^\dagger c_i c_j^\dagger c_j. \tag{1.2.2}$$

When such a system is initially prepared in a non-trivial superposition of its eigenstates, the system evolves unitarily, displays non-trivial transient dynamics and in some cases reaches a stationary state.

Alternatively, a time-dependent Hamiltonian can be considered, inducing excitations. By construction, such processes involve a large number of eigenstates, making the problem inherently more complex than computing ground-state properties only. Even from an uncorrelated initial state, a two-particle interaction generates non-trivial many-body correlations.

All models discussed throughout will be closely related to this general form. Various extensions are possible and allows for the investigation of more complex problems in the future.

## 1.3 AVAILABLE THEORETICAL TOOLS

While of large interest, strongly correlated systems, especially in one and two dimension, remain a challenge for many of the established theoretical methods. To set the stage, we will briefly sketch the idea behind some of the most prevalent methods.

ANALYTIC SOLUTION Cases, where a many-body problem can be fully solved analytically are few and far between [MA16]. Noteworthy examples are integrable systems [Fra17], where an extensive number of conserved local integrals of motion fully characterize the Hamiltonian. Integrable systems can be solved using the Bethe ansatz [LM16], allowing exact access to some properties. While tremendously simplifying the problem, these integrals of motion typically only exist in fine-tuned models. Furthermore, they restrict the dynamics and results obtained in such models do not represent the phenomenology of more generic quantum systems.

EXACT DIAGONALIZATION Exact diagonalization is the prototypical example of an exact numerical method. Once the Hamiltonian is diagonalized in the many-body basis, all properties, in and out of equilibrium can be accessed. Generally, this is however exponentially hard in the system size. Obtaining the full many-body spectrum is only realistic for $\mathcal{O}(20)$ fermionic sites (for an example relevant to this work, see [LLA15]).

To obtain quench dynamics algorithms like the Lanczos algorithm for a unitary time-evolution exist [PL86]. While making time-evolution feasible for larger systems, they do not remedy the problem fully and are usually limited to short times and typically not exceeding $\mathcal{O}(30)$ site systems [SK18; Lie+18].

DENSITY MATRIX RENORMALIZATION GROUP Introduced by S. White in [Whi92], the *density matrix renormalization group* (DMRG) produces an approximate solution to a many-body problem in the basis of *matrix product states* (MPS). While any state in a finite chain can be expressed as an MPS the required matrices are in general exponen-

tially large; DMRG provides a systematic approximation using matrices of lower dimension. For weakly entangled systems, convergence to numerically exact solutions can be achieved with much smaller computational effort. This allows DMRG to outperform exact diagonalization in a variety of problems, such as ground-state properties of gapped systems in one dimension. When entanglement is extensive, as is generically the case beyond equilibrium, DMRG becomes exponentially expensive and therefore impractical.

As an exact method, DMRG will provide a reference point for the approximate methods discussed throughout. For this reason, we will present the idea behind this method as well as its strengths and weaknesses in some more detail later on.

PERTURBATION THEORY For many cases, an approximate, perturbative approach is the only viable option to sufficiently simplify the problem and make a solution feasible. Solving first-order perturbation theory self-consistently results in the so called *mean field approximation* [Bru04], that for its simplicity is commonly used to provide a first, simplified understanding. We will discuss these methods in more detail later. Especially in low-dimensional systems, however, perturbation theory is known to introduce infrared divergencies. These require a resummation to obtain physical results. Such resummations are typically performed by a renormalization group (RG) [Alt10], where energy scales are taken into account successively.

FUNCTIONAL RENORMALIZATION GROUP One such RG scheme, that goes beyond perturbation theory is the functional renormalization group [Met+12], that we will discuss in detail. Just like perturbation theory, it is numerically efficient and can access large systems at the cost of being approximate. Throughout this thesis, we will develop and employ variants of this method to obtain results beyond those accessible by exact methods.

## 1.4 OBJECTIVE OF THIS THESIS

The field outlined above is far too vast and the theoretical challenges too demanding to address all issues. In this thesis, we want to contribute to the field of far-from-equilibrium systems in two ways: We aim to present novel, efficient methods that can be applied to a range of questions in this area. We focus on exploring larger systems at the cost of treating the two-particle interaction approximately. Furthermore, we aim to construct the methods in a flexible way that makes them a useful tool for future work.

We then employ these methods to explore some questions at the frontier of condensed matter physics. Each of the chapters discussing

applications feature their own introduction to the relevant physical phenomena.

## 1.5 OUTLINE

This thesis consists of two main parts.

In the first part, we present the formalism, that serves as the methodological foundation of this work. While most (but not all) of the formalism presented has made its way into textbooks and select lectures, we believe it is valuable to present a complete and coherent version of all the necessary concepts needed to follow the course of this work. To that end, we will first introduce the natural language of non-equilibrium transport - the Keldysh formalism (Chapter 2). We pay special attention to the concept of reservoirs as well as tight-binding chains, as they are essential to the models discussed later on. We then discuss the diagrammatic approach to perturbation theory (Chapter 3) and use this to present the functional renormalization group formalism, that is the method predominantly used throughout this work (Chapter 4).

In the second part of this thesis we apply the general formalism to a variety of physical scenarios from the realm of transport in correlated quantum systems.

As a first example, we discuss dynamics in the presence of a quasiperiodic potential (Chapter 5) and examine the emergence of anomalous transport. We find a smooth transition from ballistic transport in the non-interacting regime, to superdiffusion to subdiffusion. The observation of superdiffusive transport is novel within the field of many-body localization. As quasiperiodic disorder does not feature rare region, we demonstrate that the Griffiths picture for subdiffusive transport is incomplete.

We then turn to individual excited eigenstates (Chapter 6) and develop a scheme to access their approximate single-particle correlations. We show, that in generic eigenstates the excitation-energy can provide a cutoff to low-energy properties and itself lead to the emergence of Luttinger liquid power laws. In contrast, we identify a class of non-generic excitations, that show spectral properties, that vastly differ from a thermal expectation. As an outlook, we present a potential route to go beyond an effective single-particle picture and an algorithm, that allows for quantum quenches from an excited eigenstate.

Next, we study the effect of inelastic scattering on transport in finite chains (Chapter 7). We devise an efficient, highly parallelized scheme to include such scattering processes. We reach system-sizes of $\mathcal{O}(N = 50)$ sites and analyze the cutoff dependence of the results in the ground-state and in the driven system. We find a strong de-

pendence of physical observables on the cutoff and demonstrate, that this dependence is non-perturbative.

Finally, we investigate transport in infinite systems driven by an electric field (Chapter 8). We demonstrate, how to employ the inherent symmetries of such a system to devise a second-order fRG approximation and analyze the interplay of a driving in an open system with spontaneous symmetry breaking. In our approximation, the ordering is strongly suppressed in an open system. However, in proximity to the phase transition we observe a strong susceptibility towards order and a resistivity, that is highly sensitive to symmetry breaking. In the low-coupling limit at strong electric fields, we find that interactions delocalize the system and lead to unconventional transport.

In the last chapter, we briefly summarize our findings and discuss potential avenues for future work.

# 2

# KELDYSH GREEN'S FUNCTION FORMALISM

## 2.1 MOTIVATION

As mentioned above, the Keldysh formalism is the natural language for correlation functions out of equilibrium. Introductions to this language can be found in various books and review articles (see e.g. [Ram07; SBD16; HJ08; Cho+85; KL09; SBD16]).

Before we will introduce the Keldysh formalism [Kel+65] for Green's functions, it is worthwhile to motivate, why we need such a formalism in the first place. A many-body quantum system is typically described by its Hamiltonian $H$, containing information about all possible configurations as well as transitions between them. For the scope of this motivation, we restrict ourselves to time-independent Hamiltonians. To describe the actual configuration within a system, we employ the density operator $\rho$ such that the expectation value of any observable $A$ can be computed as

$$\langle A \rangle_\rho = \mathrm{Tr}\left(\rho A\right). \tag{2.1.1}$$

The time-evolution of the system is governed by the Heisenberg equation of motion; the density operator evolves as

$$\frac{\mathrm{d}}{\mathrm{d}t}\rho(t) = \mathrm{i}\left[H, \rho(t)\right] \tag{2.1.2}$$

which is formally solved by introducing a time-evolution operator such that

$$\begin{aligned} &U(t,t') = \mathrm{e}^{-\mathrm{i}(t-t')H} \\ &\Rightarrow \rho(t) = U(t,t_0)\underbrace{\rho(t_0)}_{=:\rho_0}U(t_0,t). \end{aligned} \tag{2.1.3}$$

As the trace is a cyclic operator, this can also be understood as

$$\begin{aligned} \langle A \rangle_{\rho(t)} &= \mathrm{Tr}\left(U(t,t_0)\rho_0 U(t_0,t)A\right) \\ &= \mathrm{Tr}\left(\rho_0 U(t_0,t)AU(t,t_0)\right) \\ &= \mathrm{Tr}\left(\rho_0 A_H(t)\right) \\ &= \langle A_H(t)\rangle_{\rho_0} \end{aligned} \tag{2.1.4}$$

which is the Heisenberg picture of quantum mechanics, where the operator evolves while the state is considered to be constant.

$$A_H(t) = U(t_0,t)AU(t,t_0) \tag{2.1.5}$$

When a system is perturbed at one time and we are interested in the system's response at a later time, one has to compute expectation values of the form

$$\begin{aligned}&\left\langle A_H(t)B_H(t')\right\rangle_{\rho_0}\\&= \mathrm{Tr}\big(\rho_0 U(t_0,t)A\underbrace{U(t,t_0)U(t_0,t')}_{=U(t,t')}BU(t',t_0)\big).\end{aligned} \tag{2.1.6}$$

Because of their physical interpretation, they are also called *response* functions. The simplest example of the appearance of such terms is the Kubo formula [Kub57], where we consider a system in some equilibrium configuration $\rho_0$ of the Hamiltonian $H$ and at time $t_0$ add a perturbation $H'$ to the system. For small perturbations one finds

$$\langle A\rangle_{\rho(t)} = \langle A\rangle_{\rho_0} - i\int_{t_0}^{t} dt' \left\langle \left[A_{H'}(t), H'_{H'}(t')\right]\right\rangle_{\rho_0}. \tag{2.1.7}$$

Similarly, higher order expansions of out-of-equilibrium expectation values can (under some conditions, see Chapter 3) be expressed in terms of such response functions. Hence, these are the objects of greatest interest throughout this thesis, as they are essential to characterize a system. However, at the same time, they are numerically expensive to compute. Evaluating the time-evolution operator involves diagonalizing the many-body Hamiltonian, which is exponentially hard in the number of particles. To obtain results using perturbative methods is hindered by the fact, that *three* time-evolution operators appear, which due to their non-trivial commutation relations can not easily be treated.

In thermal equilibrium, where

$$\rho = \frac{e^{-\beta H}}{\mathrm{Tr}\, e^{-\beta H}} = \frac{1}{Z}e^{-\beta H} \tag{2.1.8}$$

expressions like Equation 2.1.6 can be simplified by instead analyzing imaginary-time response functions as introduced by Matsubara [Mat55]. Introducing the imaginary-time ordering operator

$$\mathcal{T}_I A(it)B(it') = \begin{cases} A(it)B(it') & t > t' \\ \xi B(it')A(it) & t' > t \end{cases} \tag{2.1.9}$$

with $\xi = \mp 1$ for fermions (bosons), we realize, that we can express imaginary-time ordered correlation functions

$$\left\langle \mathcal{T}_I A_H(it)B_H(it')\right\rangle_\rho = \frac{1}{Z}\,\mathrm{Tr}\left[\mathcal{T}_I U(i\beta,0)A(it)B(it')\right] \tag{2.1.10}$$

using a single imaginary-time evolution operator. Due to the definition of the imaginary-time ordering, the operators can be rearranged freely, greatly simplifying a perturbative expansion. One can show, that all physical correlation functions can be recovered using suitable analytical continuation.

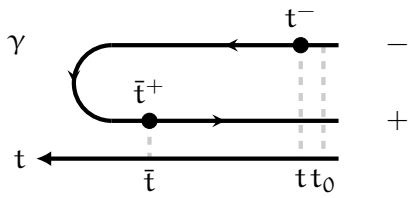


Figure 2.1: Representation of the contour that forms the basis of the contour-ordering operator. At the bottom, we see the time-line; the branch of the contour labeled $-$ is the *forward* branch and is parallel to the time-axis while the branch labeled $+$ is the *backward* branch and is anti-parallel to the time-axis.

## 2.2 THE KELDYSH CONTOUR

We now elaborate how to treat a (at this point) general density operator. In analogy to the Matsubara formalism, we strive to combine the various time-evolution operators into a single one by defining a suitable ordering operator. We do this by introducing an additional *contour index* associated with a time $t \in \mathbb{R} \to t^\sigma \in \gamma \sim \mathbb{Z}_2 \times \mathbb{R}$, indicating a *direction*. This can be understood as splitting the time axis into two distinct branches; the *forward-* and *backward-* branch, labeled with a $-$ and $+$ respectively. We can imagine the branches to loop around at a time $t_{max}$ larger than all times we are interested in. This creates a *contour* (see Figure 2.1) and a natural *contour ordering* operator $\mathcal{T}_\gamma$ defined by:

$$\mathcal{T}_\gamma A(t_1^{j_1}) B(t_2^{j_2}) = \begin{cases} A(t_1)B(t_2) & \text{if } j_1 > j_2 \\ \mathcal{T}A(t_1)B(t_2) & \text{if } j_1 = j_2 = - \\ \tilde{\mathcal{T}}A(t_1)B(t_2) & \text{if } j_1 = j_2 = + \\ \xi B(t_2)A(t_1) & \text{if } j_1 < j_2, \end{cases} \tag{2.2.1}$$

using the ordinary (anti-)time-ordering operator $\mathcal{T}$ ($\tilde{\mathcal{T}}$) where we understand $- < +$ and $\xi = \pm$ for bosonic and fermionic operators respectively. We also define the time-ordering $\mathcal{T}$ to order equal-time creators *left* of annihilators and keep them otherwise unshuffeled. Therefore, time-ordering acts trivially on normal-ordered operators, such as the Hamiltonians we will discuss. This definition effectively orders the operators along the contour. A time-dependent operator $O(t)$ in Heisenberg picture can thus be expressed as

$$\begin{aligned} O_H(t) &= \left[\tilde{\mathcal{T}} e^{-i\int_t^{t_0} dt H(t)}\right] O(t) \left[\mathcal{T} e^{-i\int_{t_0}^{t} dt H(t)}\right] \\ &= \mathcal{T}_\gamma \underbrace{e^{-i\int_\gamma dt H(t)}}_{U_\gamma} O(t^-) \end{aligned} \tag{2.2.2}$$

where the time-variable $t \in \mathbb{R}$ in $O(t)$ is used to evaluate the explicit time-dependence. When extended to $t^- \in \gamma$, the operator's position

with respect to the contour ordering of $O(t^-)$ is defined. In contrast, $O_H(t)$ indicates Heisenberg time-evolution with respect to the Hamiltonian H. Note that this result does not depend on the precise choice of the endpoint of the contour (as long as $t_{max} > t$) and the branch-index chosen for $O(t^\sigma)$. When treating two operators simultaneously

$$\begin{aligned} O^1_H(t_1)O^2_H(t_2) &= \left[\tilde{\mathcal{T}} e^{-i\int_{t_1}^{t_0} dt H(t)}\right] O^1(t_1) \left[\mathcal{T} e^{-i\int_{t_0}^{t_1} dt H(t)}\right] \\ &\times \left[\tilde{\mathcal{T}} e^{-i\int_{t_2}^{t_0} dt H(t)}\right] O^2(t_2) \left[\mathcal{T} e^{-i\int_{t_0}^{t_2} dt H(t)}\right] \\ &= \mathcal{T}_\gamma U_\gamma O^1(t_1^+)O^2(t_2^-), \end{aligned} \tag{2.2.3}$$

the choice of the contour indices on the operators ensures the correct ordering, independent of $t_{1,2}$. By definition, a contour ordered product of operators does not depend on the contour index at the largest time:

$$\begin{aligned} &\mathcal{T}_\gamma O(t_1^{\sigma_1}) \cdots O(t_{max}^{\sigma_{max}}) \cdots O(t_N^{\sigma_N}) \\ &\quad = \mathcal{T}_\gamma O(t_1^{\sigma_1}) \cdots O(t_{max}^{-\sigma_{max}}) \cdots O(t_N^{\sigma_N}) \quad \text{if } t_{max} > t_i \ \forall i \neq max \end{aligned} \tag{2.2.4}$$

Note, however, that not all n-operator expressions can be expressed so concisely using a two-branch contour ordering. If we consider $t_2 < t_1, t_3$

$$O^1_H(t_1)O^2_H(t_2)O^3_H(t_3) \neq \mathcal{T}_\gamma U_\gamma O^1(t_1^{\sigma_1})O^2(t_2^{\sigma_2})O^3(t_3^{\sigma_3}) \forall \sigma_{1,\dots,3} \in \{\pm\}.$$

To correctly order this expression, a more involved contour is needed [Ramo7]. The scope of this thesis, though, we will restrict ourselves to operators, that can be expressed in terms of ordering along the two-branch Keldysh contour.

The possibility to collect the time-evolution operators in a single object and shift the commutation relations into the definition of the ordering operator is going to be essential in Chapter 3, where we use the same idea in the interaction picture to introduce a perturbative method to efficiently compute these objects.

## 2.3 DEFINITION OF THE KELDYSH GREEN'S FUNCTION

As any observable can be decomposed into a linear combination of products of creation and annihilation operators, expectation values of such products are of paramount interest. For this reason we define the N-particle Green's function of an interacting system as

$$\begin{aligned} &G^{\sigma_1\dots\sigma_N|\sigma'_1\dots\sigma'_N}_{i_1\dots i_N|i'_1\dots i'_N}(t_1\dots t_N|t'_1\dots t'_N) \\ &= (-i)^N \left\langle \mathcal{T}_\gamma c_{i_1}(t_1^{\sigma_1}) \cdots c_{i_N}(t_N^{\sigma_N}) c^\dagger_{i'_N}(t_N^{\prime\sigma'_N}) \cdots c^\dagger_{i_{1'}}(t_{1'}^{\prime\sigma_{1'}}) \right\rangle_{\rho_0} \end{aligned} \tag{2.3.1}$$

where the creation and annihilation operators are understood to be evolved in the Heisenberg picture; as they are not explicitly time-dependent, omitting the subscript $H$ is unlikely to result in confusion. To simplify this cumbersome notation, we often times understand indices as vectors and even go as far as to introduce multi-indices $1 = (i, \sigma, t)$, containing (in this case) the single-particle index, the contour index $\sigma$ as well as the time.

$$G^{\sigma_1 \dots \sigma_N | \sigma_1' \dots \sigma_N'}_{q_1 \dots q_N | q_1' \dots q_N'}(t_1 \dots t_N | t_1' \dots t_N') = G^{\sigma|\sigma'}_{q|q'}(t|t') = G_{1|1'}. \quad (2.3.2)$$

We usually understand multi-indices to contain all indices, that are not specified otherwise. From their definition, some symmetry properties are immediately apparent: for any permutation $P$ of single particle indices we find

$$G^{P\sigma|\sigma'}_{Pq|q'}(Pt|t') = \xi^P G^{\sigma|\sigma'}_{q|q'}(t|t') = G^{\sigma|P\sigma'}_{q|Pq'}(t|Pt') \quad (2.3.3)$$

and under complex conjugation

$$G^{\sigma|\sigma'}_{q|q'}(t|t')^* = (-1)^N G^{-\sigma'|-\sigma}_{q'|q}(t'|t) \quad (2.3.4)$$

In the single-particle case, this reduces to four Green's functions

$$\begin{aligned} G^{-|-}_{q|q'}(t|t') &= G^{c}_{q|q'}(t|t') && (2.3.5)\\ &= \theta(t'-t+0^+)G^{<}_{q|q'}(t|t') + \theta(t-t'-0^+)G^{>}_{q|q'}(t|t') \\ G^{-|+}_{q|q'}(t|t') &= G^{<}_{q|q'}(t|t') = -\xi i \left\langle c^\dagger_{q'}(t')c_q(t)\right\rangle_{\rho_0} && (2.3.6)\\ G^{+|-}_{q|q'}(t|t') &= G^{>}_{q|q'}(t|t') = -\ i\left\langle c_q(t)c^\dagger_{q'}(t')\right\rangle_{\rho_0} && (2.3.7)\\ G^{+|+}_{q|q'}(t|t') &= G^{\tilde{c}}_{q|q'}(t|t') && (2.3.8)\\ &= \theta(t-t'+0^+)G^{<}_{q|q'}(t|t') + \theta(t'-t-0^+)G^{>}_{q|q'}(t|t') \end{aligned}$$

referred to as *chronological*, *lesser*, *greater* and *anti-chronological*. The infinitesimal shifts indicated by $0^+$ in $G^c$ and $G^{\tilde{c}}$ define the equal-time, equal branch behavior (compare Equation 2.2.1 and the comment thereafter).

At equal times

$$G^<(t|t) = i\mathbb{1} + G^>(t|t). \quad (2.3.9)$$

which allows us to write

$$\begin{pmatrix} G^c & G^< \\ G^> & G^{\tilde{c}} \end{pmatrix}(t,t) = \begin{pmatrix} G^< & G^< \\ -i + G^< & G^< \end{pmatrix}(t,t). \quad (2.3.10)$$

In accordance with Equation 2.2.4, we note for $t \neq t'$

$$G^{\sigma|\sigma'}(t|t') = \begin{cases} G^{\ \sigma|-\sigma'}(t|t') & t' > t \\ G^{-\sigma|\ \sigma'}(t|t') & t' < t. \end{cases} \quad (2.3.11)$$

From this, it immediately apparent that these four Green's functions are not linearly independent for $t \neq t'$:

$$G^{c}(t|t') + G^{\tilde{c}}(t|t') = G^{<}(t|t') + G^{>}(t|t') + \begin{cases} 0 & \text{if } t \neq t' \\ i\mathbb{1} & \text{if } t = t' \end{cases} \tag{2.3.12}$$

To make use of this, we introduce a basis transformation in the contour indices $\alpha, \alpha' \in \{1, 2\}$:

$$G^{\alpha|\alpha'}(t|t') = \sum_{\sigma,\sigma' \in \{\pm\}} D_{\alpha|\sigma} G^{\sigma|\sigma'}(t|t') D^{-1}_{\sigma'|\alpha'} \tag{2.3.13}$$

with

$$D = \frac{1}{\sqrt{2}} (\mathbb{1} - i\sigma_y) \qquad D^{-1} = \frac{1}{\sqrt{2}} (\mathbb{1} + i\sigma_y)\,. \tag{2.3.14}$$

The resulting Green's functions[1]

$$G^{\alpha|\alpha'}(t|t') = \begin{pmatrix} G^{P} & G^{adv} \\ G^{ret} & G^{K} + G^{P} \end{pmatrix}_{\alpha|\alpha'} (t|t') \tag{2.3.15}$$

are known as the *patch*, *advanced*, *retarded* and *Keldysh* Green's function. There are other ways to treat the transformation at equal times but we follow the convention of [Jak15]. Due to these names, we will refer to this basis as the *RKA* or *Keldysh* basis and use $\alpha$ instead of $\sigma$ to denote its components. The resulting relations between this *Keldysh* basis and the original *contour* basis written out explicitly read:

$$\begin{aligned} G^{P} &= \frac{1}{2} \left( G^{c} + G^{\tilde{c}} - G^{<} - G^{>} \right) \\ G^{ret} &= \frac{1}{2} \left( G^{c} - G^{\tilde{c}} - G^{<} + G^{>} \right) \\ G^{adv} &= \frac{1}{2} \left( G^{c} - G^{\tilde{c}} + G^{<} - G^{>} \right) \\ G^{K} &= \phantom{\frac{1}{2}} \left( \qquad\qquad G^{<} + G^{>} \right) \end{aligned} \tag{2.3.16}$$

$$\begin{aligned} G^{<} &= \frac{1}{2} \left( G^{K} + G^{adv} - G^{ret} \right) \\ G^{>} &= \frac{1}{2} \left( G^{K} - G^{adv} + G^{ret} \right) \\ G^{c} &= \frac{1}{2} \left( G^{K} + G^{adv} + G^{ret} \right) + G^{P} \\ G^{\tilde{c}} &= \frac{1}{2} \left( G^{K} - G^{adv} - G^{ret} \right) + G^{P} \end{aligned} \tag{2.3.17}$$

Using this definition and Equation 2.3.4 one finds

$$G^{ret}(t|t') = \left( G^{adv}(t'|t) \right)^{\dagger}, \qquad G^{K}(t|t') = -\left( G^{K}(t'|t) \right)^{\dagger}. \tag{2.3.18}$$

1 Note that the choice of D in not unique and different conventions exist. We chose the same convention as originally introduced by Keldysh [Kel+65]

Due to Equation 2.3.12, $G^P$ is only non-zero for equal times:

$$G^P(t|t') = \frac{1}{2}\left[G^c - G^< - G^> + G^{\tilde{c}}\right](t,t') = \begin{cases} 0 & \text{if } t \neq t' \\ \frac{i}{2} & \text{if } t = t'. \end{cases} \tag{2.3.19}$$

Furthermore, as the name suggest, the support of the retarded (advanced) Green's function is restricted to $t > t'$ ($t < t'$)

$$G^{ret}(t|t') = \theta(t\ -t')\left[G^>(t|t') - G^<(t|t')\right] \tag{2.3.20}$$
$$G^{adv}(t|t') = \theta(t'-t\ )\left[G^<(t|t') - G^>(t|t')\right], \tag{2.3.21}$$

which is known as *causality*, as it relates to the fact, that a perturbation can not cause a disturbance of the system *before* it occurs (compare Equation 2.1.7). At equal times we understand $\theta(0) = \frac{1}{2}$ (compare Equation 2.3.10):

$$G^{ret}(t,t) = -\frac{i}{2} \qquad G^{adv}(t,t) = \frac{i}{2}. \tag{2.3.22}$$

The Keldysh Green's function, on the other hand, has support for all $t, t' \in \mathbb{R}$. Using Equation 2.3.9, we note the useful identity

$$G^K_{q|q'}(t|t) = -i + 2G^<(t|t) = -i\left[1 - 2\left\langle c^\dagger_{q'}(t)c_q(t)\right\rangle_{\rho_0}\right]. \tag{2.3.23}$$

## 2.4 GREEN'S FUNCTIONS IN A STATIONARY STATE

Depending on the scenario under consideration as well as the initial preparation, the system may reach a stationary state, where all local observables appear time-translation invariant. In these cases, the single-particle Green's functions only depend on the time-difference

$$G(t|t') =: G(t-t') \tag{2.4.1}$$

and it is natural to transform to the Fourier basis:[2]

$$\begin{aligned} G(\omega) &= \int_{-\infty}^{-\infty} dt e^{i\omega t - 0^+|t|} G(t) \\ G(t) &= \int_{-\infty}^{-\infty} \frac{d\omega}{2\pi} e^{-i\omega t} G(\omega), \end{aligned} \tag{2.4.2}$$

where $0^+$ indicates a small convergence factor, that has to be sent to zero (from above) at the very end. It can be understood as an artificial decay introduced to limit the coherence time. In the presence of physical decay processes we will see that this precaution is unnecessary, in their absence however, this ensures convergence.

2 In general, i.e. without time-translation invariance, G depends on two frequencies. In the stationary state $G(\omega|\omega') = 2\pi\delta(\omega-\omega')G(\omega)$.

For a function $f(t)$ with $f(t) \to 0$ for $t \to \infty$ we note

$$F(\omega) := \int_{-\infty}^{\infty} dt e^{i\omega - 0^+|t|}\theta(t)f(t),\ \omega \in \mathbb{C} \tag{2.4.3}$$

is analytic for $\mathrm{Im}(\omega) \geqslant 0$ while it may display poles or branch-cuts in the lower half-plane. Therefore, $G^{\mathrm{ret}}(\omega)$ ($G^{\mathrm{adv}}(\omega)$) is analytic in the upper (lower) half-plane; this observations is known as part of the *theorem of analyticity* [JPS10b]. As it stems from the support of the retarded and advanced Green's function it is directly related to causality.

For higher order Green's functions time translational invariance similarly implies

$$\begin{aligned} &G(\omega_1, \ldots, \omega_N | \omega_{1'}, \ldots, \omega_{N'}) \\ &\qquad \sim \delta(\omega_1 + \cdots + \omega_N - \omega_{1'} - \cdots - \omega_{N'}), \end{aligned} \tag{2.4.4}$$

which indicates energy conservation. This allows us to reduce the number of frequencies, as we have already seen for the single-particle Green's function; for the two-particle Green's function we will use the definition [BHD14]

$$\begin{aligned} \Pi &= \omega_1 + \omega_2 = \omega_{1'} + \omega_{2'} \\ \Delta &= \omega_{1'} - \omega_1 = \omega_2 - \omega_{2'} \\ X &= \omega_{2'} - \omega_1 = \omega_2 - \omega_{1'}. \end{aligned} \tag{2.4.5}$$

## 2.5 THE FREE GREEN'S FUNCTIONS

As the simplest example, we are now going to discuss the special case of a purely quadratic Hamiltonian:

$$H(t) = \sum_{n,m \in \underline{N}} h(t)_{n,m} c_n^\dagger c_m \tag{2.5.1}$$

Here, $h(t) \in \mathbb{C}^{N \times N}$ is the single-particle matrix representation of the Hamiltonian $H(t)$ with $h(t) = h(t)^\dagger$ for all $t \in \mathbb{R}$ . In the same way we can give a single-particle representation for the time-evolution operator:

$$u(t, t') = \begin{cases} \mathcal{T} e^{-i\int_{t'}^{t} d\tau h(\tau)} & t \geqslant t' \\ \tilde{\mathcal{T}} e^{-i\int_{t'}^{t} d\tau h(\tau)} & t < t' \end{cases} \tag{2.5.2}$$

$$u(t, t') = \big(u(t', t)\big)^\dagger \tag{2.5.3}$$

With these, calculating the free Green's functions is straightforward.

### 2.5.1 *... in time-space*

Using the equation of motion for the creation and annihilation operators

$$\begin{aligned} \partial_t c_i^\dagger(t) &= +i c_j^\dagger(t) h_{j,i}(t) \\ \partial_t c_i(t) &= -i h_{i,j}(t) c_j(t) \end{aligned} \tag{2.5.4}$$

one easily proves

$$\begin{aligned}\partial_{t'} g^{<}_{q|q'}(t,t') &= +i g^{<}_{q|i}(t,t') h_{i,q'}(t') \\ \partial_{t}\ g^{<}_{q|q'}(t,t') &= -i h_{q,i}(t\ ) g^{<}_{i|q'}(t,t').\end{aligned} \tag{2.5.5}$$

Using the initial conditions

$$g^{<}(t_0,t_0) = -i\xi\bar{n}, \qquad \bar{n}_{n,m} = \left\langle c^{\dagger}_m c_n \right\rangle_{\rho_0} \tag{2.5.6}$$

one therefore identifies

$$g^{<}(t|t') = -i\xi u(t,t_0)\bar{n}u(t_0,t'). \tag{2.5.7}$$

Analogously, the greater component is obtained

$$g^{>}(t|t') = -i\ u(t,t_0)\left[\mathbb{1} + \xi\bar{n}\right] u(t_0,t'). \tag{2.5.8}$$

The (anti-)chronological Green's functions follow from Equations 2.3.5, 2.3.8, 2.5.7 and 2.5.8. To obtain the free Green's functions in the Keldysh basis, we employ Equation 2.3.20

$$g^{\mathrm{ret}}(t|t') = -i\theta(t\ - t')u(t,t') \tag{2.5.9}$$

$$g^{\mathrm{adv}}(t|t') = \ \ i\theta(t'-t\ )u(t,t') = g^{\mathrm{ret}}(t'|t)^{\dagger} \tag{2.5.10}$$

$$g^{\mathrm{K}}(t|t') = -i g^{\mathrm{ret}}(t|t_0)(\mathbb{1} + 2\xi\bar{n}) g^{\mathrm{adv}}(t_0|t'). \tag{2.5.11}$$

Note that in the RKA basis and with a quadratic Hamiltonian, the state of the system (as contained in $\rho_0$) only enters in the Keldysh Green's function while the retarded and advanced Green's functions only depend on the Hamiltonian and are independent of the preparation of the system.

Inherited from the properties of the time-evolution operator, the free Green's function obeys a group-property

$$\begin{aligned}&\text{for } t_i < \bar{t} < t_f : \\ &\quad \mathcal{T}e^{\left(\int_{t_i}^{t_f} dt\, \hat{f}(t)\right)} = \mathcal{T}e^{\left(\int_{\bar{t}}^{t_f} dt\, \hat{f}(t)\right)} \mathcal{T}e^{\left(\int_{t_i}^{\bar{t}} dt\, \hat{f}(t)\right)} \\ &\Rightarrow\ -i g^{\mathrm{ret}}(t_i,t_f) = g^{\mathrm{ret}}(t_i,\bar{t}) g^{\mathrm{ret}}(\bar{t},t_f).\end{aligned} \tag{2.5.12}$$

### 2.5.2 *... in frequency-space*

For a time-independent quadratic Hamiltonian, the retarded and advanced Green's functions only depend on the time difference and are easily Fourier transformed using the regularized Fourier transform introduced in Section 2.4

$$g^{\mathrm{ret}}(\omega) = \frac{1}{\omega - h + i0^{+}} \tag{2.5.13}$$

$$g^{\mathrm{adv}}(\omega) = \left[g^{\mathrm{ret}}(\omega)\right]^{\dagger}. \tag{2.5.14}$$

The artificial decay introduced into the Fourier transform acts like an infinitesimal broadening, shifting the poles of the retarded Green's function into the lower complex half-plane, which preserves the theorem of analyticity (compare Section 2.4). Using the Sokhotski-Plemelj theorem in the eigenbasis ($h v_i = \epsilon_i v_i$), this can be decomposed to

$$g^{\mathrm{ret/adv}}(\omega) = \sum_i \left[ \mathcal{P} \frac{1}{\omega - \epsilon_i} \mp i\pi\delta(\omega - \epsilon_i) \right] v_i v_i^\dagger, \tag{2.5.15}$$

where $\mathcal{P}$ indicates the principal value.

If, in addition to a constant Hamiltonian, we also assume that the system is prepared in a configuration with $[\bar{n}, h] = 0$ we find (compare Equation 2.5.11):

$$\begin{aligned} &[\bar{n}, h] = 0 \\ \Rightarrow\ & g^K(t|t') = (\mathbb{1} + 2\xi\bar{n}) \left( g^{\mathrm{ret}}(t|t') - g^{\mathrm{adv}}(t|t') \right) \\ \Rightarrow\ & g^K(\omega) = (\mathbb{1} + 2\xi\bar{n}) \left( g^{\mathrm{ret}}(\omega) - g^{\mathrm{adv}}(\omega) \right). \end{aligned} \tag{2.5.16}$$

Note that due to Equation 2.5.15, $g^K$ only carries weight at the eigenenergies. We call a system in such a state in (potentially non-thermal) *equilibrium*; one particular equilibrium configuration is a system in a thermal state defined by

$$\bar{n}_{n,m} = \frac{\mathrm{Tr}\, e^{-\beta H} c_m^\dagger c_n}{\mathrm{Tr}\, e^{-\beta H}} \qquad \Rightarrow \bar{n} = \frac{1}{e^{\beta h} - \xi} \tag{2.5.17}$$

with the inverse temperature $\beta$. To distinguish these, we refer to the latter as *thermal equilibrium*.

### 2.5.3 *Fluctuation-dissipation theorem for finite free systems*

In a system in an equilibrium configuration, where $[\bar{n}, h] = 0$, there is a common eigenbasis, where both, $\bar{n}$ an $h$ are diagonal. Using Equation 2.5.13, this also implies that $g^{\mathrm{ret}}$ and $g^{\mathrm{adv}}$ are diagonal. In that basis Equation 2.5.16 simplifies to

$$g^K_{k,k'}(\omega) = (1 + 2\xi\bar{n}_{k,k}) \left( g^{\mathrm{ret}}_{k,k}(\omega) - g^{\mathrm{adv}}_{k,k}(\omega) \right) \delta_{k,k'}. \tag{2.5.18}$$

In most cases, one is interested in states, where $\bar{n}_{k,k}$ is already uniquely defined by a scalar function $\mathbb{R} \to [0,1] \ : \ \omega \mapsto n(\omega)$ such that

$$\bar{n}_{k,k} = \bar{n}(\epsilon_k), \tag{2.5.19}$$

where $\epsilon_k$ denotes the k-th eigenenergy of the system. This is, for example, true for thermal states or if no eigenenergy is degenerate.

$\bar{n}(\omega)$ only carries physical meaning at eigenengies, where it defines the occupation of the corresponding eigenstate(s) at that energy.

Using this *distribution function* $n(\omega)$ we write

$$g^K_{k,k'}(\omega) = (1 + 2\xi\bar{n}(\omega)) \left( g^{ret}_{k,k}(\omega) - g^{adv}_{k,k}(\omega) \right) \delta_{k,k'}. \tag{2.5.20}$$

and in the original basis

$$g^K(\omega) = (1 + 2\xi\bar{n}(\omega)) \left( g^{ret}(\omega) - g^{adv}(\omega) \right). \tag{2.5.21}$$

This is known as the *fluctuation-dissipation* theorem. This name stems from an understanding we alluded to in Section 2.5, where we noted that $g^K$ contains information about the statistics of the system, including the fluctuations, while $g^{ret}$ contains the spectral information, which also encodes dissipation.

In the contour basis, this relation reads

$$\begin{aligned} g^<(\omega) &= \xi\bar{n} \left( g^{ret}(\omega) - g^{adv}(\omega) \right) \\ g^>(\omega) &= (1 + \xi\bar{n}) \left( g^{ret}(\omega) - g^{adv}(\omega) \right) \\ \Rightarrow g^<(\omega) &= \frac{1}{1 + \xi\bar{n}^{-1}} g^>(\omega). \end{aligned} \tag{2.5.22}$$

Note that for fully occupied (empty) fermionic states $g^>$ ($g(^<)$) vanishes in the corresponding eigenspace. In the specific case of thermal equilibrium, where

$$\bar{n} = \frac{1}{e^{\beta h} - \xi} \Rightarrow g^<(\omega) = \xi e^{-\beta h} g^>(\omega), \tag{2.5.23}$$

which we will use in Section 3.3.5 to prove the fluctuation-dissipation theorem for thermal states in interacting systems.

### 2.5.4 *Integrating out degrees of freedom*

Finite systems follow a unitary time-evolution and especially for quadratic systems this leads to recurrence. Both, numerically and physically, this is not desirable as in most systems scattering leads to a decay of these coherent oscillations. On the other hand, infinite systems are, at least without translational symmetry, difficult to treat numerically. Luckily, in many cases valuable information about the state of the system can be extracted by only computing local Green's functions of a quadratic Hamiltonian in a small region of the system. In this section we will describe the established method to obtain such local Green's functions in pedagogical fashion without relying on the path-integral formalism or the language of perturbation theory.[3]

3 We will comment on the latter in Chapter 3.

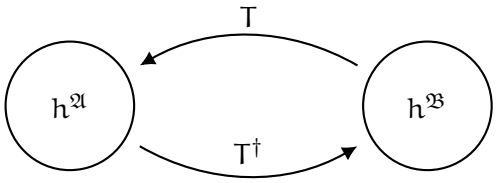


Figure 2.2: Pictorial representation of the Hamiltonian in Equation 2.5.24, if a system is decomposed in two parts $h^{\mathfrak{A},\mathfrak{B}}$ and a coupling T.

Consider a non-interacting Hamiltonian that consists of two separate parts of sizes $N_k$, $k = \mathfrak{A}, \mathfrak{B}$ and a quadratic coupling (see Figure 2.2):

$$\begin{aligned} H = &\sum_{n,m\in\underline{N_{\mathfrak{A}}}} h^{\mathfrak{A}}_{n,m} c^\dagger_n c_m + \sum_{n,m\in\underline{N_{\mathfrak{B}}}} h^{\mathfrak{B}}_{n,m} c^\dagger_{n+N_{\mathfrak{A}}} c_{m+N_{\mathfrak{A}}} \\ &+ \sum_{\substack{n\in\underline{N_{\mathfrak{A}}}\\ m\in\underline{N_{\mathfrak{B}}}}} T_{n,m} c^\dagger_n c_{m+N_{\mathfrak{A}}} + \text{h.c.} \\ =& c^\dagger \begin{pmatrix} h^{\mathfrak{A}} & T \\ T^\dagger & h^{\mathfrak{B}} \end{pmatrix} c \\ & h^{\mathfrak{A}} \in \mathbb{C}^{N_{\mathfrak{A}}\times N_{\mathfrak{A}}},\ h^{\mathfrak{B}} \in \mathbb{C}^{N_{\mathfrak{B}}\times N_{\mathfrak{B}}},\ T \in \mathbb{C}^{N_{\mathfrak{A}}\times N_{\mathfrak{B}}}, \end{aligned} \tag{2.5.24}$$

where we use the short-hand $\underline{k} = \{1, \dots, k\}$ for $k \in \mathbb{N}$. Employing the same block-matrix notation for the Green's function yields

$$g(\omega) = \begin{pmatrix} g_{\mathfrak{A}} & g_{\mathfrak{A},\mathfrak{B}} \\ g_{\mathfrak{B},\mathfrak{A}} & g_{\mathfrak{B}} \end{pmatrix}, \tag{2.5.25}$$

where we use the short-hand $g_{\mathfrak{A},\mathfrak{A}} = g_{\mathfrak{A}}$. We aim to obtain $g_{\mathfrak{A}}$ *without* explicitly computing any of the other blocks and most importantly (under some conditions) without any operations that scale with $N_{\mathfrak{B}}$, as we will later consider $N_{\mathfrak{B}} \gg 1$.

#### 2.5.4.1 *... in frequency-space*

As the retarded and advanced Green's functions of a free system are independent of the initial configuration we can immediately work in the frequency-basis. The coupling between parts of the system can be characterized in terms of the *hybridization* function[4]

$$\Gamma_{\mathfrak{A}}(\omega) = \frac{i}{2} T \left( g^{\text{ret}}_{\mathfrak{B},\text{dec}}(\omega) - g^{\text{adv}}_{\mathfrak{B},\text{dec}}(\omega) \right) T^\dagger \ \in \ \mathbb{C}^{N_{\mathfrak{A}}\times N_{\mathfrak{A}}} \tag{2.5.26}$$

$$g^{\text{ret}}_{\mathfrak{B},\text{dec}}(\omega) = \frac{1}{\omega - h^{\mathfrak{B}} + i0} \tag{2.5.27}$$

4 Conventions for the prefactor differ.

where the subscript *dec* indicates, that the Green's functions are to be obtained in the decoupled (i.e. $T = 0$) system. This hybridization function encodes information about the available states in system $\mathfrak{B}$ as well as their coupling to system $\mathfrak{A}$. It does, however, not contain any information about the occupation of these states. By decomposing this into the eigenbasis of the Hamiltonian of subsystem $\mathfrak{B}$ (compare Equation 2.5.15)

$$\begin{aligned}\Gamma_{\mathfrak{A}}(\omega) &= \pi \sum_k \delta(\omega - \epsilon_k^{\mathfrak{B}}) T \underbrace{v_k^{\mathfrak{B}} \left(v_k^{\mathfrak{B}}\right)^\dagger}_{P} T^\dagger \\ &= \pi \sum_k \delta(\omega - \epsilon_k^{\mathfrak{B}}) TP \left(TP\right)^\dagger\end{aligned} \tag{2.5.28}$$

and employing $P = P^2$, $P = P^\dagger$ we find that $\Gamma_{\mathfrak{A}}(\omega)$ is positive semi-definite for all $\omega$. Furthermore, we note that $\Gamma(\omega)$ is hermitian. For a given, general Hamiltonian it may be difficult to compute $\Gamma$ explicitly, however, in most relevant cases the matrix $T$ is sparse, and features symmetries which allows for an iterative computation of the hybridization (for an example see Section 2.8). Furthermore, it might be sufficient to define $\Gamma$, without specifying the microscopic Hamiltonian.

Using the identity

$$\begin{aligned}&\begin{pmatrix} A & B \\ C & D \end{pmatrix}^{-1} \\ &= \begin{pmatrix} A^{-1} + A^{-1}B(D - CA^{-1}B)^{-1}CA^{-1} & -A^{-1}B(D - CA^{-1}B)^{-1} \\ -(D - CA^{-1}B)^{-1}CA^{-1} & (D - CA^{-1}B)^{-1} \end{pmatrix} \\ &= \begin{pmatrix} (A - BD^{-1}C)^{-1} & -(A - BD^{-1}C)^{-1}BD^{-1} \\ -D^{-1}C(A - BD^{-1}C)^{-1} & D^{-1} + D^{-1}C(A - BD^{-1}C)^{-1}BD^{-1\prime} \end{pmatrix}\end{aligned} \tag{2.5.29}$$

which holds for all matrices where the needed inverses are defined, we easily verify

$$\begin{aligned} g^{\mathrm{ret}}_{n,m}(\omega) &= \left[\omega - \begin{pmatrix} h^{\mathfrak{A}} & T \\ T^\dagger & h^{\mathfrak{B}} \end{pmatrix} + i0\right]^{-1}_{n,m} \qquad \forall\, n, m \in \underline{N_{\mathfrak{A}}} \\ &= \left[\left(\omega - h^{\mathfrak{A}} + i0^+\right) - T\left(\omega - h^{\mathfrak{B}} + I0^+\right)^{-1} T^\dagger\right]^{-1}_{n,m} \\ &= \left[\left(g^{\mathrm{ret}}_{\mathfrak{A},\mathrm{dec}}(\omega)\right)^{-1} - T g^{\mathrm{ret}}_{\mathfrak{B},\mathrm{dec}}(\omega) T^\dagger + i0^+\right]^{-1}_{n,m}\end{aligned} \tag{2.5.30}$$

with $g_{i,\mathrm{dec}}$ denoting the retarded Green's function of system $i$ is the absence of the coupling $T$. The second term of Equation 2.5.30 can

be understood as a *self-energy*, a concept the we will elaborate on in Chapter 3:

$$\Sigma^{\mathrm{ret}}(\omega) = T g^{\mathrm{ret}}_{\mathfrak{B},\mathrm{dec}}(\omega) T^{\dagger} \tag{2.5.31}$$

$$= \frac{1}{\pi} \int d\omega' \mathcal{P} \left( \frac{\Gamma(\omega')}{\omega - \omega'} \right) - i\Gamma(\omega) \tag{2.5.32}$$

$$\Rightarrow \qquad g^{\mathrm{ret}}_{\mathfrak{A}}(\omega) = \left[ \left( g^{\mathrm{ret}}_{\mathfrak{A},\mathrm{dec}}(\omega) \right)^{-1} - \Sigma^{\mathrm{ret}}(\omega) + i0^{+} \right]^{-1} \tag{2.5.33}$$

As $\Gamma(\omega)$ is hermitian and positive semi-definite we note for the spectrum of $\Sigma^{\mathrm{ret}}$ that

$$\mathrm{Im}\left[\sigma(\Sigma^{\mathrm{ret}}(\omega))\right] \leqslant 0, \tag{2.5.34}$$

where the equality only holds if some parts of the system effectively decouple at a given energy. This is in accordance with the theorem of analyticity (see Section 2.4). For a finite system $\mathfrak{B}$ the spectrum will be real for almost all frequencies.

If the entire system is prepared in an equilibrium configuration described by single-particle correlations $\bar{n}$, we have discussed in Section 2.5.3, that knowledge of $g^{\mathrm{ret}}(\omega)$ is sufficient to compute the Keldysh component:

$$g^{K}_{\mathfrak{A}}(\omega) = (1 + 2\xi\bar{n}) \left[ g^{\mathrm{ret}}_{\mathfrak{A}}(\omega) - g^{\mathrm{adv}}_{\mathfrak{A}}(\omega) \right]. \tag{2.5.35}$$

This is, however, not usually the scenario we want to consider; there are situations, where the system as a whole is not in equilibrium and thus considerations of Section 2.5.3 do not apply. For those cases, we have to consider the time-dependent problem.

#### 2.5.4.2 *... in time-space*

In this section, we restrict ourselves to the case of a constant Hamiltonian; the more general case of a time-dependent Hamiltonian will also be considered in Chapter 3, where we introduce a more convenient formalism to discuss these problems. For real time space, we use:

$$\begin{aligned} M &= \begin{pmatrix} A & B \\ C & D \end{pmatrix} \\ \Rightarrow \exp[M]_{1,2} &= \int_0^1 d\tau \exp[M\tau]_{1,1} \, B \exp[D(1-\tau)] \end{aligned} \tag{2.5.36}$$

for any matrices $A, B, C, D$ and where the subscripts denote block-indices.

PROOF: To prove this, we note that

$$\forall k \in \mathbb{N} \exists! n \in \mathbb{N}^0 \ni \left(M^k\right)_{1,2} = \left(M^n\right)_{1,1} M_{1,2} M_{2,2}^{k-1-n} \tag{2.5.37}$$

Hence

$$\begin{aligned}
\left(e^M\right)_{1,2} &= \sum_{k\in\mathbb{N}_0} \frac{1}{k!} \left(M^k\right)_{1,2} \\
&= \sum_{k\in\mathbb{N}} \sum_{n\in\underline{k-1}} \frac{1}{k!} \left(M^n\right)_{1,1} B D^{k-n-1} \\
&= \sum_{m\in\mathbb{N}_0} \sum_{n\in\mathbb{N}_0} \frac{1}{(n+m+1)!} \left(M^n\right)_{1,1} B D^m \\
&= \sum_{m\in\mathbb{N}_0} \sum_{n\in\mathbb{N}_0} \frac{1}{n!m!} \int_0^1 d\tau\, \tau^n (1-\tau)^m \left(M^n\right)_{1,1} B D^m \\
&= \int_0^1 d\tau \exp\left[\begin{pmatrix} A & B \\ C & D \end{pmatrix}\right]_{1,1} B \exp[D(1-\tau)]
\end{aligned} \tag{2.5.38}$$

□

In terms of retarded Green's functions this reads

$$g^{ret}_{\mathfrak{A},\mathfrak{B}}(t|t') = \int_{-\infty}^{\infty} d\tau\; g^{ret}_{\mathfrak{A}}(t|\tau) T g^{ret}_{\mathfrak{B},dec}(\tau|t'). \tag{2.5.39}$$

Similarly one proves

$$\begin{aligned}
\exp\left[\begin{pmatrix} A & B \\ C & D \end{pmatrix}\right]_{1,1} &= \exp(A) + \int_0^1 d\tau_1 \int_0^{\tau_1} d\tau_0 \exp\left[\begin{pmatrix} A & B \\ C & D \end{pmatrix} \tau_0\right]_{1,1} \\
&\quad \times B \exp[D(\tau_1 - \tau_0)] C \exp[A(1-\tau_1)]
\end{aligned} \tag{2.5.40}$$

Translated to Green's functions, this can be understood as

$$\begin{aligned}
g^{ret}_{\mathfrak{A}}(t|t') &= g^{ret}_{\mathfrak{A},dec}(t|t') \\
&\quad + \int_{-\infty}^{\infty} dt_1 \int_{-\infty}^{\infty} dt_2\; g^{ret}_{\mathfrak{A}}(t|t_1) T g^{ret}_{\mathfrak{B},dec}(t_1|t_2) T^\dagger g^{ret}_{\mathfrak{A},dec}(t_2|t').
\end{aligned} \tag{2.5.41}$$

In the case of a time-translation invariant Hamiltonian all the appearing Green's functions are time-translation invariant. This allows for a straightforward Fourier transform of these results

$$\begin{aligned}
g^{ret}_{\mathfrak{A},\mathfrak{B}}(\omega) &= g^{ret}_{\mathfrak{A}}(\omega) T g^{ret}_{\mathfrak{B},dec}(\omega) \\
g^{ret}_{\mathfrak{A}}(\omega) &= g^{ret}_{\mathfrak{A},dec}(\omega) - g^{ret}_{\mathfrak{A}}(\omega) T g^{ret}_{\mathfrak{B},dec}(\omega) T^\dagger g^{ret}_{\mathfrak{A},dec}(\omega)
\end{aligned} \tag{2.5.42}$$

which reduces to the same result we obtained in Equation 2.5.30.

To obtain the Keldysh component of the Green's function we employ Equation 2.5.39 and write:

$$\begin{aligned}
&g^{K}_{\mathfrak{A}}(t|t') \\
&= -i\left[g^{ret}(t|t_0)(\mathbb{1}+2\xi\bar{n})g^{adv}(t_0|t')\right]_{\mathfrak{A},\mathfrak{A}} \\
&= -i\sum_{k,l\in\{\mathfrak{A},\mathfrak{B}\}} g^{ret}_{\mathfrak{A},k}(t|t_0)(\mathbb{1}+2\xi\bar{n})_{k,l}g^{adv}_{l,\mathfrak{A}}(t_0|t') \\
&= -i g^{ret}_{\mathfrak{A}}(t|t_0)\,(1+2\xi\bar{n})_{\mathfrak{A}}\,g^{adv}_{\mathfrak{A}}(t_0|t') \\
&\quad -i\int_{t_0}^{\infty} d\tau\; g^{ret}_{\mathfrak{A}}(t|\tau)Tg^{ret}_{\mathfrak{B},\mathfrak{B},dec}(\tau|t_0)\,(1+2\xi\bar{n})_{\mathfrak{B},\mathfrak{A}}\,g^{adv}_{\mathfrak{A}}(t_0|t') \\
&\quad -i\int_{t_0}^{\infty} d\tau' g^{ret}_{\mathfrak{A}}(t|t_0)\,(1+2\xi\bar{n})_{\mathfrak{A},\mathfrak{B}}\,g^{adv}_{\mathfrak{B},dec}(t_0|\tau')T^{\dagger}g^{adv}_{\mathfrak{A}}(\tau'|t') \\
&\quad -i\iint_{t_0}^{\infty} d\tau d\tau' g^{ret}_{\mathfrak{A}}(t|\tau)Tg^{ret}_{\mathfrak{B},dec}(\tau|t_0)\,(1+2\xi\bar{n})_{\mathfrak{B}} \\
&\qquad g^{adv}_{\mathfrak{B},dec}(t_0|\tau')T^{\dagger}g^{adv}_{\mathfrak{A}}(\tau'|t').
\end{aligned} \tag{2.5.43}$$

As the decoupled retarded and advanced Greens are block-diagonal we can identify the evolution of the single-particle correlations in the closed system

$$g^{K}_{X,Y,dec}(t|t') = -ig^{ret}_{X,X,dec}\,(1+2\xi\bar{n})_{X,Y}\,g^{adv}_{Y,Y,dec}\;\forall\; X,Y\in\{\mathfrak{A},\mathfrak{B}\}. \tag{2.5.44}$$

Therefore, the Keldysh Green's function within system $\mathfrak{A}$ can be expressed as

$$\begin{aligned}
&g^{K}_{\mathfrak{A}}(t|t') \\
&= g^{ret}_{\mathfrak{A}}(t|t_0)g^{K}_{\mathfrak{A},dec}(t_0|t_0)g^{adv}_{\mathfrak{A}}(t_0|t') \\
&\quad + \int_{t_0}^{\infty} d\tau\; g^{ret}_{\mathfrak{A}}(t|\tau)Tg^{K}_{\mathfrak{B},\mathfrak{A},dec}(\tau|t_0)g^{adv}_{\mathfrak{A}}(t_0|t') \\
&\quad + \int_{t_0}^{\infty} d\tau' g^{ret}_{\mathfrak{A}}(t|t_0)g^{K}_{\mathfrak{A},\mathfrak{B},dec}(t_0|\tau')T^{\dagger}g^{adv}_{\mathfrak{A}}(\tau'|t') \\
&\quad + \iint_{t_0}^{\infty} d\tau d\tau' g^{ret}_{\mathfrak{A}}(t|\tau)Tg^{K}_{\mathfrak{B},dec}(\tau|\tau')T^{\dagger}g^{adv}_{\mathfrak{A}}(\tau'|t').
\end{aligned} \tag{2.5.45}$$

To study the stationary state that is reached after a long evolution, we send $t_0 \to -\infty$. For a large system $\mathfrak{B}$, $g^{ret}_{\mathfrak{A}}(t|t_0)$ will typically decay[5]: expressed in the eigenbasis $\{\epsilon_k, \nu_k\}$ of the time-independent Hamiltonian

$$\left(e^{-ih(t-t_0)}\right)_{i,j} = \sum_k e^{-i\epsilon_k(t-t_0)}\nu^{*}_{k,i}\nu_{k,j} \tag{2.5.46}$$

5 If $g^{ret}_{\mathfrak{A}}$ does not decay we can not expect a stationary state to exist.

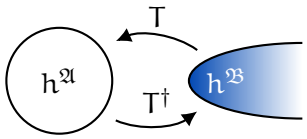


Figure 2.3: Pictorial representation of the Hamiltonian in Equation 2.5.24 for a small $h^{\mathfrak{A}}$ and large $h^{\mathfrak{B}}$. If the system $h^{\mathfrak{B}}$ acts as a *reservoir*, we depict it as an open, colored ellipse to indicate it's size.

will dephase as long as the single-particle indices overlap with many eigenstates of different single-particle energies.[6] Under these conditions, the first term can be neglected. We will call such a subsystem $\mathfrak{B}$ *reservoir*. The second and third term vanish if we assume that the initial configuration has no single-particle correlations between the two systems (as in the decoupled systems these correlations will remain zero). This leaves us with the fourth term. If system $\mathfrak{B}$ is initially prepared in an equilibrium configuration defined by a distribution function $n(\omega)$ (see Equation 2.5.19) each of the Green's functions becomes time-translation invariant (note, that the retarded and advanced Green's function of a free, time-independent Hamiltonian are always time-translation invariant) and we obtain

$$\begin{aligned} g^K_{\mathfrak{A}}(\omega) &= g^{ret}_{\mathfrak{A}}(\omega) T g^K_{\mathfrak{B},dec}(\omega) T^\dagger g^{adv}_{\mathfrak{A}}(\omega) \\ &= (1 + 2\xi n(\omega)) g^{ret}_{\mathfrak{A}}(\omega) T \left( g^{ret}_{\mathfrak{B},dec}(\omega) - g^{adv}_{1,1,dec}(\omega) \right) T^\dagger g^{adv}_{\mathfrak{B}}(\omega) \\ &= g^{ret}_{\mathfrak{A}}(\omega) \underbrace{(-2i)(1 + 2\xi n(\omega)) \Gamma_{\mathfrak{A}}(\omega)}_{\Sigma^K(\omega)} g^{adv}_{\mathfrak{B}}(\omega) \end{aligned} \tag{2.5.47}$$

in frequency space. Note that the stationary state in subsystem $\mathfrak{A}$ is characterized by the *initial* configuration of subsystem $\mathfrak{B}$ and is independent of the initial configuration in subsystem $\mathfrak{A}$.

### 2.5.4.3 *Systems consisting of multiple subsystems*

The results from the previous section can easily be generalized to any finite number of reservoirs coupled to the system (see Figure 2.4):

$$H = c^\dagger \begin{pmatrix} h^0 & T_1 & \cdots & \cdots & T_{N_{res}} \\ T_1^\dagger & h^1 & 0 & \cdots & 0 \\ \vdots & 0 & \ddots & & \vdots \\ \vdots & \vdots & & \ddots & \vdots \\ T_{N_{res}}^\dagger & 0 & \cdots & 0 & h^{N_{res}} \end{pmatrix} c. \tag{2.5.48}$$

6 For finite systems, this is only true until the revival time of the system is reached. Making the system larger will increase the revival time, hence we are usually interested in the well defined order of limits, where the system-size is sent to infinity *before* the limit $t_0 \to -\infty$.

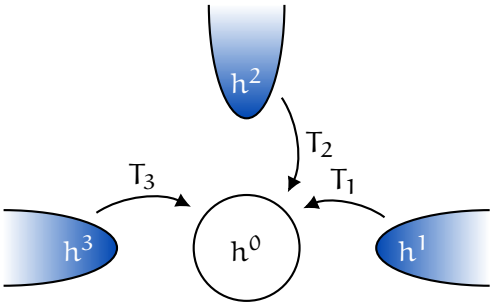


Figure 2.4: Pictorial representation of the Hamiltonian in Equation 2.5.48 if subsystems $1,\dots,N_{res}$ act as reservoirs.

We use this opportunity to summarize out findings. The corresponding retarded self-energy acting on system 0 reads:

$$\begin{aligned}\Sigma_0^{ret}(t'|t) &= \sum_{r\in\underline{N_{res}}} T_r g_{r,dec}^{ret}(t'|t) T_r^\dagger \\ &= \sum_r \frac{1}{\pi}\int d\omega' \mathcal{P}\left[\frac{\Gamma^r(\omega')}{\omega-\omega'}\right] - i\Gamma^r(\omega) \\ g_0^{ret}(t|t') &= g_{0,dec}^{ret}(t|t') \\ &\quad + \int_{-\infty}^{\infty} dt_1 \int_{-\infty}^{\infty} dt_2\; g_0^{ret}(t|t_1)\Sigma_0^{ret}(t_1|t_2) g_{0,dec}^{ret}(t_2|t')\end{aligned}$$

When Fourier transformed, these read

$$\begin{aligned}\Sigma^{ret}(\omega) &= \sum_{r\in\underline{N_{res}}} T_n g_{r,dec}^{ret}(\omega) T_r^\dagger \\ g_0^{ret}(\omega) &= \left[\left(g_{0,dec}^{ret}\right)^{-1} - \Sigma^{ret}(\omega)\right]^{-1}.\end{aligned} \tag{2.5.49}$$

Under the same assumptions we needed to arrive at Equation 2.5.47, we find:

$$\begin{aligned}\Sigma_0^K(t|t') &= \sum_{r\in\underline{N_{res}}} T_r g_{r,dec}^K(t|t') T_r^\dagger \\ g_0^K(t|t') &= \iint_{t_0}^{\infty} d\tau d\tau' g_0^{ret}(t|\tau)\Sigma_0^K(\tau|\tau') g_0^{adv}(\tau'|t') \\ \Sigma_0^K(\omega) &= \sum_{r\in\underline{N_{res}}} T_r g_{r,dec}^K(\omega) T_r^\dagger \\ &= \sum_{r\in\underline{N_{res}}} (-2i)(1+2\xi n_r(\omega))\Gamma_r(\omega) \\ g_0^K(\omega) &= g_0^{ret}(\omega)\Sigma_0^K(\omega) g_0^{adv}(\omega).\end{aligned} \tag{2.5.50}$$

Note that not all reservoirs are assumed to be prepared in the same equilibrium configuration.

Instead of discussing the details of microscopic reservoirs attached to some system of interest, we will typically only specify the microscopic Hamiltonian within the system $H^{sys}$. We will characterize the

reservoirs solely by their hybridization function and their initial distribution function.

### 2.5.5 *FDT for local Green's function in a free system coupled to reservoirs*

As we have seen in Section 2.5.3, a non-interacting system in an equilibrium configuration features a special symmetry described by the fluctuation-dissipation theorem. Here, we will discuss how this concept can be generalized to an out-of-equilibrium situation, where a small system is coupled to a number of reservoirs, each of which is considered to be initially prepared according to some distribution function $n^r(\omega)$. As discussed in Section 2.5.4, the free Green's functions restricted to the subsystem of interest in the stationary state read:

$$\begin{aligned} g^{\text{ret}}(\omega) &= \frac{1}{\omega - h^{\text{sys}} - \Sigma^{\text{ret}}_{\text{res}}(\omega)} \\ g^{\text{adv}}(\omega) &= g^{\text{ret}}(\omega)^\dagger \\ g^{\text{K}}(\omega) &= -2ig^{\text{ret}}(\omega) \sum_r \left[1 + 2\xi n^r(\omega)\right] \Gamma^r(\omega) g^{\text{adv}}(\omega) \end{aligned}$$

with

$$\Sigma^{\text{ret}}_{\text{res}}(\omega) = \sum_r \frac{1}{\pi} \int d\omega' \mathcal{P}\left[\frac{\Gamma^r(\omega')}{\omega - \omega'}\right] - i\Gamma^r(\omega)$$

and positive semi-definite, hermitian hybridization functions $\Gamma^r(\omega)$.

If all reservoirs are initially governed by the same single-particle correlations $n^r \equiv n$ (see Equation 2.5.6) we find:

$$\begin{aligned} g^{\text{K}}(\omega) &= -2i\left[1 + 2\xi n(\omega)\right] g^{\text{ret}}(\omega) \sum_r \Gamma^r(\omega) g^{\text{adv}}(\omega) \\ &= -i\left[1 + 2\xi n(\omega)\right] \left[g^{\text{ret}}(\omega) - g^{\text{adv}}(\omega)\right] \end{aligned} \tag{2.5.51}$$

where in the second line we used $\Gamma^r = (\Gamma^r)^\dagger$. This is a generalization of the fluctuation-dissipation theorem discussed in Section 2.5.3, as it applies to subsystems, that were not initially prepared in an equilibrium configuration but instead evolved into one.[7] As we discussed in Section 2.5.4, this only holds, if the reservoirs are much larger than the subsystem explicitly considered and excitations can dissipate into the reservoirs. By comparing to the result in Equation 2.5.35, we note that in such systems details of the original preparation of the (small) subsystem under consideration will not influence the value of local (single-particle) observables after a long time.

7 There is no need to specify the initial configuration of the small system under consideration. Furthermore, the stationary state will feature single-particle correlations between all parts of the system which are not present initially.

We will later see (compare Section 3.3.5), that this relation can be extended further to include interacting Hamiltonians and how an approximation to the full Green's function can preserve this important symmetry.

## 2.6 EFFECTIVE DISTRIBUTION FUNCTION

In Sections 2.5.3 and 2.5.5, we have seen how the fluctuation-dissipation theorem comes about in equilibrium and even locally in the steady state as long as the excitation above the equilibrium configuration can dissipate. We also know, that such a simple relation can not hold out of equilibrium.[8] However, we still strive for an generalization of this concept that allows us to interpret close-to-equilibrium physics or just formally simplify calculations.

The starting point of this endeavor is local Green's function within some subsystem in presence of some self-energy.

$$\begin{aligned} G^{ret}(\omega) &= \frac{1}{\omega - h^{sys} - \Sigma^{ret}(\omega)} \\ G^{adv}(\omega) &= G^{ret}(\omega)^\dagger \\ G^{K}(\omega) &= -iG^{ret}(\omega)\Sigma^{K}(\omega)G^{adv}(\omega). \end{aligned}$$

A similar form to the FDT can be achieved by introducing $N(\omega) \in \mathbb{C}^{N\times N}$ such, that [Jako9; SBD16; Kam11]

$$\begin{aligned} \Sigma^{K}(\omega) = &\quad \left[h^{sys} + \Sigma^{ret}(\omega)\right][1 + 2\xi N(\omega)] \\ &- [1 + 2\xi N(\omega)]\left[h^{sys} + \Sigma^{adv}(\omega)\right] \\ \Rightarrow G^{K}(\omega) = &-i\frac{1}{\omega - h^{sys} - \Sigma^{ret}(\omega)}\Sigma^{K}(\omega)\frac{1}{\omega - h^{sys} - \Sigma^{adv}(\omega)} \\ = &-i\left[G^{ret}(\omega)\,[1 + 2\xi N(\omega)] - [1 + 2\xi N(\omega)]\,G^{adv}(\omega)\right]. \end{aligned} \tag{2.6.1}$$

The first line of Eq. 2.6.1 is a Sylvester equation. It has a unique solution if and only if $\Sigma^{ret}(\omega)$ and $\Sigma^{adv}(\omega)$ have no common eigenvalues. This is, for example, the case if $\operatorname{Im}\sigma_{\Sigma^{ret}(\omega)} < 0\ \forall\omega$. As we have discussed previously (see Equation 2.5.34) this is ensured if all parts of the system are coupled to at least one reservoir.

In the previous section, we have seen that in equilibrium for a free system $N(\omega) = n(\omega)\mathbb{1}$. Out of equilibrium, $N(\omega)$ is a hermitian matrix, that can be loosely interpreted as an effective distribution function.

As a word of warning, let us stress again, that, if $N$ is not diagonal, the physical interpretation is difficult and $N$ is a mostly formal object.

8 This is, because the space of single-particle Green's functions that can be represented in presence of the FDT can be fully exhausted with equilibrium configurations

Furthermore, knowledge of the local Green's functions is not sufficient to obtain local elements of the effective distribution function of the entire system out of equilibrium.

To compute the effective distribution function, we use the `CTRSYL` routine from `LAPACK` [And+99]. The necessary Shur decomposition is computed with the `Eigen` library [GJ+10].

## 2.7 OBSERVABLES

As we discussed in Section 2.3, all single-particle observables can be extracted from the Keldysh Green's functions. Here, we are going to discuss some of important examples.

### 2.7.1 *Spectral function*

As we have seen in Equation 2.5.15, the imaginary part of the retarded Green's function in a non-interacting system contains information about the spectrum; as a generalization, we define the spectral function as

$$A_i(\omega) = \frac{i}{2\pi}\left[G^{\text{ret}}(\omega) - G^{\text{adv}}(\omega)\right]_{i,i} \tag{2.7.1}$$

$$= \frac{-1}{\pi}\operatorname{Im}\left[G^{\text{ret}}_{i,i}(\omega)\right]. \tag{2.7.2}$$

The prefactor is chosen such, that

$$\int d\omega\, A(\omega) = \lim_{t\to t_0} i(G^{\text{ret}}(t,t_0) - G^{\text{adv}}(t,t_0)) = \mathbb{1} \tag{2.7.3}$$

Note that while $\lim_{t\to t_0} G^{\text{ret/adv}}(t|t_0)$ are not individually well defined, the limit of the difference is.

The spectral function is of particular interest, as it can be probed using angle-resolved photoemission spectroscopy (ARPES, for a review see [Yan+18]).

### 2.7.2 *Occupation*

The occupation of a state (or site in the spatial basis) at time $t$ can be computed using

$$n_i(t) = \left\langle c_i^\dagger(t) c_i(t)\right\rangle_{\rho_0} \tag{2.7.4}$$

which, expressed in terms of real-time Green's functions reads:

$$n_i(t) = i\xi G^<_{i,i}(t|t) = \frac{\xi}{2}\left(iG^K_{i,i}(t|t) - 1\right). \tag{2.7.5}$$

In a stationary state this becomes

$$n_i = \frac{\xi}{2}\left(i\int_{-\infty}^{\infty} G^K_{i,i}(\omega)\frac{d\omega}{2\pi} - 1\right). \tag{2.7.6}$$

If the stationary state is defined by a scalar distribution function (see Section 2.5.5 as well as Section 3.3.5), this simplifies to

$$\begin{aligned} n_i =& \frac{\xi}{2}\left(i\int_{-\infty}^{\infty}(1+2\xi n(\omega))\left(G^{ret}_{i,i}(\omega)-G^{adv}_{i,i}(\omega)\right)\frac{d\omega}{2\pi}-1\right) \\ =& \frac{\xi}{2}\left(\int_{-\infty}^{\infty}(1+2\xi n(\omega))A_i(\omega)d\omega-1\right). \\ =& \int_{-\infty}^{\infty} n(\omega)A_i(\omega)d\omega. \end{aligned} \tag{2.7.7}$$

where we used the spectral functions defined above.

### 2.7.3 *Particle current*

In contrast to the occupation, the correct operator to obtain the particle current is dependent on the model. The usual definition of a current is obtained when separating a closed system into two parts, let us call them *left* and *right* (abbreviated L and R). The current from left to right is then defined as the change in particles in the right subsystem:

$$I(t) = \frac{dn_R(t)}{dt} = -\frac{dn_L(t)}{dt} \tag{2.7.8}$$

$$= i\left\langle [H, n_R]\right\rangle. \tag{2.7.9}$$

Note that the first line is not well defined for infinite systems while the second line is. For a model with a single-particle Hamiltonian $h$ and a density-density interaction only operators that connect the two subsystems contribute to the commutator; a density-density term (such as a density-density interaction) commutes with a number operator.

$$\begin{aligned} I(t) &= i\sum_{i\in L,\ j\in R}\left\langle\left[h_{i,j}c_i^\dagger c_j + h_{j,i}c_j^\dagger c_i, c_j^\dagger c_j\right]\right\rangle \\ &= 2\sum_{i\in L,\ j\in R}\mathrm{Im}\left(h_{i,j}\left\langle c_i^\dagger(t)c_j(t)\right\rangle_{\rho_0}\right) \\ &= 2\sum_{i\in L,\ j\in R}\mathrm{Im}\left(i\xi h_{i,j}G^<_{j,i}(t|t)\right) \\ &= 2\sum_{i\in L,\ j\in R}\mathrm{Im}\left(\frac{\xi}{2}h_{i,j}\left(iG^K_{j,i}(t|t)\right)\right) \\ &= \frac{\xi}{2}\mathrm{Tr}\left(h_{L,R}G^K_{R,L}(t|t) - h_{R,L}G^K_{L,R}(t|t)\right) \end{aligned} \tag{2.7.10}$$

and accordingly in the stationary state

$$I = \int\frac{d\omega}{4\pi}\xi\,\mathrm{Tr}\left(h_{L,R}G^K_{R,L}(\omega) - h_{R,L}G^K_{L,R}(\omega)\right) \tag{2.7.11}$$

To understand this result better, it is instructive to investigate a scenario, where subsystem L acts as a reservoirs prepared in an equilibrium configuration initially and then analyzing the stationary state that is reached after a long evolution. We use the equations (derivation is analogous to Equation 2.5.45)[9]

$$\begin{aligned} G^K_{R,L}(\omega) &= G^{ret}_R(\omega) h_{R,L} G^K_{L,dec}(\omega) + G^K_R(\omega) h_{R,L} G^{adv}_{L,dec}(\omega) \\ G^K_{L,R}(\omega) &= G^{ret}_{L,dec}(\omega) h_{L,R} G^K_R(\omega) + G^K_{L,dec}(\omega) h_{L,R} G^{adv}_R(\omega). \end{aligned} \tag{2.7.12}$$

Identifying $h_{R,L}\left(G^{ret}_{L,dec} - G^{adv}_{L,dec}\right) h_{L,R} = -2i\Gamma$ and using the FDT for system L we find [MW92]

$$\begin{aligned} &I_{L\to R} \\ &= \frac{i\xi}{2\pi} \int d\omega \, \mathrm{Tr}\, \Gamma(\omega) \left\{ \left[1 + 2n^L(\omega)\right] \left[G^{ret}_R(\omega) - G^{adv}_L(\omega)\right] - G^K_R(\omega) \right\}. \end{aligned} \tag{2.7.13}$$

Usually, the support of $\Gamma$ will only contain a few sites, this it is sufficient to know $G_R$ in that region, even if subsystem R will generally be infinite.

As we discussed in Section 2.6, $G^K$ can be expressed in terms of an effective distribution operator in many cases, resulting in [Jako9]

$$\begin{aligned} I_{L\to R} = \frac{i\xi}{2\pi} \int d\omega \, \mathrm{Tr}\, \Gamma(\omega) \Big\{ & G^{ret}_R(\omega) \left[n^L(\omega) - N(\omega)\right] \\ & - \left[n^L(\omega) - N(\omega)\right] G^{adv}_R(\omega) \Big\}. \end{aligned} \tag{2.7.14}$$

Hence, as one would expect, the current relates to the number of available states (encoded in $G^{ret}$) and transport occurs, if states are occupied in system L while empty in system R or vice versa.

Note that if either system L or R are finite, the steady-state current has to vanish to obey particle number conservation. As the arguments above only hold for an infinite system L (as only infinite systems can act as a reservoir) we shall demonstrate this only in the case, where system R is finite: In that case, $N(\omega)$ in the steady state will equilibrate, resulting in a vanishing current.

An especially simple form can be achieved in a non-interacting system coupled to a set of reservoirs characterized by $\Gamma^r(\omega)$, $n^r(\omega)$, $r = 1, \ldots, N_{res}$. In this case the Green's functions can be expressed as

$$\begin{aligned} g^K &= -i g^{ret} \sum_{r'} \left[1 + 2\xi n^{r'}(\omega)\right] \Gamma^{r'} g^{adv} \\ g^{ret} - g^{adv} &= g^{ret} \left[ \left(g^{adv}\right)^{-1} - \left(g^{ret}\right)^{-1} \right] g^{adv} = -2i g^{ret} \sum_{r'} \Gamma^{r'} g^{adv}. \end{aligned} \tag{2.7.15}$$

9 At this point, it is clear that this holds true for quadratic Hamiltonians; later on this can be easily generalized to interacting Hamiltonians, as long as the interaction is restricted to system R.

The current out of reservoir $r$ (compare Equation 2.7.13) can therefore be expressed as (compare [Bö86; Lan57])

$$\begin{aligned} I_r &= \sum_{r'} I_{r,r'} \\ &= \sum_{r'} \frac{2}{\pi} \int d\omega \left[ n^r(\omega) - n^{r'}(\omega) \right] \mathrm{Tr} \left[ \Gamma^r(\omega) g^{\mathrm{ret}}(\omega) \Gamma^{r'} g^{\mathrm{adv}}(\omega) \right] \end{aligned} \tag{2.7.16}$$

where the individual contributions $I_{r,r'}$ can be interpreted as the current from reservoir $r$ to $r'$, and the trace acts as the transmission coefficient.

## 2.8 EXAMPLE: QUADRATIC TIGHT-BINDING CHAINS

One-dimensional tight-binding models are the primary class of models discussed in this thesis. Because of their importance throughout, we will now study the non-interacting case for translation-invariant chains analytically and introduce numerical methods for general 1D chains with nearest-neighbor hopping.

### 2.8.1 *Translationally invariant tight-binding chains*

SEMI-INFINITE CHAINS AS RESERVOIRS Let us consider the case of a tight-binding chain of $N$ sites

$$H = t \sum_{n \in \underline{N-1}} c_n^\dagger c_{n+1} + \mathrm{h.c.}. \tag{2.8.1}$$

It is easy to verify [BP87], that the basis transformation

$$c_i^\dagger = \sqrt{\frac{2}{N+1}} \sum_{l \in \underline{N}} \sin(q_l(i+1)) d_l^\dagger, \quad q_l = \frac{\pi}{N+1}(l+1) \tag{2.8.2}$$

diagonalizes the Hamiltonian

$$H = \sum_{l \in \underline{N}} 2\cos(q_l) d_l^\dagger d \tag{2.8.3}$$

and thus allows us to obtain all Green's functions we desire.

It is, however, instructive, to obtain the two important Green's functions of this system using the results of Section 2.5.4 and the symmetry of the system.

We subdivide this system into two pieces, consisting of the first element and the remaining rest of the infinite chain. Then Equa-

tion 2.5.30 allows us to write the Green's function on the first site as

$$\begin{aligned} N_{\mathfrak{A}} = 1,\ N_{\mathfrak{B}} = N-1 \\ h^{\mathfrak{A}} = 0,\ h^{\mathfrak{B}} = \sum_{k=1}^{N-1} t\left(e_k e_{k+1}^T + e_{k+1} e_k^T\right),\ T = t e_1 e_1^T \\ \Rightarrow g_{1,1}^{\mathrm{ret}}(\omega) = \left[\omega - t g_{2,2,\mathrm{dec}}^{\mathrm{ret}}(\omega) t\right]^{-1} \\ \overset{N\to\infty}{\to} \left[\omega - t g_{1,1}^{\mathrm{ret}}(\omega) t\right]^{-1} \end{aligned} \tag{2.8.4}$$

where we used that for $N \to \infty$ the decoupled rest of the chain is, itself, a semi-infinite tight-binding chain. Solving this equation yields

$$g_{1,1}^{\mathrm{ret}}(\omega) = \frac{1}{2t^2}\left(\omega - \sqrt{\omega^2 - 4t^2}\right) \tag{2.8.5}$$

with $g^{\mathrm{ret}}(\omega) \to 0$ for $\omega \to \infty$ fixes the sign of the square root. The spectral function is therefore given by

$$A_{1,1}(\omega) = \frac{1}{\pi}\operatorname{Im}\left[g_{1,1}^{\mathrm{ret}}(\omega)\right] = \begin{cases} \frac{1}{2t^2\pi}\sqrt{4t^2-\omega^2} & \text{if } |\omega| < 2t \\ 0 & \text{otherwise.} \end{cases} \tag{2.8.6}$$

If we were to couple a system to a semi-infinite tight-binding chain by allowing hopping to the first site of said chain (hence $T \in \mathbb{R}^N$) the characterizing hybridization and corresponding self-energy are given by

$$\Gamma(\omega) = \frac{1}{2t^2} T T^\dagger \sqrt{4t^2-\omega^2}\,\theta(4t^2-\omega^2) \tag{2.8.7}$$

$$\Sigma^{\mathrm{ret}}(\omega) = T T^\dagger \frac{1}{2t^2}\left(\omega - \sqrt{\omega^2-4t^2}\right) \tag{2.8.8}$$

$$\Sigma^{K}(\omega) = -2i(1+2\xi n(\omega))\Gamma(\omega). \tag{2.8.9}$$

THE WIDE-BAND LIMIT FOR RESERVOIRS As we have seen in Sections 2.5.4 and 2.8 the effect of a semi-infinite tight-binding chain coupled to the system only by its first site can be absorbed in a self-energy correction of the form given in Equations 2.8.7, 2.8.8 and 2.8.9. Such a reservoir, however, has multiple disadvantages: as it only has a finite bandwidth, it will generally not thermalize the system. Furthermore, the edges of the band will introduce artifacts that might be undesirable. Lastly, for the low energy theory, the form of the band is irrelevant and thus one usually considers a simplified model.

If the hopping $t$ within the reservoir is much larger than all relevant energy scales in the system of interest, we can consider the limit $t/\omega \to \infty$ resulting in

$$\Gamma = \frac{T T^\dagger}{t} \tag{2.8.10}$$

$$\Sigma^{\mathrm{ret}}(\omega) = -i\frac{T T^\dagger}{t} = -i\Gamma \tag{2.8.11}$$

$$\Sigma^{K}(\omega) = -2i(1+2\xi n(\omega))\Gamma. \tag{2.8.12}$$

with a frequency independent hybridization function $\Gamma$. Note, however, that for the Green's functions in the reservoir themselves this limit is not well defined, as the spectral function goes to zero (pointwise) and the real-time retarded Green's function becomes time local.

LOCAL GREEN'S FUNCTIONS IN THE BULK The local Green's function in the bulk can be obtained similar to the case of a semi-infinite chain. Imagining an infinite chain and interpreting a single site labeled $0$ as system $\mathfrak{A}$ while the remaining system can be understood as two semi-infinite chains:

$$g^{\mathrm{ret}}_{0,0}(\omega) = \left[\omega - t g^{\mathrm{ret}}_{1,1,\mathrm{dec}}(\omega) t - t g^{\mathrm{ret}}_{-1,-1,\mathrm{dec}}(\omega) t\right]^{-1} \tag{2.8.13}$$

$$= \left[\omega - 2t g^{\mathrm{ret}}_{0,0,\mathrm{semi}}(\omega) t\right]^{-1} \tag{2.8.14}$$

$$= \frac{1}{\sqrt{\omega^2 - 4t^2}} \tag{2.8.15}$$

with the spectral function

$$A(\omega) = \frac{1}{\pi} \frac{1}{\sqrt{4t^2 - \omega^2}}. \tag{2.8.16}$$

We will later generalize this procedure to obtain interacting Green's functions in infinite systems (see Chapter 8 and Appendix D).

### 2.8.2 *Computational techniques for general, quadratic tight-binding models*

MODELS In this section, we want to consider how to efficiently compute Green's functions and observables for general quadratic tight-binding models with nearest neighbor hopping but without translational symmetry. To that end, consider the class of Hamiltonians

$$\begin{aligned} H &= \sum_{n \in \underline{N}} \epsilon_n c_n^\dagger c_n + \sum_{n \in \underline{N-1}} t_n c_n^\dagger c_{n+1} + t_n^* c_{n+1}^\dagger c_n \\ &= c^\dagger h c. \end{aligned} \tag{2.8.17}$$

These are represented by a tridiagonal matrix $h$. To efficiently compute Green's functions for these models, we will introduce some special algorithms, that rely on the structure of $h$.

RETARDED GREEN'S FUNCTION IN TIME-DOMAIN To obtain the retarded Green's function in real time, we have to evaluate the time-ordered matrix exponential (assuming $t > t'$):

$$i g^{\mathrm{ret}}(t, t') = \mathcal{T} e^{\int_{t'}^{t} d\tau h(\tau)} \tag{2.8.18}$$

This can be simplified by discretizing the time integration, allowing us to explicitly use the time-ordering to arrive at

$$i g^{\mathrm{ret}}(t, t') = \lim_{\Delta \to 0^+} e^{\Delta \frac{h(t) + h(t-\Delta)}{2}} e^{\Delta \frac{h(t-\Delta) + h(t-2\Delta)}{2}} \cdots e^{\Delta \frac{h(t'+\Delta) + h(t')}{2}}$$

(2.8.19)

where the details of the discretization is irrelevant for a Riemann integrable function $h(t)$. The problem, how to evaluate a matrix exponential for tridiagonal matrices remains, as it will generally be dense and computing dense-dense products is costly. To compute this more efficiently, one can make use of a Trotter decomposition [KMV14; KKK18]. For a tridiagonal matrix $M$ we define the block diagonal matrices $M^A$ and $M^B$ as

$$\begin{aligned} M_{i,i} &= a_i & M_{i,i+1} &= b_i = M^*_{i+1,i} \\ M^A_{i,i} &= \frac{a_i}{2} & M^A_{i,i+1} &= (M^A_{i+1,i})^* = \begin{cases} b_i & i \text{ even} \\ 0 & i \text{ odd} \end{cases} \\ M^B &= M - M^A \end{aligned} \tag{2.8.20}$$

such that $M = M^A + M^B$. The Baker-Campbell-Hausdorff formula then yields

$$\begin{aligned} e^M &= e^{\frac{M^A}{2}} e^{M^B} e^{\frac{M^A}{2}} + \mathcal{O}\left(\|M\|^3\right) \\ &= \lim_{N\to\infty} \prod_{i=1}^{N} e^{\frac{M^A}{2N}} e^{\frac{M^B}{N}} e^{\frac{M^A}{2N}}. \end{aligned}$$

Hence, the error is controlled by the size of $\|M/N\|$, where $\|\cdot\|$ denotes a matrix norm. Each individual matrix exponential is a tridiagonal matrix and can be consecutively multiplied.

As the exponential function is easily evaluated for this kind of block diagonal matrices, the above provides a computationally efficient way to calculate the retarded Green's function. For long time evolution, the computationally most demanding part is the remaining sparse-dense-product, as a product of many tridiagonal matrices has to be considered dense.

KELDYSH GREEN'S FUNCTION IN TIME-DOMAIN As we discussed, for short time intervals $g^{ret}(t,t')$ is well approximated by a sparse matrix but becomes dense for longer intervals. While retarded Green's functions for large time differences can be efficiently computed by successively multiplying the sparse matrices, computing the Keldysh component

$$g^K(t,t') = -ig^{ret}(t,t_0)(1+2\xi\bar{n})g^{adv}(t_0,t') \tag{2.8.21}$$

involves a dense-dense matrix product, even if the initial matrix $\bar{n}$ is sparse. Instead, we can successively obtain the real-time Keldysh Green's function on a given time-grid using

$$\begin{aligned} g^K(t,t') =& -ig^{ret}(t,t_0)(1+2\xi\bar{n})g^{adv}(t_0,t') \\ =& g^{ret}(t,t-\delta_t)g^K(t-\delta_t,t'-\delta_{t'})g^{adv}(t'-\delta_{t'},t'). \end{aligned} \tag{2.8.22}$$

If $\delta_{t^{(\prime)}}$ are sufficiently small, this computation can be performed using only sparse-dense products.

RETARDED GREEN'S FUNCTION IN THE STEADY STATE To obtain the retarded Green's function, we have to invert the matrix $h$. As the inverse of a tridiagonal matrix is generally dense, computing the inverse is at least of complexity $\mathcal{O}\left(N^2\right)$. In fact, as one can easily check, the full inverse can be obtained in $\mathcal{O}\left(N^2\right)$ operations, as solving the linear system $hx = y$ for a given $y \in \mathbb{C}^N$ is in $\mathcal{O}(N)$.

For many circumstances, however, it is sufficient to obtain a small number of the entries of the retarded Green's function. And, as it turns out, there is a specialized algorithm to obtain these. While a algorithm to achieve this for Green's functions was previously introduced [And+04], the algorithm discussed in [Usm94] is simple and sufficient for the course of this work. We define

$$\begin{aligned}
\theta_n &= \epsilon_n \theta_{n-1} - |t_{n-1}|^2 \theta_{n-2}, \quad \theta_{-1} = 0, \theta_0 = 1 \; n = 1, \ldots, N \\
\phi_n &= \epsilon_n \phi_{n+1} - |t_{n+1}|^2 \phi_{i+2}, \quad \phi_{N+1} = 1, \; \phi_{N+2}, \; n = N-1, \ldots, 0.
\end{aligned}$$

All of these can be computed in $\mathcal{O}(N)$ operations. Then the elements of the inverse matrix can be expressed as[10]:

$$\left(A^{-1}\right)_{i,j} = \begin{cases} (-1)^{i+j} t_i t_{i+1} \cdots t_{j-1} \theta_{i-1} \phi_{j+1} / \theta_N & i < j \\ \theta_{i-1} \phi_{i+1} / \theta_n & i = j \\ (-1)^{i+j} t_j^* t_{j+1}^* \cdots t_{j-1}^* \theta_{j-1} \phi_{i+1} / \theta_n & i > j. \end{cases} \tag{2.8.23}$$

This allows us to compute any diagonal band $\left(A^{-1}\right)_{i,i+k}$ for fixed $k$ and all $i$ in $\mathcal{O}(N)$ operations. This allows us, for example, to obtain the local density of states on all sites in $\mathcal{O}(N)$ operations.

SPECIFIC EIGENVALUES The properties of Green's functions at the Fermi-surface in the ground-state are of special importance; to identify the chemical potential at a given number of particles is, however, computationally demanding (generally $\mathcal{O}\left(N^3\right)$). To that end, we will discuss how to computationally obtain the $n$-th *individual* eigenvalue-eigenvector pair of a tridiagonal matrix.

This can be done efficiently using the algorithm presented in Ref. [DP04], which is more suited for computation of individual eigenvectors than more traditional approaches. An implementation of this algorithm has since been included in `LAPACK` [And+99] under the name `dstemr/dstegr`.

Note that there are also fast algorithms to obtain the full spectrum of a tridiagonal matrix in $\mathcal{O}(N \ln N)$ operations, [CR13]. Computing all eigenvectors takes at least $\mathcal{O}\left(N^2\right)$ operations, as they form a dense matrix.

10 To avoid over- or underflows, either a bignum type has to be used or the expressions have to be rewritten appropriately beforehand.

# 3

# PERTURBATION THEORY IN KELDYSH FORMALISM

## 3.1 THE INTERACTION PICTURE

To exactly compute the Keldysh Green's functions including interactions is extremely difficult, if not downright impossible for a given, generic Hamiltonian. Therefore, we need to approximate these objects in a controlled manor. A logical first step is the use of perturbation theory with respect to the part of the Hamiltonian that we can not treat exactly. This chapter presents the established method to do this with a focus on diagrammatic techniques [Ramo7; Jak15; Kel+65; NO88].

We can, and want to treat some parts of the Hamiltonian exactly. To separate these from the difficult to treat parts we introduce the *interaction picture*. Given a decomposition of the Hamiltonian $H(t) = H_0(t) + V(t)$ and $t \geqslant t'$, we define

$$\begin{aligned} U(t,t') &= \mathcal{T} e^{-i\int_{t'}^{t} d\tau H(\tau)} \\ U_0(t,t') &= \mathcal{T} e^{-i\int_{t'}^{t} d\tau H_0(\tau)} \\ u(t,t') &= U_0(t_0,t)U(t,t')U_0(t',t_0) \overset{(*)}{=} \mathcal{T} e^{-i\int_{t'}^{t} d\tau V_{H_0}(\tau)} \\ &\Rightarrow A_H(t) = u(t_0,t)A_{H_0}(t)u(t,t_0) \end{aligned} \tag{3.1.1}$$

To prove the equation marked by $(*)$, one verifies that $U(t,t') = U_0(t,t_0)\mathcal{T} e^{-i\int_{t'}^{t} d\tau V_{H_0}(\tau)} U(t_0,t')$ fulfills the Heisenberg equation for the time evolution operator $\frac{d}{dt}U(t,t') = -iHU(t,t')$. With that, we can rewrite the Heisenberg evolution of some operator $A(t)$ at $t > t_0$ as

$$A_H(t) = \tilde{\mathcal{T}} e^{i\int_{t_0}^{t} V_{H_0}(\tau)d\tau} A_{H_0}(t) \mathcal{T} e^{-i\int_{t_0}^{t} V_{H_0}(\tau)d\tau} \tag{3.1.2}$$

$$= \mathcal{T}_\gamma e^{-i\int_\gamma V_{H_0}(\tau)d\tau} A_{H_0}(t^\pm) \tag{3.1.3}$$

where the choice of the contour index of the time of $A$ is arbitrary. For a $n$-particle Green's function in Keldysh space (compare Equation 2.3.1), this means

$$\begin{aligned} G^{\sigma|\sigma'}_{q|q'}(t|t') =& (-i)^n \left\langle \mathcal{T}_\gamma c_{i_1}(t_1^{\sigma_1}) \cdots c_{i_n}(t_n^{\sigma_n}) c^\dagger_{i'_n}(t_n^{\prime\sigma'_n}) \cdots c^\dagger_{i'_1}(t_1^{\prime\sigma'_1}) \right\rangle_{\rho_0} \\ =& (-i)^n \left\langle \mathcal{T}_\gamma e^{-i\int_\gamma V_{H_0}(\tau)d\tau} c_{i_1,H_0}(t_1^{\sigma_1}) \cdots c^\dagger_{i'_1,H_0}(t_1^{\prime\sigma'_1}) \right\rangle_{\rho_0}. \end{aligned} \tag{3.1.4}$$

Assuming the evolution of operators with respect to $H_0$ is easily computed, this is a natural starting point for an expansion in orders of $V$.

## 3.2 DIAGRAMMATIC PERTURBATION THEORY FOR THE GREEN'S FUNCTION

To simplify the notation, we include the fermionic degrees of freedom, the contour indices as well as the time in a super-index $1 = (i_1, \sigma_1, t_1)$ (compare Section 2.3). The $n$-particle Green's function then reads:

$$\begin{aligned} &G_{1,\dots,n|1',\dots,n'} \\ &= (-i)^n \left\langle \mathcal{T}_\gamma c_1 \cdots c_n c^\dagger_{n'} \cdots c^\dagger_{1'} \right\rangle_{\rho_0} \end{aligned}$$

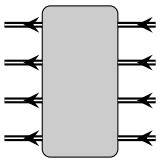

which is represented by a double line in diagrammatic language, as shown on the right for the four-particle Green's function. In the interaction picture with some decomposition $H(t) = H_0(t) + V(t)$, this reads (compare Equation 3.1.4)

$$\begin{aligned} &G_{1,\dots,n|1',\dots,n'} \\ &= (-i)^n \left\langle \mathcal{T}_\gamma e^{-i\int_\gamma V_{H_0}(\tau)d\tau} c^0_1 \cdots c^0_n c^{0\dagger}_n \cdots c^{0\dagger}_1 \right\rangle_{\rho_0}, \end{aligned}$$

where $c^0$ represents the operator evolved with respect to the Hamiltonian $H_0$. Correspondingly, the single-particle Green's function is represented by an individual double line.

$$\begin{aligned} G_{1|1'} &= -i \left\langle \mathcal{T}_\gamma c_1 c^\dagger_{1'} \right\rangle \\ &= -i \left\langle \mathcal{T}_\gamma e^{-i\int_\gamma V_{H_0}(\tau)d\tau} c^0_1 c^{0\dagger}_{1'} \right\rangle \end{aligned}$$



Expanding in orders of $V$ yields

$$\begin{aligned} &G(1,\dots,n|1',\dots,n') \\ &\quad = (-i)^n \sum_k \frac{1}{k!} \int_\gamma d\tau_1 \cdots \int_\gamma d\tau_k \\ &\qquad \left\langle \mathcal{T}_\gamma \left(-iV_{H_0}(\tau_1)\right) \cdots \left(-iV_{H_0}(\tau_k)\right) c^0_1 \cdots c^0_n c^{0\dagger}_{n'} \cdots c^{0\dagger}_{1'} \right\rangle. \end{aligned} \tag{3.2.1}$$

To simplify this expression it is convenient to expand $V$ in terms of creation and annihilation operators. For the scope of this work we only consider problems, where $V(t)$ is either quadratic or quartic.[1] For the quartic case we find

$$\begin{aligned} \int_\gamma d\tau\, V_{H_0}(\tau) &= \int_{t_0}^\infty dt \sum_{\sigma=\pm} \frac{-\sigma}{4} \sum_{i,j,k,l} \nu_{i,j,k,l}(t) c^{0\dagger}_i(t^\sigma) c^{0\dagger}_j(t^\sigma) c^0_l(t^\sigma) c^0_k(t^\sigma) \\ &= \frac{1}{4} \sum_{1',2',1,2} \bar{\nu}_{1'2'|12} c^{0\dagger}_{1'} c^{0\dagger}_{2'} c^0_2 c^0_1 \end{aligned} \tag{3.2.2}$$

with

$$\bar{\nu}_{1'2'|12} = \delta(t_{1'}, t_{2'}, t_1, t_2)\,(-\sigma_{1'})\,\delta_{\sigma_{1'},\sigma_{2'},\sigma_1,\sigma_2} \nu_{i_{1'} i_{2'}|i_1 i_2}(t_{1'}), \tag{3.2.3}$$

1 A generalization to other types of interaction terms is straightforward.

where $\delta(a,b,c)$ ($\delta_{a,b,c}$) is understood as a natural extension of the delta distribution (function). While the indices of $\nu$ are numbers ($\nu(t) \in \mathbb{C}^{N\times N\times N\times N}$), $\bar{\nu}$ features four *multi*-indices. The summation over the multi-indices $1',2',1,2$ is understood as a sum over the contour- and single-particle indices as well as integrals over the time. Without loss of generality we also require

$$\bar{\nu}_{1'2'|12} = \xi\bar{\nu}_{2'1'|1,2} = \xi\bar{\nu}_{1'2'|2,1} = \bar{\nu}_{2'1'|2,1}. \tag{3.2.4}$$

If this property is not already fulfilled by the $\nu$ given, we chose the fully antisymmetric superposition for $\bar{\nu}$.

For quadratic perturbations we similarly introduce

$$\bar{\nu}_{1'|1} = \delta(t_{1'} - t_1)(-\sigma_{1'})\delta_{\sigma_{1'},\sigma_1}\nu_{i_{1'}|i_1} \tag{3.2.5}$$

such that for a quadratic permutation $V(t)$

$$\begin{aligned}\int_\gamma d\tau\, V_{H_0}(\tau) &= \int_{t_0}^{\infty} dt \sum_{\sigma=\pm} -\sigma \sum_{i,j} \nu_{i|j}(t) c_i^{0\dagger}(t^\sigma) c_j^0(t^\sigma) \\ &= \sum_{1',2',1,2} \bar{\nu}_{1'|1} c_{1'}^{0\dagger} c_1^0.\end{aligned} \tag{3.2.6}$$

### 3.2.1 *Wick's theorem*

In order to apply Wick's theorem, it is required that the initial density has the shape

$$\rho_0 = \frac{e^K}{\operatorname{Tr} e^K}, \qquad K = \sum_{i,j} k_{i,j} c_i^\dagger c_j \tag{3.2.7}$$

for some quadratic operator $K$. Hence, throughout, we restrict all initial states to have this form. This implies

$$\bar{n}_{n,m} = \left\langle c_m^\dagger c_n \right\rangle_{\rho_0} = \frac{1}{e^k - \xi}. \tag{3.2.8}$$

Furthermore, it is only applicable if the operator (in our case $H_0$) governing the time-evolution is also quadratic. Wick's theorem [Wic50] then states for time-ordered expectation values

$$\begin{aligned}\langle \mathcal{T}_\gamma \tilde{c}_1\tilde{c}_2\tilde{c}_3\tilde{c}_4\cdots\tilde{c}_{n-1}\tilde{c}_n\rangle_{\rho_0} = {} & \tilde{c}_1\tilde{c}_2\tilde{c}_3\tilde{c}_4\cdots\tilde{c}_{n-1}\tilde{c}_n \\ & + \tilde{c}_1\tilde{c}_2\tilde{c}_3\tilde{c}_4\cdots\tilde{c}_{n-1}\tilde{c}_n \\ & + \tilde{c}_1\tilde{c}_2\tilde{c}_3\tilde{c}_4\cdots\tilde{c}_{n-1}\tilde{c}_n \\ & + \dots \\ & + \tilde{c}_1\tilde{c}_2\tilde{c}_3\tilde{c}_4\cdots\tilde{c}_{n-1}\tilde{c}_n \\ & + \dots\end{aligned} \tag{3.2.9}$$

where $\tilde{c}$ can denote either a creation or annihilation operator that is evolved with respect to a quadratic Hamiltonian and we sum over all possible pairings. The objects on the right are defined using

$$\overbracket{\tilde{c}_1 \tilde{c}_2} = \langle \mathcal{T}_\gamma \tilde{c}_1 \tilde{c}_2 \rangle_{\rho_0} . \tag{3.2.10}$$

Furthermore, for every crossing in the lines representing a two-point correlation function we have to add a factor $\xi$ to respect the commutation relations. For example

$$\overbracket{\tilde{c}_1 \overbracket{\tilde{c}_2 \tilde{c}_3} \tilde{c}_4} = \xi \langle \mathcal{T}_\gamma \tilde{c}_1 \tilde{c}_2 \rangle_{\rho_0} \langle \mathcal{T}_\gamma \tilde{c}_3 \tilde{c}_4 \rangle_{\rho_0} . \tag{3.2.11}$$

### 3.2.2 *Decomposition in terms of single-particle Green's functions*

In the case that $V(t)$ represents a two-particle interaction

$$V(t) = \frac{1}{4} \sum_{i,j,k,l} v_{i,j,k,l} c_i^\dagger c_j^\dagger c_l c_k, \tag{3.2.12}$$

Equation 3.2.1 can be expressed in terms of single-particle Green's functions as

$$\begin{aligned} &G(1,\dots,n|1',\dots,n') \\ &\quad = (-i)^n \sum_{k=0}^{\infty} \frac{1}{k!} \underbrace{\left(-\frac{i\bar{v}}{4}\right) \cdots \left(-\frac{i\bar{v}}{4}\right)}_{k \text{ times}} \sum_{\text{pairings P}} i^{2k+n} \xi^P \underbrace{g \dots g}_{2k+n \text{ times}} \end{aligned} \tag{3.2.13}$$

where we omitted the single-particle indices, contour indices, time dependence as well as contractions over these to improve readability.

As an example, let us discuss the first order contribution to the single-particle Green's function:

$$
\begin{aligned}
G_{1|1'} &= g_{1|1'} - i\frac{1}{1!}\frac{1}{4}\sum_{2'3'23}\bar{v}_{2'3'|23}\left\langle c^{0\dagger}_{2'}c^{0\dagger}_{3'}c^{0}_{2}c^{0}_{3}c^{0}_{1}c^{0\dagger}_{1'}\right\rangle_{\rho_0} + \mathcal{O}\left(v^2\right) \\
&= g_{1|1'} - \frac{i}{4}\sum_{2'3'23}\bar{v}_{2'3'|23}\Big\{ \\
&\qquad \overbrace{c^{\dagger}_{2'}c^{\dagger}_{3'}c_{2}c_{3}}c_{1}c^{\dagger}_{1'} + \overbrace{c^{\dagger}_{2'}c^{\dagger}_{3'}c_{2}c_{3}c_{1}c^{\dagger}_{1'}} \\
&\qquad + \overbrace{c^{\dagger}_{2'}c^{\dagger}_{3'}c_{2}}c_{3}\overbrace{c_{1}c^{\dagger}_{1'}} + \overbrace{c^{\dagger}_{2'}c^{\dagger}_{3'}c_{2}c_{3}c_{1}c^{\dagger}_{1'}} \\
&\qquad + \overbrace{c^{\dagger}_{2'}c^{\dagger}_{3'}c_{2}}\overbrace{c_{3}c_{1}c^{\dagger}_{1'}} + \overbrace{c^{\dagger}_{2'}c^{\dagger}_{3'}c_{2}c_{3}c_{1}c^{\dagger}_{1'}} \\
&\qquad \Big\} + \mathcal{O}\left(v^2\right) \\
&= g_{1|1'} - \frac{i}{4}\sum_{2'3'23}\bar{v}_{2'3'|23}\Big\{ \\
&\qquad - g_{2|2'}g_{3|3'}g_{1|1'} + g_{2|2'}g_{1|3'}g_{3|1'} \\
&\qquad + g_{3|2'}g_{2|3'}g_{1|1'} - g_{3|2'}g_{1|3'}g_{2|1'} \\
&\qquad - g_{1|2'}g_{2|3'}g_{3|1'} + g_{1|2'}g_{3|3'}g_{2|1'} \\
&\qquad \Big\} + \mathcal{O}\left(v^2\right)
\end{aligned}
\tag{3.2.14}
$$

To visualize the structure of this equation diagrammatically, we introduce a symbol to represent the bare interaction (compare Equation 3.2.3)

$\bar{v}_{1'2'|1,2} =$ 

.

For the first order term, the diagrams read (we will simplify this and discuss the correct prefactors later):

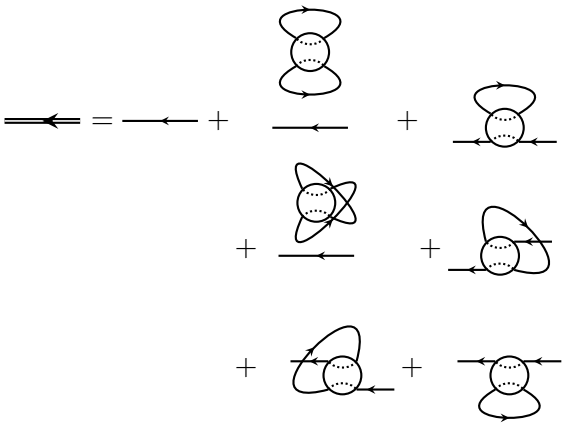


(3.2.15)

Due to the antisymmetry of $\bar{v}$ (compare Equation 3.2.4) and the fact that pair exchanges change the sign of a permutation we can fix the order of the attachment points on the vertex, canceling the factors $1/4$ in Equation 3.2.13. Hence, we only consider two diagrams to be different, if the structure of the resulting directed graph (where lines are edges and interactions are vertices) is different. However, when two lines connect the same vertices in the same direction the permutations of the two yield the same pair contractions, which is only to be counted once. To correct for this, we multiply each diagram with $2^{-n_{eq}}$ where $n_{eq}$ is the number of pairs of equivalent lines. Note that diagrams, where external indices are connected to *different* vertices (in contrast to different positions on the same vertex) are still considered to be different diagrams. For that reason, the order of the external indices (if not trivial as in the case of the single-particle Green's function) is considered part of the diagram. As an example, consider

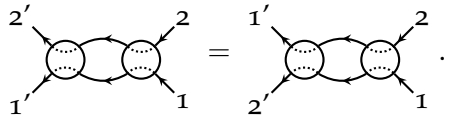


These are identified and only counted as one diagrams. On the other hand

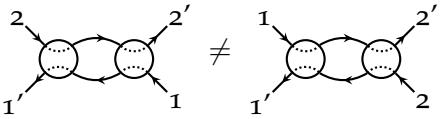


are considered different. For the case of the single-particle Green's function this reduces the number of first-order diagrams from six to just two.

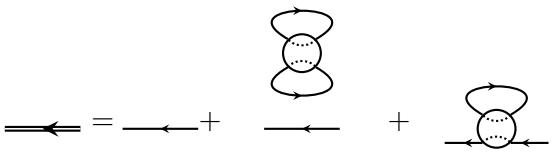


(3.2.16)

As we see in Equation 3.2.15, diagrams $3, 5, 6$ and $7$ can be combined, canceling the $1/4$ while diagram 2 is only combined with diagram 4, as two Green's functions connect the same two vertices in the same direction.

Similarly, fully exchanging the indices of one vertex with those of another yields the same result, giving an additional $k!$, canceling the $1/k!$ present in Equation 3.2.13. If a given diagram is symmetric under exchange of vertices (similar to case of a pair of equivalent Green's functions discussed prior), we prevent double counting by introducing a symmetry factor $S$, that counts the number of permutations of the vertices that leaves the diagram unchanged.

Lastly, we note that the correct sign can always be determined by computing $\xi^{P+n_{loop}}$, where $P$ denotes the permutation of the outgoing

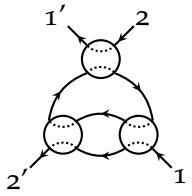


(a) $n_{eq} = 1$,
$S = 1$,
$\xi^P = -1$,
$n_{loop} = 1$

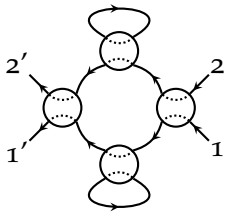


(b) $n_{eq} = 0$,
$S = 2$,
$\xi^P = 1$,
$n_{loop} = 2$

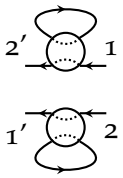


(c) $n_{eq} = 1$,
$S = 0$,
$\xi^P = -1$,
$n_{loop} = 2$

Figure 3.1: Some of the diagrams contributing to the two-particle Green's function. Diagrams (a) and (b) are *connected* while diagram (c) is not (compare Section 3.2.4).

indices with respect to the incoming ones and $n_{loop}$ is the number of closed loops in a diagram; this is due to the fact that exchanging two indices either changes the number of loops by $\pm 1$ or changes the sign of the permutation of ingoing vs. outgoing indices.

The value of a diagram is then determined as follows:

**Algorithm 3.1: Evaluating diagrams for Green's functions**

Given a diagram contributing to the expansion of the full Green's function, let (compare Figure 3.1)

- $n_{eq}$ be the number of equivalent lines, connecting the same two vertices in the same direction
- $S$ be the number of ways the vertices can be relabeled without changing the diagram
- $P$ be the perturbation of outgoing indices compared to ingoing indices
- $n_{loop}$ be the number of loops in the diagram.

Than the diagram is evaluated as

$$\frac{\xi^{P+n_{loop}}}{2^{n_{eq}} S} \left(\prod i\bar{\nu}\right) \left(\prod g\right),$$

where multi-indices are assigned to the vertices and Green's functions and all but the external indices are summed over.

To obtain the full $n$-particle Green's function we have to sum over all topologically different diagrams.

### 3.2.3 *Vacuum diagrams*

When considering all contributions to the expansion of the Green's function, many of them contain subdiagrams, that are not connected to any of the external indices, i.e. the diagram factorizes. For an example, see Equation 3.2.16. These subdiagrams do not modify the result: the sum of all such diagrams corresponds to the expansion of the 0-point Green's functions with

$$\langle 1 \rangle_{\rho_0} = 1. \tag{3.2.17}$$

The expansion of the $n$-point Green's function can thus be understood as being multiplied with an arbitrary number 0-point Green's function, contributing vacuum diagrams but not modifying the result. Therefore, we only sum over diagrams that do not contain a subdiagram, that is disconnected from all external fields.

### 3.2.4 *Connected Green's functions and vertex functions*

If a diagram contributing to the $n$-particle Green's function cannot be decomposed into a product of subdiagrams it is considered connected (see Figure 3.1). It is straightforward, that the full $n$-particle Green's function can be recovered using products of connected Green's functions.

The contributions to the connected $n$-particle *vertex function* are obtained by considering a diagram contributing to the connected $n$-particle Green's function and removing all single-particle Green's functions, that contain an external index. It is furthermore convention, to multiply diagrams contributing to the $n$-particle vertex function by $i^{1-n}$, modifying the prefactor in Algorithm 3.1 to

$$i^{1-n} \frac{\xi^{P+n_{\text{loop}}}}{2^{n_{\text{eq}}} S} \left( \prod i\bar{v} \right) \left( \prod g \right). \tag{3.2.18}$$

This convention ensures, that the $n$-particle vertex function can be used in the perturbative expansion of the Green's function in place of the bare $n$-particle interaction without modifying Algorithm 3.1.

The sum of all those diagrams is called the $n$-particle vertex function. Note that in many cases, we will still connect arrows to the end-points of vertex functions to differentiate ingoing from outgoing indices.

### 3.2.5 *One-particle irreducible vertex functions*

A diagram contributing to the connected $n$-particle vertex function is called *one-particle irreducible*, if the diagram remains connected when any one of the constituting Green's functions is removed. Examples and counter examples are shown in Figure 3.2. The sum of all these

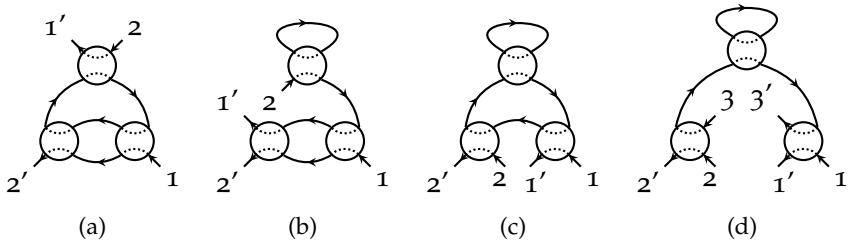


Figure 3.2: Example of contributions to the two- ((a)-(c)) and three-particle vertex functions. As (a) and (c) are one-particle irreducible, they also contribute to the irreducible vertex function while (b) and (d) are one-particle reducible.

diagrams is called the one-particle irreducible $n$-particle vertex function. Diagrammatically, we represent these by

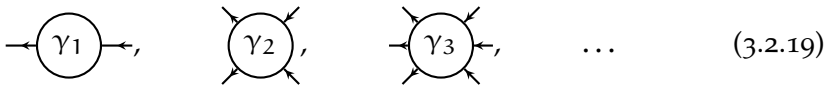


(3.2.19)

The one-particle irreducible one-particle vertex function is called the *self-energy* $\Sigma$ and therefore diagrammatically represented by

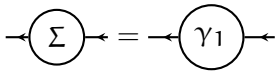


(3.2.20)

### 3.2.6 *Basis transformation*

As we discussed in Section 2.3, it is often convenient to change from the contour basis to the RKA-basis. Transforming all bare Green's functions in a given diagram and associating the corresponding transformation matrices with the vertex functions instead gives us the transformation formulas

$$\Sigma^{\alpha'|\alpha} = \sum_{\sigma',\sigma} D_{\alpha'|\sigma'} \Sigma^{\sigma'|\sigma} D^{-1}_{\sigma|\alpha} \tag{3.2.21}$$

$$\gamma_2^{\alpha_{1'}\alpha_{2'}|\alpha_1\alpha_2} = \sum_{\sigma_{1'},\sigma_{2'},\sigma_1,\sigma_2} D_{\alpha_{1'}|\sigma_{1'}} D_{\alpha_{2'}|\sigma_{2'}} \gamma_2^{\sigma_{1'}\sigma_{2'}|\sigma_1\sigma_2} D^{-1}_{\sigma_1|\alpha_1} D^{-1}_{\sigma_2|\alpha_2}$$

and so on for the vertex functions as well as the two-particle bare interaction. The transformation of the bare interaction results in

$$\bar{v}^{\alpha_{1'}\alpha_{2'}|\alpha_1\alpha_2}_{1'2'|12} = \begin{cases} \delta(t_{1'}, t_{2'}, t_1, t_2) \frac{1}{2} v_{i_{1'}, i_{2'}, i_1, i_2}(t_{1'}) & \text{for } \alpha'_1 + \alpha'_2 + \alpha_1 + \alpha_2 \text{ odd} \\ 0 & \text{otherwise.} \end{cases} \tag{3.2.22}$$

Similarly, a quadratic perturbation to the Hamiltonian in the Keldysh-basis is represented by

$$\bar{v}_{1'|1} = \begin{cases} \delta(t_{1'} - t_{1,})\nu_{i_{1'}|i_1}(t_{1'}) & \text{for } \alpha_1' + \alpha_1 \text{ odd} \\ 0 & \text{otherwise,} \end{cases} \tag{3.2.23}$$

hence it only has a retarded and advanced component.

### 3.2.7 *The Dyson equation*

By definition, the full one-particle vertex functions can be reproduced by adding an arbitrary number of free single-particle Green's functions in between irreducible vertex functions. Adding the outer legs we amputated, one retrieves the full one-particle Green's function:

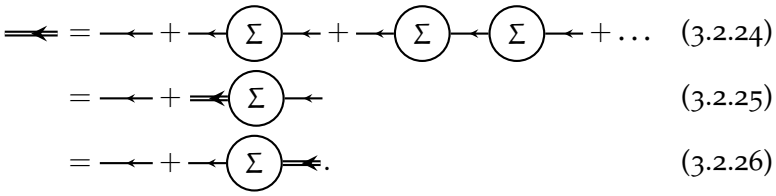


$$= \quad + \quad + \quad + \ldots \tag{3.2.24}$$

$$= \quad + \tag{3.2.25}$$

$$= \quad + \quad . \tag{3.2.26}$$

Equation 3.2.25 is also known as the *Dyson* equation. In terms of Green's functions it reads

$$G_{1|1'} = g_{1|1'} + g_{1|2'}\Sigma_{2'|2}G_{2|1'}. \tag{3.2.27}$$

Formally solving this for $G$ or $\Sigma$ using a matrix notation in the space of super-indices yields

$$G = \frac{1}{g^{-1} - \Sigma} \Leftrightarrow \Sigma = g^{-1} - G^{-1}. \tag{3.2.28}$$

Using Equation 2.5.29 and Equation 2.3.15, we find [Jak15]

$$G^{-1} = \begin{pmatrix} -\left(G^{\text{ret}}\right)^{-1} G^{K} \left(G^{\text{adv}}\right)^{-1} & \left(G^{\text{ret}}\right)^{-1} \\ \left(G^{\text{adv}}\right)^{-1} & 0 \end{pmatrix}, \tag{3.2.29}$$

which implies the form

$$\Sigma = \begin{pmatrix} \Sigma^{K} & \Sigma^{\text{ret}} \\ \Sigma^{\text{adv}} & 0 \end{pmatrix}, \tag{3.2.30}$$

for the self-energy in the Keldysh basis. The fact, that there are only three non-zero components in the Keldysh basis can be understood as an inherited theorem of causality.[2]

2 Note that in contrast to the Green's functions, the self-energy only has three components, even at equal times

The resulting equations for the individual components read[KKK18]:

$$\begin{aligned}
&G^{\mathrm{ret}}(t,t') \\
&= g^{\mathrm{ret}}(t,t') + \int_{t_0}^{\infty} dt_1\, dt_2\, g^{\mathrm{ret}}(t,t_1)\Sigma^{\mathrm{ret}}(t_1,t_2)G^{\mathrm{ret}}(t_2,t') \\
&G^{\mathrm{K}}(t,t') \\
&= \left\{ g^{\mathrm{ret}}\Sigma^{\mathrm{ret}}G^{\mathrm{K}} + g^{\mathrm{ret}}\Sigma^{\mathrm{K}}G^{\mathrm{adv}} + g^{\mathrm{K}}\Sigma^{\mathrm{adv}}G^{\mathrm{adv}} \right\}(t,t') \\
&\overset{(3.2.29)}{=} \left\{ G^{\mathrm{ret}} \left[ \left(g^{\mathrm{ret}}\right)^{-1} g^{\mathrm{K}} \left(g^{\mathrm{adv}}\right)^{-1} + \Sigma^{\mathrm{K}} \right] G^{\mathrm{adv}} \right\}(t,t') \\
&= -iG^{\mathrm{ret}}(t,t_0)\,(1+2\xi\bar{n})\,G^{\mathrm{adv}}(t_0,t') \\
&\quad + \int_{t_0}^{\infty} dt_1\, dt_2\, G^{\mathrm{ret}}(t,t_1)\Sigma^{\mathrm{K}}(t_1,t_2)G^{\mathrm{adv}}(t_2,t'),
\end{aligned} \tag{3.2.31}$$

In the steady state the Dyson equation reads

$$\begin{aligned}
G^{\mathrm{ret}}(\omega) &= g^{\mathrm{ret}}(\omega) + g^{\mathrm{ret}}(\omega)\Sigma^{\mathrm{ret}}(\omega)G^{\mathrm{ret}}(\omega) \\
G^{\mathrm{K}}(\omega) &= G^{\mathrm{ret}}(\omega)\big[g^{\mathrm{ret}}(\omega)^{-1} g^{\mathrm{K}}(\omega) g^{\mathrm{adv}}(\omega)^{-1} \\
&\qquad + \Sigma^{\mathrm{K}}(\omega)\big] G^{\mathrm{adv}}(\omega) \\
&= G^{\mathrm{ret}}(\omega)\Sigma^{\mathrm{K}}(\omega)G^{\mathrm{adv}}(\omega),
\end{aligned}$$

where in the second line of the last equation decay processes are assumed to lead to a fading memory of the initial density $\rho_0$ in Equation 3.2.31 (compare Section 2.4). The Dyson equation for the retarded Green's function can be formally solved as

$$G^{\mathrm{ret}}(\omega) = \frac{1}{(g^{\mathrm{ret}})^{-1} - \Sigma^{\mathrm{ret}}(\omega) + i0} \tag{3.2.32}$$

$$= \frac{1}{\omega - h - \Sigma^{\mathrm{ret}}(\omega) + i0} \tag{3.2.33}$$

As we will discuss in Section 3.4.1, a first order perturbation theory expansion (and as we will later see, a first-order fRG truncation) yield self-energies which are time-local and have a vanishing Keldysh component:

$$\Sigma^{\mathrm{K}}(t,t') = 0, \qquad \Sigma^{\mathrm{ret}}(t,t') = \Sigma^{\mathrm{ret}}(t)\delta(t-t'),$$

which renders it particularly simple to evaluate Eq. (3.2.31)[KKK18]:

$$\begin{aligned}
G^{\mathrm{ret}}(t,t') &= -i\theta\left(t-t'\right) \mathcal{T} e^{-i\int_{t'}^{t} dt_1 \left[h^0(t_1)+\Sigma^{\mathrm{ret}}(t_1)\right]} \\
G^{\mathrm{K}}(t,t') &= -iG^{\mathrm{ret}}(t,t_0)\,(1+2\xi\bar{n})\,G^{\mathrm{adv}}(t_0,t').
\end{aligned} \tag{3.2.34}$$

Hence, $h^0 + \Sigma^{\mathrm{ret}}$ takes the role of an effective Hamiltonian.

### 3.2.8 *The tree expansion*

Higher order vertex functions are of importance, as any connected Green's function can be build up from one-particle irreducible vertex functions using the *tree expansion* [KSF01; KBS10].

This expansion forms a tree, as loops are forbidden: if a set of vertices was connected by a loop of Green's functions, they together form a single-particle irreducible unit and are already included in some other diagram. Furthermore, note that in the tree expansion of the connected $n$-particle Green's function only $2, 3, \ldots, n$-particle vertex functions appear.

The Dyson equation (see Section 3.2.7) can be understood as a one-particle tree expansion.

As a non-trivial example, let us give the expansion of the connected three-particle Green's function:

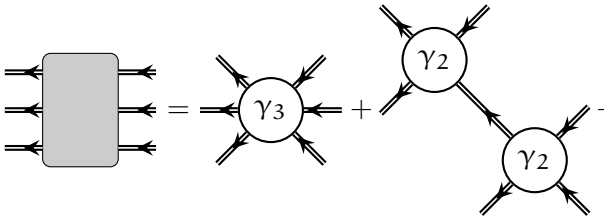


(3.2.35)

where refrained from explicitly writing down the different ways to arrange two $\gamma_2$ vertices. Note that for a more general Hamiltonian (that has three-point terms) also three-point vertex functions are generated and lead to a more complex tree expansion (see e.g. [KBS10]).

### 3.2.9 *Quadratic perturbations*

When assuming a quadratic perturbation $V(t)$, $v$ only has a single in- and outgoing index. The resulting perturbative series is significantly simpler as no higher order irreducible vertex functions are generated. As an example, let us consider two subsystems coupled by a one-particle term $\hat{T}$, that is considered as a perturbation to the Hamiltonian. Without any additional changes to the formalism, the self-energy, as the only one-particle irreducible diagram, is just the vertex representing $\hat{T}$. This only contributes a retarded self-energy and in the stationary state the retarded component of the Green's functions is

$$g^{\mathrm{ret}}(\omega) = \frac{1}{\omega - H_0 - \Sigma + i0} \tag{3.2.36}$$

$$= \frac{1}{\omega - \begin{pmatrix} h_0 & 0 \\ 0 & h_1 \end{pmatrix} - \begin{pmatrix} 0 & T^\dagger \\ T & 0 \end{pmatrix} + i0} \tag{3.2.37}$$

which is both correct and trivial. This formalism was, however, based on the assumption, that the unperturbed Green's functions are easy

to calculate. This might not necessarily be true for a large reservoir; let us thus modify the formalism to consider diagrams irreducible when removing lines within system 0.[3] The only resulting irreducible diagrams is

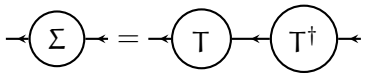


(3.2.38)

Note that due to Equation 3.2.23, the coupling is either retarded or advanced, but does not contribute a Keldysh component. For a potentially time-dependent coupling $T(t)$ we therefore find

$$\begin{aligned}\Sigma^{\mathrm{ret}}(t'|t) =& T(t')g^{\mathrm{ret}}(t'|t)T^\dagger(t)\\ \Sigma^{K}(t'|t) =& T(t')g^{K}(t'|t)T^\dagger(t)\end{aligned} \tag{3.2.39}$$

and for time-independent couplings in the stationary state

$$\begin{aligned}\Sigma^{\mathrm{ret}}(\omega) =& \quad Tg^{\mathrm{ret}}(\omega)T^\dagger\\ \Sigma^{K}(\omega) =& \quad Tg^{K}(\omega)T^\dagger,\end{aligned} \tag{3.2.40}$$

which is exactly what we already found in Section 2.5.4. Note that the Green's functions in Equations 3.2.39 and 3.2.40 are the ones in the disconnected reservoir.

### 3.2.10 *Reservoirs and two-particle interactions*

For the case of systems with both, reservoirs and two-particle interactions, we restrict ourselves to non-interacting reservoirs (i.e. the support of the interaction is restricted to the system without the reservoirs).

$$\begin{aligned}H =& \sum_{n,m\in\underline{N_{\mathfrak{A}}}} h^{\mathfrak{A}}_{n,m}c^\dagger_n c_m + \sum_{n,m\in\underline{N_{\mathfrak{B}}}} h^{\mathfrak{B}}_{n,m}c^\dagger_{n+N_{\mathfrak{A}}}c_{m+N_{\mathfrak{A}}}\\ &+ \sum_{\substack{n\in\underline{N_{\mathfrak{A}}}\\ m\in\underline{N_{\mathfrak{B}}}}} T_{n,m}c^\dagger_n c_{m+N_{\mathfrak{A}}} + \mathrm{h.c.}\\ &+ \sum_{k,l,m,n\in\underline{N_{\mathfrak{A}}}} v_{k,l,m,n}c^\dagger_k c^\dagger_l c_n c_m\end{aligned} \tag{3.2.41}$$

When performing the perturbative expansion in the two-particle interaction we realize that: (a) the vertex functions are only non-zero within system $\mathfrak{A}$ and (b) within a diagram, we only need Green's functions in the absence of the two-particle interaction with both indices within system $\mathfrak{A}$ to compute the vertex functions. As we discussed, it is possible to obtain these non-interacting Green's functions by integrating out the reservoirs. Subsequently, we can treat the interaction in the diagrammatic formalism discussed in this chapter.

3 This formulation of perturbation theory can be formally justified by considering $h_1$ part of the perturbation and an adequate resummation.

## 3.3 SYMMETRIES IN THE LIGHT OF PERTURBATION THEORY

A detailed discussion of symmetries of the Green's and vertex functions can be found in [JPS10b]. Here, we present some of these symmetries and argue, under what condition they are preserved within perturbation theory. Based on this, we will argue in Chapter 4 how to preserve them in an fRG approximation.

### 3.3.1 *Particle exchange*

Just like the Green's functions, vertex functions are (anti-)symmetric under the exchange of particle. For any permutation we find

$$\gamma^{P\sigma'|\sigma}_{Pi'|i}(Pt'|t) = \xi^P \gamma^{\sigma'|\sigma}_{i'|i}(t'|t) = \gamma^{\sigma'|P\sigma}_{i'|Pi}(t'|Pt). \tag{3.3.1}$$

This property is conserved in any diagrammatic approximation that includes all diagrams related via exchange of external indices.

### 3.3.2 *Complex conjugation*

As we have discussed, Greens function are connected under complex conjugation. Furthermore, the time-local two-particle interactions considered here fulfill

$$\bar{v}^{\sigma'|\sigma}_{i'|i}(t'|t)^* = \bar{v}^{\sigma'|\sigma}_{i'|i}(t'|t) = \bar{v}^{\sigma|\sigma'}_{i|i'}(t|t') = -\bar{v}^{-\sigma|-\sigma'}_{i|i'}(t|t') \tag{3.3.2}$$

where the second equality used the antisymmetry of the interaction and the third employed Equation 3.2.3. Therefore, the complex conjugate of an individual diagram can be obtained by reverting all lines and inverting all contour indices. Counting the number of signs appearing through conjugation of free Green's functions, bare vertices and the prefactor of the diagram[4] results in

$$\gamma^{\sigma'|\sigma}_{i'|i}(t'|t)^* = -\gamma^{-\sigma|-\sigma'}_{i|i'}(t|t') \tag{3.3.3}$$

and when transformed into the RKA-basis

$$\gamma^{\alpha'|\alpha}_{i'|i}(t'|t) = (-1)^{1+\sum_k \alpha_k + \alpha'_k} \gamma^{\alpha|\alpha'}_{i|i'}(t|t'). \tag{3.3.4}$$

From this derivation, it is obvious that this symmetry is conserved for all diagrammatic approximations that are invariant under inverting all lines.

### 3.3.3 *The stationary state*

For a time-independent Hamiltonian and when a stationary state is reached both, the bare Green's and vertex functions are local in frequency space (compare Section 2.4). Similarly, a time-independent

4 Note that we defined an additional factor of $i^{1-n}$ to be part of the $n$-particle vertex function in the factor obtained from Algorithm 3.1

two-particle interaction preserves energy. With these two ingredients, it is straightforward to show that for every diagram contributing to any N-particle vertex function energy is conserved.

$$\gamma(\omega|\omega') \sim \delta\left(\sum \omega - \sum \omega'\right). \tag{3.3.5}$$

This reduces the number of independent frequencies.

### 3.3.4 *Causality and perturbation theory*

The causality relation, that we already discussed in Equation 2.3.20 also has immediate impact on the vertex functions [JPS10b].[5] To exemplify this, consider a diagram contributing to some $n$-particle vertex function. We will now prove, that the time associated with an external index with RKA-index 2 can not be the strictly largest time.

Starting at any of the external indices with RKA-index 2 (let us label it $x$), we realize, that due to Equation 3.2.22, at least one of the adjacent Green's functions has to feature a 1-index. If the second vertex this Green's function is connected to ($y$) is connected to an external index, we have shown that $t_x \leqslant t_y$ as $g^{1|\bullet}(t|t') = 0 = g^{\bullet|1}(t'|t)\ \forall t > t'$. If the vertex is internal, the corresponding time is integrated over and the patch Green's function (that is only non-zero on a set of size zero), does not contribute; therefore the second index of the Green's function is a 2 and still $t_x \leqslant t_y$. If this internal vertex is unvisited thus far (hence we only know of a single index 2 connected to it), we can repeat the procedure, as another 1 has to be connected to it. If, on the other hand, this vertex has been visited, all vertices visited in between are restricted to have to same time index (we are building up a sequence of increasing times and found a loop) and therefore are only non-zero on a zero-set of the integration manifold. If no vertices were visited in between (i.e. the line discussed is simple loop), we employ the fact that $g^{\mathrm{ret}}(t|t) + g^{\mathrm{adv}}(t|t) = 0$, hence the last unknown index is a 1 and we can proceed. This proves, that the time $t_x$ associated with an index 2 can not be the strictly largest external time argument.

From this, it finally follows, that

$$\gamma^{2\ldots2|2\ldots2}(t'_1 \ldots t'_n|t_1 \ldots t_n) \tag{3.3.6}$$

is only non-zero on a set of measure zero. Note that, while in accordance with Equation 3.2.30 the above statement is not sufficient to prove Equation 3.2.30.

### 3.3.5 *Perturbation theory and the fluctuation-dissipation theorem*

We will now demonstrate, how the fluctuation-dissipation theorem in a thermal state is preserved within diagrammatic approximations.

5 The proof included in [JPS10b] is slightly different, due to the omission of the patch Green's function.

Understanding the preconditions to preserve this symmetry will guide our approximation in the later chapters (compare Chapter 8). The proof presented here is an adapted and simplified version of the one provided in [JPS10b] that works on a diagrammatic level.

Using the definitions

$$\begin{aligned} m^{\sigma|\sigma'} &= \sum_{\substack{k=1,\dots,n \\ \sigma'_k=+}} 1 - \sum_{\substack{k=1,\dots,n \\ \sigma_k=+}} 1 \\ \Delta^{\sigma|\sigma'}(\omega|\omega') &= \sum_{\substack{k=1,\dots,n \\ \sigma'_k=+}} \omega'_k - \sum_{\substack{k=1,\dots,n \\ \sigma_k=+}} \omega_k \end{aligned} \tag{3.3.7}$$

we have shown (compare Sections 2.5.3 and 2.5.5), that the free, single-particle, reservoir dressed Green's functions in thermal equilibrium fulfill

$$g^{\sigma|\sigma'}_{q|q'}(\omega|\omega') = e^{-\beta\Delta^{\sigma|\sigma'}(\omega|\omega')}\xi^{m^{\sigma|\sigma'}} g^{\sigma'|\sigma}_{q|q'}(\omega|\omega'). \tag{3.3.8}$$

For a symmetric $H$ (note that $g(\omega|\omega') \sim \delta(\omega-\omega')$ in equilibrium and compare Equations 2.5.13 and 2.5.21)[6]

$$g^{\sigma|\sigma'}_{q|q'}(\omega|\omega') = e^{-\beta\Delta^{\sigma|\sigma'}(\omega|\omega')}\xi^{m^{\sigma|\sigma'}} g^{\sigma'|\sigma}_{q'|q}(\omega'|\omega). \tag{3.3.9}$$

Furthermore, for a time reversal invariant bare interaction (as discussed throughout this work) it is easy to verify that

$$\bar{v}^{\sigma'|\sigma}_{q'|q}(\omega'|\omega) = e^{-\beta\Delta^{\sigma'|\sigma}(\omega'|\omega)}\xi^{m^{\sigma'|\sigma}} \bar{v}^{\sigma|\sigma'}_{q|q'}(\omega|\omega'). \tag{3.3.10}$$

Let us now consider a diagrammatic approximation to a vertex function that satisfies

$$\gamma_{Px'|x} = \xi^P \gamma_{x'|x} = \gamma_{x'|Px} \tag{3.3.11}$$

for all permutation $P$. Now let $D$ be an individual, arbitrary diagram contributing to the vertex function under consideration. By using Eqs. 3.3.9 and 3.3.10 we revert the direction of each bare vertex and Green's function, subsequently changing the ingoing indices of the vertex function with its outgoing indices. In this process we acquire prefactors according to Eqs. 3.3.9 and 3.3.10 as well as potentially a permutation of the external indices. Not all diagrams map to themselves (topologically) when changing the direction of all lines (compare Figure 3.3). To preserve the fluctuation-dissipation theorem, we therefore have to require, that a diagrammatic approximation as a whole must map to itself when reverting all bare Green's and vertex functions. Using

$$\Delta^{1'|1} = \Delta^{1'|2} + \Delta^{2|1}, \qquad m^{1'|1} = m^{1'|2} + m^{2|1}$$

6 It is also possible to discuss the general case of a complex (bare) Hamiltonian. Details can be found in Ref. [Jako9; JPS10b]. Throughout, we restrict ourselves to real Hamiltonians, where the proof of the FDT is simpler.

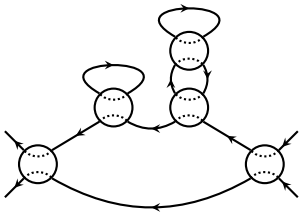

Figure 3.3: An example of a diagram, that does not map to itself when reverted. A diagrammatic approximations that includes this diagram also has to include the reverted one to potentially fulfill the FDT. Any finite-order perturbative expansion is invariant under the inversion of all lines.

we find:

$$D^{1'|1} = e^{-\beta\Delta^{1'|1}}\xi^{m^{1'|1}}\bar{D}^{P1|P^{-1}1'}.$$

where $\bar{D}$ is the reversed of D. Due to condition 3.3.11, however, we are guaranteed that either D itself is invariant under the permutation of the indices and reversion or that a second diagram exists, that ensures this symmetry (note that $\xi^P = \xi^{P^{-1}}$). Hence, we have finally proven, that

$$\gamma^{\sigma'|\sigma}_{q'|q}(\omega'|\omega) = e^{-\beta\Delta^{\sigma'|\sigma}(\omega'|\omega)}\xi^{m^{\sigma'|\sigma}}\gamma^{\sigma|\sigma'}_{q|q'}(\omega|\omega'). \tag{3.3.12}$$

Using this property and the expansion of the self-energy dressed propagator in terms of the self-energy one finally also finds:

$$G^{\sigma|\sigma'}_{q|q'}(\omega|\omega') = e^{-\beta\Delta^{\sigma|\sigma'}(\omega|\omega')}\xi^{m^{\sigma|\sigma'}}G^{\sigma'|\sigma}_{q'|q}(\omega'|\omega)$$

for symmetric Hamiltonians and diagrammatic approximations preserving Eq. 3.3.11 and mapping to themselves when reverted. For single-particle Green's functions in the RKA basis, this reads:

$$G^K(\omega) = (1 + 2\xi n(\omega)\left(G^{ret}(\omega) - G^{adv}(\omega)\right). \tag{3.3.13}$$

With this, we have also shown that Eq. 3.3.13 holds in all orders of perturbation theory. The analog expression holds for the self-energy. While not as clear with respect to arbitrary diagrammatic approximations, the proof provided in [JPS10b] does not rely on a symmetric H and has guided the simplified arguments provided here.

Note that the proof presented here, in contrast to the statements about Green's functions in quadratic Hamiltonians made in Sections 2.5.3 and 2.5.5, is restricted to the case of a thermal equilibrium.

## 3.4 LOWEST ORDER PERTURBATIVE EXPANSIONS

As a reference, we will now explicitly discuss the lowest order perturbative expansions.

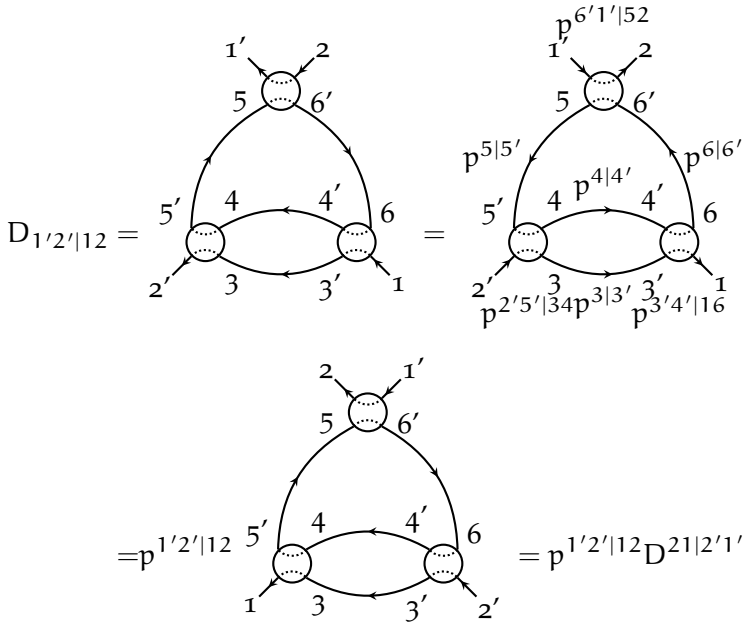


Figure 3.4: Demonstration of the procedure used to prove the fluctuation-dissipation theorem for diagrammatic approximations. Note that this diagram alone will not satisfy Equation 3.3.12, as it does not fulfill Equation 3.3.11. The approximation $D_{1'2'|12} + D_{2'1|21'}$ however, does.

### 3.4.1 *First order*

When reducing the results of the previous section to plain first order we are left with the diagram

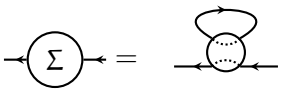


(3.4.1)

With $n_{\text{loop}} = 1$, we evaluate this to

$$\Sigma_{1'|1} = -i\bar{v}_{1'2'|12} g_{2|2'}. \tag{3.4.2}$$

Employing Equations 3.2.22 and 2.3.22, we find

$$\begin{aligned}
\Sigma^{K}_{i'|i}(t'|t) =& 0 \\
\Sigma^{\text{ret}}_{i'|i}(t'|t) =& -\frac{i}{2} \nu_{i'j'|ij}(t)\delta(t'-t)\left(2g^{P}_{j|j'}(t|t) + g^{K}_{j|j'}(t|t)\right) \\
=& \nu_{i'j'|ij}(t)\delta(t'-t) \underbrace{\frac{-i}{2}\left(i + g^{K}_{j|j'}(t,t)\right)}_{=\left\langle c^{0}_{j'}(t)^{\dagger} c^{0}_{j}(t)\right\rangle_{\rho_0}}.
\end{aligned} \tag{3.4.3}$$

When interpreted as an effective contribution to the Hamiltonian this can be understood as the density of the free fermions acting on the system, modifying the time-evolution.

Assuming a time-independent interaction, the self-energy is easily Fourier transformed

$$\Sigma^{\mathrm{ret}}_{1'|1}(\omega) = v_{1'2'|12}\frac{-i}{2}\left(i + \int \frac{d\Omega}{2\pi} g^{K}_{2|2'}(\Omega)\right). \tag{3.4.4}$$

Note that the self-energy is time-local and thus frequency independent when Fourier transformed.

### 3.4.2 *Mean field theory*

The above approximation is obviously not self-consistent as the density of fermions contributing effective potentials are computed in the absence of the interaction. This can be resolved by instead using the full Green's function on the rhs. The set of equations that needs to be solved can thus diagrammatically be represented as

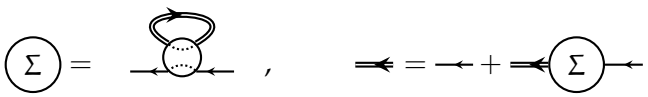


or written out explicitly:

$$\Sigma^{\mathrm{ret}}_{1'|1}(t) = \frac{-i}{2} v_{1'2'|12}(t)\left(i + G^{K}_{2|2'}(t,t)\right),$$

where $G^{K}$ is obtained using the Dyson equation (see Equation 3.2.31). This set of equations has to be solved self-consistently.

While being self-consistent and containing contributions of arbitrarily high order, all processes included are local in time. MFT is known to underestimate the influence of fluctuations and over-estimate long-range order; as an example, consider the 1D Ising model [Isi25], where mean-field theory produces a finite-temperature phase transition, although thermal fluctuations destroy the ordered phase at any finite T.

### 3.4.3 *Second order*

To obtain second order perturbation theory we write all single-particle irreducible diagrams:

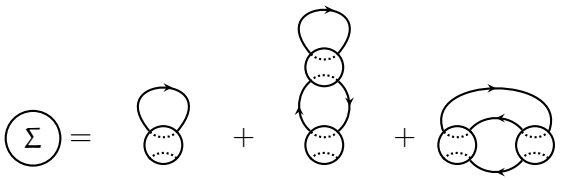

Thus the full second order perturbation theory for the self-energy reads[7]:

$$\begin{aligned}\Sigma_{1'|1} = &-\mathrm{i}\bar{v}_{1'2'|12}g_{2|2'} \\ &-\bar{v}_{1'2'|12}\bar{v}_{3'4'|34}g_{3|2'}g_{2|3'}g_{4|4'} \\ &+\frac{1}{2}\bar{v}_{1'2'|34}\bar{v}_{3'4'|12}g_{3|3'}g_{2|2'}g_{4|4'}\end{aligned} \tag{3.4.6}$$

While we do not explicitly aim to solve second-order perturbation theory within this work, we use it as a reference point and demonstrate, how fRG relates to this approximation.

7 Note that the third contributing diagram has a symmetry factor of 2

# 4

# FUNCTIONAL RENORMALIZATION GROUP

## 4.1 INTRODUCTION

The functional renormalization is an implementation of the Wilsonian renormalization group idea in terms of Green's- and vertex functions in that it treats energy scales successively. As we will see, it also has a close relation to the perturbation theory discussed in Chapter 3.

Exact flow equations for the generating functional for Green's and vertex functions have already been published early on in the development the RG techniques [WH73; Pol84]. The method was then further developed in the early 1990s [Wet93; Mor94; KSK92] and has since evolved into a versatile tool that is applied in fields as varied as quantum gravity [Reu98], high energy physics [BJW99] as well, as is our main focus, lattice models in the context of condensed matter physics.

Even within the realm of lattice models, the equilibrium formulation of the fRG was used to investigate a wide variety of problems, ranging from quantum impurity problems [KEM06; Kar+08], over chains [Med+02a; Med+02b; Ens+05; And+04; Jak+07] to spontaneous symmetry breaking in the Hubbard model [HS01] and spin systems [RTT11]. For a more complete overview of its applications, see [Met+12].

It was extended beyond equilibrium and employed to discuss stationary states [GPM07], transient time evolution [Ken+12] and periodic driving [EMK16b].

At this point, there is number overview articles [SH01; BTW02; Pol03; Met+12] as well as books [KBS10] giving a detailed introduction into this method. For this reason, we will refrain from presenting a full, path-integral based derivation of the functional renormalization group but instead present a derivation of the defining equations based on the diagrammatic expansion discussed in Chapter 3 [Jak09; JMS07].

We will then discuss under what conditions the truncated fRG flow equations preserves the fluctuation-dissipation theorem and causality (Sections 4.3.1 and 4.3.2). Thereafter, we present two specific examples of implementations of the fRG using a reservoir cutoff in time- and frequency-space (Sections 4.4.1 and 4.4.2). Lastly, we discuss how to simplify fRG and reuse functions already present in a typical fRG implementation to obtain perturbative results (Section 4.5).

## 4.2 THE FRG FLOW EQUATIONS

### 4.2.1 *Scale dependence of Green's and vertex functions*

To analyze the energy-scale dependence of the vertex functions, we introduce a cutoff parameter $\Lambda$ into the free propagator:

$$g_{1|1'} \to g^{\Lambda}_{1|1'} \tag{4.2.1}$$

such that there is a $\Lambda_{\text{final}}$ with

$$g^{\Lambda_{\text{final}}}_{1|1'} = g_{1|1'} \tag{4.2.2}$$

and the cutoff dependence is in some sense well behaved. The derivative of the free propagator is called the single-scale propagator[1] and visualized by a slashed line

$$s^{\Lambda}_{1|1'} = \frac{\partial g^{\Lambda}_{1|1'}}{\partial \Lambda} = \text{—⁄←}. \tag{4.2.3}$$

By virtue of the perturbative expansion, this induces a scale dependence in all diagrams and thus all vertex functions and the full, interacting Green's function

$$\begin{aligned} \gamma_{1'\ldots n'|1\ldots n} &\to \gamma^{\Lambda}_{1'\ldots n'|1\ldots n} \\ G_{1'\ldots n'|1\ldots n} &\to G^{\Lambda}_{1'\ldots n'|1\ldots n} \end{aligned} \tag{4.2.4}$$

To analyze the scale dependence of the Green's function, and finally calculate the full Green's function in the physical limit ($\Lambda = \Lambda_{\text{final}}$), consider the expansion of the vertex functions in terms of diagrams

$$\frac{\partial \gamma^{\Lambda}_{n}}{\partial \Lambda} = \sum_{\text{diagrams } d} \frac{\partial d^{\Lambda}}{\partial \Lambda}. \tag{4.2.5}$$

Each diagram represents a linear combination of products of (now scale-dependent) bare Green's functions as well as bare vertex functions. Hence, the derivative is to be performed using the product rule. Consider this diagram contributing to the two-particle vertex:

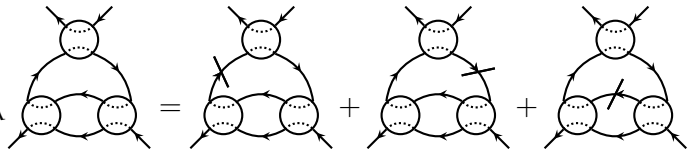


(4.2.6)

There are different ways to handle *equivalent* lines, as introduced in Chapter 3: the last diagram should appear twice due to the derivative of the two equivalent lines. We decide to only write down one of

1 If the $\Lambda$ dependence characterizes a low-energy cutoff the single-scale propagator will be (more or less) sharply peaked at a given energy.

these; the missing factor of two cancels with the factor $2^{-n_{eq}}$ of Algorithm Algorithm 3.1 (we do not consider dashed and undashed lines to be equivalent anymore). This represents the simple realization that for two equivalent lines including the symmetry factor:

$$\partial_\Lambda \frac{1}{2} \bar{v}_{1'2'|34} g^\Lambda_{3|3'} g^\Lambda_{4|4'} \bar{v}_{3'4'|12} = \bar{v}_{1'2'|34} s^\Lambda_{3|3'} g^\Lambda_{4|4'} \bar{v}_{3'4'|12}. \quad (4.2.7)$$

When considering the derivative of the sum of all contributing diagrams one can identify one-particle irreducible vertex functions. For the diagram above we find:

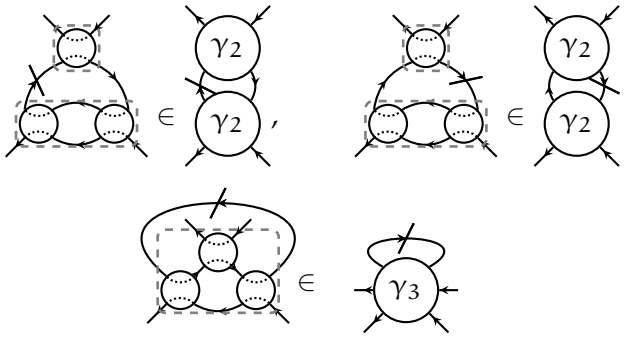


(4.2.8)

where the resummed diagrams are understood as a set of the constituents. Similarly, we can see that self-energy insertions can arise

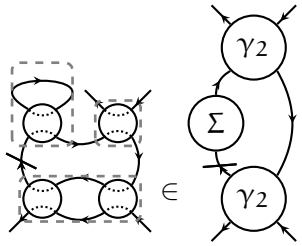


(4.2.9)

on either side of the single-scale propagator or within the free Green's function. One can easily convince oneself that not only are all diagrams contained in one of these resummed diagrams but also all necessary diagrams for the resummation appear exactly once.

Summing up all self-energy contribution turns all bare Green's functions into full ones and replaces the single-scale propagator with

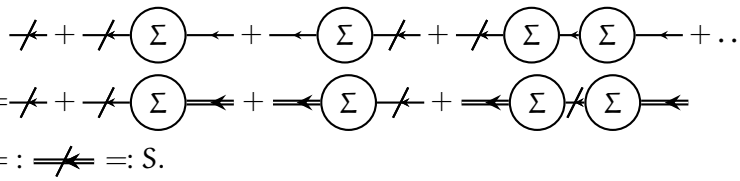


(4.2.10)

Note that in this construction

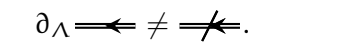


(4.2.11)

Instead

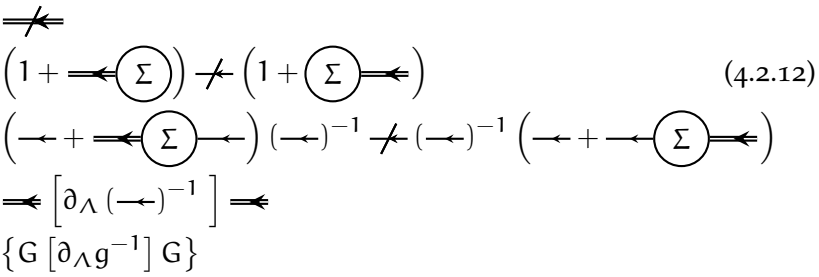


(4.2.12)

Inspecting Equation 4.2.10, we can also interpret $S$ as being the $\Lambda$ derivative of $G$, but *only* acting on the bare Green's function (where we introduced the cutoff), while not acting on the self-energy. We formally denote this by

$$S_{1|1'} = \partial_\Lambda^* G_{1|1'} \tag{4.2.13}$$

which we call the derivative with respect to the *explicit* $\Lambda$ dependence. Note that due to the definition of the single-scale propagator the bare and full patch-component (compare Equation 2.3.15) vanish:

$$s^P_{i|i'}(t|t') \equiv 0 \equiv S^P_{i|i'}(t|t') \; \forall t, t'. \tag{4.2.14}$$

To exemplify the procedure, let us consider the one-particle vertex (i.e. the self-energy, see Equation 3.4.5):

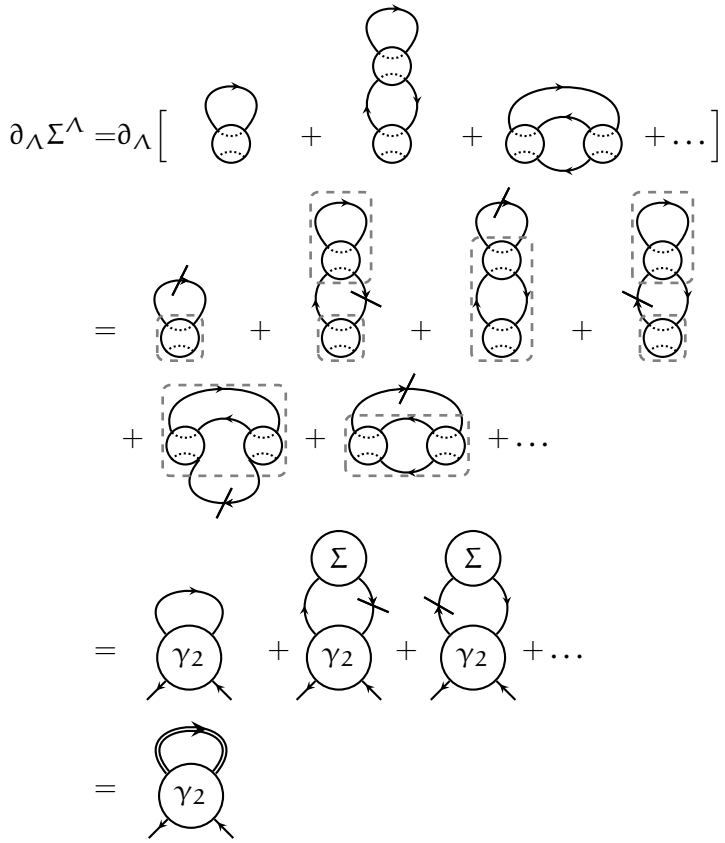


(4.2.15)

where we used the expansion of the two-particle vertex:

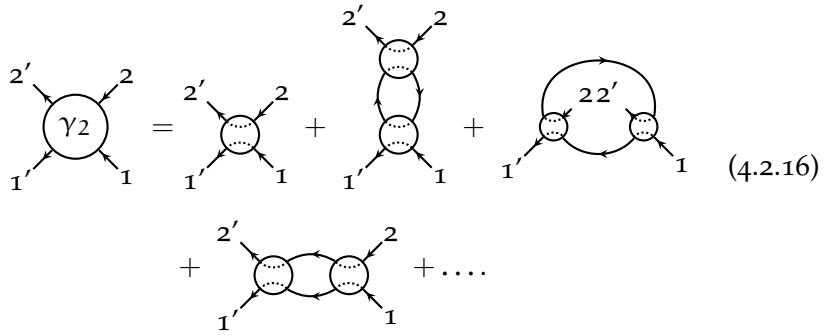


(4.2.16)

Similarly, one shows

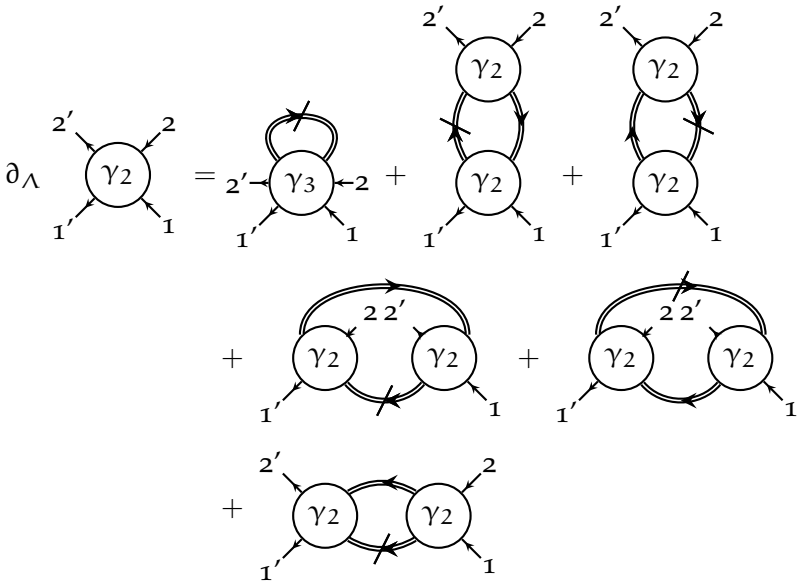


(4.2.17)

This procedure results in an infinite hierarchy of differential equations. Each differential equation has the form

$$\begin{aligned}\partial_\Lambda \gamma^n &= \mathcal{F}\left(\gamma^2, \ldots, \gamma^{n+1}, G, S\right) \\ &= \tilde{\mathcal{F}}\left(\gamma^1, \ldots, \gamma^{n+1}, g, s\right)\end{aligned} \tag{4.2.18}$$

making each of the equations an ordinary first order differential equation. Conventional derivations based on the path-integral formalism can be found in the literature (e.g. [KBS10]).

### 4.2.2 *Initial conditions*

For a well behaved cutoff introduced in the free Green's function the above (infinite) set of differential equations defines how the vertex functions in the presence of two different values of the cutoff are related. For this to be of any use, we need at least one value of $\Lambda = \Lambda_{\text{ini}}$ where the vertex functions are known.

We will usually chose $\Lambda_{\text{ini}} = \infty$ and introduce the cutoff $\Lambda$ in the bare Green's function in a way that they become simple enough to evaluate all vertex functions at $\Lambda = \Lambda_{\text{ini}}$ analytically. The details of the cutoff introduced will differ but generally, it is desirable that

$$\begin{aligned} g^{K,\Lambda_{\text{ini}}}(t|t') &= 0 \ \forall t, t' > t_0 \\ g^{\text{ret},\Lambda_{\text{ini}}}(t|t') &= 0 \ \forall t, t' > t_0, \ t \neq t' \end{aligned} \tag{4.2.19}$$

while maintaining

$$g^{\text{ret},\Lambda_{\text{ini}}}(t|t) + g^{\text{adv},\Lambda_{\text{ini}}}(t|t) = 0. \tag{4.2.20}$$

With this, the initial condition for the self-energy becomes (note that the patch Green's function contributes finite weight at equal times, compare Equations 2.3.15 and 3.4.3)[2]

$$\begin{aligned} \Sigma^{K,\Lambda_{\text{ini}}}_{i'|i}(t|t') &= 0 \\ \Sigma^{\text{ret},\Lambda_{\text{ini}}}_{i'|i}(t|t') &= \nu_{i'j'|ij}(t)\delta(t'-t)\frac{1}{2} \ \forall t, t' > t_0. \end{aligned} \tag{4.2.21}$$

This corresponds to the self-energy of half-filled, uncorrelated sites as emerges in an infinite temperature state or when strongly coupled to partially filled reservoirs. For the higher vertex functions (for times larger than $t_0$) we find

$$\begin{aligned} \gamma^{2,\Lambda_{\text{ini}}}_{1'2'|12} &= \bar{\nu}_{1'2'|12} \\ \gamma^{k,\Lambda_{\text{ini}}} &= 0 \ \forall k > 2. \end{aligned} \tag{4.2.22}$$

Generally the initial conditions depend on the details of the cutoff scheme.

While in principle, the set of differential equations in combination with the initial conditions is sufficient to solve the entire problem, in practice we have to truncate the hierarchy defined in Equation 4.2.18.

### 4.2.3 *Truncation*

Thus far, we have just rewritten the full problem in terms of differential equation without any approximation; the solution of this formulation is, however, as hard as the original problem. To be able to approximately solve this infinite hierarchy of differential equations presented above we note that all diagrams contributing to the rhs of the flow equation of the $n$-particle vertex function are at least of order $n$ in the bare interaction. For small interactions a reasonable truncation is therefore to approximate all right-hand sides of the differential equations by 0 beyond a given *truncation order*. More involved truncation schemes exist [Kato4], but are not considered throughout this work.

2 The equal time Keldysh component will in general not vanish and depend on the cutoff used. Later, we will discuss concrete examples.

So far we have not specified how to introduce the cutoff parameter $\Lambda$ and expect the solution of the exact flow equations to be independent of this choice; after truncating the flow equations, however, the results will generally depend on it. To obtain an RG scheme in the traditional sense, it is essential to choose the $\Lambda$ dependence such that it properly regularizes divergences; in our case, that means that the $\Lambda$ should act as in infrared cutoff. If done properly, the fRG equations act as an RG scheme and the resummation regularizes divergencies.

### 4.2.4 *Why fRG is not a diagrammatic approximation*

As we have derived the flow equations using diagrammatic techniques one might be tempted to classify the (truncated) fRG as a diagrammatic approximations. This line of thought is erroneous: we have seen in the example discussed in Equation 4.2.8, a single diagram can be associated with different vertex functions and thus associated with different orders of the flow equation; a simple truncation disregarding the flow of the three-particle vertex will *partially* disregard the diagram presented in Equation 4.2.8.

One can easily see that in a first order truncation scheme only the first order diagram is fully contained in fRG while an infinite number of additional diagrams is partially resummed.

In addition to the perturbation theory diagrams a second order truncation contains ladder diagrams for the vertex function while most other higher order diagrams are only partially included.

### 4.2.5 *Flow equations in the stationary state*

In the stationary state it is straightforward to Fourier transform the flow equations and immediately obtain the stationary state vertex functions. As we will discuss approximations to the stationary state explicitly in Chapters 7 and 8, we deem it beneficial to explicitly state the stationary state flow equation. The self-energy flows as (compare Equation 2.4.5)

$$\partial_\Lambda \Sigma_{1'|1}(\omega) = \frac{-i}{2\pi} \int d\Omega \gamma_{1'2'|12}(\Pi = \Omega + \omega, X = \Omega - \omega, \Delta = 0) S_{2|2'}(\Omega) \tag{4.2.23}$$

while for the (truncated) flow of the two-particle vertex function we write

$$\partial_\Lambda \gamma_{1'2'|12}(\Pi, X, \Delta) = \sum_{\alpha \in \{p,d,x\}} \partial_\Lambda \gamma^{\alpha}_{1'2'|12}(\Pi, X, \Delta) \tag{4.2.24}$$

with the individual channels:

$$\begin{aligned}\partial_\Lambda \gamma^{p}_{1'2'|12}(\Pi, X, \Delta) =& \frac{i}{2\pi}\int d\omega \\ & \gamma_{1'2'|34}\left(\Pi, \omega + \frac{X-\Delta}{3}, \omega - \frac{X-\Delta}{2}\right) S_{3|3'}\left(\frac{\Pi}{2} - \omega\right) \\ & G_{4|4'}\left(\frac{\Pi}{2} + \omega\right) \gamma_{3'4'|12}\left(\Pi, \frac{X+\Delta}{2} + \omega, \frac{X+\Delta}{2} - \omega\right)\end{aligned} \tag{4.2.25}$$

$$\begin{aligned}\partial_\Lambda \gamma^{x}_{1'2'|12}(\Pi, X, \Delta) =& \frac{i}{2\pi}\int d\omega \gamma_{1'4'|32}\left(\frac{\Pi+\Delta}{2} + \omega, X, \frac{\Pi+\Delta}{2} - \omega\right) \\ & \left[S_{3|3'}\left(\omega - \frac{X}{2}\right) G_{4|4'}\left(\omega + \frac{X}{2}\right) + G_{3|3'}\left(\omega - \frac{X}{2}\right) S_{4|4'}\left(\omega + \frac{X}{2}\right)\right] \\ & \gamma_{3'2'|14}\left(\omega + \frac{\Pi-\Delta}{2}, X, \omega - \frac{\Pi-\Delta}{2}\right)\end{aligned} \tag{4.2.26}$$

$$\begin{aligned}\partial_\Lambda \gamma^{d}_{1'2'|12}(\Pi, X, \Delta) =& \frac{-i}{2\pi}\int d\omega \gamma_{1'3'|14}\left(\omega + \frac{\Pi-X}{2}, \omega - \frac{\Pi-X}{2}, \Delta\right) \\ & \left[S_{3|3'}\left(\omega - \frac{\Delta}{2}\right) G_{4|4'}\left(\omega + \frac{\Delta}{2}\right) + G_{3|3'}\left(\omega - \frac{\Delta}{2}\right) S_{4|4'}\left(\omega + \frac{\Delta}{2}\right)\right] \\ & \gamma_{4'2'|32}\left(\frac{\Pi+X}{2} + \omega, \frac{\Pi+X}{2} - \omega, \Delta\right).\end{aligned} \tag{4.2.27}$$

The three terms on the rhs of the second flow-equations represent the three types of diagrams shown in Equation 4.2.9.

### 4.2.6 *Cutoff in the for of a self-energy*

Some cutoff schemes can be more intuitively understood as a self-energy via the Dyson equation

$$\begin{aligned} G^\Lambda &= G + G\Sigma^\Lambda_{cut} G^\Lambda \\ \Rightarrow S^\Lambda &= \partial^*_\Lambda G = G\left(\partial_\Lambda \Sigma^\Lambda_{cut}\right) G^\Lambda + G\Sigma^\Lambda_{cut} S^\Lambda \\ &= G^\Lambda\left(\partial_\Lambda \Sigma^\Lambda_{cut}\right) G^\Lambda. \end{aligned} \tag{4.2.28}$$

Such an interpretation of the cutoff can be useful in real-time as well as in frequency space. In the stationary state the Dyson equation can be solved especially easily and yields

$$\begin{aligned} G^{\mathrm{ret},\Lambda}(\omega) &= \frac{1}{G^{\mathrm{ret}}(\omega)^{-1} - \Sigma_{\mathrm{cut}}^{\mathrm{ret},\Lambda}(\omega)} \\ &= \frac{1}{g^{\mathrm{ret}}(\omega)^{-1} - \Sigma_{\mathrm{cut}}^{\mathrm{ret},\Lambda}(\omega) - \Sigma^{\mathrm{ret},\Lambda}(\omega)} \\ G^{\mathrm{K},\Lambda}(\omega) &= G^{\mathrm{ret},\Lambda}(\omega)\left[\Sigma_{\mathrm{cut}}^{\mathrm{K},\Lambda}(\omega) + \Sigma^{\mathrm{K},\Lambda}(\omega)\right] G^{\mathrm{adv},\Lambda}(\omega) \end{aligned} \tag{4.2.29}$$

with corresponding single-scale propagator.

## 4.3 SYMMETRIES WITHIN FRG

### 4.3.1 *Fluctuation dissipation theorem*

As we discussed in Section 3.3.5, the fluctuation-dissipation theorem is conserved when making a diagrammatic approximation, as long as the diagrammatic approximation conserves antisymmetry with respect to particle exchange and maps to itself when inverted. The proof we presented was based on properties of diagrams as well as the fluctuation-dissipation theorem of the bare propagator and vertex function. Hence, it is straightforward to generalize it for approximations to the fRG flow-equations. This is possible, if

(a) the truncation and all further approximations includes all diagrams such that the antisymmetry with respect to particle exchange is conserved and the rhs of the flow equations maps to itself when inverted and

(b) the bare single scale propagator and bare Green's functions fulfill the fluctuation-dissipation theorem in presence of the cutoff $\Lambda$.

Following the same steps as outlined in Section 3.3.5 one then shows that all vertex functions fulfill Equation 3.3.12.

### 4.3.2 *Causality*

Similar to the fluctuation-dissipation theorem, the proof of the causality relation (compare Section 3.3.4) is reduced to individual diagrams and based on properties of the bare vertex function as well the bare propagators.

This prove can be directly generalized to the flow-equations of fRG by realizing that any vertex function in the truncated fRG equations can be understood as a linear combination (i.e. integral) of diagrams containing bare interactions, non-interacting Green's functions and single-scale propagators at various values of the cutoff. As the theorem of causality is linear, it remains true as long as the bare Green's

function and single-scale propagator fulfill causality in presence of the cutoff.

Note that even if the cutoff breaks causality, the exact solution will recover this symmetry at the end of the flow if solved exactly; when the hierarchy of equations is truncated, however, we can expect causality only if the cutoff does not explicitly break it.

## 4.4 EXAMPLES: FIRST ORDER FRG SCHEMES

As examples, we will now discuss three implementations of the first-order fRG equations designed for time-dependent problems, stationary states and equilibrium scenarios.

### 4.4.1 *Reservoir cutoff in real time*

In this scheme, first implemented in [Ken+12], all single-particle states of the system are initially coupled infinitely strongly to a wide-band reservoir which suppresses all dynamics and immediately forces the system into a thermal state regardless of the interaction; by lowering the hybridization strength $\Lambda$, one eventually retrieves the original problem. The description presented here is based on [KKK18]. [3]

The causality relation in this scheme is preserved as the system in presence of the cutoff is still a physical system (that naturally preserves causality) and the fRG equations do not violate causality (see Section 4.3.2). We can therefore directly work in the RKA basis.

If we conveniently choose the reservoir's temperature to be infinite, its effects can be understood in terms of the following self-energy (compare Eq. (4.4.7)):

$$\begin{aligned} \Sigma_{\text{cut}}^{\text{K},\Lambda}(t,t') &= 0 \\ \Sigma_{\text{cut}}^{\text{ret},\Lambda}(t,t') &= -i\delta(t-t')\Lambda\mathbb{1}. \end{aligned} \tag{4.4.1}$$

The Green's functions of the time-dependent, noninteracting system read (compare Eq. (3.2.34))

$$\begin{aligned} g^{\text{ret},\Lambda}(t,t') &= e^{-(t-t')\Lambda} g^{\text{ret},\Lambda=0}(t,t') \\ g^{\text{K},\Lambda}(t,t') &= -i g^{\text{ret},\Lambda}(t,t_0)\,(1+2\xi\bar{n})\, g^{\text{adv},\Lambda}(t_0,t'). \end{aligned} \tag{4.4.2}$$

Note that the cutoff is introduced such that Equations 4.2.19 and 4.2.2 are fulfilled with $\Lambda_{\text{ini}} = \infty$ and $\Lambda_{\text{final}} = 0$.

3 Authored by C. Klöckner, D. M. Kennes and C. Karrasch, published in the journal *Physical Review B* by the American Physical Society [KKK18]. Copyright remains with the APS.

The fRG flow equations truncated to leading order are given by (note that $S^P = 0$, compare Equation 4.2.14) [Ken+12]:

$$\begin{aligned}
&\partial_\Lambda \Sigma^{\mathrm{ret},\Lambda}_{i,j}(t,t') = -\frac{i}{2}\delta(t-t')\sum_{k,l} S^{K,\Lambda}_{l,k}(t,t)\nu_{i,k|j,l}(t) \\
&\partial_\Lambda \Sigma^{K,\Lambda}_{i,j}(t,t') \\
&\quad = -\frac{i}{2}\delta(t-t')\sum_{k,l}\left(S^{\mathrm{ret},\Lambda} + S^{\mathrm{adv},\Lambda}\right)_{l,k}(t,t)\nu_{i,k|j,l}(t)
\end{aligned} \tag{4.4.3}$$

with the single-scale propagator (see Equation 4.2.28)

$$\begin{aligned}
&S^{\mathrm{ret},\Lambda}(t,t') \\
&= \int dt_1\, dt_2 G^{\mathrm{ret},\Lambda}(t,t_1)\left[\partial_\Lambda \Sigma^{\mathrm{ret},\Lambda}_{\mathrm{cut}}(t_1,t_2)\right] G^{\mathrm{ret},\Lambda}(t_2,t') \\
&S^{K,\Lambda}(t,t') \\
&= \int dt_1\, dt_2 \Big\{ G^{\mathrm{ret},\Lambda}(t,t_1)\left[\partial_\Lambda \Sigma^{\mathrm{ret},\Lambda}_{\mathrm{cut}}(t_1,t_2)\right] G^{K,\Lambda}(t_2,t') \\
&\qquad + G^{\mathrm{ret},\Lambda}(t,t_1)\left[\partial_\Lambda \Sigma^{K,\Lambda}_{\mathrm{cut}}(t_1,t_2)\right] G^{\mathrm{adv},\Lambda}(t_2,t') \\
&\qquad + G^{K,\Lambda}(t,t_1)\left[\partial_\Lambda \Sigma^{\mathrm{adv},\Lambda}_{\mathrm{cut}}(t_1,t_2)\right] G^{\mathrm{adv},\Lambda}(t_2,t') \Big\},
\end{aligned} \tag{4.4.4}$$

where $G^\Lambda$ refers to the full Green's function obtained via Equation 3.2.31. For the specific cutoff used here (see Equation 4.4.1) the above equation takes the form

$$\begin{aligned}
&S^{\mathrm{ret},\Lambda}(t,t') = -i\int dt_1\, G^{\mathrm{ret},\Lambda}(t,t_1)G^{\mathrm{ret},\Lambda}(t_1,t') \\
&\Rightarrow S^{\mathrm{ret},\Lambda}(t,t) = 0.
\end{aligned} \tag{4.4.5}$$

The equal-time single-scale propagator vanished due to the causality relation Equation 2.3.20. Thus, in this scheme, the Keldysh self-energy does not flow:

$$\partial_\Lambda \Sigma^{K,\Lambda}(t,t') = 0$$

The initial conditions correspond to the self-energy contribution of the thermalized system at infinite temperature (compare Equation 4.2.20):

$$\begin{aligned}
\Sigma^{K,\Lambda=\infty}(t,t') &= 0 \\
\Sigma^{\mathrm{ret},\Lambda=\infty}_{i,j}(t,t') &= \frac{1}{2}\delta(t-t')\sum_{k,l}\nu_{i,k|j,l}(t).
\end{aligned}$$

Hence, the Keldysh self-energy remains zero throughout the flow and the retarded self-energy is time-local. This type of self-energy has been discussed in Eq. (3.2.34) and Eq. (2.5.12).

Due to the time-local structure of the self-energy, the group property presented in Eq. (2.5.12) holds and the single-scale propagator of Eq. (4.4.5) can be simplified further:

$$\begin{aligned} S^{\mathrm{ret},\Lambda}(t,t') &= -(t-t')G^{\mathrm{ret},\Lambda}(t,t') \\ S^{\mathrm{K},\Lambda}(t,t') &= \partial^*_\Lambda \left[ G^{\mathrm{ret},\Lambda}(t,0)(1+2\xi\bar{n})G^{\mathrm{adv},\Lambda}(0,t') \right] \\ &= S^{\mathrm{ret},\Lambda}(t,0)(1+2\xi\bar{n})G^{\mathrm{adv},\Lambda}(0,t') \\ &\quad + G^{\mathrm{ret},\Lambda}(t,0)(1+2\xi\bar{n})S^{\mathrm{adv},\Lambda}(0,t') \\ &= -(t+t')G^{\mathrm{K},\Lambda}(t,t'), \end{aligned}$$

resulting in the final form of the flow equation:

$$\partial_\Lambda \Sigma^{\mathrm{ret},\Lambda}_{i,j}(t,t') = it\delta(t-t') \sum_{k,l} G^{\mathrm{K},\Lambda}_{l,k}(t,t) v_{i,k|j,l}(t). \tag{4.4.6}$$

### 4.4.2 *Reservoir cutoff scheme for stationary states*

As an example of an fRG-formulation to obtain correlations in the stationary state, we discuss a reservoir cutoff scheme in first order truncation. [JPS10a; GPM07; JMS07; Kar+10]

Similar to Section 4.4.1 we employ an auxiliary reservoir cutoff scheme which is implemented by introducing a wide-band bath that couples to every single-particle degree of freedom of the system with a strength $\Lambda$. [Jak09] Such a reservoir (which itself is initially prepared in equilibrium) can be taken into account using a self-energy of the form (compare Section 2.5.4)

$$\begin{aligned} \Sigma^{\mathrm{ret},\Lambda}_{\mathrm{cut}}(\omega) &= -i\Lambda \mathbb{1} \\ \Sigma^{\mathrm{K},\Lambda}_{\mathrm{cut}}(\omega) &= [1-2n_{\mathrm{cut}}(\omega)] \underbrace{\left[ \Sigma^{\mathrm{ret},\Lambda}_{\mathrm{cut}}(\omega) - \Sigma^{\mathrm{adv},\Lambda}_{\mathrm{cut}}(\omega) \right]}_{-2i\Lambda\mathbb{1}} \end{aligned} \tag{4.4.7}$$

where $n_{\mathrm{cut}}(\omega)$ is the auxiliary reservoir's distribution function and the second equation is enforced by the fluctuation-dissipation theorem (note, that the reservoir self-energy only depends on the dynamics of the *disconnected*, i.e. equilibrium, reservoir). In contrast to Section 4.4.1 we allow for a general distribution function and in absence of physical reservoirs the auxiliary ones define the statistics of the system.

The reservoir-dressed Green's function is given by

$$\begin{aligned} G^{\mathrm{ret},\Lambda}(\omega) &= \frac{1}{g^{\mathrm{ret}}(\omega)^{-1} + i\Lambda\mathbb{1} - \Sigma^{\mathrm{ret},\Lambda}(\omega)} \\ G^{\mathrm{K},\Lambda}(\omega) &= G^{\mathrm{ret},\Lambda}(\omega) \left[ \Sigma^{\mathrm{K},\Lambda}_{\mathrm{cut}}(\omega) + \Sigma^{\mathrm{K},\Lambda}(\omega) \right] G^{\mathrm{adv},\Lambda}(\omega) \end{aligned}$$

and Equation 4.2.28 yields

$$\begin{aligned}
S^{\mathrm{ret},\Lambda}(\omega) &= \partial^*_\Lambda G^{\mathrm{ret},\Lambda}(\omega) = -iG^{\mathrm{ret},\Lambda}(\omega)G^{\mathrm{ret},\Lambda}(\omega) \\
S^{\mathrm{K},\Lambda}(\omega) &= \partial^*_\Lambda G^{\mathrm{K},\Lambda}(\omega) \\
&= S^{\mathrm{ret},\Lambda}(\omega)\left[\Sigma^{\mathrm{K},\Lambda}_{\mathrm{cut}}(\omega) + \Sigma^{\mathrm{K},\Lambda}(\omega)\right] G^{\mathrm{adv},\Lambda}(\omega) \\
&\quad + G^{\mathrm{ret},\Lambda}(\omega)\left[\Sigma^{\mathrm{K},\Lambda}_{\mathrm{cut}}(\omega) + \Sigma^{\mathrm{K},\Lambda}(\omega)\right] S^{\mathrm{adv},\Lambda}(\omega) \\
&\quad + G^{\mathrm{ret},\Lambda}(\omega)\left[\partial_\Lambda \Sigma^{\mathrm{K},\Lambda}_{\mathrm{cut}}(\omega)\right] G^{\mathrm{adv},\Lambda}(\omega)
\end{aligned}$$

Finally, the flow equations read

$$\partial_\Lambda \Sigma^{\mathrm{ret},\Lambda}_{i,j} = -\frac{i}{4\pi}\sum_{k,l} v_{i,k,j,l} \int d\omega \left[S^{\mathrm{K},\Lambda}(\omega)\right]_{l,k} \tag{4.4.8}$$

$$\begin{aligned}
\partial_\Lambda \Sigma^{\mathrm{K},\Lambda}_{i,j} &= -\frac{i}{4\pi}\sum_{k,l} v_{i,k,j,l} \int d\omega \left[S^{\mathrm{ret},\Lambda}(\omega) + S^{\mathrm{adv},\Lambda}(\omega)\right]_{l,k} \\
&= -\frac{i}{4\pi}\sum_{k,l} v_{i,k,j,l} \\
&\qquad \int d\omega \left[i\partial_\omega G^{\mathrm{ret},\Lambda}(\omega) - i\partial_\omega G^{\mathrm{adv},\Lambda}(\omega)\right]_{l,k} \\
&= 0
\end{aligned}$$

Therefore, as we have seen in the time-dependent case, we do not obtain a finite Keldysh self-energy in the first-order truncation. Furthermore, the retarded self-energy is frequency independent and thus constitutes a correction to the non-interacting Hamiltonian (compare Equation 3.2.34).

### 4.4.3 *Matsubara fRG*

While not the focus of this work, we will also discuss equilibrium properties of some of the systems considered and use the equilibrium formalism as a point of reference. To this end, we will briefly introduce the Matsubara fRG formalism but will refrain from the details. Furthermore, we will restrict ourselves to the $T = 0$ case, where a pure state is obtained and only discuss the first order truncation.

The simplest way to introduce an infrared regularization in Matsubara frequency space at $T = 0$ (i.e., in the ground state) is a sharp cutoff [And+04]

$$\begin{aligned}
g^{\mathrm{eq},\Lambda}(i\omega) &= g^{\mathrm{eq}}(i\omega)\theta(|\omega| - \Lambda) \\
S^{\mathrm{eq},\Lambda}(i\omega) &= -\left[\delta(\omega - \Lambda) + \delta(\omega + \Lambda)\right] G^{\mathrm{eq},\Lambda}(i\omega) \\
G^{\mathrm{eq},\Lambda}(i\omega) &= \frac{1}{\left(g^{\mathrm{eq},\Lambda}(\omega)\right)^{-1} - \Sigma^{\mathrm{eq},\Lambda}}.
\end{aligned} \tag{4.4.9}$$

Using Morris lemma [Mor94; And+04] results in the following flow equation for the self-energy at $T = 0$:

$$\partial_\Lambda \Sigma^{\mathrm{eq},\Lambda}_{i,j} = -\frac{1}{2\pi} \sum_{k,l} \sum_{\omega=\pm\Lambda} v_{i,k|j,l} \left( \frac{1}{i\omega - h^0 - \Sigma^{\mathrm{eq},\Lambda}} \right)_{l,k} , \quad (4.4.10)$$

where $\Lambda$ is integrated from $\Lambda_{\mathrm{ini}} = \infty$ to $\Lambda_{\mathrm{final}} = 0$. If one removes the feedback of the self-energy on the right-hand side of this equation, one obtains standard first order Matsubara perturbation theory. As it is sometimes desirable to compare to perturbation theory results, we will now discuss how to remove higher order resummations from an fRG algorithm.

## 4.5 HOW REDUCE FRG TO PERTURBATION THEORY

As we already discussed in Section 4.2.4, fRG is *not* a diagrammatic approximation. Beyond the perturbation theory diagrams only few additional diagrams are fully included while an infinite series of higher, non-diagrammatic contributions are resummed. It is now reasonable to ask (while not trivial to answer) whether perturbation theory results can be extracted from an algorithm that is set up to compute a truncated fRG flow. To that end, let us inspect the diagrammatic form of the flow equation of the self-energy:

$\partial_\Lambda$ (Σ) = (γ2) .

As

$$= + \mathcal{O}(U), \qquad (\gamma_2) = (\cdots) + \mathcal{O}(U^2)$$

we can reproduce perturbation theory from fRG by (i) truncating the flow by setting $\gamma_2 = \bar{v}$ and (ii) setting $\Sigma = 0$ on the rhs of the flow equation:

$\partial_\Lambda$ (Σ) = (γ2) → → = $\partial_\Lambda$ (Σ) (4.5.1)

Hence solving this flow equation will result in first-order perturbation theory.

In a typical implementation of a first order fRG algorithm, perturbation theory results can be achieved even more directly by replacing $S \to G$ and evaluating the rhs only at the final value of the cutoff parameter without solving the flow equation.

**Algorithm 4.1: 1st order perturbation theory from fRG**

Given an fRG implementation that provides:

$$G^\Lambda(\Sigma^\Lambda),\ S^\Lambda(\Sigma^\Lambda),\ \partial_\Lambda\Sigma^\Lambda(\gamma^\Lambda, G^\Lambda, S^\Lambda)$$

then 1st order PT can be obtained as:

$$\Sigma^{1\mathrm{PT}} = \partial_\Lambda\Sigma(\gamma = \bar{v}, G = g, S = g)$$

where $g = G^{\Lambda_{\mathrm{final}}}(\Sigma = 0)$.

Following the same steps to second order does not yield the desired result, as discussed in [Kar10]. While truncating beyond the two-particle vertex, replacing the two-particle vertex with the bare interaction and removing the self-energy feedback for in the flow equation of the two-particle vertex yields the perturbative results:

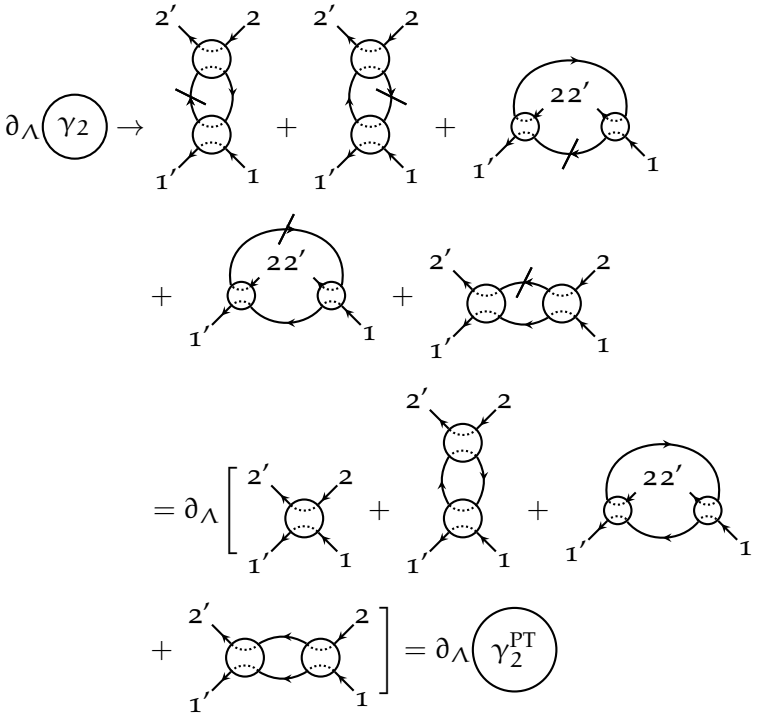


(4.5.2)

the same can not be said for any such algorithm for the self-energy (compare Equation 3.4.5):

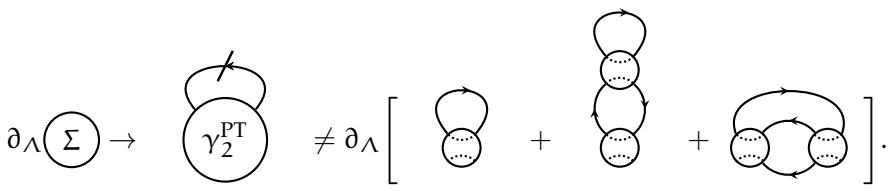


(4.5.3)

When compared to Equation 4.2.15, we realize that self-energy insertions are missing in the single-scale propagator.

This is due to the (in this scheme neglected) $\mathcal{O}(U)$ contributions of $S$. Instead, we should replace

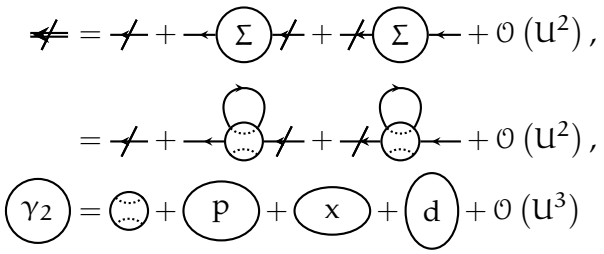


(4.5.4)

with

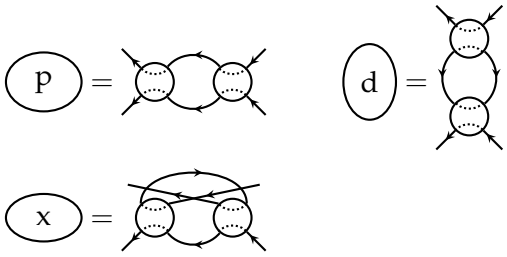


(4.5.5)

while being careful to only keep the higher orders when needed. While it is straightforward to prove that one can indeed reproduce perturbation theory with these replacements, it is inconvenient for an actual implementation to have to use two different approximations to the full single-scale propagator and extracting perturbation theory results without writing code specifically for this purpose will rarely be possible with this procedure.

If the implementation, however, includes functions to evaluate the channel-decomposed two-particle vertex we can instead use these to obtain the perturbation theory self-energy:

**Algorithm 4.2: 2nd order perturbation theory from fRG**

Given an fRG implementation that provides:

$$G(\Sigma),\ S(\Sigma),\ \partial_\Lambda \Sigma(\gamma, G, S),\ \partial_\Lambda \gamma^\alpha(\gamma, G, S),\ \alpha = x, p, d$$

then 2nd order PT can be obtained as:

$$\Sigma^{2PT} = \partial_\Lambda \Sigma \left[\gamma = \bar{v} + \gamma^d_{2PT} + \gamma^p_{2PT}, G = g, S = g\right]$$
$$\gamma^\alpha_{2PT} = \partial_\Lambda \gamma^\alpha(\gamma^\alpha = 0, G = g, S = g)$$

where $g = G^{\Lambda_{\text{final}}}(\Sigma = 0)$.

Note that to second order $\gamma^p$ and $\gamma^x$ contribute equally (up to a factor) to the self-energy and we thus only use one of them. The validity of this algorithm is easily seen within the diagrammatic representation.

# 5 TRANSPORT IN A QUASIPERIODIC POTENTIAL

## 5.1 INTRODUCTION

This chapter is based on the paper *Transport in quasiperiodic interacting systems: From superdiffusion to subdiffusion*, authored by Y. Bar Lev[1], D. M. Kennes[1], C. Klöckner[1], D. R. Reichmann and C. Karrasch, published in the journal *Europhysics Letters* by the Institute of Physics Publishing [Lev+17]. Copyright remains with the IOP. The DMRG data presented and discussed in Sections 5.4 and 5.5 as well as Figure 5.7 was provided by D. M. Kennes and C. Karrasch.

It is devoted to the study of transport in quasiperiodic potentials. Interacting quasiperiodic (QP) systems are believed to exhibit many body localization (MBL) like in systems with quenched disorder while being easier to experimentally realize. Hence, they form the basis for several recent experimental studies on MBL [Sch+15a; Lue+17]. Unfortunately, very little is known about transport in such systems in the interacting case. Here, we fill this vital gap.

As a point of reference, we will begin by recapitulating conventional ballistic and diffusive transport as well as the effect of disorder in one-dimensional systems. We then introduce the model and the notion of a quasiperiodic potential and employ a finite-temperature version [KBM12; Bar13; KK16b] of the time-dependent matrix renormalization group (tDMRG)[2] [Whi92; Sch11] to demonstrate unconventional transport in this system on short to intermediate time-scales and obtain the AC-conductivity. We than use the functional renormalization group (fRG) [Sal99; Met+12] introduced in Chapter 4 to access larger times and system sizes and provide a naive single-particle picture of the relevant physics.

### 5.1.1 *Normal transport*

In semi-classical approximations, systems generally feature one of only two types of transport:

Ballistic transport is present, when no scattering occurs and therefore the conductance is independent of the length of the system. This implies an infinite DC-conductivity. Ballistic transport is a hallmark of integrable systems (such as free fermions), where an extensive number of conserved quantities prevents scattering.

1 Y. Bar Lev, D. M. Kennes, C. Klöckner contributed equally.

2 The tDMRG results presented in this chapter were obtained and provided by D. M. Kennes and C. Karrasch.

If, on the other hand, particles scatter incoherently, transport is diffusive and conductance decreases with the system size as $G \sim \frac{1}{N}$. For example, adding a two-particle interaction to a quadratic Hamiltonian will generically break integrability and induce scattering resulting in diffusive transport. For a diffusive system in the quasi-classical approximation, the conductivity at small frequencies takes the Drude form [RS86; Ram04; Ash76]

$$\sigma(\omega) \sim \frac{1}{1 + i\omega\tau} \tag{5.1.1}$$

with the scattering time $\tau$. In the limit $\tau \to \infty$, we recover ballistic transport.

When a system features non-vanishing transport, that is neither ballistic nor diffusive it is referred to as *anomalous*.

### 5.1.2 *Anderson localization*

If the system is coherent, random scattering can (and in 1D generically will) lead to interference effects that entirely forbid transport [KM93]. This effect is referred to as *Anderson localization* [And58]. As a simple example, consider a semi-infinite 1D tight binding chain with on-site potentials $\epsilon_i$ chosen from a random distribution

$$H = \sum_{i=0}^{\infty} \epsilon_i c_i^\dagger c_i + c_i^\dagger c_{i+1} + c_{i+1}^\dagger c_i. \tag{5.1.2}$$

Solving the eigenvalue equation for a general single-particle state $|\phi\rangle = \sum_i \alpha_i c_i^\dagger |\text{vac}\rangle$ leads to the equation [KM93]

$$\begin{pmatrix} \alpha_{i+1} \\ \alpha_i \end{pmatrix} = \underbrace{\begin{pmatrix} E - \epsilon_i & -1 \\ 1 & 0 \end{pmatrix}}_{T_i} \begin{pmatrix} \alpha_i \\ \alpha_{i-1} \end{pmatrix} = \cdots = T_i T_{i-1} \cdots T_1 \begin{pmatrix} \alpha_1 \\ \alpha_0 \end{pmatrix}. \tag{5.1.3}$$

The theorem of Fürstenberg then guarantees the existence of a

$$\gamma(E) = \lim_{i\to\infty} \log(\|T_i \cdots T_1\|) > 0 \tag{5.1.4}$$

which shows

$$\left\| \begin{pmatrix} \alpha_{i+1} \\ \alpha_i \end{pmatrix} \right\| \leqslant e^{-\gamma(E)i} \left\| \begin{pmatrix} \alpha_1 \\ \alpha_0 \end{pmatrix} \right\| \quad \text{for } i \to \infty. \tag{5.1.5}$$

Hence, all single-particle eigenstates are exponentially localized, i.e.

$$\exists\, j, \gamma \;\ni\; \alpha_i \sim e^{-\gamma|i-j|} \quad \text{for } |i-j| \to \infty. \tag{5.1.6}$$

and no transport is possible. This type of localization is generic in disordered, one-dimensional quadratic systems.

To measure localization on a single-particle level, one commonly uses the *inverse participation ratio*. Using the example of the state $\phi$ introduced above, one defines

$$\mathrm{IPR}(\phi) := \sum_i |\alpha_i|^4. \tag{5.1.7}$$

As the majority of the weight of a localized state is restricted to a finite region, its inverse participation ratio is independent of system size while the weight of an extended state is distributed over the hole system, resulting in $\mathrm{IPR} \sim \frac{1}{N}$.

### 5.1.3 *Many-body localized phase*

As this picture is based on a single-particle framework and requires coherence to fully localize the spectrum, it was long assumed that the system would delocalize upon introducing a two-particle interaction. This believe was challenged by a seminal work [BAA06] describing localization in weakly interacting fermion systems. Using perturbative methods, the authors argued, that localization can persist, even at finite temperature in the presence of interactions. This sparked a large amount of scientific interest (for reviews, see [AV15; NH15]), producing many analytical and numerical works as well as experimental evidence in cold atomic gases.

The many-body localized phase is, just like its non-interacting counterpart, characterized by an absence of DC transport and thermalization [NH15]. However, the interaction allows entanglement to spread logarithmically [Chi+06; ŽPP08; BPM12; HNO14] and therefore some propagation of information. This leads to dephasing without inducing dissipation or thermalization. As it retains some information of the local details of its initial state at long time-scales it is considered to be *non-ergodic*. This also implies that many-body localized systems violate the *eigenstate thermalization hypothesis* [Deu18], which states that all local observables of individual eigenstates are defined by the energy density and appear thermal.

### 5.1.4 *The ergodic side of the many-body localization transition*

On the delocalized side of the phase transition, transport is possible and equilibration occurs. All microscopic information about the initial configuration of the system is lost over time and thus the system is considered to be ergodic. However, even deep in the metallic phase self-consistent Born approximation indicates abnormally slow relaxation rates [LR14] in disordered systems. Further investigation [Aga+15; LCR15; Aga+15; LL17; Aga+17] has shown, that surprisingly transport is subdiffusive in a parameter regime close to the many-body localized phase (i.e. characterized by slower propagation than diffusive transport). Far from the MBL phase transport

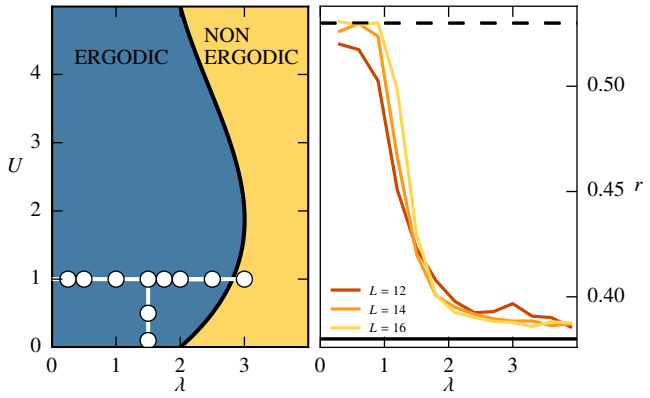


Figure 5.1: *Left panel*: A schematic phase diagram $(U, \lambda)$ of the system (c.f. Fig. 19 in Ref. [Ber+17]) based on exact diagonalization for $N = 16$ sites. The white circles represent the points studied using the tDMRG (see Figure 5.2) . *Right panel*: The average gap ratio $r$ in the middle of the spectrum for various strengths of the QP potential, $U = 1$, and different system sizes (lighter shades represent larger system sizes). The dashed black line corresponds to the Wigner-Dyson limit (expected for an ergodic system) and the solid black line to the Poisson limit (expected in the localized case) [OH07; Ata+13]. This figure was previously published in [Lev+17].

is diffusive. This suppression of transport close to the phase transition is proposed to be explained by the presence of rare-region effects [Aga+15; Gop+15; Gop+16; Aga+17], where anomalously high disorder in some region induces (quasi) localization, significantly hampering transport (for a review, see [Aga+17]). These rare regions lead to a broad distribution of various dynamical observables and dominate the average, long range transport. This can result in corrections of the low-frequency exponent of dynamical quantities and produce sub-diffusive transport. This phenomenological picture has been named *Griffiths picture* and was first described in Ref. [Gri69].

## 5.2 MODEL HAMILTONIAN

The model we employ throughout this chapter is based on a 1D tight-binding chain with quasiperiodic disorder

$$H^0 = \sum_{n \in \underline{N}} \lambda \cos(2\pi\beta n + 2\pi\phi) c_n^\dagger c_n + \sum_{n \in \underline{N-1}} c_n^\dagger c_{n+1} + \text{h.c.} \quad (5.2.1)$$

This Hamiltonian is known as the *Aubry-Andre* (AA) model. It has been studied extensively as it arises as an effective model for two-dimensional electrons in the presence of an electric field and exhibits rich spectral properties such as the Hofstadter butterfly [Hof76]. This

model features an Anderson localization transition for irrational[3] $\beta$ at a critical potential strength $\lambda_c = 2$. Using the inverse golden ratio

$$\beta = \frac{\sqrt{5}-1}{2} = \varphi^{-1}, \tag{5.2.2}$$

for the incommensurate potential leads to short localization lengths and thus a sharp phase transition and is therefore commonly chosen [Mod09]. For $\lambda < \lambda_c = 2$, all single-particle eigenstates are delocalized while for stronger disorder all individual states localize exponentially (compare Section 5.1.2). Hence, in this model independent of the preparation of the system, DC-transport is either ballistic for $\lambda < 2$ and absent for $\lambda > 2$.

When a two-particle interaction is added

$$H^{\text{int}} = \sum_{n \in \underline{N-1}} U \left( c_n^\dagger c_n - \frac{1}{2} \right) \left( c_{n+1}^\dagger c_{n+1} - \frac{1}{2} \right) \tag{5.2.3}$$

$$H = H^0 + H^{\text{int}} \tag{5.2.4}$$

the critical disorder strength to localize the spectrum increases with the interaction but a many-body localized phase persists at large disorder and all energies. At $\lambda = 0$ the system is integrable and transport is ballistic for $U < 2$ [Pro11; IN17] and diffusive for $U > 2$ [ZP96; SB11; Žni11]. For finite $U$ and $\lambda$ the system is not integrable and the phase diagram is separated into an ergodic and a many-body localized phase. A high-temperature phase diagram can be obtained using the statistics of the level-spacing [OH07; Ata+13] as is shown in Figure 5.1.

This interacting variant of the AA model owes its importance to cold atomic gasses [Sch+15a], where a quasiperiodic potential can be generated by superimposing an additional, incommensurate disorder lattice using lasers with a detuned wavelength. At the same time, the two-particle interaction can be tuned using Feshbach resonance. For a review of these experimental methods see [Lew+07]. Experiments (see for example [Sch+15a]) show, that in atomic gases realizing this interacting version of the AA model, localization persists on long time-scales.

While the many-body localized phase has been studied intensively, the transport properties in this model are largely unknown. To characterize the transport in the delocalized phase we employ two complementary methods: first we utilize the numerically exact tDMRG (Section 5.4), which is limited by the growth of entanglement. We then supplement this with the time-dependent variant of the fRG introduced in Chapter 4, which allows us to access significantly larger

3 For rational values of $\beta$ one obtains a crystal; Bloch's theorem forbids localization in that case. Strictly speaking, not all irrational numbers result in an insulating phase; irrational numbers that are exceptionally well approximated by a fraction do not necessarily result in a phase transition. [Jit99; Aul+04; Mod09]

system sizes and longer times (Section 5.6) at the cost of being approximate.

## 5.3 DMRG AS A REFERENCE POINT

Introduced by S. White in [Whi92], the *density matrix renormalization group* (DMRG) evolved into a valuable tool for a variety of problems. For a review of this numerical technique, see Ref. [Sch11].

In a modern formulation of the DMRG, a general many-body spin-state in a N-site lattice

$$|\Psi\rangle = \sum_{\sigma_1,\ldots,\sigma_N \in \{\uparrow,\downarrow\}} A_{\sigma_1,\ldots,\sigma_N} |\sigma_1,\ldots,\sigma_N\rangle \tag{5.3.1}$$

is expressed as a *matrix product state* (MPS)

$$|\Psi\rangle = \sum_{\sigma_1,\ldots,\sigma_N \in \{0,1\}} A_1^{\sigma_1} \cdots A_N^{\sigma_N} |\sigma_1,\ldots,\sigma_N\rangle \tag{5.3.2}$$

with $A_k^{\sigma_k} \in \mathbb{C}^{2^{k-1}\times 2^k}$ for $k \leqslant N/2$ and $A_k^{\sigma_k} \in \mathbb{C}^{2^{N-k+1}\times 2^{N-k}}$ otherwise. The largest matrix dimension that appears in this expression is $2^{N/2}$ and therefore exponentially large in the system size.

Similarly, operators can be decomposed into matrix product operators. Using a singular-value decomposition the dimension of the matrices $A$ can be reduced by retaining their largest eigenvalues up to a finite *bond dimension*.

This approximation can be shown to be optimal in the 2-norm compared to all possible MPS of the same bond dimension [Sch11]. Its quality is directly related to the decay of eigenvalues in the $A$-matrices. These eigenvalues of the matrix $A_k$ are in turn linked to the bipartite entanglement entropy

$$S = -\operatorname{Tr}[\rho_k \log \rho_k] \tag{5.3.3}$$

with the reduced density-matrix $\rho_k$ for sites $1,\ldots,k$.

For short-ranged, gapped Hamiltonian, the bipartite entanglement of the ground-state has been shown to scale as an area law [ECP10]. This refers to the area of the boundary between the two subsystems. Therefore, ground-states of gapped, 1D systems are well described by matrix-product states of finite dimension and DMRG is well suited to access their properties. For gapless systems, that are of the main focus of this work, one finds a logarithmic correction to the area-law in the ground-state. Excited states on the other hand typically feature volume-law entanglement, and therefore pose a challenge. Many-body localized systems form a peculiar exception to this rule, as even excited states feature entanglement that only logarithmically increases with the system size [KK16a].

Using these approximate forms of states imaginary and real time-evolution can be computed. In a time-dependent formulation a matrix

product state of low dimension is typically used as initial preparation. The dynamics induced by the Hamiltonian, however, yield a mixing with excited states, that successively increase the entanglement and eventually make the treatment in the DMRG framework exponentially difficult. This typically restricts the time-scales accessible to this method.

## 5.4 MEAN SQUARE DISPLACEMENT USING TDMRG

A first indication of anomalous (i.e. neither ballistic nor diffusive) transport is provided using tDMRG[2]. Here, we study the quantum version of the *mean square displacement*

$$x^2(t) = \frac{1}{N}\sum_{i,j=1}^{N}(i-j)^2 C_{i,j}(t), \tag{5.4.1}$$

where $C_{i,j}$ denotes the density-density correlation function:

$$C_{i,j}(t) = 2^{-N}\mathrm{Tr}\left(\hat{n}_i^z(t) - \frac{1}{2}\right)\left(\hat{n}_j^z - \frac{1}{2}\right). \tag{5.4.2}$$

When evaluated in equilibrium, the MSD is directly related to the current-current correlation function [LL17]

$$\frac{d^2}{dt^2}x^2(t) = \langle J(t)J(0)\rangle \tag{5.4.3}$$

and therefore also to the frequency resolved conductivity (compare Section 5.5)

$$\begin{aligned}\sigma(\omega) =& \frac{1-e^{-\omega/T}}{\omega}\int_0^\infty dt e^{i\omega t}\lim_{N\to\infty}\frac{\langle J(t)J(0)\rangle}{N}\\ \sim& \omega^2\int dt e^{i\omega t}x^2(t).\end{aligned} \tag{5.4.4}$$

The MSD typically scales as a power-law with time, $x^2 \sim t^\alpha$, where $\alpha$ is the dynamical exponent and is related to the exponent of the conductivity as $\sigma(\omega) \sim |\omega|^{1-\alpha}$ (compare Equation 5.1.1). For systems with ballistic transport, $\alpha = 2$, and for diffusive systems $\alpha = 1$. Systems with no transport or transport with a MSD growing more slowly than any power law will have $\alpha = 0$.

As we discussed above, for quenched disorder transport is generically *subdiffusive*, resulting in dynamical exponent $\alpha < 1$, phenomenologically explained by rare regions. We will use the MSD to investigate transport in the presence of a quasiperiodic potential.

### 5.4.1 *Superdiffusive regime*

To obtain numerical results we average over all eigenstates, effectively setting the temperature to infinity. To reduce the effects of the boundaries we use systems of sizes $N = 100 - 200$.

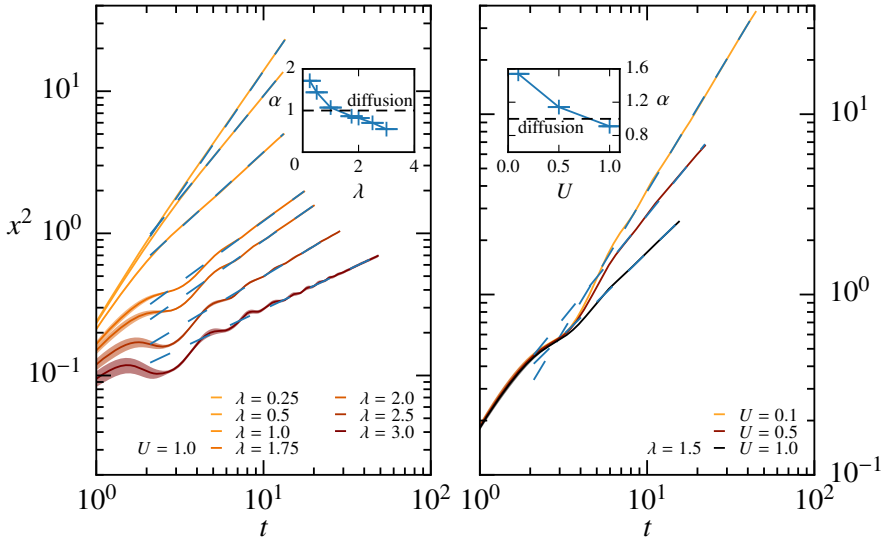


Figure 5.2: Mean-square displacement as a function of time on a log-log scale, for various amplitudes of the QP potential obtained using tDMRG². The left panel shows the horizontal cut through the phase-diagram at Figure 5.1, and the right panel shows the vertical cut. Darker colors represent larger parameters, and the width of the lines represent the statistical error bars. Blue dashed lines show the quality of the power-law fits, and the insets present the corresponding dynamical exponents. The system size used is $N = 100$. The results indicate a smooth transition from superdiffusive to subdiffusive transport. This figure was previously published in [Lev+17].

We start by analyzing the vicinity of the integrable limits $U = 0$ and $\lambda = 0$. For $U < 2$ conserved quantities lead to ballistic transport [Pro11; IN17] (compare Section 5.1.1) while for $U > 2$ transport is found to be diffusive [ZP96; SB11; Žni11]. Neither in the vicinity of $U = 0$ nor close to $\lambda = 0$ we observe diffusive behavior but uncover an extended *superdiffusive regime* where the MSD grows as a power law in time, $x^2 \sim t^\alpha$, with an exponent $1 < \alpha < 2$. This is illustrated in the left (right) panels of Figure 5.2 for the horizontal (vertical) cuts through the phase diagram (see Figure 5.1). The occurrence of superdiffusive transport in the presence of interactions and disorder is in striking contrast to the behavior of clean systems where integrability breaking normally leads to diffusion (for spin systems, see Refs. [JHR06; Zot04; Ste+14; KKHM15], compare Section 5.1.1). However, a simple estimate of the mean free time of scattering from the external potential gives a time-scale of $\tau \sim 1/\lambda^2$, which is about $\tau \approx 16$ for the smallest $\lambda$ we study and is comparable to our maximal simulation times. Therefore while we convincingly observe superdiffusion over one decade in time, we cannot rule out the scenario where it is merely a transient phenomenon. Simulating longer times is exponentially hard within tDMRG since the accessible time scales are

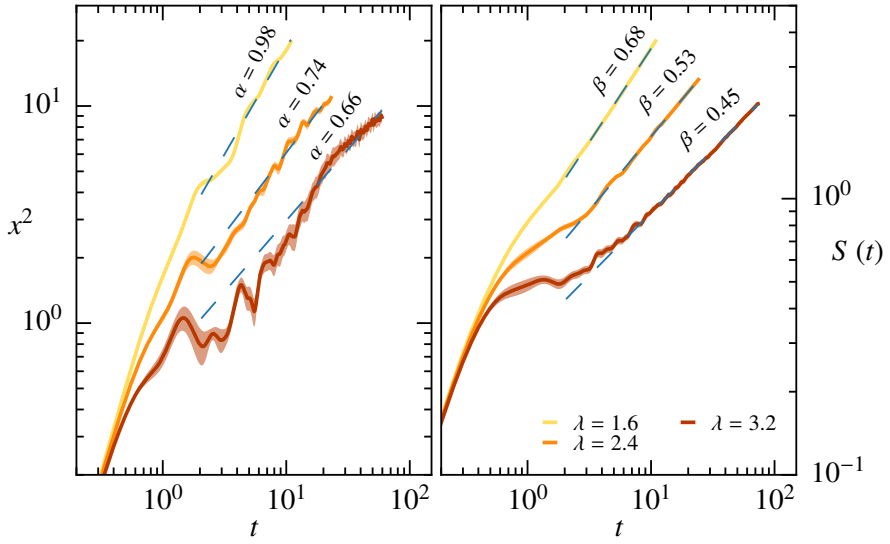


Figure 5.3: Mean-square displacement (left) and entanglement entropy (right) on a log-log scale as a function of time for the CDW as the initial state, obtained with tDMRG². Parameters used: $N = 100$, interaction strength $U = 2$ and $\lambda = 1.6$, 2.4 and ,3.2 (darker colors designate higher values). Dashed lines represent linear fits used to extract the dynamical exponents. Diffusion corresponds to, $\alpha = \beta = 1$. This figure was previously published in [Lev+17].

bounded by the growth of entanglement entropy. Therefore to substantiate our observation of superdiffusion, we will later on complement the tDMRG simulation by a different approach which can reach much longer times at the price of being approximate (see Section 5.6). Since transport in the system is characterized by power laws it is natural to use a renormalization-group based method for this purpose.

### 5.4.2 *Subdiffusive regime*

From the inset of Figure 5.2, which shows the extracted dynamical exponent, it is clear that there is actually no *finite* regime of parameters for which the system is diffusive. This is in stark contrast to the case of quenched disorder (compare Section 5.1.4). Similar behavior was observed in an experimental and numerical study [Lue+17]. To verify that the observed behavior occurs also for *pure* initial states, we calculated the MSD and the entanglement entropy (EE) (see Equation 5.3.3) starting form a charge density wave (CDW), i.e. even (odd) sites initially prepared full (empty) (see Figure 5.3). We note that for the system we study the CDW is a state with relatively high energy density for interactions $U < 2$, lying close to the center of the many-body band, and has been successfully utilized to analyze MBL in cold atoms experiments [Sch+15a; Lue+17]. However unlike the experiments, we do *not* allow volatility in the initial state, namely we

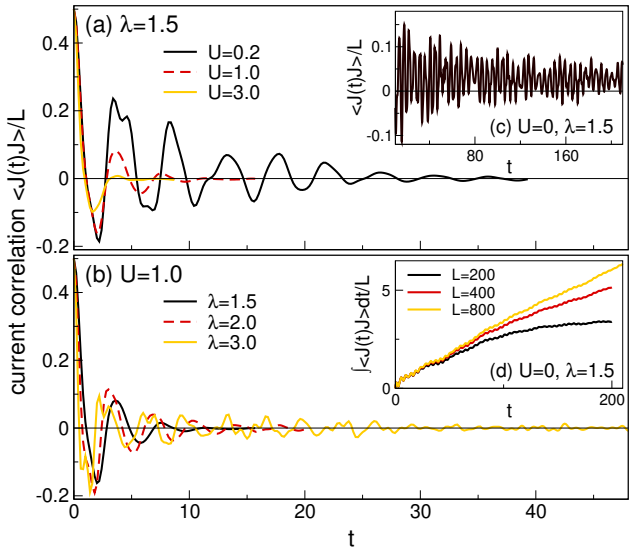


Figure 5.4: The time dependent current-current correlation function[2] for (a) fixed $\lambda = 1.5$, (b) fixed $U = 1.0$ and (c) $U = 0$, $\lambda = 1.5$. In the non-interacting case, the correlations persist indefinitely, indicating ballistic transport while the decay due to scattering is well captured in all other cases.

have exactly one particle sitting on every other lattice site. Similarly to the infinite temperature initial state, for the CDW both the MSD and the EE show power law growth with time with dynamical exponents which depend on the amplitude of the QP potential (EE was also studied in Ref. [NER16]). We note that while for the CDW the growth of the MSD appears to be subdiffusive for the simulated times the extraction of the exponent is extremely unreliable due to presence of oscillations in the data, *which do not disappear with better averaging*. This precludes from making meaningful comparison between the dynamical exponent of the EE $(\beta)$ with the dynamical exponent of the MSD $(\alpha)$. For a comparison of such exponents in disordered systems see [LL17].

## 5.5 CURRENT-CURRENT CORRELATION AND FULL AC-CONDUCTIVITY USING TDMRG

While $x^2$ and the current-current correlation function $\langle J(t)J(0)\rangle$ are closely related, the latter yields a different perspective on the problem, which we will now discuss. To this end, Figure 5.4 shows $\langle J(t)J(0)\rangle$ in the infinite temperature limit. If transport is ballistic, a system driven out of equilibrium displays a persistent current. Therefore, in the integrable limit the current-current correlation function is expected to oscillate around a finite value (compare Figure 5.4 (c)). If scattering is present in a system the current decays. The data obtained with

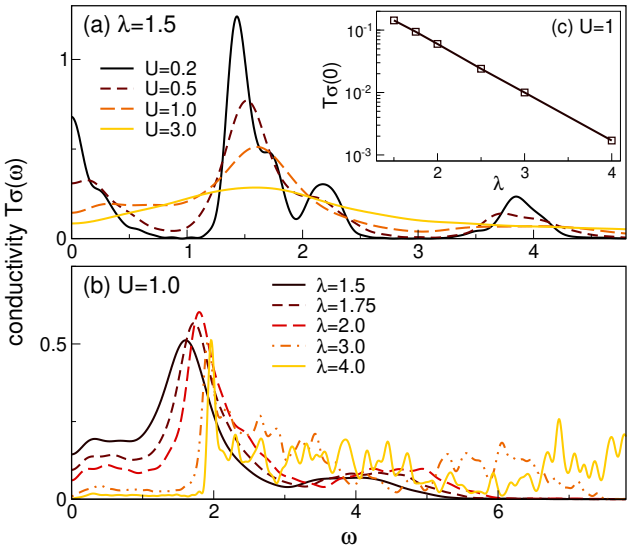


Figure 5.5: The AC-conductivity $\sigma(\omega)$ can be obtained as a Fourier transform of the current-current correlation function using tDMRG. Subfigure (a) shows $\sigma(\omega)$ at constant potential-strength varying the interaction $U$ and demonstrates, that the DC-conductivity $\sigma(0)$ is diminished by the interaction. Similarly, subfigure (b) shows, how at constant $U$ increasing the QP potential results in a gap in the conductivity, when the system transitions to an insulating phase. The DC-conductivity decreases exponentially as a function of the potential strength (see inset (c)).

tDMRG[2] indicates that transports at $U > 0$, $\lambda > 0$ is not ballistic and the decay is well captured in the times accessible with tDMRG for the parameters shown.

Therefore we can employ a Fourier transform of the current-current correlation function, and use tDMRG to provide the entire, frequency dependent AC-conductivity (compare Equation 5.4.4), presented in Figure 5.5. As tDMRG is limited to finite times, the results are averaged over intervals of width $\Delta\omega = 0.1$.

For weak interaction, the conductivity shows a sharp peak at $\omega = 0$, reflecting the ballistic nature of the free system. The frequency dependence reveals the presence of distinct single-particle bands.

The DC conductivity $\sigma(0)$ decreases monotonously in the metallic phase upon increasing the two-particle interaction (see Figure 5.5 (a)). When approaching the localized phase, the DC conductivity decreases exponentially and a gap in $\sigma(\omega)$ appears (see Figure 5.5 (b) and (c)).

## 5.6 SUPERDIFFUSIVE REGIME USING FRG

To establish superdiffusive transport unambiguously, it is necessary to exceed the typical scattering times in the system, which poses a

problem to tDMRG when transport is close to ballistic. In order to access longer time scales and larger system sizes we use the functional renormalization group [Sal99; Met+12] implemented on the real-time Keldysh contour [JMS07; Ken+12; KM13] that we discussed in Section 4.4.1. As we truncated the flow equations to leading order, the framework is approximate with respect to the interaction strength. Due to its RG nature, the fRG can capture power laws, and the corresponding exponents can be computed up to the linear order in the interaction strength, $U$ (all higher-order contributions are uncontrolled). The computational effort of the fRG calculation is not sensitive to the build up of entanglement in the system, which is especially advantageous when transport is almost ballistic. When the Trotter decomposition (discussed in Section 2.8) is used the computational effort scales linearly with time and quadratic in the system size if sparse matrices are used whenever appropriate. Using these simplifications one can access times of $t \sim 1000$ for systems of up to $N \sim 1000$ sites. However, since the MSD is a two-body correlation function, it cannot be computed reliably using a first-order fRG scheme.

### 5.6.1 *Choice of the setup and observable*

To circumvent this issue we aim to investigate transport via a quench protocol which can be simulated both by the fRG and the tDMRG. One potential choice is the CDW we already discussed in Section 5.4.2. The imbalance

$$I(t) = \frac{1}{2N} \sum_i (-1)^i n_i \tag{5.6.1}$$

is a natural measure of the relaxation of the system and can be used to characterize transport. However, as the QP potential is strongly correlated on long length-scales, it is numerically difficult to reliably extract the exponents (compare Figure 5.6 and Section 5.4.2).

Instead, we turn to another highly excited state: a domain wall with

$$n_i^{\text{ini}} = \begin{cases} 1 & i \leqslant N/2 \\ 0 & i > N/2. \end{cases} \tag{5.6.2}$$

Domain wall dynamics provide a natural sensor for MBL physics [HHMP16] that can be realized straightforwardly in cold-atom experiments [Cho+16]. As this initial configuration itself breaks translational symmetry, it is expected to self-average when suitable observables are analyzed. In the localized phase, the melting of the domain wall is suppressed, while in the ergodic phase it is characterized by a power law growth of various transport quantities.

A variety of quadratic observables could be used as a indicator for transport. Among those are the number of transported particles,

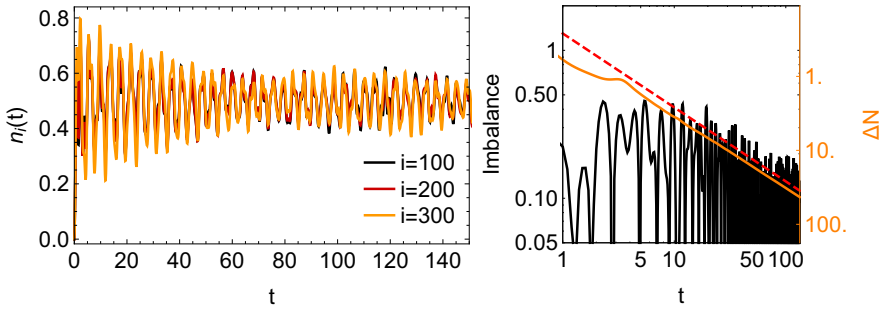


Figure 5.6: *Left panel*: Evolution of the local occupation $n_i$ of individual sites ($i = 100, 200, 300$) in a free Aubry-Andre chain of $N = 400$ sites at a disorder strength $\lambda = 1$ when initially prepared in a Néel state. At this QP potential strength, the system is metallic and all single-particle eigenstates are extended; this results in a strong correlation of the dynamics, even for far apart sites. *Right panel*: The black line shows the corresponding imbalance $|n_{even} - n_{odd}|$ and its expected decay (dashed red line). We also show the evolution of the number of transported particles $\Delta N$ (see Equation 5.6.3) when starting from a domain-wall configuration (see Equation 5.6.2 (orange line). We find that a domain-wall preparation produces more accurate estimates of the transport exponents.

the variance of the distribution as well as the mean position of the transported particles, which we respectively define as

$$\begin{aligned} \Delta N &= \sum_{i>N/2} n_i \\ VAR^2 &= 2 \sum_{i>N/2} (i - N/2)^2 n_i \\ \bar{n} &= \sum_{i>N/2} i n_i. \end{aligned} \tag{5.6.3}$$

The number of transported particles as well as their mean position is expected to asymptotically scale as $\Delta N \sim t^{\alpha/2}$, with the same exponent $\alpha$, as the MSD while the variance scales as $VAR \sim t^{\alpha}$ (if calculated for the *same* initial conditions). The agreement between the exponents extracted from these observables is however not trivial within the fRG approximation.

### 5.6.2 *Comparison to DMRG*

The evolution of this initial preparation as obtained using tDMRG[2] is shown in the right panel of Figure 5.7, while Figure 5.8 shows time slices of the corresponding fRG calculation. In the absence of interactions, $\Delta N$ grows linearly with time indicating ballistic transport for $\lambda < 2$. Finite $U > 0$ leads to slower transport. As these figures demonstrate, the speed of the melting of the domain-wall strongly

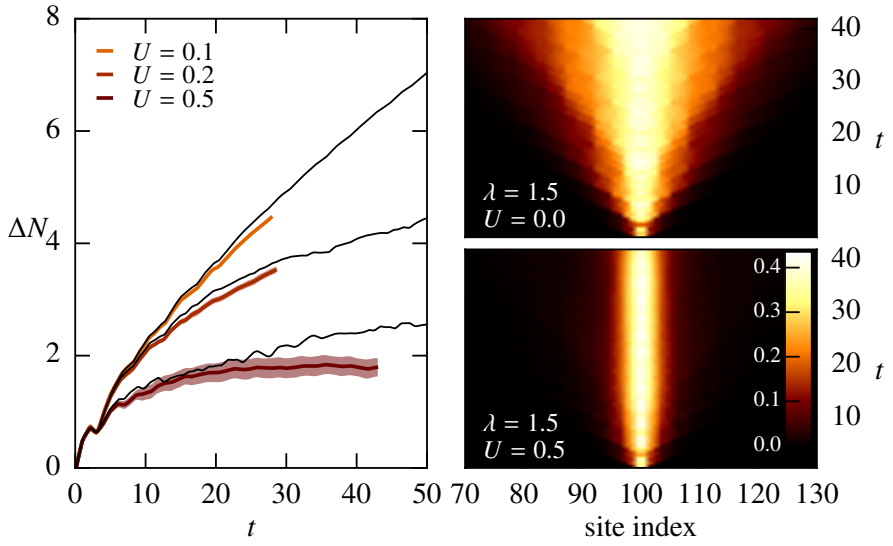


Figure 5.7: Mass transport for a domain wall initial condition. The right side shows the mass difference as obtained with tDMRG², $|n_i(t) - n_i(0)|$, as a function of time for two values of the interaction $U = 0$ and 0.5, and demonstrates that transport, which is ballistic at $U = 0$, becomes successively suppressed when switching on interactions. The left side compares tDMRG² (colored lines) and fRG (black lines) results for the total mass transferred to the left side as a function of time, for fixed $\lambda = 1.5$ and varying $U$. The width of the colored lines represent the statistical error. This figure was previously published in [Lev+17].

depends on the strength of the QP potential and interaction. Thus the system-size has to be chosen correspondingly. Both methods are in qualitative agreement; to verify this quantitatively the left panel of Figure 5.7 compares $\Delta N$ and demonstrates good agreement between fRG and the numerically exact reference provided by the tDMRG² on intermediate time scales.

### 5.6.3 *Transport close to integrability using fRG*

The fRG can now be used to push the calculation to significantly larger times. Since fRG is exact in the limit of $U = 0$ and to first order in the interactions, we focus on the vicinity of $U = 0$, $\lambda = 2$, where first order interaction effects are most pronounced.

A superdiffusive power law with $1 < \alpha < 2$ can be identified unambiguously for all observables given in Equation 5.6.3 as long as the interaction is small (see Figure 5.9). To verify that the extracted dynamical exponents do not drift with time we also compute the log-derivative of the measures defined in Equation 5.6.3 ($d\log O / d\log t$) and observe that it saturates to a plateau (see right panel of Figure 5.9), which indicates that the calculated dynamical exponents are asymptotic within the fRG scheme.

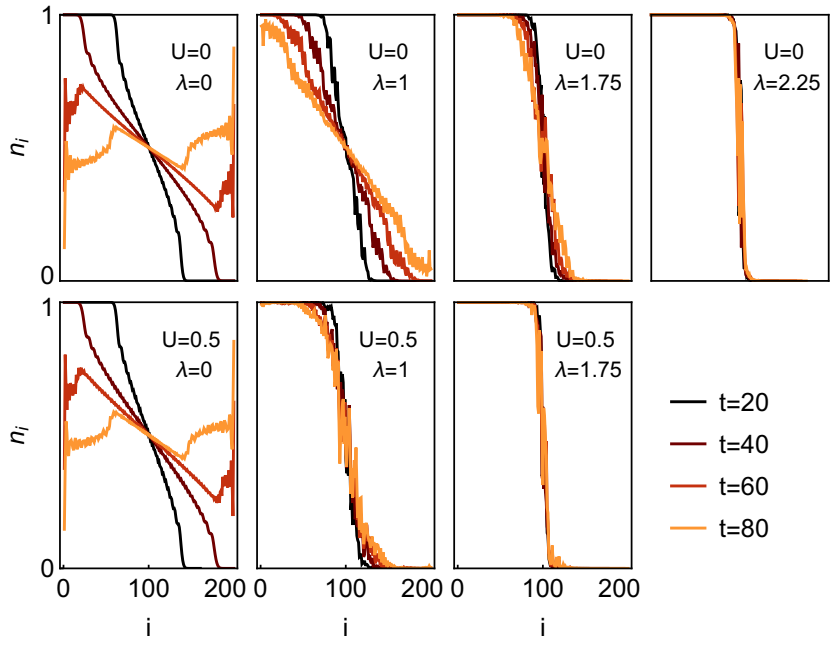


Figure 5.8: Time evolution of a system initially prepared in a domain-wall configuration (see Equation 5.6.2) in the presence of different strengths of the quasiperiodic potential and two-particle interaction as obtained with fRG. The different colors signify different times. We find that interaction significantly hinders the melting of the domain wall in presence of the potential. Note that the results for large times in the absence of the potential ($\lambda = 0$) show severe finite-size effects; these are shown to demonstrate, that the accessible time-scales with at a given system size strongly depends on the other model parameters.

It is important to check that the extracted dynamical exponent $\alpha$ scales linearly with $U$, which is consistent with the assumptions of fRG (see inset of Figure 5.9). We also observe, that systems becomes increasingly sensitive to the interaction close to the critical potential strength $\lambda_c = 2$. Note that the exponents extracted for different observables are in good qualitative agreement; for the example of $\lambda = 1.5$, this is demonstrated in the inset of Figure 5.9.

Since in this setup we use small interactions it is important to work with times longer then the mean-free time of scattering between two particles, $\tau_{ee} \sim 1/U^2$, otherwise a transient ballistic transport would be observed. Not only the transport we observe is always sub-ballistic, but in our simulations we reach times significantly longer than longer then the scattering mean-free time.

In the vicinity of $U = 0$, the dynamical exponents agree qualitatively with those governing the growth of the MSD (see Figure 5.2). A strict quantitative comparison is however not possible since we did not find a parameter set for which the exponents can be determined reliably in *both* setups. E.g., at $\lambda = 1.5$, $U = 0.1$ (see Figure 5.2), the

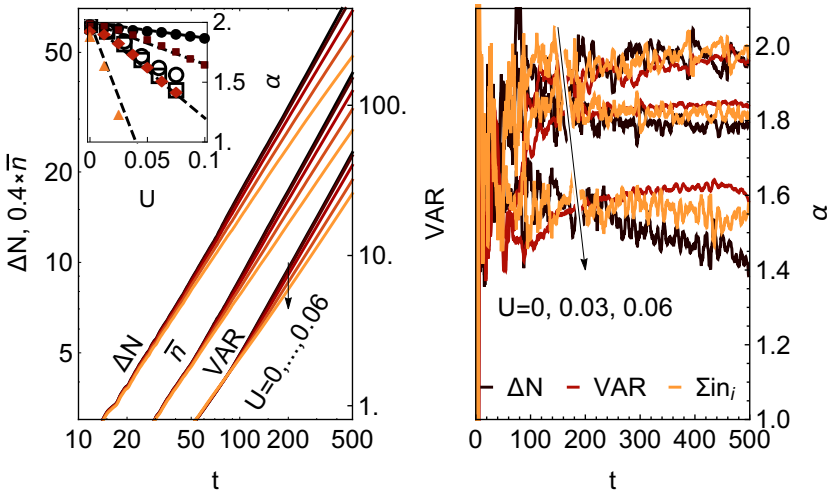


Figure 5.9: *Left panel:* Log-log plot of the observables $\Delta N$, $VAR, \bar{n}$ as a function of time for interactions $U = 0, 0.015, \ldots, 0.06$. *Inset*: Solid symbols shows the dynamical exponent as computed from fRG for $\Delta N$ various interaction strengths. The disorder strengths used are (dark to light colors of the inset) $\lambda = 1, 1.25, 1.5, 1.75$. Additionally, the open squares (circles) show the exponents for $\bar{n}$ ($VAR$) at $\lambda = 1.5$. *Right panel*: Log-derivative of the $\Delta N$, $VAR$ and $\bar{n}$ (see Equation 5.6.3) as function of time, $\lambda = 1.5$.

domain-wall exponent is no longer in the purely linear regime, and the higher-order corrections cannot be computed reliably by the fRG. More importantly, there is no general reason to expect that the exponents governing the spreading of the domain wall and the MSD, computed for an infinite temperature initial condition, should coincide: the former is a far out-of-equilibrium initial condition while the latter describes linear response. The difference between both setups becomes particularly apparent at larger $U \sim 0.5$ where we can no longer unambiguously identify power laws in the evolution of the domain wall but observe a strong suppression of transport (see Figures 5.7 and 5.8). Since this effect appears to be a specific hallmark of the (domain wall) initial conditions and does not directly coalesce with the focus of this work, we leave the exploration of this interesting regime to future work.

To investigate the strong suppression of transport and the emergence of superdiffusive transport within fRG further, we present a simplistic single-particle treatment.

### 5.6.4 *Simplistic explanation using equilibrium fRG*

Some simple-minded insights can be obtained within an effective single-particle treatment of the problem. To this end, we employ the

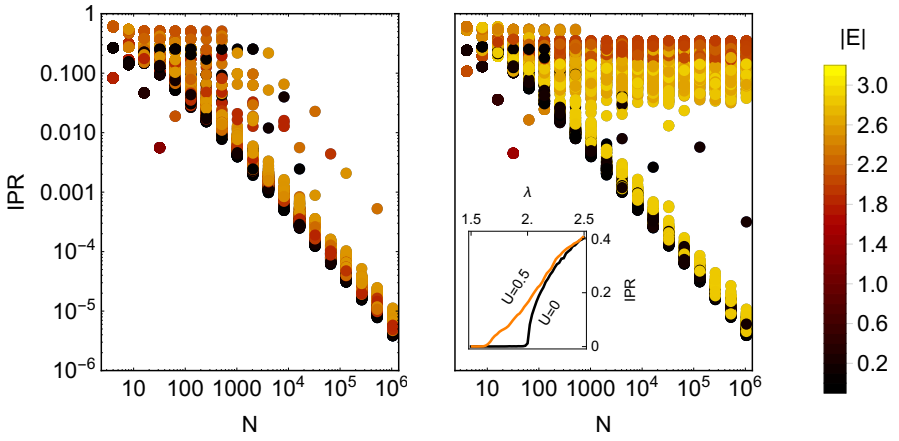


Figure 5.10: Results of the equilibrium fRG calculation. *Main panels*: The system-size dependence of the inverse participation ratio of the effective single-particle states for $U = 0.5$ and $\lambda = 1.9$. While the system-size is increased up to $N = 2^20 \approx 10^6$, only a fixed number of 400 randomly selected single-particle states are shown. *Inset*: Average inverse participation ratio of all states as a function of the disorder strength for two values of $U = 0,\ 0.5$ and a system size of $N = 10^4$ using $N = 10^3$ randomly sampled states.

equilibrium version of the fRG presented in Section 4.4.3 to obtain the effective Hamiltonian in the ground-state.

Using the inverse participation ratio $\sum_i |\psi(i)|^4$ (compare Section 5.1.2), we characterize the extent of the individual effective single-particle eigenstates $\psi$. If the inverse participation ratio of a quadratic system decays to zero (becomes constant) with the system size, the associated effective levels $\psi$ are metallic (localized). Results for the AA model are presented in Figure 5.10 for $U = 0$ and $U = 0.5$ as a function of the system size and color-coded with respect to their single-particle energy. To reach large system sizes, we only show a randomly selected sample obtained using the algorithms discussed in Section 2.8.2.

Where for the free system all states are delocalized at a disorder $\lambda = 1.9 < \lambda_c$, some of the effective single-particle states in the interacting system display a finite inverse participation ratio in the limit $N \to \infty$. This shows that in this approximation scheme, an energy band within the spectrum is localized by interactions. This directly affects the average inverse participation ratio $\frac{1}{N}\sum_i \mathrm{IPR}(\psi_i)$ shown in the inset of Figure 5.10.

While we emphatically note that this procedure is not a controlled approximation and that its predictions should be taken with a grain of salt, it could be the basis for a more thorough analytical investigation into why the domain wall dynamics look almost frozen in Figure 5.7 for $U \sim 0.5$.

## 5.7 CONCLUSION

In this chapter we have demonstrated that a simple but generic one dimensional interacting system with a quasiperiodic potential exhibits an unexpectedly rich dynamical behavior, exhibiting a crossover from superdiffusive to subdiffusive transport. Close to an integrable point, transport is traditionally expected to appear superdiffusive on intermediate time scales while asymptotically exhibiting diffusion. In striking contrast, we provide evidence, that in quasiperiodic potential superdiffusion survives to substantial integrability breaking (i.e. finite interaction and QP potential) and appears stable for long times. We find evidence of this superdiffusive transport using tDMRG at infinite temperature as well as in a quench scenario employing fRG. Within the effective single-particle picture provided by fRG we demonstrate, how interactions can significantly reduce transport close to the phase transition without inducing diffusion.

We have also presented numerical evidence for subdiffusive transport and sublinear spreading of entanglement entropy. This indicates that the prevailing explanation for subdiffusion in MBL systems, namely the Griffiths picture [Aga+15; Gop+15; Gop+16; Aga+17], is incomplete. The Griffiths picture relies on the presence of uncorrelated quenched disorder in the system, which is crucial for generating a sufficient density of rare blocking inclusions. If subdiffusion was purely explained by rare region, transport for systems with uncorrelated disorder in dimensions greater than one, those with strongly correlated disorder, or for the quasiperiodic case studied here, were expected to be diffusive. While our numerical results are valid only for relatively short time scales, there is no *a priori* reason why subdiffusive behavior should manifest within the Griffiths picture on any time scale in the quasiperiodic case studied here. Our results are in line with an experimental study [Lue+17]. There it was argued that while rare regions cannot be a result of the quasiperiodic potential, they may follow from rare spatial regions in the initial state [Lue+17]. We stress that the infinite temperature state, which we use as the initial state here, is clearly translationally invariant, but still exhibits subdiffusion. Moreover we have verified that subdiffusion is robust also when a *pure* initial state without any special spatial structure is taken (here we considered the experimentally relevant CDW).

# 6

# EXCITED EIGENSTATES USING FRG

## 6.1 INTRODUCTION

This chapter is based on the paper *Exploring excited eigenstates of many-body systems using the functional renormalization group*, authored by C. Klöckner, D. M. Kennes and C. Karrasch, published in the journal *Physical Review B* by the American Physical Society [KKK18]. Copyright remains with the APS.

The complexity of diagonalizing the Hamiltonian or solving the time-dependent Schrödinger equation of generic interacting quantum problems grows exponentially with the number of particles involved. Over the last decades, a plethora of techniques were developed to study the physics of many-body systems which are in thermal equilibrium (most importantly in the ground state) as well as the out-of-equilibrium dynamics induced by pre-defined initial states. In contrast, far less attention was devoted to devising methods which can access pure excited eigenstates at arbitrary energies. This is, because up to very recently these questions were of minor relevance as pure excited eigenstates are difficult to realize in quantum many-body systems. However, the newly-emerging field of many-body localization [GMP05; BAA06], has changed this viewpoint drastically. This phenomenon, which cannot be analyzed using thermal ensembles as it defies our understanding of statistical mechanism as well as the eigenstate thermalization hypothesis [Deu91; NH15] renders the characterization and description of individual excited eigenstates imperative. Before many-body localized systems were discovered it was believed that generic interactions wipe out the localization behavior induced by disorder in non-interacting systems [And58] on the level of the eigenstates. To scrutinize this behavior one needs to go beyond the ground state as the prediction of many-body localization entails that the eigenstates of the entire spectrum can localize. Such a localization gives rise to interesting consequences for, e.g., the transport properties. Another fascinating question concerns the existence and characterization of a mobility edge separating localized and delocalized eigenstates in the spectrum. While in the non-interacting case such an edge does not appear for one-dimensional systems, first numerical results indicate that it will show up in interacting one-dimensional systems [LLA15]. To characterize this edge access to single eigenstates is essential. Yet, a 'golden standard' approach to access single excited states has to be discovered. Exact diagonalization is restricted to small systems. Proposals how to obtain

a matrix product state representation of excited states are limited to one dimension and work only if the area law holds (i.e., in localized phases, compare Section 5.3) [KPS16; KK16b; Fri+15; LS16; YPC17]. This means that within this low-entanglement methods the crossover to the delocalization transition is difficult to approach. Analytical approaches [Mou+17] such as the Bethe ansatz can only be used for integrable models. Hence, it is desirable to develop additional pure state techniques which feature their own, unique set of strengths and shortcomings.

In this chapter, we introduce several, functional renormalization group (fRG) based algorithms to compute correlation functions in pure excited states of fermionic many-body systems.

While being approximate in the interaction, the fRG can be utilized to access large systems and is not a low-entanglement framework. Thus, an approximate, fRG-based description of correlation functions in pure excited states would complement more accurate predictions obtained, e.g., via exact diagonalization. It is the goal of this work to develop and test such a 'x-fRG' approach.

One way to obtain a pure eigenstate of a generic Hamiltonian is to analytically determine an excited state of a noninteracting system and to then switch on interactions adiabatically. We illustrate how to simplify the real-time Keldysh fRG of Ref. [Ken+12], that we presented in Section 4.4.1, under the assumption of adiabaticity in order to efficiently implement this protocol (this method will be called x-fRG-t-$\Gamma$). Thereafter, a new RG cutoff scheme is devised which is specifically tailored to the adiabatic nature of the problem (x-fRG-t-$\rho$).

After developing the different x-fRG schemes and deriving the corresponding flow equations (Section 6.2), we carry out several algorithmic tests and document the limitations and promises of our approach (Section 6.3). Thereafter, two 'toy applications' from the world of one-dimensional Luttinger liquid physics are presented: the survival of power laws in lowly-excited states as well as the spectral function of high-energy block excitations which feature multiple Fermi edges (Section 6.4).

As an outlook and a potential route to go beyond linear order in the two-particle interactions, we briefly discuss how to obtain an eigenstate directly (i.e., without resorting to the time evolution protocol) via a coupling to a non-thermal bath (x-fRG-$\omega$) in Section 6.5. Furthermore, in Section 6.6 we also discuss a way to investigate quenches from an excited eigenstate, that in the future could be used to directly investigate transport properties of excited eigenstates.

### 6.1.1 *Model*

The fRG methods presented in this section can be applied to general fermionic, particle-number conserving Hamiltonians with single- and two-particle contributions:

$$H = H^0 + H^{\text{int}}$$
$$H^0 = \sum_{i,j} h^0_{i,j} c^\dagger_i c_j \qquad H^{\text{int}} = \frac{1}{4} \sum_{i,j,k,l} v_{i,j,k,l} c^\dagger_i c^\dagger_j c_l c_k.$$

To obtain an especially efficient algorithm, however, it is essential to restrict the Hamiltonian. To that end, we discuss how to implement the method efficiently for large, one-dimensional tight-binding chains with $N$ sites with a nearest-neighbor interaction.

## 6.2 EXCITED STATE FRG

For these models, we now introduce two ways to obtain correlation functions in excited eigenstates of an interacting Hamiltonian using the fRG, which we label x-fRG.

Both approaches are based on an adiabatic time-evolution: The system is first prepared in an excited eigenstate of the noninteracting system and the interaction is then adiabatically turned on. This process is approximated using the functional renormalization group in real-time Keldysh space.

A third method employs the stationary-state Keldysh fRG of Section 4.4.2 and will be presented as an outlook Section 6.5.

### 6.2.1 *x-fRG-t-Γ: Adiabatic time-evolution in Keldysh space with a reservoir cutoff*

#### 6.2.1.1 *Time-space formulation*

The goal is to use the time-dependent fRG described in Section 4.4.1 to approximate the evolution of an excited eigenstate of the noninteracting system when interactions are switched on adiabatically. The initial time is set to $t = t_0$. As we discussed in Section 4.4.1, we employ an auxiliary reservoir cutoff, where the auxiliary reservoir temperature is infinite and truncate the fRG flow equations after the single-particle vertex. Since the self-energy in that fRG scheme is time-local,

$$h(t) := h^0 + \Sigma^{\text{ret}}(t), \qquad h(t) \in \mathbb{C}^{N\times N}$$

takes the place of an effective single-particle Hamiltonian (compare Equation 3.2.34). As all self-energies discussed in this chapter are of this type, we use $G$ to represent the Green's function of the

*effectively* free system, that might potentially include a time-local, purely retarded self-energy; beyond this first-order approximation it is a priori unclear whether a similarly designed algorithm would yield the desired results. We suppress the $\Lambda$-dependence to keep the expressions more readable and introduce the notation

$$\begin{aligned} &h(t)\,|\Psi_i(t)\rangle = \epsilon_i(t)\,|\Psi_i(t)\rangle \\ &h(t) \in \mathbb{C}^{N\times N}, \qquad |\Psi_i(t)\rangle \in \mathbb{C}^N \\ &\epsilon_i(t) < \epsilon_j(t) \qquad \forall i < j \\ &\left|\epsilon_i(t) - \epsilon_j(t)\right| > \Delta \qquad \forall i \neq j, t, \end{aligned} \tag{6.2.1}$$

where $\epsilon_i(t)$ and $|\Psi_i(t)\rangle$ denote the instantaneous single-particle eigenvalues and eigenstates of the matrix $h(t)$. $\Delta$ is an arbitrary, non-zero gap that ensures the absence of level crossings. Without symmetries, crossings are avoided and such a $\Delta$ is expected to exist. The adiabatic theorem [BF28] then states that if

$$\begin{aligned} &\|\dot{h}(t)\| \ll \Delta^2 \;\forall t \\ \Rightarrow &\left|\langle\Psi_j(t)|\, u(t,t_0)\,|\Psi_i(t_0)\rangle - \delta_{i,j}\right| \ll 1 \quad \forall i,j \end{aligned} \tag{6.2.2}$$

where $u$ denotes the single-particle time-evolution operator. For a pure many-body eigenstate of the noninteracting, initial Hamiltonian the matrix of single-particle correlations (compare Equation 2.5.6) is characterized by a sequence of occupations $n_i$ of the single-particle eigenstates $|\Psi_i(t_0)\rangle$ of $h^0$:

$$\begin{aligned} \bar{n}(t_0) = \sum_i n_i\,|\Psi_i(t_0)\rangle\langle\Psi_i(t_0)|, \;\; n_i \in \{0,1\}, \\ n_{i,j}(t_0) = \left\langle c_j^\dagger c_i \right\rangle. \end{aligned} \tag{6.2.3}$$

If the rate of change of the effective Hamiltonian $h(t)$ is slow enough (compare Equation 6.2.2), the time evolution of this matrix is given by

$$\bar{n}(t) = \sum_i n_i\,|\Psi_i(t)\rangle\langle\Psi_i(t)| \tag{6.2.4}$$

with the *same* sequence of $n_i$.

As these results are restricted to finite systems they can not directly be applied in presence of an auxiliary reservoir. However, the infinite temperature in the auxiliary reservoirs used in the cutoff presented in Section 4.4.1 allows to formally rewrite the Keldysh Green's function (see Equation 3.2.34) as

$$\begin{aligned} &G^{K,\Lambda}(t,t) \\ &\quad = -iG^{ret,\Lambda}(t,t_0)\,[1-2\bar{n}(t_0)]\,G^{adv,\Lambda}(t_0,t) \\ &\quad = -ie^{-2\Lambda(t-t_0)}\left[1-2G^{ret,\Lambda}_{dec}(t,t_0)\bar{n}(t_0)G^{adv,\Lambda}_{dec}(t_0,t)\right] \\ &\quad =: -ie^{-2\Lambda(t-t_0)}\left[1-2\bar{n}^\Lambda(t)\right], \end{aligned} \tag{6.2.5}$$

where we introduced

$$e^{-\Lambda(t-t_0)} G^{\mathrm{ret},\Lambda}_{\mathrm{dec}}(t,t') := G^{\mathrm{ret},\Lambda}(t,t').$$

By virtue of this definition $\bar{n}^{\Lambda}(t)$ is the matrix of single-particle correlations of a closed system that evolves according to the effective single-particle Hamiltonian $h(t)$ (see Equations 3.2.34, 4.4.1 and 4.4.2). Thus, $\bar{n}^{\Lambda}(t)$ can be obtained using Equation 6.2.4 and only implicitly depends on $\Lambda$ (the instantaneous eigenstates will change with the flow, as a self-energy is generated). Under these circumstances, the flow Equation 4.4.6 can be rewritten conveniently by the following change of variables:

$$\xi = e^{-2\Lambda(t-t_0)} \Rightarrow \partial_\Lambda f(\Lambda) = \Big(\partial_\Lambda \xi\Big)\partial_\xi f\Big(\Lambda(\xi)\Big)$$
$$\partial_\Lambda = -2(t-t_0)\xi\partial_\xi.$$

The final differential equations read:

**Algorithm 6.1: x-fRG-t-Γ**

$$\begin{aligned}
\partial_\xi \Sigma^{\mathrm{ret},\xi}_{i,j}(t,t') &= -\frac{i}{2}\delta(t-t') \sum_{k,l} \left[\tilde{G}^{K,\xi}(t,t)\right]_{l,k} v_{i,k,j,l}(t) \\
\tilde{G}^{K,\xi}(t,t) &= -i\left[1-2\bar{n}^{\xi}(t)\right] \\
\bar{n}^{\xi}(t) &= \sum_i n_i \left|\Psi^{\xi}_i(t)\right\rangle \left\langle\Psi^{\xi}_i(t)\right| \\
\left(h^0 + \Sigma^{\mathrm{ret}}(t)\right)\left|\Psi^{\xi}_i(t)\right\rangle &= \epsilon_i(t)\left|\Psi^{\xi}_i(t)\right\rangle,
\end{aligned} \tag{6.2.6}$$

with $\xi_{\mathrm{ini}} = 1$, $\xi_{\mathrm{final}} = 0$. Note that this flow equation is simpler than the original, time-dependent formalism (see Equation 4.4.6), since it is to be evaluated only at a single fixed time and interaction.

The essential step in this algorithm is obtaining $\left|\Psi^{\xi}_i(t)\right\rangle \left\langle\Psi^{\xi}_i(t)\right|$ at a given self-energy. The act of diagonalizing a given effective Hamiltonian is already of complexity $\mathcal{O}\left(N^3\right)$. Even if we restrict ourselves to tridiagonal matrices, where some more efficient algorithms exist, we have to perform a sum over all eigenstates and obtain all diagonal and first off-diagonal components of $G^K$, requiring at least $\mathcal{O}\left(N^2\right)$ operations. To understand how to obtain this result more efficiently, we first discuss, how this is possible in thermal equilibrium.

#### 6.2.1.2 *Single-particle correlations in thermal equilibrium*

We now elaborate how to obtain equal-time correlations of effectively noninteracting systems in thermal equilibrium efficiently using an analytic continuation; after we discussed how this is achieved, we apply

the same techniques for excited eigenstates. In the context of the Matsubara Green's function, the resulting formulas may appear trivial but we use the same line of arguments to derive efficient formulas to obtain correlation functions in excited eigenstates where the complexity class achieved for the final algorithm may appear surprising.

The conventional method to compute correlations would be, using the same notation as in Algorithm 6.1

$$h\,|\Psi_i\rangle = \epsilon_i\,|\Psi_i\rangle \tag{6.2.7}$$

$$\Rightarrow \left\langle c_k^\dagger c_l \right\rangle = \sum_i n_F(\epsilon_i) \left\langle k \middle| \Psi_i^\xi(t) \right\rangle \left\langle \Psi_i^\xi(t) \middle| l \right\rangle, \tag{6.2.8}$$

where $n_F$ denotes the Fermi-distribution function and $|i\rangle$ denotes the $i$th unit vector. After the single-particle Hamiltonian is diagonalized, it still takes $N$ operations to obtain an individual component of the single-particle correlation function. Expressed in terms of Green's functions (using the Fourier transform of the fluctuation-dissipation theorem, Equation 2.5.51), the analogous expression reads

$$G^K(t,t) = \frac{1}{2\pi}\int d\omega\,[1-2n_F(\omega)]\left[G^{ret}(\omega) - G^{adv}(\omega)\right]. \tag{6.2.9}$$

The time label $t$ in equilibrium is arbitrary; we keep it to differentiate between time- and frequency-space. For a closed system $G^{ret}(\omega) - G^{adv}(\omega)$ consists of $N$ $\delta$-peaks; if these are broadened, $\mathcal{O}(N)$ evaluations are needed to approximate the integral. To improve on this, we recast this expression as a contour integral,

$$G^K(t,t) = \frac{1}{2\pi}\sum_\pm \lim_{R\to\infty}\int_{\gamma_\pm^{R,1}} dz\,[1-2n_F(z)]\,G^{eq}(z), \tag{6.2.10}$$

where we employed the equilibrium Green's function:

$$G^{eq}(z) = \frac{1}{z - h^0}$$

$$\Rightarrow G^{ret}(\omega) = G^{eq}(\omega + i0^+), \quad G^{adv}(\omega) = G^{eq}(\omega - i0^+).$$

The contours $\gamma_\pm^{R,i}$, $i = 1,\ldots,4$ are schematically shown in Figure 6.1. The integrand of Equation 6.2.10 has poles in the complex plane which are located at the eigenenergies of the Hamiltonian as well as at $i\omega_n + \mu$ with the fermionic Matsubara frequencies $i\omega_n \in i\frac{2\pi}{\beta}\left(\mathbb{Z} + \frac{1}{2}\right)$; the latter originate from the Fermi distribution. The integrand is analytic within the closed contours formed by $\gamma_\pm^{R,1} + \cdots + \gamma_\pm^{R,4}$ and at any finite chemical potential (and independently of the width enclosed by $\gamma^{R,3}$)

$$\begin{aligned}&\frac{1}{2\pi}\sum_\pm \lim_{R\to\infty}\int_{\gamma_\pm^{R,2}} dz\,[1-2n_F(z)]\,G^{eq}(z)\\ =&-\frac{1}{2\pi}\sum_\pm \lim_{R\to\infty}\int_{\gamma_\pm^{R,4}} dz\,[1-2n_F(z)]\,G^{eq}(z),\end{aligned}$$

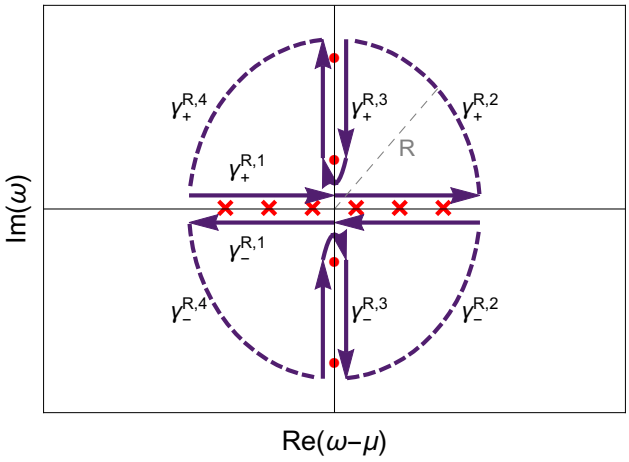


Figure 6.1: Schematic depiction of the integrations discussed in Equation 6.2.10. The red crosses represent poles associated with eigenenergies while the red circles signify divergences in the distribution function. The contours $\gamma_\pm^{R,1}$ along the real axis are used to evaluate Equation 6.2.10 while the contours $\gamma_\pm^{R,3}$ enclosing the imaginary axis are used to evaluate Equation 6.2.11. This figure was previously published in [KKK18].

as $G^{eq}(z) \to 1/(z-\mu) + \mathcal{O}(1/(z-\mu)^2)$ for $|z| \to \infty$. Hence, the Keldysh Green's function is given by the contribution of the contour segment $\gamma^{R,3}$.[1]

$$\begin{aligned} G^K(t,t) &= -\frac{1}{2\pi} \sum_\pm \lim_{R\to\infty} \int_{\gamma_\pm^{R,3}} dz\, [1 - 2n_F(z)]\, G^{eq}(z), \\ &= \frac{2i}{\beta} \lim_{N\to\infty} \sum_{n=-N}^{N} G^{eq}(i\omega_n + \mu) \end{aligned} \tag{6.2.11}$$

and in the limit of $T \to 0$

$$\begin{aligned} G^K(t,t) &= \frac{i}{\pi} \lim_{A\to\infty} \int_{-A}^{A} d\omega G^{eq}(i\omega + \mu) \\ &= \frac{i}{\pi} \int d\omega e^{-|\omega|0^+} G^{eq}(i\omega + \mu). \end{aligned} \tag{6.2.12}$$

As the wick rotated equilibrium Green's function is not sharply peaked, the number of evaluations of the integrand in Equation 6.2.12 is not expected to scale with the number of states in the system which already is an improvement compared to Equation 6.2.10.

As we discussed in Section 7.5, for tight-binding models of linear dimension N, the diagonal and first off-diagonal components of this expression can be evaluated in $\mathcal{O}(N)$ operations [And+04; Usm94]

1 The contribution by the contour element needed to close $\gamma^{R,3}$ vanishes for $R \to \infty$. It can always be chosen such, that the distance between the contour and the singularities remains finite.

(compare Section 2.8.2). This will be important for later applications where we want to study Luttinger liquid power-laws for $N \gg 1$.

#### 6.2.1.3 *Generalization to excited eigenstates*

Equation 6.2.9, as the starting point of the previous section, is based on the fluctuation-dissipation theorem. As we discussed in Section 2.5.3, in an (non-thermal) equilibrium configuration (i.e. $[h, \bar{n}] = 0$) and without degeneracies for an (effectively) free Hamiltonian $h$ there exists a (generally not unique) functions $n(\omega)$ such that

$$G^K(\omega) = [1 - 2n(\omega)] \left[ G^{ret}(\omega) - G^{adv}(\omega) \right].$$

Next, we generalize Equation 6.2.12. From now on, we focus on the most relevant case which is a state characterized by the distribution function

$$1 - 2n(\omega) = \frac{\sigma_{N_\omega} - \sigma_1}{2} + \sum_{i=1}^{N_\omega} \sigma_i \mathrm{sign}(\omega - \omega_i), \qquad \sigma_i \in \{\pm 1\},\ i = 1 \dots N_\omega \tag{6.2.13}$$

where successive $\sigma_i$ need to have opposite sign and the $\omega_i$ are in increasing order

$$\sigma_i = -\sigma_{i+1}, \qquad \omega_{i+1} > \omega_i$$

in order to obtain a physical density. For example, a block excitation (as will be considered in Section 6.4.4) can be encoded as

$$\begin{aligned} &\sigma_i = (1, -1, 1)_i,\ \omega_i = (-1, 0, 1)_i \\ \Rightarrow\ &n(\omega) = \begin{cases} 1 & \omega < -1 \vee 0 < \omega < 1 \\ 0 & \text{otherwise.} \end{cases} \end{aligned} \tag{6.2.14}$$

Thus, this object is analogous to the $n_i$ of the previous section (see Equation 6.2.3) and describes the sequence of occupied and unoccupied single-particle eigenstates. Note that the first summand of Equation 6.2.13 only contributes for an even number of steps, in which case $\lim_{\omega\to\infty} n(\omega) = \lim_{\omega\to-\infty} n(\omega)$. Furthermore, the $\omega_i$ are assumed not to be part of the spectrum. As we discussed in Section 2.5.3, $n(\omega)$ only carries physical meaning on the eigenenergies, thus given a sequence of $n_i$, $n(\omega)$ is not unique; due to Liouville's theorem, however, it is not possible to chose a entire function with $n(\epsilon_i) = n_i$ that does not diverge for $|\omega| \to \infty$.[2]

Generalizing Equation 6.2.13 to other distribution functions is straightforward.

2 More formally: for any entire $n(\omega)$ that is not constant, there is a $\varphi \in \mathbb{R}$ such that $\lim_{R\to\infty} \left| n\left( |R| e^{i\varphi} \right) \right| \to \infty$

As Equation 6.2.13 can be understood as a superposition of Fermi distributions the considerations that led to Equation 6.2.10 apply for each summand:

$$G^K(t,t) = i\frac{\sigma_1 - \sigma_{N_\omega}}{2} + \sum_j \sigma_j \frac{i}{\pi}\int d\omega e^{-|\omega|0^+} G^{eq}(i\omega + \omega_j). \quad (6.2.15)$$

#### 6.2.1.4 *Frequency-space formulation*

It is now clear that Equation 6.2.6 can be evaluated without the need to fully diagonalize $h(t)$. Using Equation 6.2.15 immediately yields

**Algorithm 6.2: x-fRG-t-Γ in frequency space**

$$\begin{aligned}
\partial_\xi \Sigma^{ret,\xi}_{i,j}(t,t') &= -\frac{i}{2}\delta(t-t')\sum_{k,l}\left[\tilde{G}^{K,\xi}(t,t)\right]_{l,k} v_{i,k,j,l}(t) \\
G^{K,\xi}(t,t) &= i\,(n_1 + n_N - 1) \\
&\quad + \sum_{\substack{i \\ n_i \neq n_{i+1}}} \frac{i\bar{\sigma}_i}{\pi}\int d\omega e^{-|\omega|0^+} \frac{1}{i\omega + \bar{\omega}_i(t) - h^0 - \Sigma^{ret,\xi}(t)}
\end{aligned} \quad (6.2.16)$$

where we have introduced

$$\begin{aligned}
\bar{\sigma}_i &= n_i - n_{i+1} \\
\bar{\omega}_i(t) &= \frac{\epsilon_i(t) + \epsilon_{i+1}(t)}{2}
\end{aligned}$$

in analogy to Equation 6.2.13. The $\epsilon_i(t)$ in this expression are the eigenvalues of the effective single-particle Hamiltonian $h(t) = h^0 + \Sigma^{ret,\xi}(t)$. As we discussed in Section 2.8, the necessary elements of the inverse of a tridiagonal matrix as well as specific eigenvalues (i.e. the $n$th smallest) can be obtained in $\mathcal{O}(N)$ operations. Hence, Equation 6.2.6 can be evaluated in $\mathcal{O}(N)$ operations[3] for tight-binding models (which we will discuss in Section 6.3-Section 6.4) using Equation 6.2.16.

However, the functional form of Equation 6.2.16 also hints towards a problem: in every step the Green's function is integrated over all imaginary frequencies. This is structurally different from the ground-state flow equation (compare Equation 4.4.9) and will be investigated more closely in Section 6.3.3.

The algorithm presented in this section can also be applied to the ground-state but will not necessarily give the same results due to

3 In this, we assume that the sum in Equation 6.2.16 only runs over a finite number of changes in $n_i$ that does not scale with N.

the truncation of the flow equations and difference in cutoff. Hence, comparing the results for the ground-state provides a nontrivial check that will be discussed in Section 6.3.3.

### 6.2.2 *x-fRG-t-$\rho_{1,2}$: Adiabatic time-evolution in Keldysh space with an initial-configuration cutoff*

We now introduce a second approach which is also based on an adiabatic time-evolution. We still use Keldysh space fRG but develop a specialized cutoff for the case that the initial state is an excited eigenstate.

The cutoff in the free Green's functions is introduced by choosing an initial density matrix that depends on $\Lambda$. The causality relation is conserved by construction and one can work in the Keldysh basis. Thus, the cutoff can be introduced on the level of the initial Keldysh Green's function (compare Equation 6.2.15):

$$\begin{aligned} G^{K,\Lambda}(t_0,t_0) &= g^{K,\Lambda}(t_0,t_0) = -i(1-2\bar{n}^{\Lambda}) \\ &:= i\,(n_1+n_N-1) \\ &\quad + \sum_{\substack{i \\ n_i \neq n_{i+1}}} \frac{i\bar{\sigma}_i}{\pi} \left[\int_{-\infty}^{-\Lambda} + \int_{\Lambda}^{\infty}\right] d\omega e^{-|\omega|0^+} \frac{1}{i\omega + \bar{\omega}_i(t_0) - h^0} \end{aligned}$$

while the time evolution is still given by Equation 3.2.34. This definition of $\bar{n}$ differs from that employed in Section 6.2.1 and can be understood as a generalization of the sharp cutoff in the Matsubara fRG (compare Section 4.4.3). A similar idea has been employed in Ref. [JMS07] for steady states of open systems. By construction, $\left[h^0, \bar{n}^{\Lambda}\right] = 0$, and thus the time-evolved Keldysh Green's function $G^K(t,t)$ can be computed purely from $h^0 + \Sigma(t)$ (compare Section 6.2.1). The free retarded and advanced Green's functions do not acquire a cutoff in this scheme. The initial condition at $\Lambda = \infty$ is simply the $T = \infty$ state (at $\mu = \pm\infty$ or half filling, depending on $n_1 + n_N - 1$) while for $\Lambda = 0$ one retrieves the physical density. The time-evolved single-scale propagator in the instantaneous eigenbasis together with Equation 4.4.3 constitute the flow equations:

**Algorithm 6.3: x-fRG-t-$\rho_1$**

$$
\begin{aligned}
S^{K,\Lambda}(t,t) &= \partial^*_\Lambda G^{K,\Lambda}(t,t) \\
&= -\sum_k \sum_{\substack{i \\ n_i \neq n_{i+1}}} \sum_{\omega=\pm\Lambda} \frac{i\bar{\sigma}_i}{\pi} |\psi_k(t)\rangle \langle\psi_k(t)| \frac{1}{i\omega + \bar{\omega}_i(0) - \epsilon_k(0)} \\
S^{ret,\Lambda}(t,t) &= 0 \\
\partial_\Lambda \Sigma^{ret,\Lambda}_{i,j}(t,t') &= -\frac{i}{2}\delta(t-t') \sum_{k,l} \left[S^{K,\Lambda}(t,t)\right]_{l,k} v_{i,k,j,l}(t),
\end{aligned}
\tag{6.2.17}
$$

As in the previous scheme, the vanishing retarded component of the single-scale propagator leads to a vanishing flow of the Keldysh self-energy. To calculate the Keldysh component of the single-scale propagator, in general one has to diagonalize the effective Hamiltonian at time $t$ to obtain the instantaneous eigenstates, which is costly for large systems. A physical approximation can be made by replacing

$$
\frac{1}{i\omega + \bar{\omega}_i(0) - \epsilon_k(0)} \to \frac{1}{i\omega + \bar{\omega}_i(t) - \epsilon_k(t)}.
$$

This approximation ensures that the correct number of levels is above and below $\bar{\omega}_i(t)$ and only deviates from an exact treatment of Equation 6.2.17 in higher orders of the interaction since $\bar{\omega}_i(t_0) - \bar{\omega}_i(t) \in \mathcal{O}(v)$, $\epsilon_k(t_0) - \epsilon_k(t) \in \mathcal{O}(v)$. Using this approximation, $S^{K,\Lambda}$ takes the more convenient form

$$
S^{K,\Lambda}(t,t) \approx -\sum_{\substack{i \\ n_i \neq n_{i+1}}} \sum_{\omega=\pm\Lambda} \frac{i\bar{\sigma}_i}{\pi} G^{eq,\Lambda}\left(i\omega + \bar{\omega}_i(t)\right).
$$

The resulting flow equation reads:

**Algorithm 6.4: x-fRG-t-$\rho_2$**

$$
\begin{aligned}
\partial_\Lambda \Sigma^{ret,\Lambda}_{n,j}(t,t') = -\frac{1}{2\pi} \sum_{k,l} \sum_{\substack{i \\ n_i \neq n_{i+1}}} \sum_{\omega=\pm\Lambda} \bar{\sigma}_i v_{n,k,j,l} \\
\left[\frac{1}{i\omega + \bar{\omega}_i(t) - h^0 - \Sigma^{ret,\Lambda}(t)}\right]_{l,k} \delta(t-t'),
\end{aligned}
\tag{6.2.18}
$$

which for tight-binding chains can be evaluated in $\mathcal{O}(N)$ operations.

## 6.3 COMPARISON OF THE DIFFERENT SCHEMES

In this section, we perform various tests to explore the range of validity of the different x-fRG schemes. Due to the first order truncation, results are only guaranteed to agree to linear order in the interaction strength. All higher orders are uncontrolled and may differ.

### 6.3.1 *Tight-binding Hamiltonian*

For the rest of this chapter, we focus on a tight-binding model:

$$\begin{aligned} H^{tb} &= H^{hop} + H^{int} + H^{ph} \\ H^{hop} &= \sum_{i=1}^{N-1} c_i^\dagger c_{i+1} + \text{h.c.} \\ H^{int} &= U \sum_{i=1}^{N-1} c_i^\dagger c_i c_{i+1}^\dagger c_{i+1} \\ H^{ph} &= -\frac{U}{2}(c_1^\dagger c_1 + c_N^\dagger c_N) - U \sum_{i=2}^{N-1} c_i^\dagger c_i, \end{aligned} \tag{6.3.1}$$

where the single-particle index enumerates the Wannier basis states. Here, $H^{ph}$ is introduced to enforce particle-hole symmetry. We use the hopping amplitude between adjacent sites as the energy-scale.

In the thermodynamic limit, the model described by Equation 6.3.1 is gapless for $U < 2$ and thus its low-energy physics is governed by the Luttinger liquid fixed point [Gia03]. The Luttinger parameter is known from Bethe ansatz calculations [Sir12] and at half filling reads

$$K_{\frac{1}{2}} = \frac{1}{\frac{2}{\pi}\arccos\left(-\frac{U}{2}\right)} = 1 - \frac{U}{\pi} + \mathcal{O}\left(U^2\right). \tag{6.3.2}$$

For other fillings, the expressions take more involved forms, but for the scope of this chapter only the first order expansion is needed at quarter- and three-quarter filling:

$$K_{\frac{1}{4}} = 1 - \frac{U}{\pi\sqrt{2}} + \mathcal{O}\left(U^2\right) = K_{\frac{3}{4}}. \tag{6.3.3}$$

### 6.3.2 *Comparison of the excited state schemes*

Here, we compare the results of the x-fRG-t-$\Gamma$ with those obtained from explicit time evolution using the t-fRG of Section 4.4.1 as well as the different x-fRG schemes among one another. The x-fRG schemes do not make use of an explicit time-evolution but are instead based on Equation 6.2.4. Hence, if a gap $\Delta$ as introduced in Equation 6.2.1 exists the x-fRG schemes describe the adiabatic limit of a corresponding scheme with an explicit time-evolution where $\|\dot{h}(t)\| \ll \Delta^2$; if

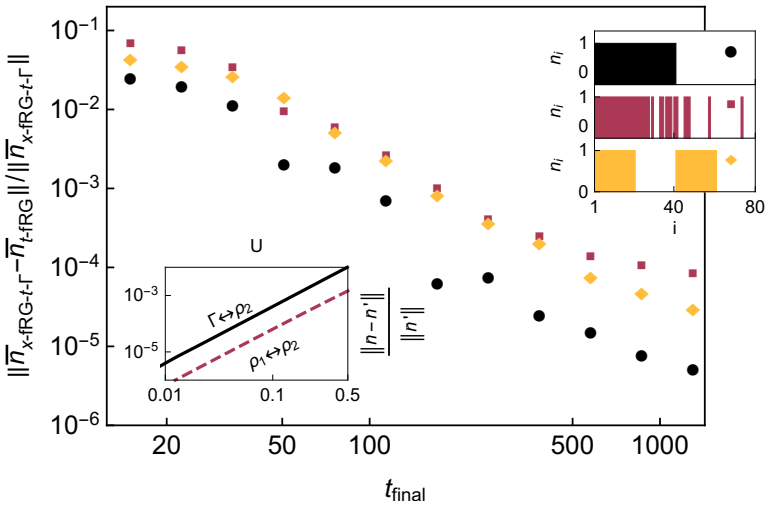


Figure 6.2: *Main plot:* Relative difference in $\bar{n}$ (containing the occupations and all other single-particle correlations, compare Equation 6.2.3) as predicted by the t-fRG of Section 4.4.1 and the x-fRG-t-Γ of Section 6.2.1 using the Frobenius norm. For this comparison, a noninteracting tight-binding chain of $N = 80$ sites was prepared in three different many-body eigenstates of the non-interacting system (visualized in the top right inset). Subsequently, the interaction was smoothly increased to its final value of $U_{final} = 0.5$ at the final time $t_{final}$. This calculation was repeated for various speeds within the t-fRG and compared with the x-fRG-t-Γ, which is by construction in the adiabatic limit. *Top right inset:* The sequences of $n_i$ that define the initial states (sorted by energy, see Section 6.2.1). *Bottom left inset:* Deviations as obtained with x-fRG-t-$\rho_1$ (dashed line) and the x-fRG-t-Γ (solid line) relative to the x-fRG-t-$\rho_2$ result as function of the final interaction strength $U_{final}$. For this comparison the middle state (red squares in the main plot) was used. This figure was previously published in [KKK18].

higher-order terms are taken into account more care has to be taken. As the x-fRG-t-Γ and the t-fRG are based on the same regularization scheme they are expected to yield identical results in this limit while the other schemes are expected to differ in quadratic order in the interaction.

To test this, we prepare the system in eigenstates of the noninteracting system with $N = 80$ sites (the three choices used are illustrated in the upper right inset of Figure 6.2). The interaction is ramped up smoothly from $U = 0$ to $U_{final} = 0.5$ in an increasingly long time span of length $t_{final}$:

$$\frac{U(t)}{U_{final}} = \sin^2\left(\frac{t}{t_{final}}\frac{\pi}{2}\right).$$

The relative difference of the matrix $\bar{n}$ containing all single-particle correlations (compare Equation 6.2.3) in the final state is shown in Fig-

ure 6.2. The difference between the results decreases with increasing $t_{\text{final}}$ with no qualitative difference between the initial states chosen. This explicitly shows that in this case the adiabatic limit can be reached. The saturation at large $t_{\text{final}}$ can be explained by numerical inaccuracies in the integration and time evolution.

The bottom left inset of Figure 6.2 shows the average difference $\bar{n}$ obtained by the x-fRG-t-$\Gamma$, x-fRG-t-$\rho_1$ and x-fRG-t-$\rho_2$ methods. The pairwise difference is quadratic in the interaction, as expected. Even though the x-fRG-t-$\rho_2$ and x-fRG-t-$\rho_1$ do also differ in quadratic order, their deviation is small compared to the difference between the x-fRG-t-$\rho_{1,2}$ and the x-fRG-t-$\Gamma$. For this reason, we will not discuss the x-fRG-t-$\rho_1$ method in the rest of this chapter and instead focus on the computationally cheaper x-fRG-t-$\rho_2$.

### 6.3.3 *Comparison with ground-state fRG*

Another important test for the different x-fRG-techniques is to compare them to the ground-state fRG of Section 4.4.3. As different cutoffs are used and the hierarchy of flow equations is truncated, only agreement to first order is guaranteed.

To study this in detail, we compute the spectral function

$$A_i(\omega) = -\frac{1}{\pi}\mathrm{Im}\left[G^{\mathrm{ret}}(\omega)\right]_{i,i}.$$

To obtain an approximation of the continuous spectral function of an infinite system, the single-particle levels are broadened by weakly coupling the system to a reservoir. This is equivalent to adding a small imaginary part of the order of the level-spacing to the frequency.

Luttinger liquid theory predicts that for frequencies around the Fermi edge, a power-law suppression occurs in the ground-state at the boundary of our tight-binding chain:

$$A_1(\omega) \sim \omega^{\frac{1}{K}-1}. \tag{6.3.4}$$

The exponent has a nontrivial linear contribution in the interaction, rendering this spectral function an ideal testbed for the different x-fRG methods.

For definiteness, we will now discuss the half and quarter filled ground-state. In the half-filled case the approximate x-fRG-t-$\rho_2$ scheme (see Section 6.2.2) yields the same flow equations as the Matsubara fRG: in the ground-state, there is only one jump in the sequence of occupations of eigenstates (at $N/2$). Due to particle-hole symmetry,[4] $\epsilon_i = \epsilon_{N-i}$ and thus $\bar{\omega}_{N/2}(t) = 0$. Therefore, Equation 6.2.18 is identical to Equation 4.4.10. In the quarter-filled case,

4 For simplicity, we assume $N \in 2\mathbb{Z}$.

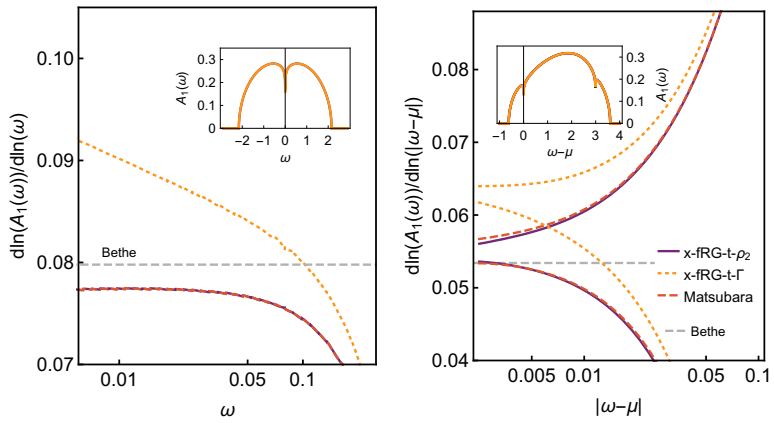


Figure 6.3: Spectral function at the edge of a tight-binding chain in the ground-state as computed with the ground-state fRG and the excited-state fRG methods (used for the ground-state). The system was chosen particle-hole symmetric with $N = 10^5$ sites and $U = 0.25$ at half and quarter filling (left and right plot, respectively). The insets show the spectral functions while the main plots display the logarithmic derivatives. The horizontal, dashed line shows the Bethe-ansatz expectation for the exponent. This figure was previously published in [KKK18].

however, Matsubara fRG and x-fRG-t-$\rho_2$ deviate. In contrast, the x-fRG-t-$\Gamma$ leads to different flow equations in both, the half and the quarter-filled ground-state.

The spectral function $A_1$ and its logarithmic derivative are shown in Figure 6.3. The logarithmic derivative illustrates that the x-fRG-t-$\rho_2$ and the Matsubara fRG (i.e. ground state) indeed yield a power-law suppression. In contrast, the $T = \infty$ reservoir cutoff used in the x-fRG-t-$\Gamma$ fails at this task. This is plausible since the infinite temperature reservoir does not provide a proper low-energy cutoff in the adiabatic limit; all energy scales enter in every step of the calculation (see Equation 6.2.16).

Simple and self-consistent perturbation theory is known to fail to reproduce power-law behavior in most cases.

## 6.4 APPLICATIONS

### 6.4.1 *Generic excitations*

In Sections 6.4.2 and 6.4.3 we study the survival of Luttinger liquid physics in lowly excited states above the ground-state. To this end, we

choose the initial occupations $n_i \in \{0, 1\}$ of single-particle eigenstates with respect to the probability distribution

$$p_1(n_i = 1) = \frac{1}{1 + e^{(i-N/2)\tilde{\beta}}}$$
$$p_1(n_i = 0) = 1 - p_1(n_i = 1),$$

where $\tilde{\beta}$ acts as an effective inverse temperature of the *initial* state in units of the level spacing. $\tilde{\beta}$ should, however, not be understood as a temperature of the *interacting* state but instead just as a measure of the number of excitations in the system. This scheme is used as a convenient way to obtain excited states in a given energy window. The energy of the final state is however not fixed. To make sure the results are independent of the precise way the initial states are generated we also investigate the distributions

$$p_2(n_i = 1) = \begin{cases} 1 & & i - N/2 & < 1/\tilde{\beta} \\ \frac{1}{2} & -1/\tilde{\beta} \leqslant & i - N/2 & < 1/\tilde{\beta} \\ 0 & 1/\tilde{\beta} \leqslant & i - N/2 & \end{cases}$$
$$p_3(n_i = 1) = \begin{cases} 1 & & i - N/2 & < 1/\tilde{\beta} \\ \frac{1}{2} - \frac{\tilde{\beta}(i-N/2)}{2} & -1/\tilde{\beta} \leqslant & i - N/2 & < 1/\tilde{\beta} \\ 0 & 1/\tilde{\beta} \leqslant & i - N/2 & \end{cases}$$
$$p_k(n_i = 0) = 1 - p_k(n_i = 1) \qquad k = 2, 3.$$

The energy of the final state can be obtained computationally cheaply by calculating

$$E = \mathrm{Tr}\left[\bar{n}\left(h^0 + \Sigma\right)\right]$$

where the $\bar{n}$ is only needed on its diagonal and first off-diagonal. Usually, we will be interested in the excitation-energy density defined as $(E - E_{GS})/N$.

### 6.4.2 *Friedel oscillations*

We first investigate the Friedel oscillations that emerge around boundaries. A finite tight-binding chain will display oscillations in the density profile (i.e., the occupation numbers) at the ends (or near any other impurity) at zero temperature and if particle-hole symmetry is broken. We restrict ourselves to the case of a clean, half filled, finite chain and set $H^{ph} = 0$ (see Equation 6.3.1) to break particle-hole symmetry explicitly. Luttinger liquid physics predicts that

$$\left|\left\langle c_i^\dagger c_i \right\rangle - \frac{1}{2}\right| \sim i^{-K}.$$

This power law can be obtained via a ground-state fRG calculation, and the linear correction to the non-interacting exponent can be computed from a leading-order scheme. [And+04]

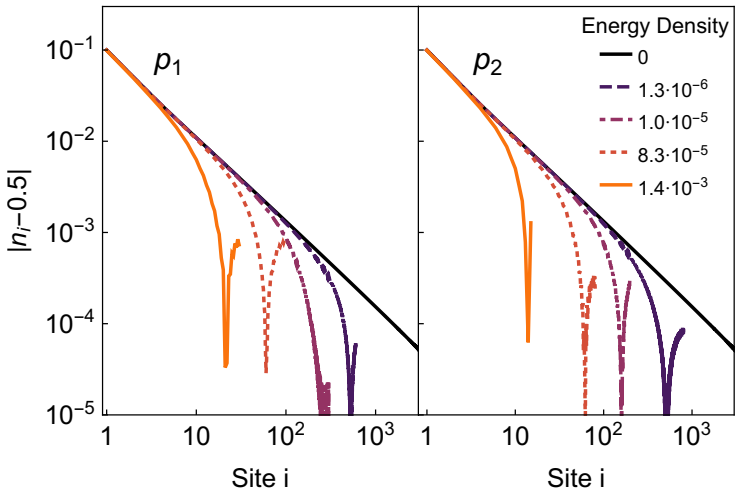


Figure 6.4: Density profile near the boundary of a tight-binding chain (interaction $U = 0.5$) prepared in pure eigenstates with different energies above the ground-state. The initial states in the left and right panel were drawn with the probability distributions $p_1$ and $p_2$, respectively. The data was obtained via the x-fRG-t-$\rho_2$. The Friedel oscillations are cut off on a length-scale related to the energy-density. The system sizes vary between $N = 1.2 \cdot 10^3$ and $N = 0.7 \cdot 10^5$; for clarity, the curves are only shown up to the cutoff. This figure was previously published in [KKK18].

We now employ our x-fRG framework to explore the effects of finite excitation energies and try to draw analogies with the thermal case: At finite temperatures, the algebraic decay is cut off on a length-scale proportional to $1/T$. We investigate whether Friedel oscillations persist in excited eigenstates and if their energy provides a cutoff in a similar fashion as temperature does in the thermal case. Since for small $T$ and a linearized dispersion at the Fermi-edge the energy of a thermal state $E_T$ scales as

$$E_T - E_{GS} \sim T^2,$$

we expect the Friedel oscillations to be cut off on a scale proportional to $1/\sqrt{E - E_{GS}}$.

As the x-fRG algorithms scale linear in the number of changes in the sequence $n_i$ (compareEquations 6.2.16 and 6.2.18), the computational cost can be kept low by fixing the number of single-particle excitations (by choosing a constant $\tilde{\beta}$) while varying the system size. This way, the algorithm scales linearly in the square root of the inverse energy density in the initial state.

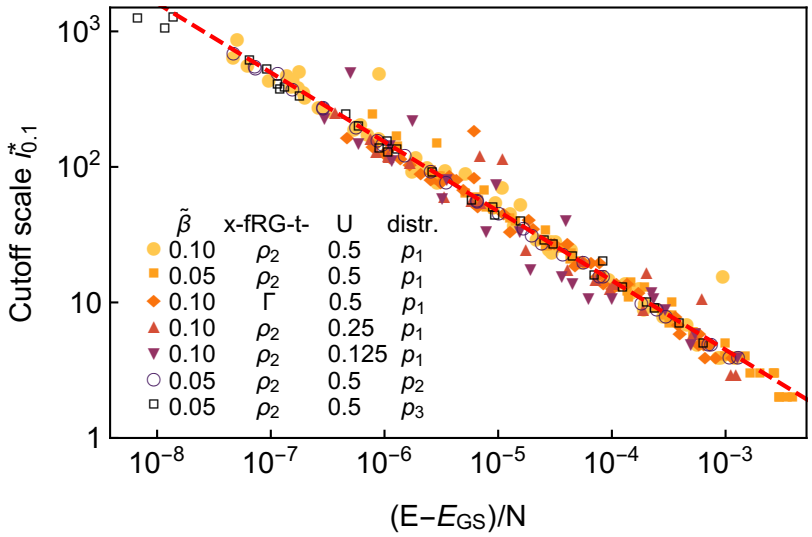


Figure 6.5: Length scale on which the Friedel oscillations are cut off as function of the excitation energy. The interaction varies between $U = 0.125$ and $U = 0.5$, and the size varies from $N = 10^3$ up to $N = 1.6 \cdot 10^5$. The behavior is consistent between the probability distributions $p_{1,2,3}$. The dashed red line is a power-law fit with an exponent $\alpha \approx 0.512$. This figure was previously published in [KKK18].

The resulting occupation numbers are presented in Figure 6.4 for various states at different excitation-energy densities relative to the ground-state. One can see that even at finite energy density a power-law decay is visible close to the boundary. This decay is cut off at an energy dependent length-scale. To objectively measure the deviations from the ground-state Friedel oscillations, we define a cutoff scale

$$i^*_\alpha = \min\left\{ i \middle| \frac{|n_i^{GS} - n_i^{ex}|}{|n_i^{GS} - 0.5|} > \alpha \right\}$$

such that $i^*_\alpha$ gives the first site where the relative error compared to the Friedel oscillations of the ground-state exceeds $\alpha$. This scale is plotted in Figure 6.5 as a function of the excitation energy density for various eigenstates and systems of different lengths. The line is a power-law fit resulting in

$$i^*_{0.1} \sim \left(\frac{E - E_{GS}}{N}\right)^{-0.512},$$

which is reasonably close to the thermal expectation of $-1/2$. This result does not depend on the chosen $\tilde{\beta}$, the cutoff or the distribution used to generate the initial state. We thus conclude that Friedel

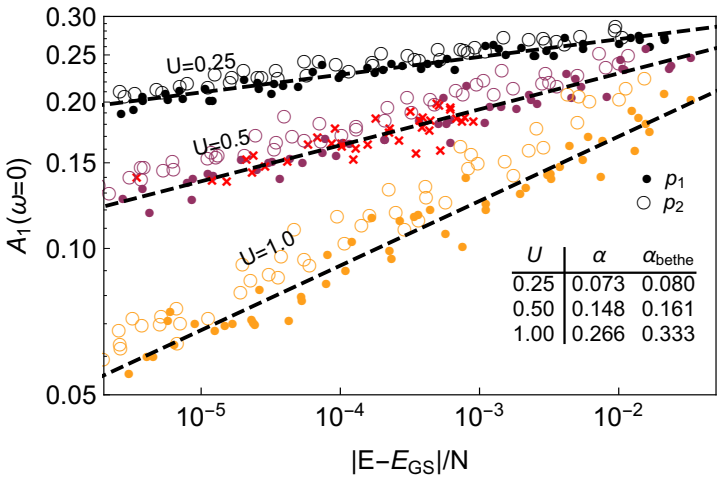


Figure 6.6: Local spectral function on the first site of a chain in an excited eigenstate. The circles show systems of lengths varying form $N = 4 \cdot 10^2$ to $N = 5 \cdot 10^4$ using the probability distribution $p_1$ (filled circles) and $p_2$ (empty circles) with $\tilde{\beta} = 0.05$ at the indicated interaction strengths. To obtain the data represented by the red crosses a fixed system size $N = 5000$ was used varying $\tilde{\beta}$ from 0.025 to 0.3 in the distribution $p_1$ with a fixed $\gamma = 0.0025$. The results obtained at fixed system size and $\gamma$ are compatible with those obtained from simultaneously varying the size and Lorentzian broadening justifying this procedure. This figure was previously published in [KKK18].

oscillations survive to finite energy-densities and that the excitation energy density simply provides an infrared cutoff.

Due to the shortcomings of x-fRG-t-$\Gamma$ discussed in Section 6.3 we solely employ the x-fRG-t-$\rho_2$ from now on.

### 6.4.3 *Spectral function at* $\omega = 0$

Another characteristic of Luttinger liquids is the finite-temperature behavior of the local spectral function introduced in Equation 6.3.4 at $\omega = 0$. In a thermal state

$$A_1(\omega = 0) \sim T^{\frac{1}{K}-1}.$$

In analogy to the previous section we thus investigate whether in an generic, excited many-body eigenstate

$$A_1(\omega = 0) \overset{?}{\sim} \left(\sqrt{\frac{E - E_{GS}}{N}}\right)^{\frac{1}{K}-1}.$$

As discussed before, it is computational advantageous to keep $\tilde{\beta}$ constant while varying the system-size. To compensate for finite-size

effects a small imaginary part $\gamma$ is added to the frequency when evaluating the spectral function, effectively widening the sharp single-particle levels to Lorentzian peaks. We chose $\gamma = 1/(N\tilde{\beta})$. To ensure that $\gamma$ is big enough to remove finite-size effects while being small enough not to influence the observed behavior Figure 6.6 also shows the results obtained at a fixed size $N = 5000$ and fixed smearing $\gamma = 2.5 \cdot 10^{-3}$ by varying $\tilde{\beta}$ of the distribution $p_1$. As the data obtained in either way is compatible, the scaling observed can be attributed to the excitation energy. Data was obtained for states generated with the distribution $p_1$ and $p_2$. While the data shows different prefactors, the exponents are similar. For clarity, the analysis of the exponent will thus be restricted to the distribution $p_1$. The exponent is extracted with a power-law of the form

$$A_1(i\gamma) \sim \left(\sqrt{\frac{E - E_{GS}}{N}}\right)^{\alpha}$$

and compared to the thermal expectation from Bethe-ansatz calculations (see Figure 6.6).

The results indicate that generic excitations can not only provide a cutoff but can also be the origin of Luttinger liquid-like power-laws.

### 6.4.4 *Block excitations*

So far, we have analyzed generic excitations which leave the general shape of the function $n(\omega)$ unchanged and just alter it around the Fermi-edge where the (free) dispersion is nearly linear. As all observables in a Luttinger liquid are governed by the Hamiltonian at low energies, it is not surprising that the results are similar to those of thermal states. There is, however, a different set of excited states which are highly non-generic and different from thermal states, and thus we have no intuition for their physics. As an example, we consider a state where a whole block of fermions is excited to a higher energy region. In the simplest, most symmetric case this is modeled by

$$n_i = \begin{cases} 1 & i \leqslant \frac{1}{4}N \\ 0 & \frac{1}{4}N < i \leqslant \frac{1}{2}N \\ 1 & \frac{1}{2}N < i \leqslant \frac{3}{4}N \\ 0 & \frac{3}{4}N < i \leqslant N \end{cases} \tag{6.4.1}$$

which in contrast to the ground-state has three sharp, distinct edges in the distribution function. To investigate the physics in this state, we again study the spectral function at the boundary (compare Section 6.3.3, we employ the same Lorentzian broadening). Results are shown in Figure 6.7, where one can identify several points of non-analytic behavior. The logarithmic derivatives around these points

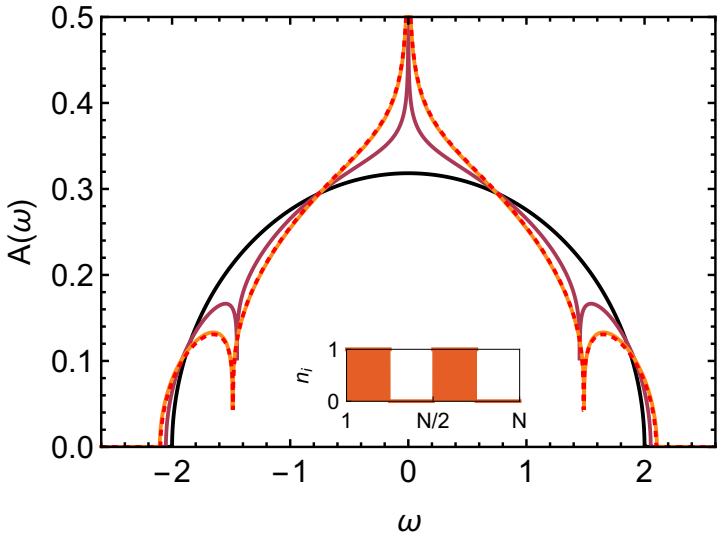


Figure 6.7: Spectral function of a tight-binding chain at the boundary. The interactions are $U = 0, 0.2, 0.4$ (dark to light colors) and the initial sequence of occupied eigenstates of the noninteracting system is shown in the inset, representing a block excitation defined by Equation 6.4.1 in a system of $N = 10^5$ sites. The results shown as solid lines were obtained using the x-fRG-t-$\rho_2$. The dashed, red line represents results obtained using the x-fRG-$\omega$ presented in Section 6.5. This figure was previously published in [KKK18].

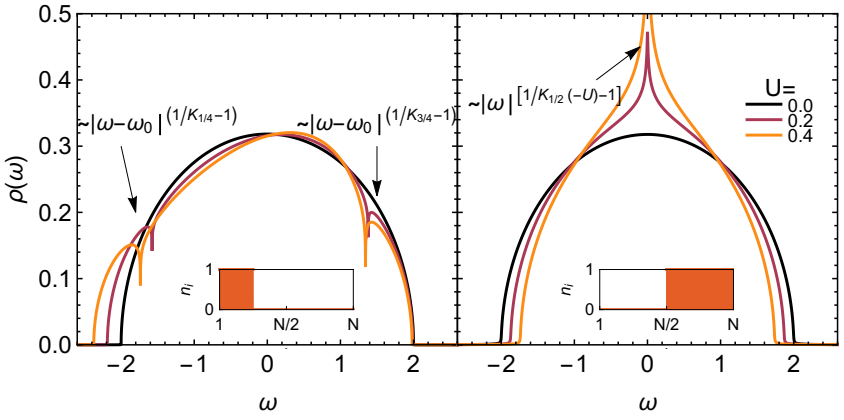


Figure 6.8: Spectral function of a tight-binding chain at the boundary (compare Figure 6.7). The interactions are $U = 0, 0.2, 0.4$ and the initial sequence of occupied eigenstates of the noninteracting system is shown in the insets. *Left panel:* Quarter filled ground-state with $N = 10^5$. The three-quarter filled ground-state gives the mirrored result. *Right panel:* Inverted ground-state using $N = 4 \cdot 10^3$ sites. This figure was previously published in [KKK18].

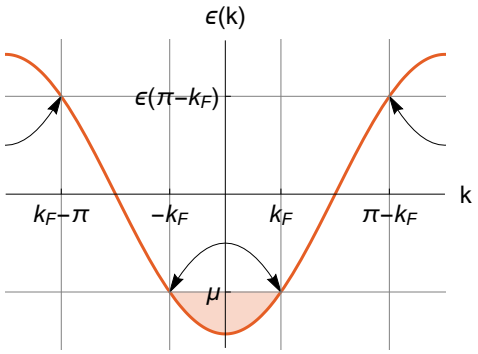


Figure 6.9: Illustration of umklapp processes contributing a second cusp in the local density of states for all filling fractions other than the half filled case (compare left panel of Figure 6.8). This figure was previously published in [KKK18].

are plotted in Figure 6.10 and indicate the existence of power-laws. The spectral function around the center divergence seems to scale as

$$A_1(\omega) \sim |\omega|^{-\frac{U}{\pi}}$$

while the outer cusps are described by

$$A_1(\omega) \sim \left|\omega - \omega_0^{1,3}\right|^{\frac{U\sqrt{2}}{\pi}}.$$

The rest of this section is devoted to understanding this result in terms of known Luttinger liquid physics.

To this end, the left panel of Figure 6.8 shows the spectral function in the quarter filled ground-state as obtained with the x-fRG-t-$\rho_2$; the three-quarter filled case is the same but mirrored. Both show two cusps, one at the Fermi energy and a second one at the energy associated with $\pi - k_F$. The first cusp is the one well studied in the literature while the second cusp is the result of umklapp scattering [Ando6]: the long-ranged potential, acquired by the Friedel oscillations, allows for processes with wave vector $2k_F$, which is either close to the Fermi surface or an umklapp term higher up in the spectrum (compare Figure 6.9). Each of these is described by a power-law $A_1(\omega) \sim |\omega - \omega_0|^{1/K-1}$. K has to be calculated using the dispersion at the corresponding position in the spectrum (i.e., at quarter and three-quarter filling), and to first order the exponent is given by $U/\pi\sqrt{2}$ (compare Equation 6.3.3).

Next, we discuss the inverted half filled ground-state (right panel of Figure 6.8) which can still be obtained from the ground-state algorithm by using a infinitesimal negative temperature, or equivalently by analyzing the ground-state of $-H$. As the sign of the hopping is arbitrary, we are thus just inspecting the ground-state of a tight-binding chain with attractive interactions; to leading order, the corresponding exponent is just $-U/\pi$.

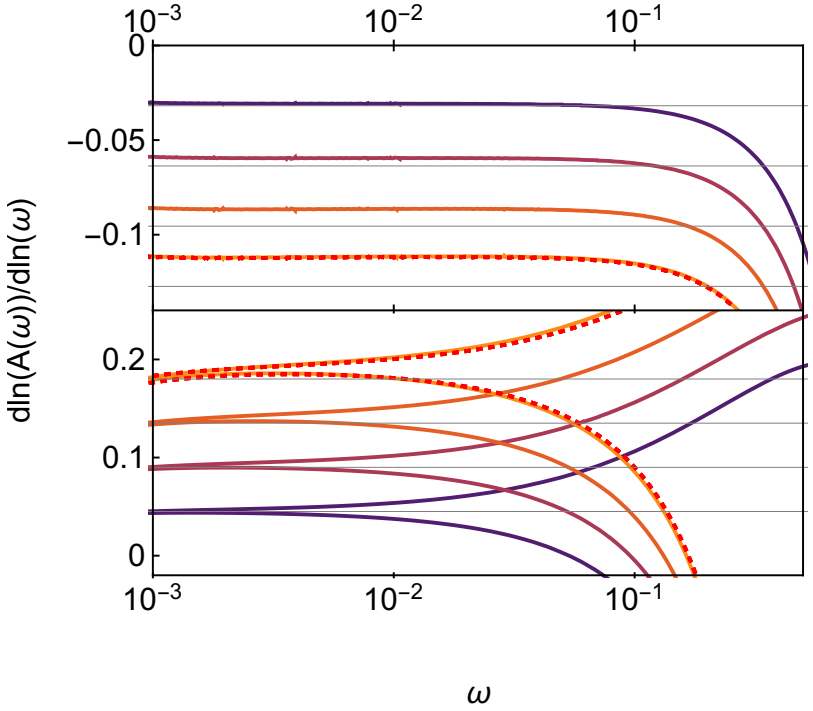


Figure 6.10: Logarithmic derivatives of the power-laws in the spectral function at the boundary in a block-excited state of a tight-binding chain (compare Figure 6.7). The top panel shows the derivative around $\omega = 0$ while the bottom panel shows the two sides around the outer cusp. The interactions depicted are (from dark to light colors) $U = 0.1, 0.2, 0.3, 0.4$. The horizontal lines in the respective panels show $-U/\pi$ and $\sqrt{2}U/\pi$. The dashed, red line represents results obtained using the x-fRG-$\omega$ presented in Section 6.5. This figure was previously published in [KKK18].

We now observe that Figure 6.7 can be interpreted as a superposition of the effects associated with the different jumps in the distribution function: The first and third discontinuity are located at the Fermi energy of a quarter- and three-quarter filled system, respectively. Their contributions coincide and (in the present approximation scheme) the exponents just add up to

$$2\left(\frac{1}{K_{\frac{1}{4}}} - 1\right) = \frac{U\sqrt{2}}{\pi} + \mathcal{O}\left(U^2\right) = 2\left(\frac{1}{K_{\frac{3}{4}}} - 1\right).$$

The divergence in the center is described purely by the inverted ground-state.

Hence, the phenomenology of the very highly excited, non-generic case of a block-excitation can (at least to leading order) be interpreted in terms of ground-state Luttinger liquid physics.

## 6.5 TOWARDS SECOND ORDER: STEADY-STATE KELDYSH FRG WITH A NON-THERMAL RESERVOIR CUTOFF

We now devise a third way of obtaining an effective noninteracting description of an excited eigenstate for an interacting model which is not based on an adiabatic time-evolution but instead employs the steady-state Keldysh formalism of Section 4.4.2. This could be of central importance in going beyond linear order in interactions: the x-fRG-t-$\Gamma$, $\rho$ discussed before are based on a picture of discrete, separated levels. In second order these levels will be broadened resulting in a finite lifetime of quasiparticles. Hence, a picture of adiabatic time-evolution becomes questionable. While a generalization to second order of the algorithm presented here is still non-trivial it could be a promising starting point. Whether a second-order treatment would result in relevant entanglement to the auxiliary bath at arbitrarily weak couplings remains to be investigated.

The system is assumed to be in the steady-state induced by a wide-band reservoir. As in Section 4.4.2, the hybridization to this reservoir is used as the cutoff, but the reservoir is now no longer in thermal equilibrium but instead chosen to be in a non-thermal, pure state described by the distribution function (compare Section 6.2.1.3)

$$1 - 2n(\omega) = \frac{\sigma_{N_\omega} - \sigma_1}{2} + \sum_{i=1}^{N_\omega} \sigma_i \mathrm{sign}(\omega - \omega_i), \tag{6.5.1}$$

At the beginning of the flow where the coupling $\Lambda$ to the reservoir is strong, all levels are infinitely broadened and thus empty, half-filled or full (according to the first term of Equation 6.5.1) and uncorrelated (i.e., described by a $T = \infty$ state, independently of the precise state of the reservoir). For small couplings (i.e., at the end of the flow), the energy-scales of the physical Hamiltonian dominate and the distribution function governing the steady state becomes equal to the one of the reservoir. Hence, one recovers the physical system featuring a non-thermal distribution function.

As no physical reservoirs are considered and all auxiliary reservoirs are governed by the same statistics, the system is in an (non-thermal) equilibrium configuration throughout the flow and the fRG preserves the fluctuation-dissipation theorem (see Section 4.3.1). This

allows us to simplify the flow Equation 4.4.8 of the retarded self-energy:

$$\begin{aligned}
\partial_\Lambda \Sigma^{\mathrm{ret},\Lambda}_{i,j} &= -\frac{i}{4\pi} \sum_{k,l} \nu_{i,k,j,l} \int d\omega \left[ S^{K,\Lambda}(\omega) \right]_{l,k} \\
&\overset{\text{FDT}}{=} -\frac{i}{4\pi} \sum_{k,l} \nu_{i,k,j,l} \int d\omega \ (1 - 2n(\omega)) \\
&\qquad \left[ \partial^*_\Lambda G^{\mathrm{ret},\Lambda}(\omega) - \partial^*_\Lambda G^{\mathrm{adv},\Lambda}(\omega) \right]_{l,k} \\
&= -\frac{i}{4\pi} \sum_{k,l} \nu_{i,k,j,l} \int d\omega \ (1 - 2n(\omega)) \\
&\qquad \left[ i\partial_\omega G^{\mathrm{ret},\Lambda}(\omega) + i\partial_\omega G^{\mathrm{adv},\Lambda}(\omega) \right]_{l,k} \\
&\overset{(6.5.1)}{=} -\frac{1}{2\pi} \sum_{k,l,i} \nu_{i,k,j,l} \sigma_i \left[ G^{\mathrm{ret},\Lambda}(\omega_i) + G^{\mathrm{adv},\Lambda}(\omega_i) \right]_{l,k}
\end{aligned}$$

where we employ the specific distribution function in the last line and partially integrate. The final flow equations therefore read:

**Algorithm 6.5: x-fRG-ω**

$$\begin{aligned}
&\partial_\Lambda \Sigma^{\mathrm{ret},\Lambda}_{n,m} \\
&\quad = -\frac{1}{2\pi} \sum_{k,l} \sum_{i} \sigma_i \nu_{n,k,m,l} \left[ G^{\mathrm{ret},\Lambda}(\omega_i) + G^{\mathrm{adv},\Lambda}(\omega_i) \right]_{l,k} \\
&\quad = -\frac{1}{2\pi} \sum_{k,l,i} \sum_{\omega = \pm\Lambda} \sigma_i \nu_{n,k,m,l} \left[ \frac{1}{i\omega + \omega_i - h^0 - \Sigma^{\mathrm{ret},\Lambda}} \right]_{l,k},
\end{aligned}$$

which is remarkably similar to the one found in the schemes discussed previously (see Equation 6.2.18) and even coincides, if the relevant parts of the spectrum are invariant when lowering the cutoff. In general, however, the effective single-particle spectrum will change during the flow. By definition of the cutoff scheme, at no point the particle number is fixed, only the occupation in energy space. The actual number of particles in the final system cannot be fixed beforehand. To obtain a state with a desired sequence of occupations $n_i$ of the effective single-particle levels the frequencies $\omega_i$ have to be iteratively adjusted.

For the case of a block excitation this optimization procedure is straightforward and the results of such a calculation are shown as dashed lines in Figure 6.7. For this problem, the x-fRG-ω produces power-laws; to obtain more generic states using this method is, however, connected to a significant overhead.

## 6.6 QUENCHES FROM EXCITED EIGENSTATES

We are now going to discuss, how to combine the x-fRG with a quench. While in principle all the algorithms presented in this chapter can conceivably be extended by a subsequent quench, the time-dependent fRG equation following the quench can not easily be solved for all proposed schemes.

The x-fRG-t-$\rho_1$ presented in Algorithm 6.3 is a natural choice for an extension to a quench scenario. It was successfully used to obtain excited eigenstates and (in contrast to the x-fRG-t-$\rho_2$ and x-fRG-$\omega$) is defined in time-space. Furthermore, the cutoff used can be argued to provide a low-energy cutoff (even after the quench): a quench protocol is generically not expected to significantly reduce the (effective) temperature of the system, so even after the quench, low frequencies are suppressed. As this argument is not rigorous, validity has to be checked on a case-by-case basis.

For this algorithm, we assume that the system is prepared in some eigenstate of the non-interacting Hamiltonian at time $t = 0$. The interaction is then adiabatically increased up to time $t = t_0$. From then on, an arbitrary quench protocol can be applied. The resulting algorithm reads:

**Algorithm 6.6: Quench from excited eigengestate**

$$
\begin{aligned}
&S^{K,\Lambda}(t_0,t_0) = \partial^*_\Lambda G^{K,\Lambda}(t_0,t_0)\\
&\quad = -\sum_k \sum_{\substack{i\\ n_i \neq n_{i+1}}} \sum_{\omega=\pm\Lambda} \frac{i\bar{\sigma}_i}{\pi} \left|\psi_k(t_0)\right\rangle \left\langle\psi_k(t_0)\right| \frac{1}{i\omega + \bar{\omega}_i(0) - \epsilon_k(0)}\\
&S^{K,\Lambda}(t,t) = G^{ret}(t,t_0) S^K(t_0,t_0) G^{adv}(t_0,t)\ \forall t > t_0\\
&S^{ret,\Lambda}(t,t) = 0\ \forall t\\
&\partial_\Lambda \Sigma^{ret,\Lambda}_{i,j}(t,t') = -\frac{i}{2}\delta(t-t') \sum_{k,l} \left[S^{K,\Lambda}(t,t)\right]_{l,k} \nu_{i,k,j,l}(t)
\end{aligned}
\tag{6.6.1}
$$

Note that this also proposes a new variant of the time-dependent fRG, where the cutoff is purely encoded in the initial configuration.

## 6.7 SUMMARY AND OUTLOOK

In this chapter, we have shown how correlation functions in pure excited states of many-body systems can be obtained within the realm of the functional renormalization group; the key idea is to start out with a Slater determinant and to slowly switch on interactions. To this end, we simplified existing real-time Keldysh fRG flow equations for

the special case of adiabaticity (x-fRG-t-Γ) and also devised a novel cutoff scheme which is specifically tailored to this problem (x-fRG-t-ρ). Due to the approximate nature of the method, the x-fRG results do not necessarily agree with those of standard equilibrium fRG when targeting the ground state, which thus provides a nontrivial testing ground. Importantly, only the x-fRG-t-ρ manages to reproduce the power-law suppression of the spectral function at the boundary of a Luttinger liquid; the x-fRG-t-Γ fails at this task.

We subsequently employed the x-fRG to study two toy problems. First, we demonstrated that Luttinger liquid power law behavior survives in lowly-excited pure states whose excitation energy density serves as an infrared cutoff. Second, we determined the spectral function of highly-excited, nongeneric block excitations featuring multiple Fermi edges and illustrated that the system is effectively governed by a superposition of several Luttinger liquids.

The key drawback of the x-fRG is its approximate character. Even though the underlying RG idea entails an infinite resummation of Feynman diagrams, all results presented in this paper are only guaranteed to be correct up to leading order in the interaction. The strengths of the x-fRG are that it is not bound by the growth of entanglement and that large systems of up to $10^5$ sites (in one dimension) can be treated easily.

Future directions include an extension of the x-fRG flow equations to second order. The x-fRG-ω could provide a good starting point for a second-order treatment as it is less dependent on an effective single-particle picture. This cutoff procedure can be readily applied in second-order opening up the interesting question of whether the final state remains pure up to the truncation order.

Furthermore, we proposed a method, that can be used to investigate quenches, where the initial state is a pure, excited eigenstate of an interacting Hamiltonian. This method can be used to investigate transport properties of individual eigenstates, which might be essential to characterize mobility edges.

The methodology developed in this paper is directly applicable to questions arising in the field of many-body localization [GMP05; BAA06]. Using this one can obtain access to the entire spectrum of an interacting disorder system. In future work we hope to contribute to the debate about the existence of a mobility edge separating localized and delocalized eigenstates.

Going beyond this, an application to many-body localized systems is enticing. Because of the small overlap of far apart localized states, explicit adiabatic time-evolution is expected to be exponentially hard. Due to the smooth distribution function used in the flow-equations of the x-fRG-t-ρ it might be a promising method to circumvent this problem and explore the many-body spectrum of interacting, localized systems.

# 7

# STEADY STATE OF LARGE, OPEN SYSTEMS

## 7.1 INTRODUCTION

A system that is driven out of equilibrium by some form of local quench-protocol will display many interesting, non-equilibrium phenomena (for a review, see [Mit18]). However, it is generally believed, that after some transient period, a generic, infinite (or in practice large) system equilibrates; not only is time-translational invariance recovered but also all local observables are well described by a thermal distribution [D'A+16; Sre99; Neu29; Gol+10].

A simple way to prevent thermalization is continuous driving of the system. When periodically driving a system, however, energy is not conserved and thus in an ergodic system the unique stationary state is an infinite temperature state [HKK97; LDM14a; DR14]. Whether or not this holds true for a given model is not always easy to determine. Well known exceptions are integrable systems (such as all non-interacting models) [LDM14b] as well as many-body localized systems [Pon+15], which display emergent integrability [RMS15; Imb16b; Imb16a; IRS17].

To circumvent heating, it is necessary to consider an infinite (i.e. open) system, where an infinite amount of energy can dissipate. While open systems are attractive from a theoretical perspective, as they prevent recurrence, allow for non-trivial stationary states without time-dependent driving and more closely resemble a realistic system (as all systems are to some extent coupled to the environment) they also present a hurdle to many methods. It is a priori unclear, how long transient dynamics persist and when a stationary state will be reached. Additionally, effects like prethermalization [BBW04] make the use of time-evolution based methods questionable. As we already discussed, it is essential to consider infinite systems, and perturbative approaches with respect to the environment might not be able to capture the correct long time behavior. Due to these difficulties, methods are usually restricted to small interacting regions, weak coupling to reservoirs or translationally invariant systems.

In this chapter, we present a method that is designed to compute single-particle correlation functions in the stationary state of open systems that feature two-particle interactions. To drive the system out of equilibrium, we consider a scenario, where the non-interacting reservoirs are initially prepared in different equilibrium configurations. The method presented is based on the functional renormalization group and thus perturbative in the interaction strength. In

contrast to previous approaches to this problem [Jak+07], we incorporate second-order contributions and can therefore describe heating effects. As we mentioned above, these are essential to the physics in the stationary state. Due to the computational cost, these inelastic processes have only been considered in relatively small quantum-dot structures [JPS10a; RJM14]. The equilibrium treatment of such terms was discussed in [SK17; BHD14].

First, we will formally define the models that are accessible (Section 7.2) to the method we propose. We describe the method in detail (Section 7.3) and put emphasis on an efficient, highly parallelized implementation. The single-impurity Anderson model provides a nontrivial check of out implementation (Section 7.4). In the second half of this chapter, we focus on one-dimensional tight-binding chains coupled to reservoirs (Section 7.5), which we study in equilibrium (Section 7.5.3) and at a finite bias voltage (Section 7.5.4). Throughout, we critically evaluate the results.

## 7.2 CLASS OF MODELS DISCUSSED

In this chapter, we consider time-independent, fermionic models with a finite number $N \in \mathbb{N}$ of interacting degrees of freedom:

$$H_{\text{sys}} = \sum_{n,m \in \underline{N}} h_{n,m} c_n^\dagger c_m + \frac{1}{4} \sum_{n,m,k,l \in \underline{N}} v_{n,m,k,l} c_n^\dagger c_m^\dagger c_k c_l.$$

These are assumed to be coupled to a finite number $N_{\text{res}}$ of infinite, non-interacting wide-band reservoirs with a quadratic coupling (compare Equation 2.8.12). The reservoirs are assumed to be initially prepared in thermal equilibrium at $T = 0$ or $T = \infty$ at arbitrary chemical potential. Hence, their contribution to the self-energy in the Keldysh basis has a particularly simple frequency dependence:

$$\Sigma_{\text{res}}^{\text{ret}}(\omega) = \sum_{n \in \underline{N_{\text{res}}}} -i\Gamma_n \qquad \Sigma_{\text{res}}^{K}(\omega) = \sum_{\substack{n \in \underline{N_{\text{res}}} \\ T_n = 0}} -2i\,\text{sgn}(\omega - \mu_n)\Gamma_n, \quad (7.2.1)$$

where $\Gamma_n \in \mathbb{C}^{N \times N}$ are positive, hermitian matrices characterizing the coupling to the individual reservoirs and $T_n,\ \mu_n \in \mathbb{R}$ for $n \in \underline{N_{\text{res}}}$ define the statistics of each reservoir. Note that the Keldysh self-energy vanishes for all infinite-temperature reservoirs (see Equation 2.8.12). As discussed previously, we do not allow for a direct coupling between the reservoirs. Every part of the system is assumed to have a decay channel into at least one of the reservoirs to obtain a well-defined steady state.

For a numerically efficient implementation of the algorithms presented here, it is crucial to also presuppose that $v$ is sparse. Generally, we will assume that $\text{supp}(v) \in \mathcal{O}(N)$. An example, and the focus of

this chapter, is a nearest-neighbor interaction. Importantly, we impose no restrictions on $h$.

Furthermore, we focus on the parameter regime, where all entries of the bare two-particle interaction are small compared to the relevant single-particle energy scales such that the validity of perturbative arguments is warranted.

## 7.3 SECOND ORDER FRG FORMULATION

While these systems can be easily treated in a first order approximation (we will discuss this on one example in Section 7.5.2), such an approximation only produces frequency-independent corrections to the spectrum. Contributions to the Keldysh component of the self-energy is, however, expected to be essential to describe heating. Especially in systems coupled only weakly to the environment such effects may fundamentally change the phenomenology.

To amend this, we aim to include all second order contributions to the self-energy to obtain corrections to the prediction of the first-order fRG.

### 7.3.1 *Choice of the cutoff*

When choosing the cutoff, we have two main goals: (i) we want to preserve as many symmetries as possible while (ii) aiming for a numerically efficient algorithm. As we will see, not both of these goals can be achieved simultaneously, hence the approach presented is a compromise and a different choice might yield different, and potentially better, results.

The cutoffs presented thus far have fallen in one of three categories. They either add inelastic terms, effectively smearing the spectrum (see Section 4.4.1 and Algorithm 6.2), they modify the distribution function of the system (see Section 6.2.2) or both (see Section 6.5 and Section 4.4.2). The system we want to study is only weakly coupled to reservoirs, resulting in a sharply peaked density of states. This poses a significant problem numerically. We thus aim to introduce additional scattering to aid an efficient implementation. At the end of the flow, physical decay processes are expected to be generated to guarantee sufficient smoothing, allowing for efficient numerical integration. To preserve the fluctuation-dissipation theorem in equilibrium we refrain from modifying the distribution function through the cutoff (compare Section 4.3.1).

For these reasons, we decide to use a reservoir cutoff scheme. In equilibrium, the initial distribution function of the auxiliary reservoirs can be chosen identical to the physical one, conserving the fluctuation-dissipation theorem (see Section 4.3.1). We will also analyze, how choosing different temperature in the auxiliary reservoirs

affects the equilibrium results (see Section 7.5.3). This cutoff furthermore has the advantage, that the Green's functions at finite flow parameter have the same form as physical Green's functions, allowing us to simplify the flow equations significantly. Moreover, due to the physical choice of the cutoff, causality is automatically conserved.

### 7.3.2 *Vertex feedback*

Our main interest in this section is to analyze the effect of inelastic processes on the system and how it modifies the first order behavior. Therefore, we aim to extend the first order functional renormalization group in the simplest way possible, that still includes all second order contributions in a perturbative sense. As a reminder, the flow of the vertex functions truncated after the second order reads (see Section 4.2.5):

$$\begin{aligned}&\partial_\Lambda \Sigma_{1'|1}(\omega)\\ &= \frac{-i}{2\pi}\int d\Omega \gamma_{1'2'|12}(\Pi = \Omega+\omega, X = \Omega-\omega, \Delta = 0) S_{2|2'}(\Omega)\end{aligned} \tag{7.3.1}$$

$$\begin{aligned}\partial_\Lambda \gamma_{1'2'|12}(\Pi, X, \Delta) = \frac{i}{2\pi}\int d\omega \\ \gamma_{1'2'|34} S_{3|3'} G_{4|4'} \gamma_{3'4'|12} \\ +\gamma_{1'4'|32}\left[S_{3|3'}G_{4|4'} + G_{3|3'}S_{4|4'}\right]\gamma_{3'2'|14} \\ -\gamma_{1'3'|14}\left[S_{3|3'}G_{4|4'} + G_{3|3'}S_{4|4'}\right]\gamma_{4'2'|32}\end{aligned} \tag{7.3.2}$$

where we left out the frequency arguments to improve readability. The multi-indices $1', 2', \ldots$ contain the single-particle indices as well as the Keldysh indices. If we consider a frequency discretization with $N_\Omega$ points, the resulting two-particle vertex has

$$|\gamma| \in \mathcal{O}\left(N^4 N_\Omega^3\right) \tag{7.3.3}$$

non-vanishing entries. Computing the rhs of an individual element is associated with a cost of $\mathcal{O}\left(N^4 N_\Omega\right)$[1] resulting in an complexity class of

$$\text{full } 2^{\text{nd}} \text{ Order fRG} \in \mathcal{O}\left(N^8 N_\Omega^4\right) \tag{7.3.4}$$

to compute the flow of the two-particle vertex (the flow of the self-energy is computationally significantly cheaper). Computing this, without any additional approximations is impossible, even for small systems.

1 In this argument, we assume the grid is chose fine enough to approximate the integration.

As a first step to reduce this complexity, we remove the feedback of the two-particle vertex in the second order flow equations, i.e. replacing $\gamma$ with $\bar{v}$ on the rhs. As $\gamma = \bar{v} + \mathcal{O}\left(U^2\right)$, this only generates an error of $\mathcal{O}\left(U^3\right)$.

$$\begin{aligned}
\partial_\Lambda \gamma_{1'2'|12}(\Pi, X, \Delta) =& \frac{i}{2\pi} \int d\omega \\
& \bar{v}_{1'2'|34} S_{3|3'}\left(\frac{\Pi}{2} - \omega\right) G_{4|4'}\left(\frac{\Pi}{2} + \omega\right) \bar{v}_{3'4'|12} \\
& + \bar{v}_{1'4'|32} \bar{v}_{3'2'|14} \\
& \left[S_{3|3'}\left(\omega - \frac{X}{2}\right) G_{4|4'}\left(\omega + \frac{X}{2}\right) + G_{3|3'}\left(\omega - \frac{X}{2}\right) S_{4|4'}\left(\omega + \frac{X}{2}\right)\right] \\
& - \bar{v}_{1'3'|14} \bar{v}_{4'2'|32} \\
& \left[S_{3|3'}\left(\omega - \frac{\Delta}{2}\right) G_{4|4'}\left(\omega + \frac{\Delta}{2}\right) + G_{3|3'}\left(\omega - \frac{\Delta}{2}\right) S_{4|4'}\left(\omega + \frac{\Delta}{2}\right)\right]
\end{aligned} \tag{7.3.5}$$

This approximation is additively separable into three independent flow-equations. $\gamma = v + \gamma^d(\Delta) + \gamma^p(\Pi) + \gamma^x(X)$. We will call this the channel decomposition. The flow-equation of the self-energy can be decomposed correspondingly:

$$\begin{aligned}
\partial_\Lambda \Sigma_{1'|1}(\omega) =& \sum_{\alpha \in \{p,x,d\}} \partial_\Lambda \Sigma^\alpha_{1'|1}(\omega) \\
\partial_\Lambda \Sigma^p_{1'|1}(\omega) =& \frac{-i}{2\pi} \int d\Omega \gamma^p_{1'2'|12}(\Omega + \omega) S_{2|2'}(\Omega) \\
\partial_\Lambda \Sigma^p_{1'|1}(\omega) =& \frac{-i}{2\pi} \int d\Omega \gamma^x_{1'2'|12}(\Omega - \omega) S_{2|2'}(\Omega) \\
\partial_\Lambda \Sigma^d_{1'|1}(\omega) =& \frac{-i}{2\pi} \left(\gamma^d_{1'2'|12}(0) + \bar{v}_{1'2'|12}\right) \int d\Omega S_{2|2'}(\Omega).
\end{aligned} \tag{7.3.6}$$

In addition to reducing the frequency dependence from 3D to 1D it also reduces the spatial dimension of these tensors as

$$\begin{aligned}
\gamma^p_{1'2'|12}(\Pi) =& 0 \qquad \forall 1', 2', 1', 2 \ni v_{i_1 i_{2'}|\bullet\bullet} = 0 \vee v_{\bullet\bullet|i_1 i_2} = 0 \\
\gamma^x_{1'2'|12}(X) =& 0 \qquad \forall 1', 2', 1', 2 \ni v_{i_{1'}\bullet|\bullet i_2} = 0 \vee v_{\bullet i_{2'}|i_1 \bullet} = 0 \\
\gamma^d_{1'2'|12}(\Delta) =& 0 \qquad \forall 1', 2', 1', 2 \ni v_{i_{1'}\bullet|i_1\bullet} = 0 \vee v_{\bullet i_{2'}|\bullet i_2} = 0.
\end{aligned} \tag{7.3.7}$$

For a nearest-neighbor interaction, this simplifies to

$$\begin{aligned}
\gamma^p_{1'2'|12}(\Pi) &= 0 \qquad \forall |1' - 2'| \neq 1 \vee |2' - 1| \neq 1 \\
\gamma^x_{1'2'|12}(X) &= 0 \qquad \forall |1' - 2| > 1 \vee |2' - 1| > 1 \\
\gamma^d_{1'2'|12}(\Delta) &= 0 \qquad \forall |1' - 1| > 1 \vee |2' - 2| > 1,
\end{aligned} \tag{7.3.8}$$

where we understand $|\bullet|$ to mean the distance in the *spatial*, single-particle indices.

Finally, we remove the self-energy feedback back to the two-particle vertex by replacing $G \to g$ and $S \to s$. Yet again, this approximation is controlled in the interaction and only introduces errors of $\mathcal{O}\left(U^3\right)$ and is only used for the flow of the two-particle vertex; the self-energy is not approximated further. Numerically, this might appear to make the problem more complicated, as without feeding back the inelastic contributions of the self-energy, the Green's functions might be sharply peaked, making the evaluation of the integrals more difficult. However, this allows us to analytically integrate the flow equations. To that end, we use $\partial\Lambda g_{3|3'} g_{4|4'} = s_{3|3'} g_{4|4'} + g_{3|3'} s_{4|4'}$. The resulting form of the two-particle vertex

$$\begin{aligned}
\gamma^{p}_{1'2'|12}(\Pi) &= \frac{i}{4\pi} \int d\omega \bar{\nu}_{1'2'|34} g_{3|3'} \left(\frac{\Pi}{2} - \omega\right) g_{4|4'} \left(\frac{\Pi}{2} + \omega\right) \bar{\nu}_{3'4'|12} \\
\gamma^{x}_{1'2'|12}(X) &= \frac{i}{2\pi} \int d\omega \bar{\nu}_{1'4'|32} g_{3|3'} \left(\omega - \frac{X}{2}\right) g_{4|4'} \left(\omega + \frac{X}{2}\right) \bar{\nu}_{3'2'|14} \\
\gamma^{d}_{1'2'|12}(\Delta) &= \frac{-i}{2\pi} \int d\omega \bar{\nu}_{1'3'|14} g_{3|3'} \left(\omega - \frac{\Delta}{2}\right) g_{4|4'} \left(\omega + \frac{\Delta}{2}\right) \bar{\nu}_{4'2'|32}.
\end{aligned} \tag{7.3.9}$$

This corresponds to the perturbation theory result for the two-particle vertex (compare Section 4.5) in the presence of a finite flow parameter $\Lambda$. The cutoff enters in the bare Green's functions. The computational cost of obtaining all these contributions to the two-particle vertex is of complexity

$$\underbrace{\mathcal{O}\left(N^2 N_\Omega\right)}_{\text{\#components}} \underbrace{\mathcal{O}\left(N_\Omega\right)}_{\text{integration}}. \tag{7.3.10}$$

This does not include the cost of computing the Green's functions which should be done beforehand (and thus contributes additively). Computing all components of the Green's functions is expected to scale like $\mathcal{O}\left(N^3 N_\Omega\right)$. While these equations can be solved numerically, we found it to be more efficient to obtain and evaluate a semi-analytical solution.

### 7.3.3 *Analytically computing the perturbative two-particle vertex*

To obtain analytic expressions of the perturbative two-particle vertex at finite values of $\Lambda$, we make use of the restrictive choice of reservoirs in Equation 7.2.1. As the cutoff employed (see Section 7.3.1) can be simply understood as an additional reservoir, we will not consider the cutoff parameter separately but treat is as yet another physical reservoir. To improve readability we use the short hand notation

$$\bar{h} = h - i\Gamma \tag{7.3.11}$$

for the effective (retarded) Hamiltonian, where in the spirit of this section $\Gamma = \sum_n \Gamma_n + \Lambda$ . As $\bar{h}$ is not hermitian, it has separate left and right eigensystems:

$$\begin{aligned} \bar{h}\,|q\rangle &= \lambda_q\,|q\rangle \\ \langle\bar{q}|\,h &= \langle\bar{q}|\,\lambda_q. \end{aligned} \tag{7.3.12}$$

The positivity of $\Gamma$ ensures that $\mathrm{Im}(\lambda_q) < 0\ \forall q$. We can rewrite the non-interacting retarded and advanced Green's functions as:

$$g^{\mathrm{ret}}(\omega) = \frac{1}{\omega - \bar{h}} = \sum_q \frac{1}{\omega - \lambda_q}\,|q\rangle\,\langle\bar{q}| =: \sum_q \frac{1}{\omega - \lambda_q} Q_q \tag{7.3.13}$$

$$g^{\mathrm{adv}}(\omega) = \frac{1}{\omega - \bar{h}^\dagger} = \sum_q \frac{1}{\omega - \lambda_q^*}\,|\bar{q}\rangle\,\langle q| =: \sum_q \frac{1}{\omega - \lambda_q^*} Q_q^\dagger \tag{7.3.14}$$

where we also introduced the matrix $Q_q = |q\rangle\,\langle\bar{q}|$. Next, we simplify the Keldysh Green's function:

$$\begin{aligned} g^{\mathrm{K}}(\omega) &= g^{\mathrm{ret}}(\omega)\Sigma^{\mathrm{K}}(\omega)g^{\mathrm{adv}}(\omega) \\ \Sigma^{\mathrm{K}}_{\mathrm{res}}(\omega) &= -2i \sum_{\substack{n \\ T_k = 0}} \Gamma_n \mathrm{sgn}(\omega - \mu_k). \end{aligned} \tag{7.3.15}$$

This self-energy includes the contributions of both, the physical as well as the auxiliary reservoirs which might be of different temperature. For every reservoir of zero temperature we introduce a distribution operator $\eta_n$ (compare Section 2.6):

$$\begin{aligned} -2i\Gamma_n &= -\eta_n h^\dagger + h\eta_n \\ \Rightarrow \mathbb{1} - 2N(\omega) &= \sum_{\substack{n \\ T_n = 0}} \eta_n \mathrm{sgn}(\omega - \mu_k). \end{aligned} \tag{7.3.16}$$

resulting in:

$$\begin{aligned} g^{\mathrm{K}}(\omega) &= g^{\mathrm{ret}}(\omega)\Sigma^{\mathrm{K}}(\omega)g^{\mathrm{adv}}(\omega) \\ &= \sum_{\substack{n \\ T_n = 0}} \mathrm{sgn}(\omega - \mu_n)\left[g^{\mathrm{ret}}(\omega)\eta_n - \eta_n g^{\mathrm{adv}}(\omega)\right]. \end{aligned} \tag{7.3.17}$$

This can also be understood as a partial fraction decomposition. $\eta_k$ is defined as a Sylvester equation and the solution of this class of matrix equations has been discussed in Section 2.6.

Using this decomposition, we can write down concise, complex valued integrals to express the two-particle vertex functions. For example

$$\begin{aligned}
&\int d\omega\; g^{\mathrm{ret}}_{i|i'}(\pm\omega) g^{K}_{j|j'}(\omega+\Omega) \qquad (7.3.18)\\
&\quad = \int d\omega \sum_{q_1} \frac{1}{\pm\omega - \lambda_{q_1}} (Q_{q_1})_{i,i'} \sum_{q_2} \sum_{n\in\underline{N_{\mathrm{res}}}} \mathrm{sgn}(\omega-\mu_n)\\
&\qquad \times \left[ \frac{1}{\omega+\Omega-\lambda_{q_2}} (Q_{q_2}\eta_n)_{j,j'} - \frac{1}{\omega+\Omega-\lambda^*_{q_2}} \left(\eta_n Q^\dagger_{q_2}\right)_{j,j'} \right]\\
&\quad = \pm \sum_{q_1,q_2} \sum_{n\in\underline{N_{\mathrm{res}}}} (Q_{q_1}\otimes Q_{q_2}\eta_n)_{i,i',j,j'}\, f_1(\pm\lambda_{q_1}, \lambda_{q_2}-\Omega, \mu_n)\\
&\qquad\qquad - \left(Q_{q_1}\otimes \eta_n Q^\dagger_{q_2}\right)_{i,i',j,j'} f_1(\pm\lambda_{q_1}, \lambda^*_{q_2}-\Omega, \mu_n)
\end{aligned}$$

where we used

$$\begin{aligned}
f_0(a,b) &= \int d\omega \frac{1}{\omega-a}\frac{1}{\omega-b}\\
f_1(a,b,\mu) &= \int d\omega \frac{1}{\omega-a}\frac{1}{\omega-b}\mathrm{sgn}(\omega-\mu) \qquad (7.3.19)\\
f_2(a,b,\mu,\mu') &= \int d\omega \frac{1}{\omega-a}\frac{1}{\omega-b}\mathrm{sgn}(\omega-\mu)\mathrm{sgn}(\omega-\mu').
\end{aligned}$$

With these, all required frequency integrals can be computed separately from the fermionic indices. A detailed account how to express all other cases in terms of $f_{1,2,3}$ as well as analytic expressions for these integrals can be found in Appendix A.

The complexity of evaluating the two-particle vertices using these formulas are drastically different and in some cases favorable

$$\underbrace{\mathcal{O}\left(N^2 N_\Omega\right)}_{\#\text{components}} \qquad \underbrace{\mathcal{O}\left(N^2\right)}_{\text{internal summation}} \quad . \qquad (7.3.20)$$

The main advantage is the reduction from $\mathcal{O}\left(N_\Omega^2\right)$ to $\mathcal{O}\left(N_\Omega\right)$ by avoiding the numerical calculation of the integrals; this is achieved at the cost of an additional internal summation over $N$ entries. Note that to obtain this complexity class, it is essential to compute and store all $Q_q, \eta_k, Q_q\eta_k, \eta_k Q_q$ *beforehand*. Furthermore, for an efficient algorithm it is important to note that the arguments of $f_{1,2,3}$ are independent of the indices $i, i', j, j'$ in Equation 7.3.18. As the evaluation of the functions $f_{1,2,3}$ is much more time-consuming than accessing the elements of the $\eta$ and $Q$ matrices, it is important for an efficient implementation to only evaluate $f$ once and than iterate over the necessary values of $i, i', j, j'$.

### 7.3.4 *Size of the effective two-particle vertex*

For a local interaction, the two-particle vertex functions in the channel decomposition are sparse, as noted in Equation 7.3.8. If

$$\left\{ n_\sigma^i \middle| \sigma \in \underline{CN} \right\} \text{ where } i \in \underline{N}, \tag{7.3.21}$$

enumerates the sites that a given site $i$ interacts with and CN denotes the maximal number of such sites for any $i$, the vertex functions can be expressed as

$$\gamma^{p}_{1'|1}{}^{\sigma_{1'}|\sigma_1} := \gamma^{p}_{1',\, n^{1'}_{\sigma_{1'}}|1,\, n^{1}_{\sigma_1}} \tag{7.3.22}$$

and analogously for $\gamma^{x,d}$. These can efficiently be stored in 1D-arrays of size

$$\gamma^p : \qquad 16 \cdot N^2 \; CN^2 \tag{7.3.23}$$

$$\gamma^x : \qquad 16 \cdot N^2 (CN+1)^2 \tag{7.3.24}$$

$$\gamma^d : \qquad 16 \cdot N^2 (CN+1)^2 \tag{7.3.25}$$

which amounts to $\mathcal{O}(10\text{MB})$ of memory per frequency for a $\mathcal{O}(50)$ site system with a nearest-neighbor interaction in a 1D chain (note that $\gamma^d$ is only needed at $\Delta = 0$).

### 7.3.5 *Frequency integrations*

DISCRETIZATION OF THE SELF-ENERGY After implementing the analytical formulas for the two-particle vertex we are left with the challenge to evaluate the remaining first order flow equations (see Equation 7.3.6). At the beginning of the flow, the single-scale propagator as well as the two-particle vertex decay on a scale given by the coupling to the auxiliary reservoir. Hence it is necessary, to evaluate them for large frequencies. On the other hand, at the end of the flow, the physical bandwidth limits the support of the integrations and thus the Green's function is only needed for frequencies on the scale of the bandwidth. To avoid having to adapt the grid during the solution of the flow equations, we note that $\Sigma_{1'|1}(\omega) - \Sigma_{1'|1}(\omega') \in \mathcal{O}\left(U^2\right)$ as the first order self-energy is frequency independent. At large frequencies we can, therefore, always approximate the self-energy with the value at the largest frequency in our grid and only acquire errors in $\mathcal{O}\left(U^3\right)$ when evaluating the flow-equations.[2]

We explicitly tested convergence with respect to the spacing in the frequency grid as well as the maximal frequencies. In Chapter 8, we

2 Note that to evaluate observables in the physical limit, i.e. the end of the flow, the self-energy is required on all frequencies within the support of the Green's functions. For that reason, the grid has to be chosen wide in comparison to the bandwidth of the physical system.

will discuss an entirely different approach to deal with this problem with it's own advantages and disadvantages.

INDEFINITE INTEGRALS Following this strategy, we chose a fixed grid of frequencies on which to evaluate the self-energy. Outside this grid, the self-energy is approximated to be constant. This approximation allows us to numerically evaluate all the integrals. Infinite integrals are evaluated using

$$\int_{-\infty}^{\infty} d\omega f(\omega) = \int_{-A}^{A} d\omega f(\omega) + \int_{-\frac{1}{A}}^{\frac{1}{A}} \frac{d\eta}{\eta^2} f\left(\frac{1}{\eta}\right), \qquad (7.3.26)$$

where the substitution $\eta = \frac{1}{\omega}$ was employed. To solve these integrals, we employ the `runge_kutta_cash_karp54` implementation provided by `boost`[Boo15]. Integrals, that contain a Keldysh Green's function will also display discontinuities at every chemical potential of any of the reservoirs. As their position is known, it is most efficient to decompose all integrals such that none of them contain a discontinuity.

LOOKUP TABLES FOR VERTEX FUNCTIONS The flow equations for the self-energy, just like those for the two-particle vertex functions, involve convolutions (compare Equation 7.3.6). To evaluate the flow equations on the entire grid (of $\mathcal{O}(N_\Omega)$ frequencies) requires evaluating the integrand $\mathcal{O}\left(N_\Omega^2\right)$ times in total. As the evaluation of the vertex functions is numerically expensive (see Section 7.3.3), it is favorable to compute a lookup table of the vertex function beforehand. To this end, we (ab)use an integration routine to sample the vertex function,[3] where we made sure that the grid produced is fine enough to not influence the results. We then proceed to approximate the vertex function at intermediate points using a spline interpolation.[4] An alternative way of efficiently obtaining the convolutions needed in the flow equations will be discussed in Chapter 8.

Note that the number of points needed to approximate the vertex functions does not necessarily (and specifically in the system we intend to apply the algorithm to) scale with the system size. For a long chain coupled to leads with a constant coupling strength the (bare) Green's functions obtain $\mathcal{O}(N)$ peaks of width $\mathcal{O}(\Gamma/N)$. Hence it requires $\mathcal{O}(N)$ points to approximate or integrate the Green's functions. The vertex functions, however, feature $\mathcal{O}\left(N^2\right)$ peaks of comparable width, making it smooth for $N \to \infty$. This is explicitly shown in Figure 7.1.

3 To this end, we integrate $\int_{-\infty}^{\infty} d\omega \frac{\gamma(\omega}{1+|\omega|}$ using Equation 7.3.26 and the `boost` implementation [Boo15] of the `runge_kutta_cash_karp54` integrator with $\epsilon_{abs} = 10^{-6}$ and $\epsilon_{rel} = 10^{-5}$.

4 We use the cubic spline implementation provided by the GSL (`gsl_interp_cspline`)[Gal09].

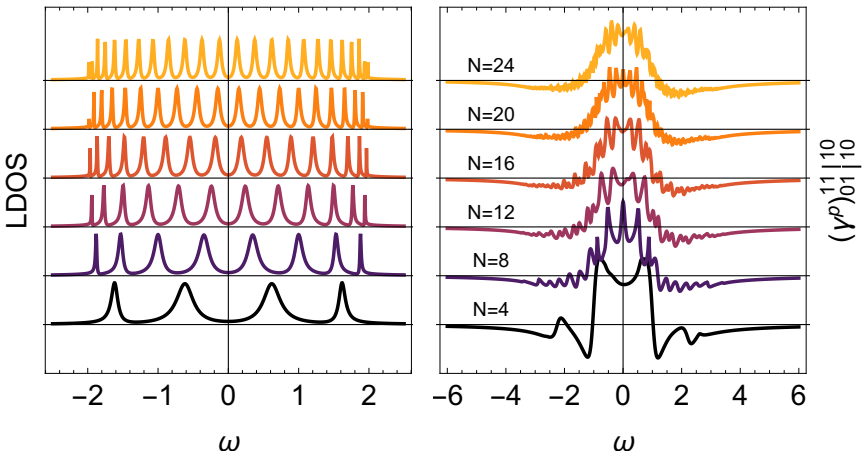


Figure 7.1: *Left panel*: The local density of states of a non-interacting chain of length (bottom to top) $N = 4, 8, \ldots, 24$ with to two reservoirs coupled to the ends of the chain with $\Gamma = 0.2$ (compare Section 7.5). It shows N peaks of width $\sim \Gamma/N$. Neither a uniform, nor a pointwise convergence is found for $N \to \infty$. *Right panel*: The $(\gamma^p)^{22|21}_{12|21}(\omega)$ component of the perturbative two-particle vertex. In contrast to the LDOS, it features $\mathcal{O}(N^2)$ peaks, leading to a convergence to a smooth function.

### 7.3.6 *Parallelization*

There are two reasons, why we might want to parallelize this algorithm. First, the computational effort required to obtain numerical results for large systems ($\mathcal{O}(50)$) sites is significant and wall-time performance can be enhanced greatly using parallelization. The second reason is, that the tabulated version of the vertex function for large systems takes up large amounts of memory. Therefore, in practice, a single machine is unable to store the representation of all components of the vertex functions at the same time in memory. We thus aim to distribute this task over many machines. When distributing the workload, it is essential to minimize the necessary communication between the machines as the bandwidth between them is limited.

To this end, we chose two numbers $p_1, p_2$ that divide N. The number of machines used is then $p_1 \cdot p_2$. Machine $(i, j) \in \{0, \ldots, p_1 - 1\} \times \{0, \ldots, p_2 - 1\}$ is then tasked to calculate all $\Sigma_{k+1,l+1}$ for[5]

$$i\frac{N}{p_1} \leqslant k < (i+1)\frac{N}{p_1}, \qquad j\frac{N}{p_2} \leqslant l < (j+1)\frac{N}{p_2}. \tag{7.3.27}$$

It needs access to all vertex functions $\gamma^{p,x,d}_{1'2'|12}$ with the indices $1', 1$ restricted to the same region. For $\gamma^{p,x}$, this already restricts $2', 2$ while (the computationally cheaper) $\gamma^d$ is required for $\mathcal{O}(N)$ values of $2', 2$

5 Note that for convenience, we number the machines starting a 0 while the self-energy indices start at 1.

on every machine. To obtain these elements of the two-particle vertex, on each machine needs to evaluate the analytical expressions for the two-Green's-function integrals only a small number of times.

As an example, consider a 1D chain with nearest neighbor interaction and even number $N \in 2\mathbb{Z}$ of sites. We discuss $2 \times 2$ machines attempting to calculate $\partial_\Lambda \Sigma^p$. The $(0,0)$ machine has to obtain (compare Equations 7.3.6 and 7.3.7)

$$\gamma^p_{1'2'|12} \text{ for } i_{1'}, i_1 \in \underline{\frac{N}{2}},\ i_{2'}, i_2 \in \underline{\frac{N}{2}+1} \tag{7.3.28}$$

and thus requires the almost all two-Green's-function integrals with (compare Equation 7.3.9, in our implementation we only compute the necessary elements)

$$\begin{aligned} &\int d\omega g_{3|3'}\left(\frac{\Pi}{2}-\omega\right) g_{4|4'}\left(\frac{\Pi}{2}+\omega\right) \\ &\text{with } i_{3'}, i_3, i_{4'}, i_4 \in \underline{\frac{N}{2}+1},\ |i_3 - i_4| = 1 \wedge |i_{3'} - i_{4'}| = 1. \end{aligned} \tag{7.3.29}$$

This exemplifies that in the case of a 1D chain and nearest-neighbor interaction, we achieve a speedup of approximately

$$\frac{p_1 p_2}{\left(1+2\frac{p_1}{N}\right)\left(1+2\frac{p_2}{N}\right)}. \tag{7.3.30}$$

After each machine obtained its portion of the rhs of the flow equations, all contributions are sent to machine $(0,0)$, which then in turn sends back the full rhs to all other machines. Note that the amount of data sent is significantly smaller than the space needed to store $\gamma$, as there are less components and the frequency-grid will generally be more coarse than the one needed to store the representations of the (perturbative) two-particle vertex. A visualization of the parallelized version of the algorithm discussed here is shown in Figure 7.2.

### 7.3.7 *Perturbation theory*

To obtain perturbation theory results to compare to, we have to remove all higher order terms generated by the flow of the self-energy. How to do this was discussed in Section 4.5. As the integrals for the solution of the flow of the self-energy become sharply peaked, we implemented the analytic expressions for the three-Green's-function integrals. How to obtain these is sketched in Appendix B.

## 7.4 COMPARISON WITH SIAM

The single impurity Anderson model describes a single magnetic impurity on a metallic reservoir [And61], as can be obtained in mesoscopic systems. At low temperatures it shows strongly correlated

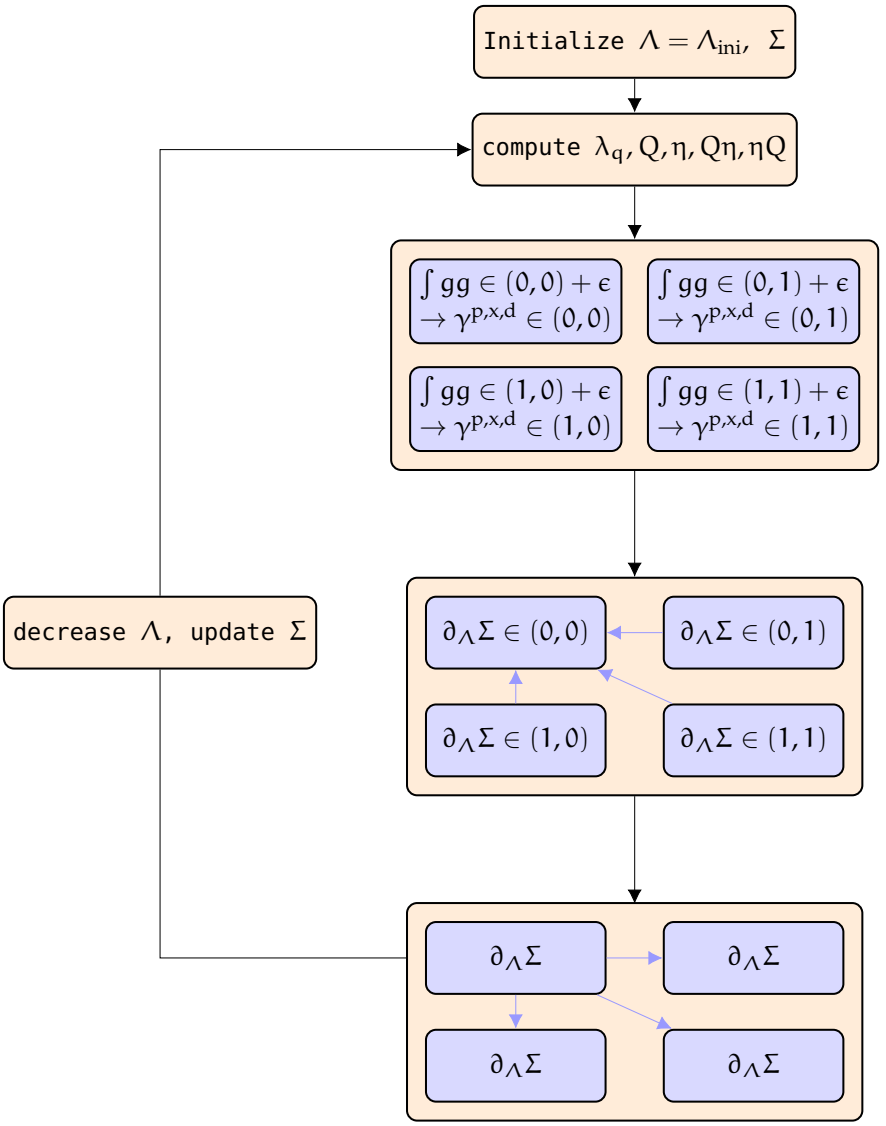


Figure 7.2: Diagram representing the algorithm used. Orange blocks represent computation done on all machines while the blue blocks show where individual machines perform separate operations. The black arrows represent the program flow, the blue arrows symbolize data transfer. Each machine is tasked to compute a block $(i, j)$ of the self-energy (compare Section 7.3.6). This requires the evaluation of the corresponding elements of the two-particle vertex function and therefore the analytic expression for the two-Green's-function integrals (indicated by $\int gg$). The indices required by each machine relate to the block of the self-energy that is to be obtained (compare Equations 7.3.28 and 7.3.29). $(i, j) + \epsilon$ indicates, that the indices extend beyond the block and thus some are computed on more than one machine (reducing efficiency). While the lookup tables for $\gamma$ are large, they are not sent between machines; only the (significantly smaller) self-energy is transferred. All machines need knowledge of the self-energy to compute the single-scale propagators in the next iteration. The loop in this diagram is stopped, when $\Lambda = 0$.


Figure 7.3: Pictorial representation of the single-impurity Anderson model in a fermionic representation. It features two interacting, but otherwise decoupled sites, each of which is connected to a fermionic reservoir.

Kondo physics [SW66] that has been studied extensively in the literature. For simplicity, we only consider the case of vanishing magnetic field.

In the language of spinless fermions it can be understood as a specific example of the models discussed in this chapter: the system is described by two interacting sites

$$H_{\text{sys}} = U\left(c_1^\dagger c_1 - \frac{1}{2}\right)\left(c_2^\dagger c_2 - \frac{1}{2}\right),$$

each coupled to structureless reservoirs with strength $\Gamma$. Figure 7.3 shows a graphical representation of this Hamiltonian. The second order perturbation theory self-energy is given by [HHZ84]

$$\Sigma(\Omega) = U^2 \int d\omega_1 d\omega_2 d\omega_3 \rho(\omega_1)\rho(\omega_2)\rho(\omega_3) \frac{1}{\Omega - \omega_1 - \omega_2 + \omega_3} \\ [f(\omega_1)f(\omega_2)f(-\omega_3) + f(-\omega_1)f(-\omega_2)f(\omega_3)] \quad (7.4.1)$$

where

$$\rho(\omega) = \frac{1}{\pi}\,\mathrm{Im}\left(\frac{1}{\omega - i\Gamma}\right), \qquad f(\omega) = \theta(-\omega).$$

This can directly be compared with the fRG results found with the algorithm described in Section 7.3. As fRG contains higher order contributions the resulting self-energy is only expected to agree in leading order (i.e. $U^2$). The comparison obtained is shown in Figure 7.4.

In this model, perturbation theory results can be retrieved by removing the self-energy feedback.[6] Without this feedback, agreement between perturbation theory and our implementation is confirmed explicitly (see right panel of Figure 7.4).

## 7.5 APPLICATION TO 1D CHAINS

While the Tomonaga-Luttinger model is motivated as providing the correct close-to-equilibrium phenomenology of a 1D metal, it also

6 In this model, $G^K(t,t)$ vanishes and with it the first order corrections as well as the contributions from the $\gamma^d$-channel (compare Section 4.5). Hence perturbation theory results can be retrieved by removing the self-energy feedback into the flow equations. The vertex is not fed back at this point, anyways.

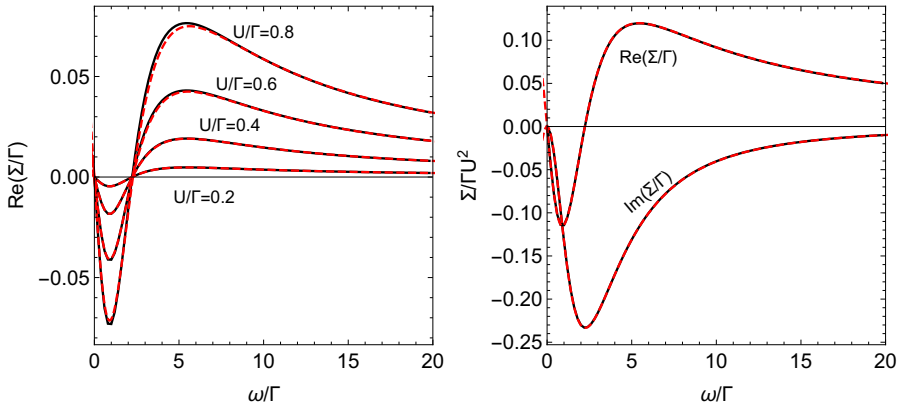


Figure 7.4: *Left panel*: Real part of the frequency dependent self-energy in the SIAM without magnetic field as computed by second-order perturbation theory (solid black line) and the fRG algorithm discussed in Sec Section 7.3 (dashed red line). *Right panel*: When removing the self-energy feedback, the fRG algorithm reproduces the perturbation theory result. This is a non-trivial check of the algorithms used to compute $\Sigma^{p,x}(\omega)$.

predicts power-law scaling for out-of-equilibrium observables. Taking into account non-linear contributions due to the band-curvature (i.e. non-linear Luttinger liquids) leads to some qualitative changes while some features may survive beyond equilibrium[IG09; ISG12]. To investigate the non-equilibrium behavior in a microscopic model, however, is numerically difficult. Therefore, it is generally hard to asses which, if any, of the non-equilibrium properties of the Tomonaga-Luttinger model persist in a model with finite band-curvature.

### 7.5.1 *Studied system*

Let us consider a one-dimensional chain of sites attached to leads only at the two ends. For the time being, we will restrict ourselves to the simplest case described by the Hamiltonian:

$$\begin{aligned} H^{sys} &= H^{tb} + H^{int} \\ H^{tb} &= \sum_{n=1}^{N} t c_n^\dagger c_{n+1} + \text{h.c.} \\ H^{inter} &= U \sum_{n=1}^{N-1} \left( c_n^\dagger c_n - \frac{1}{2} \right) \left( c_{n+1}^\dagger c_{n+1} - \frac{1}{2} \right) \end{aligned}$$

where $N$ denotes the number of sites in the interacting chain, $U$ denotes the strength of the nearest neighbor interaction. Two wide-band reservoirs (called *left* and *right*) are coupled to the ends of the chain (compare Sections 2.5.4 and 2.8)

$$\Gamma_L = \Gamma e_1 e_1^T, \qquad \Gamma_R = \Gamma e_N e_N^T \tag{7.5.1}$$

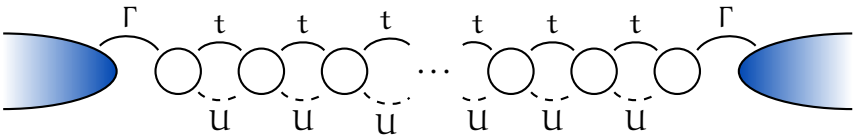


Figure 7.5: Pictorial representation of the system considered in Section 7.5. The dashed lines represent a nearest-neighbor interaction, the solid lines indicate quadratic couplings; the couplings labeled $t$ represent a nearest neighbor hopping, those labeled $\Gamma$ indicate a hybridization with wide-band reservoirs (compare Section 2.5.4).

and initially prepared in thermal equilibrium characterized by temperatures $T_\alpha = 0$ and chemical potentials $\mu_\alpha$, $\alpha = L,R$. Throughout, we use the hopping amplitude as the unit of energy and therefore set $t = 1$. A pictorial representation of the system described above can be found in Figure 7.5.

### 7.5.2 *Previous work and first order physics*

This model was already studied in [JMS07] and more extensively in [Jak09]. As the approach used was guided by this previous work it is instructive to include the central ideas brought forward by [JMS07]. Furthermore these known results can be understood in the light of Chapter 6, adding a new perspective.

#### 7.5.2.1 *Cutoff used*

In [JMS07], a first order fRG approach was used based on flow-parameter dependent distribution functions in the reservoirs, similar to what we discussed in Section 6.2.2. The distribution function at temperature $T$ is given by

$$\begin{aligned} 1 - 2n(\Omega) &= -2T \sum_{\omega_m} \frac{e^{i\omega_m 0^+}}{i\omega_m - \Omega + \mu} \overset{T\to 0}{\to} \frac{-1}{\pi} \int d\omega \frac{e^{i\omega 0^+}}{i\omega - \Omega + \mu} \\ &= \tanh\left[(\Omega - \mu)/2T\right] \qquad \overset{T\to 0}{\to} \operatorname{sgn}(\Omega - \mu) \end{aligned} \tag{7.5.2}$$

This is smoothed out by limiting the contributing Matsubara frequencies:

$$\begin{aligned} 1 - 2n^\Lambda(\Omega) &:= -2T \sum_{\omega_m} \theta(|\omega_m| - \Lambda) \frac{e^{i\omega_m 0^+}}{i\omega_m - \Omega + \mu} \\ &\overset{T\to 0}{\to} \frac{-1}{\pi} \int_{\mathbb{R}\setminus[-\Lambda,\Lambda]} d\omega \frac{e^{i\omega 0^+}}{i\omega - \Omega + \mu}. \\ &= \operatorname{arccot}\left[(\Omega - \mu)/\Lambda\right] \end{aligned} \tag{7.5.3}$$

When computing the resulting single-scale propagator we will also require

$$\Rightarrow \partial_\Lambda n^\Lambda(\Omega) \quad = \quad -T\sum_{\omega_m} \delta(\Lambda - |\omega_m|)\frac{1}{i\omega_m - \Omega + \mu} \tag{7.5.4}$$

$$\text{“}\overset{T\to 0}{\to}\text{”} -\frac{1}{2\pi}\sum_{\pm}\frac{1}{\pm i\Lambda - \Omega + \mu}, \tag{7.5.5}$$

where the $T \to 0$ limit, while mathematically ambiguous, is to be understood in the context of Equation 7.5.3.

In the case of two reservoirs at zero temperature this results in a simple pole-structure of $\partial_\Lambda n^\Lambda$. The single scale propagators using this cutoff are easily determined to be[7]

$$\begin{aligned} S^{\text{ret}}(\omega) &= 0 \\ S^{K}(\omega) &= -2i\sum_r (-2\partial_\Lambda n_r^\Lambda(\omega)) G^{\text{ret}}(\omega)\Gamma^r(\omega)G^{\text{adv}}(\omega). \end{aligned}$$

### 7.5.2.2 *Weak coupling limit*

In the weak coupling limit we use Equation 7.3.16 and find

$$\| -2i\Gamma_k + h^\dagger - h\| \to 0 \qquad \text{for } \Gamma \to 0, \tag{7.5.6}$$

hence $\eta_k \sim \mathbb{1} + \mathcal{O}(\Gamma)$; the distribution operator $N(\omega)$ becomes diagonal and thus commutes with $G^{\text{ret}}$.

$$\begin{aligned} G^K(\omega) &= \left[1 - \sum_r n_r(\omega)\right]\left[G^{\text{ret}}(\omega) - G^{\text{adv}}(\omega)\right] + \mathcal{O}(\Gamma) \\ S^K(\omega) &= \left[-\sum_r \partial_\Lambda n_r^\Lambda(\omega)\right]\left[G^{\text{ret}}(\omega) - G^{\text{adv}}(\omega)\right] + \mathcal{O}(\Gamma). \end{aligned} \tag{7.5.7}$$

Therefore, to leading order in the coupling, the system behaves exactly like a system, where both reservoirs attached are governed by the distribution function $1 - \sum n_r(\omega)$. Similar states were already discussed in Chapter 6 and while not being thermal could still be considered to be in equilibrium; this state does not carry a current.

Taking advantage of the structure of this setup and the corresponding steady state the first order flow equation can be simplified, removing the need to compute any integrals. In the end, one obtains a superposition of equilibrium flow equations at multiple chemical potentials. The resulting flow equations are very similar to those obtained in Section 6.5, with the only difference being (a) the steps in the distribution function being smaller and (b) the presence of the physical reservoir at the end, giving a constant contribution to the retarded self-energy.

7 Note that the cutoff preserves causality. We thus restrict our discussion to the Keldysh basis.

#### 7.5.2.3 *First-order results and open questions*

Using this approach, [JMS07] finds Luttinger liquid like behavior in observables like the local density of states or the conductance. The exponents of the power law behavior is found to be dependent on the ratio of the coupling strengths to the reservoirs.[8]

However, as we already argued above, this approach is perturbative in the coupling and is based on the (effective) absence of currents. In addition to these essential non-equilibrium features, it also entirely lacks inelastic terms to study the influence of scattering on the results.

### 7.5.3 *Results in equilibrium*

We will now employ our approach, that goes beyond the weak coupling limit and includes inelastic scattering, to investigate this problem. The equilibrium situation, where both reservoirs are prepared in the $\mu_{L/R} = 0$ ground-state, provides a natural starting point to evaluate our specific implementation as well as the performance of the algorithm as a whole. In contrast to the non-equilibrium scenario, the phenomenology in equilibrium is well understood.

FLUCTUATION DISSIPATION THEOREM When no bias voltage is applied, the steady state of the system is fully thermal and expected to fulfill the fluctuation-dissipation theorem. To verify this, we analyzed this case without explicit use of known equilibrium features of the system. For this reason, and as in equilibrium scattering is suppressed, this case is numerically more challenging for the algorithm presented and we are restricted to relatively small system sizes.

As we have discussed in Section 4.3.1, a $T = 0$ reservoir cutoff preserves the fluctuation-dissipation theorem. With a $T = \infty$ cutoff, the FDT only holds without truncation. To investigate the severity of this cutoff (or truncation) dependence, we simulate small systems using both of these cutoffs. To that end, Figure 7.6 shows the $(1, 1)$-component of the effective distribution function. As expected, up to numerical errors the $T = 0$ cutoff reproduces the correct distribution while the $T = \infty$ cutoff induces artificial heating, even at the end of the flow.

The dependence of the heating on the coupling to the physical reservoirs is analyzed in Figure 7.7. A strong coupling to the cold reservoirs keeps the contacts between the system and the reservoir cold. With diminishing coupling an infinite temperature reservoir cutoff artificially heats the system. Furthermore, when spatially resolving the size of the step at the chemical potential, we find that the cooling effect of the physical reservoir is local (compare right panel of Figure 7.7), leading to deteriorating results for larger systems.

8 In our simplified presentation both couplings are identical.

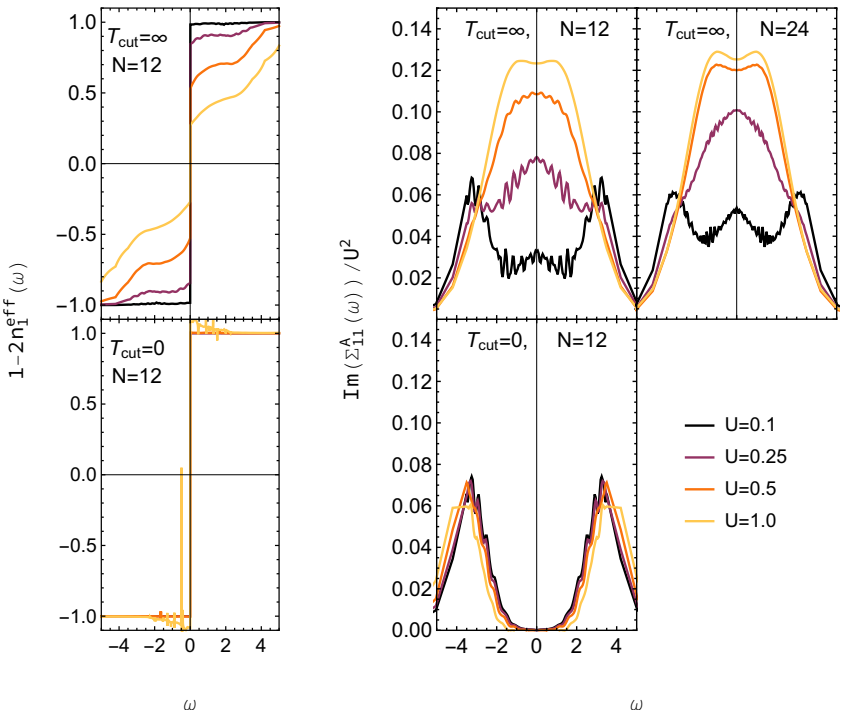


Figure 7.6: Equilibrium simulation of a finite chains coupled to two reservoirs at the ends with $\Gamma = 0.1$ (in units of the hopping) with varying two-particle interaction. *Left panel*: $1 - 2n^{\mathrm{eff}}(\omega)$ (compare Section 2.6) for a system with $N = 12$ sites. Due to the fluctuation-dissipation theorem, the exact dependence $1 - 2n^{\mathrm{eff}}(\omega) = \mathrm{sgn}(\omega)$ is known. The upper panel shows an infinite temperature cutoff while the lower panel shows the results for a zero-temperature reservoir cutoff. As discussed in Section 4.3.1, the zero-temperature reservoirs cutoff is expected to reproduce the correct distribution function where the infinite might (and is found to) fail at this. *Right panel*: $\mathrm{Im}(\Sigma^{\mathrm{adv}}_{1,1}(\omega))$ as a measure of the inelastic processes at a given energy $\omega$. The upper panel is obtained using a $T = \infty$ reservoir cutoff, while the lower panels show a $T = 0$ reservoir cutoff. The left panels show results for a chain of length $N = 12$ and the top-right panel shows results for a $N = 24$-site chain. In equilibrium, scattering at the Fermi surface is suppressed [Gia03; Sam98]; while the $T = 0$ cutoff reproduces this correctly, the infinite temperature cutoff introduces unphysical scattering.

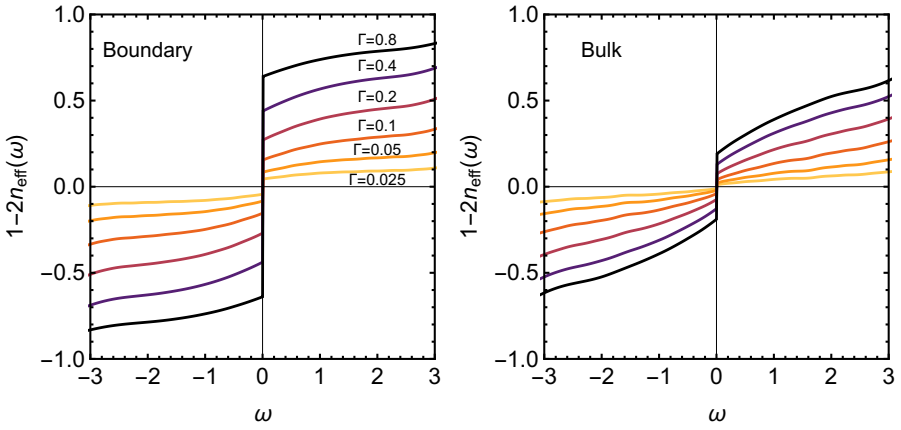


Figure 7.7: Analysis of the dependence of the effective distribution (compare Section 2.6) function on the coupling to the physical reservoirs using a $T = \infty$ reservoir cutoff scheme. The interaction is set to $U = 1$ and the system consists of $N = 12$ sites. As the physical reservoirs are at $T = 0$, the exact result is $1 - 2n_{\text{eff}}(\omega) = \text{sgn}(\omega)$. We observe, that the physical reservoirs efficiently cool the system to $T = 0$ temperature only at strong coupling and close to the boundary. In the middle of the chain, the cutoff scheme yields artificial heating in form of a decreased discontinuity at the Fermi surface. Note that the distribution obtained is not thermal.

SCATTERING INDUCED BY HOT RESERVOIRS This can be associated with additional inelastic processes at the Fermi-edge: Using the $T = 0$ cutoff no scattering at the Fermi surface is generated [Gia03; Sam98]. In our approach, this is indicated by $\text{Im}(\Sigma^{A}_{1,1}) = 0$. In contrast, the $T = \infty$ cutoff artificially enhances such processes. This is shown in the right panel of Figure 7.6. This problem exacerbates for larger system as the physical coupling per degree of freedom in the chain decreases.

DENSITY OF STATES As both, the effective distribution functions as well as $\text{Im}(\Sigma^{\text{adv}})$, are rather unphysical, let us also inspect the local density of states (Figure 7.8). While we cannot reproduce Luttinger liquid physics for a $N = 12$ site system, we can clearly see that the $T = \infty$ cutoff already for such a small system yields a smooth DOS, both at the end as well as in the bulk of the chain. This indicates correlation lengths (even at the Fermi-surface) that are comparable to (or smaller than) the system size. Using the $T = 0$ cutoff the DOS remains sharply peaked.

### 7.5.4 *Results at finite bias*

Now, we apply finite a bias voltage $V = \mu_L - \mu_R = 2$ while keeping the system half filled. This drives the system out of equilibrium; as we

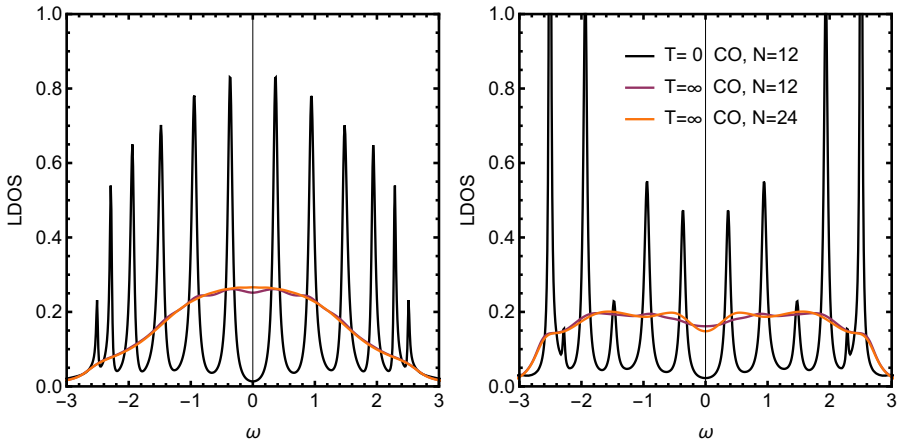


Figure 7.8: The local density of states on the first (left panel) and middle (right panel) site of a $N = 12$ site system coupled to $T = 0$ reservoirs with $\Gamma = 0.1$ at $U = 1$ in equilibrium. The black line shows the results of a $T = 0$ cutoff, the others depict results for a $T = \infty$ reservoir cutoff. In a Luttinger liquid, the local density of states is expected to vanish at the Fermi surface. In contrast, we find that the $T = \infty$ cutoff introduces inelastic scattering (compare Figure 7.6) resulting in a correlation length comparable to the system size and thus in a smooth LDOS. We can not expect larger system sizes to improve this result.

will see, the state obtained is drastically different from equilibrium as well as the states discussed in Section 7.5.2 and [JMS07]. The induced inelastic scattering allows us to access chains of up to $N = 60$ sites. Out of equilibrium, it is however a priori not clear how to choose the statistics in the auxiliary reservoirs.

CUTOFF DEPENDENCE OF PHYSICAL OBSERVABLES We employ perturbation theory as well as three different fRG cutoff schemes and obtain the effective distribution function, local density of states, local occupation and current within our system with $N = 24$ sites (see Figure 7.9). We find that all observables show a strong cutoff dependence: All methods show strong deviations from the distribution function obtained in a first-order treatment (compare Equation 7.5.7) but the quantitative changes differ between cutoffs. The local density of states on the first site is especially interesting for $T = 0$, $\mu = 0$ as it appears to show a cusp at $\omega = 0$, indicating unphysical Luttinger-liquid properties induced by the cutoff. Most strikingly, the local occupations in the $T = \infty$ cutoff show a gradient with only minor corrections due to Friedel oscillations while in the other schemes Friedel oscillations dominate. As expected, the current in perturbation theory is conserved while the fRG schemes violate particle-number conservation; especially the $T = \infty$ cutoff indicates a strong suppression of the current in the middle of the chain.

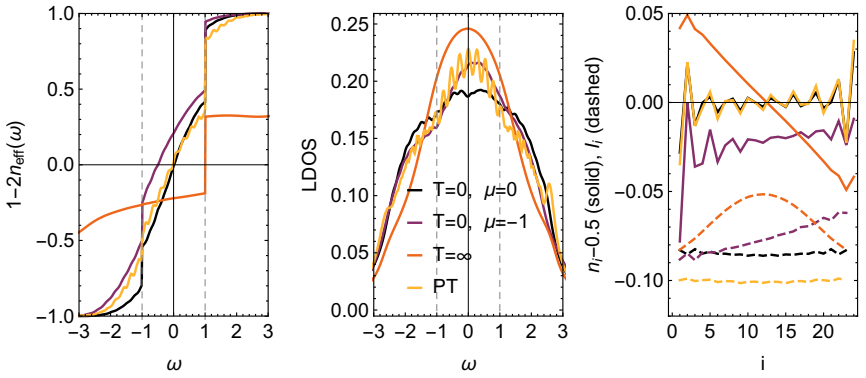


Figure 7.9: Comparison of different cutoff schemes of a $N = 24$ site chain with leads attached to the end with hybridization $\Gamma = 0.2$ held at $T = 0$ with $\mu_{L,R} = \pm 1$. This drives the system out of equilibrium and a steady-state current flows from left to right. *Left panel*: 1, 1-entry of the effective distribution function (compare Section 2.6). For small couplings and interactions, this function is expected to be piecewise constant with two steps of height 1/2 at the reservoirs chemical potential. *Center panel*: local density of states on the left-most side with an artificial broadening $\Gamma_{\text{smear}} = 0.2$ to obtain smooth curves. *Right panel*: The occupation of the individual sites (solid) and the current through each link (dashed).

INELASTIC SCATTERING AND SCALING It is, as it was in equilibrium, insightful to analyze the imaginary part of the diagonal of the retarded self-energy (See Figure 7.10). Comparing a $T = 0$, $T = \infty$ cutoff and perturbation theory, we find, that the $T = 0$ cutoff consistently under- and the $T = \infty$ consistently overestimates the amount of inelastic processes compared to perturbation theory. As perturbation theory is in no way inherently better than fRG, this is not necessarily problematic. However, we also observe, that the difference between perturbation theory and the fRG schemes systematically increases when increasing the system size. Hence, even for small interactions, a large system will display physics that strongly depends on the cutoff used. In that sense, the system does not behave perturbatively. Note that this strong cutoff dependence not only occurs in the bulk, far from the cold physical reservoirs but also right at the boundary of the interacting system.

## 7.6 CONCLUSION

We have shown that it is possible to set up a numerically feasible fRG formulation describing the steady state of extended, fermionic systems out of equilibrium. To that end, we argued that a reservoir cutoff scheme is physical, easy to implement, numerically efficient and has proven to provide good results in other physical systems. The cutoff scheme presented encompasses a whole class of cutoffs, as

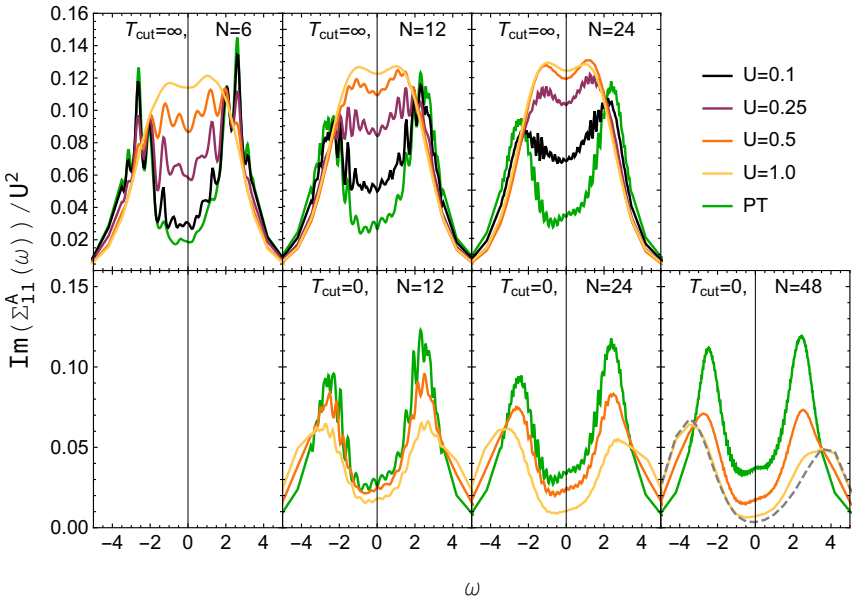


Figure 7.10: $\mathrm{Im}(\Sigma^{adv}_{1,1}(\omega))/U^2$ of a chain coupled to wide band reservoirs at the ends ($\Gamma = 0.1$) using a reservoir cutoff with auxiliary temperature $T = 0$ ($T = \infty$) in the top (bottom) panels. The imaginary part of the self-energy is used as a measure of inelastic processes in the system. The system-sizes from left to right are $N = 6, 12, 24, 48$. The green line shows the perturbation theory result. The other colors show fRG results using the same colors as in Figure 7.6 to encode $U = 0.1, 0.25, 0.5, 1$. With increasing system size the dependence of the results on the cutoff becomes more pronounced. The dashed gray line shows the results for a calculation with $N = 60$ sites at $U = 1$ performed on 100 machines.

the statistics of the auxiliary reservoirs can be varied. It is rare that in a RG procedure cutoff independence can be explicitly analyzed or demonstrated.

On the example of a one-dimensional tight-binding model with nearest neighbor interaction weakly coupled to reservoirs, we demonstrate that system-sizes of $\mathcal{O}(60)$ sites are accessible with this method. However, analyzing the results of this chapter, we conclude that adding decay channels for the fermions into the reservoirs and introducing decoherence during the flow is detrimental in the case of long, closed chains. We find a strong dependence of physical observables on the cutoff used and can associate this dependence with scattering introduced throughout the chain. Analyzing the inelastic processes, we argued that this effect is not perturbative and will strongly impact observables in long chains, even at low interaction. For this reason, the method discussed is not suitable to treat long chains that are only weakly coupled to reservoirs at the ends. A different cutoff or a more

thorough treatment of the higher order vertices might yield better results in the future.

For systems where inelastic processes limit the coherence length the method presented is, however, still expected to provide insights on how small interaction modifies the behavior through heating.

# 8

# SYSTEMS IN AN ELECTRIC FIELD

## 8.1 INTRODUCTION

In the previous chapter, we have discussed how to set up an fRG scheme for large but finite fermionic systems in one dimension. This method is well suited to investigate boundary effects and more generally spatially non-uniform problems. To access bulk properties of a system this way, however, is computationally costly. Furthermore, we found that using a reservoir cutoff scheme on a closed or almost closed, coherent system is questionable.

For these reasons, we now shift our interest to infinite, translationally invariant systems coupled to an environment like a substrate that allows for particle exchange. To drive the system out of equilibrium, we consider a longitudinal electric field applied to the one-dimensional chain and reservoirs. The reservoirs are considered to be initially prepared in equilibrium with respect to their local chemical potential and induce a current in the system. Systems like these are experimentally relevant but pose a great challenge to most current theoretical methods. Numerically exact methods like DMRG or exact diagonalization are in practice incapable to access the stationary state of these systems. Therefore approximate methods are commonly employed. An approximate method used with growing popularity to tackle the questions that emerge at the interface of open, correlated systems and continuous driving is the dynamical mean-field theory (introduced in [FTZ06]), that assumes all correlations to be purely local and is exact in the limit of infinite coordination number.

Going beyond the assumption of a purely local self-energy, we developed an fRG based method to analyze the stationary state of this class of systems (Section 8.2 to Section 8.4.5) that systematically takes into account finite range correlations and discuss its efficient implementation. We go beyond a perturbative treatment of the two-particle vertex, as we aim to apply this method in the presence of ordering tendencies. At the core of this development is an algorithm to obtain local correlation functions in such correlated, infinite systems, that was inspired by procedures used in DMFT for a local self-energy [Aok+14]. Due to its RG foundation it is ideally suited for low dimensional applications and fRG has previously had great success in investigating phase transitions [Met+12].

We then focus on a simple tight-binding chain with nearest neighbor interaction (see Section 8.5). While only one representative model of the class of models that could be studied with the method pre-

sented here, it is well suited to study emergent phenomena in interacting systems out of equilibrium: Many aspects of this model, including a metal-insulator transition as well as Wannier-Stark localization, are well understood in limiting cases. After discussing the model in these cases, we employ our fRG algorithm to investigate the interplay of the driving, ordering and localization.

While we already present a variety of results, this chapter also reflects ongoing research, including open questions that we wish to answer in future work.

### 8.1.1 *Electric fields in a lattice*

The non-relativistic Hamiltonian for a single, spinless fermion in an electromagnetic field characterized by

$$B = \nabla \times A \qquad E = -\nabla\phi - \frac{\partial A}{\partial t} \tag{8.1.1}$$

is given by

$$H = \frac{1}{2m}\left(p - qA\right)^2 + q\phi. \tag{8.1.2}$$

As we will be interested in the case of a constant electric field in the absence of a magnetic field, there are two natural ways to gauge the potential; either $\phi = 0$, $A = -tE$ or $\phi = xEe_x$, $A = 0$. In a lattice model, the first choice translates to

$$h_A(t) = \begin{pmatrix} \ddots & \ddots & & & \\ \ddots & 0 & t_{hop}e^{-iEat} & & \\ & t_{hop}e^{iEat} & 0 & t_{hop}e^{-iEat} & \\ & & t_{hop}e^{iEat} & 0 & \ddots \\ & & & \ddots & \ddots \end{pmatrix}, \tag{8.1.3}$$

with the lattice spacing $a$. This representation is known as the Peierls substitution [Pei33]. While it does not break spatial translational symmetry, it introduces an artificial time dependence. The choice of $\phi = xEe_x$, $A = 0$ on the other hand yields

$$h_\phi = \begin{pmatrix} \ddots & \ddots & & & \\ \ddots & -Ea & t_{hop} & & \\ & t_{hop} & 0 & t_{hop} & \\ & & t_{hop} & Ea & \ddots \\ & & & \ddots & \ddots \end{pmatrix} \tag{8.1.4}$$

which conserves time-translational invariance while breaking spatial translational invariance. On the level of physical observables,

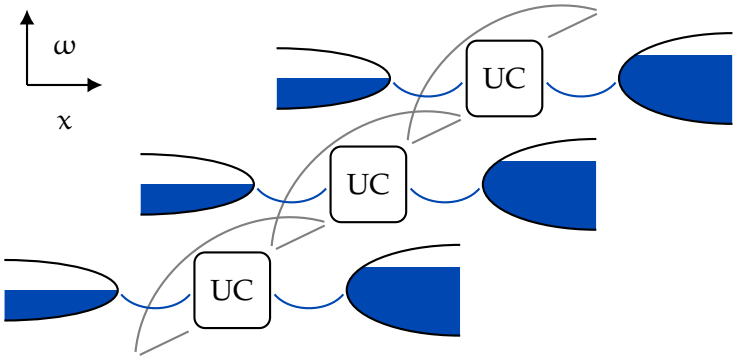


Figure 8.1: Illustration of the class of models discussed. The central property is the translational symmetry associated with a shift in energy. The Hamiltonian in each unit cell, as well as the couplings of each cell to the reservoirs and their respective distribution function are identical up to this shift. Note that we allow for couplings not only between nearest neighbor unit cells; we do however restrict the coupling to a finite range.

both, temporal and spatial translational invariance are recovered. The equivalence of these models is easily seen considering the action

$$S_{k,l} = \Psi_k^\dagger \left(i\partial_t \mathbb{1} - H\right)_{k,l} \Psi_l \tag{8.1.5}$$

under the gauge transformation $\Psi_k = e^{iEakt}\tilde{\Psi}_k$.[1] To describe the steady state, it is more convenient for us to choose a gauge, where $A = 0$ and discuss a time-invariant Hamiltonian.

## 8.2 CLASS OF MODELS DISCUSSED

In this section, we will outline the class of models that can be treated within the method developed. As a starting point, we consider a general fermionic Hamiltonian of a countably infinite system with quadratic terms, a two-particle interaction

$$H_{\text{sys}} = \sum_{i,j\in\mathbb{Z}} h_{i,j} c_i^\dagger c_j + \frac{1}{4} \sum_{n,m,k,l\in\mathbb{Z}} v_{n,m,k,l} c_n^\dagger c_m^\dagger c_l c_k \tag{8.2.1}$$

and coupling to reservoirs characterized by hybridization functions $\Gamma^k(\omega)$, $k \in \mathbb{Z}$ as discussed in Section 2.5.4. The initial state is assumed to be a product state of equilibrium configurations in each of the reservoirs with a quadratic initial state in the system itself.

1 Note that a density-density interaction is invariant under this gauge transformation and thus identical in both gauges.

We restrict ourselves to Hamiltonians, which have a discrete translational shift symmetry (compare Equation 8.1.4). With a given $L \in \mathbb{N}$ defining a unit cell, we demand[2]

$$\begin{aligned} h_{n+L,m+L} &= h_{n,m} + LE \\ \nu_{n+L,m+L,k+L,l+L} &= \nu_{n,m,k,l} \qquad \forall n, m, k, l \in \mathbb{Z}. \end{aligned} \tag{8.2.2}$$

Similarly, we require that the reservoirs are characterized by corresponding hybridization and initial distribution functions

$$\begin{aligned} \Gamma^{k+L}_{n+L,m+L}(\omega) &= \Gamma^{k}_{n,m}(\omega - LE) \\ n^{k+L}(\omega) &= n^{k}(\omega - LE) \qquad \forall n, m \in \mathbb{Z}. \end{aligned} \tag{8.2.3}$$

Furthermore, we assume that all terms in the Hamiltonian are strictly local, i.e. there exists an $M \in \mathbb{N}$ such that

$$\begin{aligned} h_{n,m} &= 0 \ \forall |n-m| \geqslant M \\ \Gamma^{k}_{n,m} &= 0 \ \forall |n-m| \geqslant M \\ \nu_{n,m,k,l} &= 0 \ \forall \mathrm{dist}(n,m,k,l) \geqslant M. \end{aligned} \tag{8.2.4}$$

While this restricts the method presented in this chapter to one-dimensional interacting regions we do not impose any constraints on the size of the unit cell; this would allow us to consider stripes, cylinders or other more complex structures in the future. Note that for a given model the value of $M$ is not unique and it can always be increased. We will later use $M$ to approximate the vertex functions and therefore consider $M$ to be variable.

## 8.3 IMPLIED SYMMETRIES

The symmetry of the Hamiltonian discussed above has direct implications on all Green's and vertex functions. It is obvious from the steady-state form (see Equations 2.5.13 and 2.5.47) that free Green's function obeys the symmetry

$$g_{1|1'}\left(\omega|\omega'\right) = g_{1+L|1'+L}\left(\omega + LE|\omega' + LE\right).$$

Considering any diagram contributing to $n$-particle vertex function one easily verifies, that this, together with Equation 8.2.2 results in

$$\gamma_{1'|1}(\omega_1'|\omega_1) = \gamma_{1'+L|1+L}(\omega_1' + LE|\omega_1 + LE). \tag{8.3.1}$$

For the self-energy and two-particle vertex functions this symmetry reads:

$$\begin{aligned} \Sigma_{1'|1}(\omega) &= \Sigma_{1'+L|1+L}(\omega + LE) \\ \gamma_{1'2'|12}(\Delta, \Pi, X) &= \gamma_{1'+L\ 2'+L|1+L\ 2+L}(\Delta, \Pi + 2LE, X) \end{aligned}$$

2 We incorporate the lattice spacing $a$ into the electric field; hence from here on $E$ denotes the electric field in units of the lattice spacing.

where we used energy conservation to reduce the number of frequencies (compare Section 2.4).

Similarly, this implies

$$G_{1|1'}\left(\omega|\omega'\right) = G_{1+L|1'+L}\left(\omega + LE|\omega' + LE\right) \tag{8.3.2}$$

for the full Green's function.

## 8.4 METHOD

To treat this problem systematically we employ the fRG in a second order truncation, similar to our approach in the previous chapter. As the systems considered here feature physical reservoirs, these present a natural choice of the cutoff parameter; in contrast to the prior chapters the results at any value of the cutoff can be considered physical at that particular coupling.

However, as we want to analyze ordering tendencies, we include the flow of the two-particle vertex. To make the solution of the full flow equations of Section 4.2.5 numerically feasible we have to employ a series of approximations.

### 8.4.1 *Channel decomposition*

Thus far, the separation into the $\gamma^\alpha$, $\alpha \in \{p, d, x\}$ with $\gamma = \bar{v} + \sum_\alpha \gamma^\alpha$ made in Section 4.2.5 was just a formal rewriting. We can, however, restrict the feedback of the two-particle vertex of each of the channels to itself, i.e.

$$\begin{aligned}
\bar{\gamma}^p =& \bar{v} + \gamma^p \\
\partial_\Lambda \gamma^p_{1'2'|12}(\Pi, X, \Delta) =& \frac{i}{2\pi}\int d\omega \\
& \bar{\gamma}^p_{1'2'|34}\left(\Pi, \omega + \frac{X-\Delta}{2}, \omega - \frac{X-\Delta}{2}\right) S_{3|3'}\left(\frac{\Pi}{2} - \omega\right) \\
& G_{4|4'}\left(\frac{\Pi}{2} + \omega\right) \bar{\gamma}^p_{3'4'|12}\left(\Pi, \frac{X+\Delta}{2} + \omega, \frac{X+\Delta}{2} - \omega\right) + \mathcal{O}\left(U^3\right)
\end{aligned} \tag{8.4.1}$$

while only introducing errors of higher orders in the interaction. Analogous approximations are made for the other two channels. A similar approximation was successfully used in Ref. [Mar+18].

As the initial conditions of the two-particle vertex are frequency independent and due to the structure of the individual flow equations only one frequency dependence per channel is generated and one simplifies without further approximation

$$\begin{aligned}
\gamma^p_{1'2'|12}(\Pi, X, \Delta) &= \gamma^p_{1'2'|12}(\Pi, 0, 0) =: \gamma^p_{1'2'|12}(\Pi) \\
\gamma^x_{1'2'|12}(\Pi, X, \Delta) &= \gamma^x_{1'2'|12}(0, X, 0) =: \gamma^x_{1'2'|12}(X) \\
\gamma^d_{1'2'|12}(\Pi, X, \Delta) &= \gamma^d_{1'2'|12}(0, 0, \Delta) =: \gamma^d_{1'2'|12}(\Delta).
\end{aligned} \tag{8.4.2}$$

With this, the flow equations reduce to

$$\begin{aligned}
\partial_\Lambda \gamma^{p}_{1'2'|12}(\Pi) =& \frac{i}{2\pi}\int d\omega \\
& \bar{\gamma}^{p}_{1'2'|34}(\Pi)\, S_{3|3'}\left(\frac{\Pi}{2}-\omega\right) G_{4|4'}\left(\frac{\Pi}{2}+\omega\right) \bar{\gamma}^{p}_{3'4'|12}(\Pi) \\
\partial_\Lambda \gamma^{x}_{1'2'|12}(X) =& \frac{i}{2\pi}\int d\omega \\
& \bar{\gamma}^{x}_{1'4'|32}(X)\left[S_{3|3'}\left(\omega-\frac{X}{2}\right) G_{4|4'}\left(\omega+\frac{X}{2}\right)\right. \\
& \qquad \left. + G_{3|3'}\left(\omega-\frac{X}{2}\right) S_{4|4'}\left(\omega+\frac{X}{2}\right)\right] \bar{\gamma}^{x}_{3'2'|14}(X) \\
\partial_\Lambda \gamma^{d}_{1'2'|12}(\Delta) =& \frac{-i}{2\pi}\int d\omega \bar{\gamma}^{d}_{1'3'|14}(\Delta)\left[S_{3|3'}\left(\omega-\frac{\Delta}{2}\right) G_{4|4'}\left(\omega+\frac{\Delta}{2}\right)\right. \\
& + \qquad \left. G_{3|3'}\left(\omega-\frac{\Delta}{2}\right) S_{4|4'}\left(\omega+\frac{\Delta}{2}\right)\right] \bar{\gamma}^{d}_{4'2'|32}(\Delta)\,.
\end{aligned} \tag{8.4.3}$$

With a similar argument, we also find that the spatial extent of these constituents of the two-particle vertex is restricted in the same way as discussed in the previous chapter (see Equation 7.3.7). Consider for example the p-channel: for the initial condition we immediately find

$$\begin{aligned}
&\text{for } 1',2' \text{ such that } \nu_{1'2'|12} = 0\ \forall 1,2 \\
&\qquad \Rightarrow\ \bar{\gamma}^{p,\Lambda=\infty}_{1'2'|12}(\Pi) = 0.
\end{aligned} \tag{8.4.4}$$

Since

$$\bar{\gamma}^{p,\Lambda}_{1'2'|12}(\Pi) = 0\ \forall 1,2 \Rightarrow \partial_\Lambda \bar{\gamma}^{p,\Lambda}_{1'2'|12}(\Pi) = 0\ \forall 1,2 \tag{8.4.5}$$

these components are not generated during the flow and

$$\begin{aligned}
&\text{for } 1',2' \text{ such that } \nu_{1'2'|12} = 0\ \forall 1,2 \\
&\qquad \Rightarrow \gamma^{p,\Lambda}_{1'2'|12}(\Pi) = 0\ \forall 1,2,\Lambda.
\end{aligned} \tag{8.4.6}$$

Similarly

$$\begin{aligned}
&\text{for } 1,2 \text{ such that } \nu_{1'2'|12} = 0\ \forall 1',2' \\
&\qquad \Rightarrow \gamma^{p,\Lambda}_{1'2'|12}(\Pi) = 0\ \forall 1',2',\Lambda.
\end{aligned} \tag{8.4.7}$$

Analogous arguments can be made for the other channels and we finally arrive at

$$\begin{aligned}
\gamma^{p}_{1'2'|12}(\Pi) =& 0 \qquad \forall 1',2',1',2 \ni \nu_{i_1 i_{2'}|\bullet\bullet} = 0 \vee \nu_{\bullet\bullet|i_1 i_2} = 0 \\
\gamma^{x}_{1'2'|12}(X) =& 0 \qquad \forall 1',2',1',2 \ni \nu_{i_{1'}\bullet|\bullet i_2} = 0 \vee \nu_{\bullet i_{2'}|i_1\bullet} = 0 \\
\gamma^{d}_{1'2'|12}(\Delta) =& 0 \qquad \forall 1',2',1',2 \ni \nu_{i_{1'}\bullet|i_1\bullet} = 0 \vee \nu_{\bullet i_{2'}|\bullet i_2} = 0.
\end{aligned} \tag{8.4.8}$$

where we use a simplified notation. Furthermore, this allows us to decompose the flow-equation for the self-energy (compare Equation 4.2.23) into three separate parts

$$\begin{aligned}
\partial_\Lambda \Sigma_{1'|1}(\omega) &= \sum_{\alpha\in\{p,x,d\}} \partial_\Lambda \Sigma^\alpha_{1'|1}(\omega) \\
\partial_\Lambda \Sigma^p_{1'|1}(\omega) &= \frac{-i}{2\pi}\int d\Omega \gamma^p_{1'2'|12}(\Omega+\omega) S_{2|2'}(\Omega) \\
\partial_\Lambda \Sigma^p_{1'|1}(\omega) &= \frac{-i}{2\pi}\int d\Omega \gamma^x_{1'2'|12}(\Omega-\omega) S_{2|2'}(\Omega) \\
\partial_\Lambda \Sigma^d_{1'|1}(\omega) &= \frac{-i}{2\pi}\bar{\gamma}^d_{1'2'|12}(0)\int d\Omega S_{2|2'}(\Omega),
\end{aligned} \tag{8.4.9}$$

where the bare interaction is combined with the d-channel. Note that the restriction on the support of the individual $\gamma^\alpha$ in turn restricts the summations and/or support of the $\Sigma^\alpha$.

### 8.4.2 *Flow equations as convolutions*

These flow equations can all be rewritten in terms of convolutions, where we define the convolution of two functions as

$$(f * g)(y) = \int dx f(x) g(y-x) \tag{8.4.10}$$

and use the shorthand

$$\tilde{f}(x) = f(-x). \tag{8.4.11}$$

We then find

$$\begin{aligned}
\partial_\Lambda \Sigma^p_{1'|1}(\omega) &= \frac{-i}{2\pi}\tilde{S}_{2|2'} * \gamma^p_{1'2'|12} \\
\partial_\Lambda \Sigma^x_{1'|1}(-\omega) &= \frac{-i}{2\pi}\tilde{S}_{2|2'} * \gamma^x_{1'2'|12} \\
\partial_\Lambda \Sigma^d_{1'|1}(\omega) &= \frac{-i}{2\pi}\bar{\gamma}^d_{1'2'|12}(0)\int d\Omega S_{2|2'}(\Omega)
\end{aligned} \tag{8.4.12}$$

$$\begin{aligned}
\partial_\Lambda \gamma^p_{1'2'|12}(\Pi) &= \frac{i}{2\pi}\bar{\gamma}^p_{1'2'|34}(\Pi)\left(G_{4|4'} * S_{3|3'}\right)(\Pi)\bar{\gamma}^p_{3'4'|12}(\Pi) \\
\partial_\Lambda \gamma^x_{1'2'|12}(X) &= \frac{i}{2\pi}\bar{\gamma}^x_{1'4'|32}(X)\left[G_{4|4'} * \tilde{S}_{3|3'} + S_{4|4'} * \tilde{G}_{3|3'}\right](X)\bar{\gamma}^x_{3'2'|14}(X) \\
\partial_\Lambda \gamma^d_{1'2'|12}(\Delta) &= \frac{-i}{2\pi}\bar{\gamma}^d_{1'3'|14}(\Delta)\left[G_{4|4'} * \tilde{S}_{3|3'} + S_{4|4'} * \tilde{G}_{3|3'}\right](\Delta)\bar{\gamma}^d_{4'2'|32}(\Delta)
\end{aligned} \tag{8.4.13}$$

This shows, that an efficient implementation of the flow-equations has to be based on an efficient implementation of convolutions.

### 8.4.3 *Discretization of the frequencies and efficient convolutions*

As this approximation scheme is much more sophisticated than including the two-particle vertex perturbatively, there is no hope to solve any of the needed integrals analytically. Instead, we aim for an efficient numerical convolution.

In contrast to our approach in the previous chapter, we will use the discretization of the frequencies not only to approximate the self-energy but instead only evaluate the Green's functions on the chosen grid. Therefore, the grid chosen must always be wide enough to capture the decay of the Green's functions in the presence of the cutoff parameter and we furthermore assume the grid to be fine enough to justify a linear interpolation of the Green's function in between two points. This is hindered by the fact that the Keldysh component will generally not be continuous but instead feature jumps at the chemical potential of each reservoir.

To produce accurate results, it is necessary to resolve both these features. We found it difficult to reach convergence with an equidistant grid. Hence, we decided to employ a composite of an equidistant grid in combination with additional points around the chemical potentials of the reservoirs.

This presents us with a mathematical challenge: while it is straightforward, how to efficiently compute convolutions on an equidistant grid using fast Fourier transforms (FFT), an arbitrary, non-equidistant grid will generally rule out the use of an FFT. To that end, we developed a specialized algorithm to perform such convolutions in $\mathcal{O}(N_\omega \log(N_\omega))$ operations with $N_\omega$ being the number of points in the equidistant grid and the number of additional points considered to be constant and small. The algorithm and its derivation are outlined in Appendix C.

To efficiently approximate the Green's functions throughout the whole flow we adapt the grid. Whenever the grid is updated the values of the vertex functions on the new grid are obtained using linear interpolation.

### 8.4.4 *Support of the vertex functions*

While the channel decomposition already imposes restrictions on the support of the vertex functions, the number of non-zero elements that is not connected by symmetry (compare Equation 8.3.1) is still infinite. We therefore have to make additional, physically motivated approximations to efficiently produce numerical results. A natural starting point for this is the typical correlation length in the system at different energy scales. In the beginning of the flow the cutoff will restricts correlations. At smaller energy scales the electric field is expected limit the correlation length by localization (see Section 8.5.1)

or the generation of inelastic processes that provide a finite lifetime and thus correlation length.Therefore, it is natural to assume

$$\Sigma_{1'|1} = 0 \; \forall \; \mathrm{dist}(1'|1) \geqslant M, \tag{8.4.14}$$

which leaves us with $L \cdot (2M-1)$ independent spatial elements. This approximation can be considered non-consequential if convergence in $M$ is reached. Similarly, we restrict the range of the two-particle vertex

$$\gamma_{1'2'|12} = 0 \; \forall \; \mathrm{dist}(1',2',1,2) \geqslant M, \tag{8.4.15}$$

which automatically implies Equation 8.4.14.

To simplify the computations of the rhs of the second-order flow equations we (for now, compare Section 8.7) impose a more restrictive approximation

$$\nu_{i_{1'}i_{2'}|i_1i_2} = 0 \;\Rightarrow\; \gamma^{\alpha_{1'}\alpha_{2'}|\alpha_1\alpha_2}_{i_{1'}i_{2'}|i_1i_2}(\omega_{1'}\omega_{2'}|\omega_1\omega_2) = 0. \tag{8.4.16}$$

on the *feedback* of the two-particle vertex into the second-order flow equations (i.e. on the rhs of Equation 8.4.13). For the example of the p-channel this approximation yields

$$\begin{aligned}
&\partial_\Lambda \gamma^{p,\alpha_{1'}\alpha_{2'}|\alpha_1\alpha_2}_{i_{1'}i_{2'}|i_1i_2}(\Pi) \\
=&\frac{i}{2\pi} \sum_{\substack{3,4 \\ \nu_{i_{1'}i_{2'}|i_3,i_4}\neq 0}} \sum_{\substack{3',4' \\ \nu_{i_{3'},i_{4'}|i_1i_2}\neq 0}} \bar{\gamma}^{p}_{1'2'|34}(\Pi)\left(G_{4|4'} * S_{3|3'}\right)(\Pi)\bar{\gamma}^{p}_{3'4'|12}(\Pi).
\end{aligned} \tag{8.4.17}$$

In a perturbative regime, this approximation is justified as it omits only terms of $\mathcal{O}\left(U^3\right)$; in the context of a CDW phase transition (as we will consider later) this approximation is motivated by the fact, that the CDW is driven by nearest-neighbor density-density type interactions (compare Section 8.5.1), which are included and flow within this scheme. Note that we only restrict the feedback with respect to the spatial indices and allow for the full frequency dependence as well as all combinations of Keldysh indices.

While there are numerous conceivable ways to reduce the number of independent flow equations and the complexity of each one, great care has to be taken to conserve the symmetries of the vertex functions. Omitting some of the symmetry connected elements while retaining others will explicitly break the symmetry.[3] In particular, the approximations made here preserve (compare Section 3.3)

$$\begin{aligned}
\Sigma_{1'|1}(\omega',\omega) &= \left[\Sigma_{1|1'}(\omega,\omega')\right]^* \\
\gamma_{1'2'|12} &= -\gamma_{2'1'|12}(\omega_{2'},\omega_{1'}|\omega_1,\omega_2) \\
&= -\gamma_{1'2'|21}(\omega_{1'},\omega_{2'}|\omega_2,\omega_1) \\
\gamma_{1'2'|12} &= (-1)^{1+\alpha_1+\alpha_2}\left[\gamma_{12|1'2'}\right]^*
\end{aligned} \tag{8.4.18}$$

3 As an example, consider two-particle vertex with the spatial indices $\gamma_{01|12}$ and $\gamma_{0-1|01}$, which are connected by symmetry.

with the RKA-indices $\alpha$. As we discussed, this implies the conservation of the fluctuation-dissipation theorem in equilibrium (see Sections 3.3.5 and 4.3.1). We explicitly verified this numerically.

### 8.4.5 *Green's functions and single-scale propagators*

While we restrict the support of the self-energy, it is essential to compute the full Green's functions and single-scale propagators of the infinite system. To solve the approximate flow equations it is, however, sufficient to obtain $G_{1|1'}$ with the spatial components $i_1, i_{1'} \in \{-M+2, \dots, L+M-1\}$. This can be achieved with techniques similar to those presented in Section 2.5.4 employing the symmetries of the Green's function. Using $S = \partial_\Lambda^* G$ also leads to corresponding formulas for the single-scale propagators.

As the resulting procedure to obtain the Green's functions is rather lengthy, we refer the interested reader to Appendix D, where we give a detailed derivation; here, we will only note that the resulting formulas are of complexity $\mathcal{O}\left(N_\omega (2M+L)^3\right)$ and provide the full Green's functions and single-scale propagators without further approximations.

### 8.4.6 *Summary of the approximations made*

For easier reference, let us briefly summarize the approximations made.

1. We truncate the flow-equations by neglecting the flow of the three-particle vertex, introducing errors that are of $\mathcal{O}\left(U^3\right)$.

2. We perform a channel decomposition, which restricts the feedback of the vertex functions; each of the three channels $p, x, d$ is only fed back into itself, introducing errors that are of $\mathcal{O}\left(U^3\right)$ (compare Equation 8.4.1).

3. We restrict the support of all vertex functions such that the spatial distance between single-particle indices is limited by $M$. If convergence in $M$ is reached this becomes exact (compare Equations 8.4.14 and 8.4.15).

4. We restrict the *spatial* support of the feedback of the two-particle vertex function into itself to the support of the bare two-particle interaction, introducing errors that are of $\mathcal{O}\left(U^3\right)$ (compare Equation 8.4.17).

We emphasize, that no additional approximations to the frequency dependence are performed and due to the construction of our correlation functions, our results do not suffer any finite-size effects.

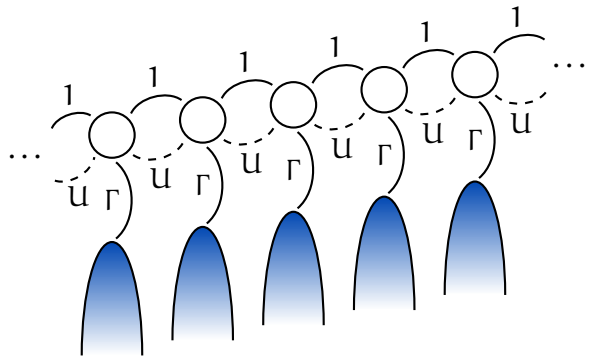


Figure 8.2: Visualization of the model Hamiltonian with hopping amplitude $t$ used as energy scale throughout, interaction $U$ and coupling to an environment $\Gamma$.

## 8.5 A SIMPLE CHAIN IN AN ELECTRIC FIELD

To describe an interacting, one-dimensional metal in an electric field coupled to a fermionic environment, we analyze the model Hamiltonian:

$$
\begin{aligned}
H &= \sum_{n\in\mathbb{Z}} H_0^n + H_{\text{int}} + H_{\text{env}}^n + H_{\text{coup}}^n \\
H_0^n &= nE c_n^\dagger c_n + c_n^\dagger c_{n+1} + \text{h.c.} \\
H_{\text{int}}^n &= U\left(c_n^\dagger c_n - \frac{1}{2}\right)\left(c_{n+1}^\dagger c_{n+1} - \frac{1}{2}\right) \\
H_{\text{env}}^n &= \sum_k (\epsilon_k + nE)\, f_{n,k}^\dagger f_{n,k} \\
H_{\text{coup}}^n &= \sum_k t_k c_n^\dagger f_{n,k} + \text{h.c.}.
\end{aligned}
$$

Throughout, the coupling between neighboring sites is used as unit of energy. We assume the environment acts as a particle reservoir and is initially prepared in thermal equilibrium at the local chemical potential $\mu_n = nE$. In this work, we only consider the $T = 0$ case. Furthermore, the bandwidth of these reservoirs is assumed to be large compared to all other energy scales. Hence, it is fully characterized by a in a constant hybridization $\Gamma$ (see Section 2.8). The model used is visualized in Figure 8.2.

A non-interacting version of this model was already discussed in [Han13]. Related models have also been studied using DMFT [TOA08; TOA09; Ama+12; Fre08].

### 8.5.1 *Phenomenology*

While being the simplest member within the class of models introduced in Section 8.2, this model hosts a variety of physical phenom-

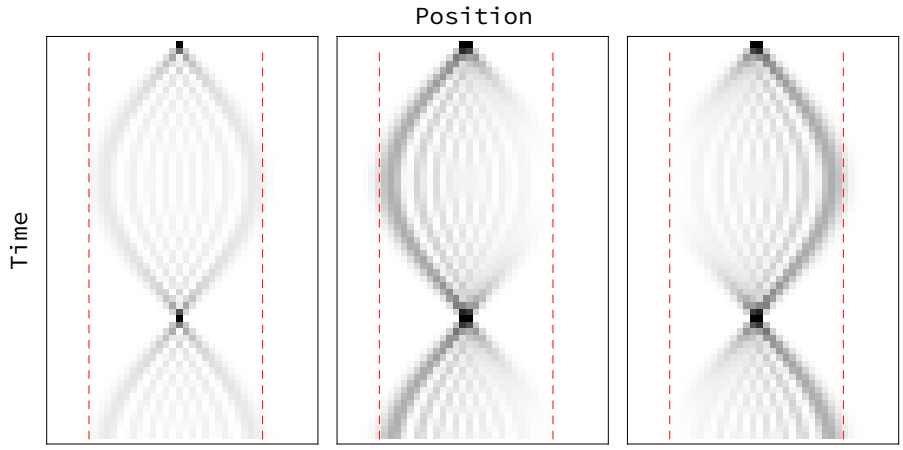


Figure 8.3: Propagation of particle density in a chain penetrated by a longitudinal electric field. The on-site potential increases to the right. The initial state is chosen as $\cos(\phi)\,|0\rangle + \sin(\phi)\,|1\rangle$ with (from left to right) $\phi = 0, \pm\frac{\pi}{4}$, where $|i\rangle$ are Wannier states localized at site $i$. The dashed right lines indicate the reflection points $B/E$.

ena. A brief introduction of these will set the stage for the discussion of the results we find when applying the method described above.

#### 8.5.1.1 *Wannier Stark localization and Bloch oscillations* ($U = 0$, $E > 0$, $\Gamma = 0$)

In the 1930s, Zener predicted a breakdown of DC conductivity [Zen34] in pristine crystals by providing evidence, that the propagation of a wave packet is exponentially suppressed. This can be easily understood when analyzing the eigenstates of fermions in the presence of an electric field, as done by Wannier [Wan60].

To gain an intuition for this localization, we imagine a chain with a small electric field (compared to the bandwidth). Local properties, such as the local density of states, are only weakly affected by the electric field and a localized wave packet will initially propagate following the dynamics of a bare chain. When the wavepacket has, however, traversed far enough the local density of states is shifted significantly and no more states are available; the wavepacket is reflected.

Therefore, the state prepared initially can never propagate further than $B/E$, where $B$ denotes the bandwidth of the system. This is exemplified in Figure 8.3. There we also see, how the initial state influences the initial movement: if the fermion is prepared on an individual site (and thus is a superposition of all eigenstates of a chain without electric field), it evolves in both directions equally. When lowering the energy of the initial state by using a symmetric superposition $(|0\rangle + |1\rangle$ with $|0, 1\rangle$ being the localized Wannier states on site $0$ and $1$ respectively), it initially propagates to the lower potential while a higher energy state $(|0\rangle - |1\rangle)$ propagates to higher energies (against the elec-

tric field).[4] None of these configurations feature long range transport. The oscillations that emerge are known as *Bloch oscillations*.

So, if even a small electric field localizes all eigenstates, why is DC transport even possible and why are Bloch oscillations not ubiquitous? To form coherent oscillations, the mean free path in the system has to be large compared to the electric field (in appropriate units). In a realistic crystal at finite temperature, phonon scattering will destroy coherence all together [MB93]. For this reason it took around 60 years until Zener's prediction was experimentally verified [Was+93].

Note that no finite electric field in a pristine, non-interacting, long chain can be considered to be a small perturbation in the sense of linear response, as it induces an infinite number of coherent scattering processes. The finite linear response conductivity obtained using the Kubo formula has to be understood as the limit, where the electric field *times the system size* $EL$ (i.e. the largest potential) is small compared to the bandwidth.

In the system we consider, the inelastic processes are provided by the reservoirs; if the typical distance traveled by a fermion before scattering in a reservoir is small compared to the ratio of bandwidth to electric field, Bloch oscillations are suppressed. In the opposite limit, transport halts if no other scattering processes are present. How these transport properties occur will be discussed next.

#### 8.5.1.2 *Wannier Stark localization in open systems* ($U = 0$, $E > 0$, $\Gamma > 0$)

When the system is attached to reservoirs, they induce incoherent scattering, resulting in a finite coherence length $l_c \sim \frac{1}{\Gamma}$. When the coherence length is short compared to $B/E$ the local potentials in the decoupled system can be neglected, in the other limit localization dominates. To characterize transport, we analyze the contributions to the current (compare Equation 2.7.16)

$$I_{r,r'} = c \int d\omega \left[ n^r(\omega) - n^{r'}(\omega) \right] \Gamma^2 \left| g^{\text{ret}}_{r,r'}(\omega) \right|^2 \tag{8.5.1}$$

that can be interpreted as the current from reservoir $r'$ into reservoir $r$. For small electric fields we can distinguish three regimes:

$\Gamma \gg B$ In this case, the dominant transport channel is from one reservoir to its nearest neighbor. As $\Gamma$ dominates the Hamiltonian of the closed system we find[5]

$$G^{\text{ret}}_{r,r+1}(\omega = 0) \sim \frac{B}{\Gamma^2} \;\Rightarrow\; I \sim \frac{EB^2}{\Gamma^2}. \tag{8.5.2}$$

4 Without electric field, the initial states chosen evolve symmetrically.

5 An analysis of the longer-range terms reveals, that their contribution is sub-leading.

$E/B \ll \gamma \lessapprox B$ In this limit, the Hamiltonian of the closed system provides the relevant scale for the transport and the decay of the retarded Green's function can be shown to scale as

$$G^{\mathrm{ret}}_{r,r+\Delta}(\omega = 0) \sim \frac{1}{B} \exp(-\alpha \Delta \Gamma / B) \tag{8.5.3}$$

and thus the current through the chain is computed as

$$I = \sum_{r<0, r' \geqslant 0} I_{r,r'} \sim \sum_{\Delta=1}^{\infty} \frac{E \Delta^2 \Gamma^2}{B^2} \exp(-2\alpha \Delta \Gamma / B) \sim \frac{EB}{\Gamma} \tag{8.5.4}$$

$E/B \gg \Gamma$ In this limit, a particle, that has entered the system is expected to scatter from the electric field many times before leaving the system again. The average distance of the particle traveled before leaving the system will generally depend on its energy but is independent of $\Gamma$ and expected to scale as $B/E$. As the chance of a particle entering the system in the first place is scales as $\Gamma$ the overall current is expected to scale as

$$I \sim \frac{\Gamma B}{E}. \tag{8.5.5}$$

A more rigorous discussion of the limits $E, \Gamma \ll B$ can be found in [Han13].

#### 8.5.1.3 *Charge Density Wave transition*

In a closed, translationally invariant system ($\Gamma = E = 0$) with a density-density interaction strong enough to dominate the non-interacting part of the Hamiltonian, we approximate

$$H \approx \sum_{\langle i,j \rangle} U \hat{n}_i \hat{n}_j \tag{8.5.6}$$

which in the absence of frustration and at half filling has a two-fold degenerate ground state with a staggered occupation. Once translation symmetry is broken, the formed charge-density wave is immovable and incapable of hosting transport.

We already discussed, that a tight-binding chain with small nearest neighbor interaction forms a Luttinger liquid and is thus gapless, featuring transport. Therefore, we expect a interaction driven metal-insulator transition. The simplest way to obtain a phase diagram is mean-field theory, which we will discuss next.

#### 8.5.1.4 *Mean field theory transition*

To investigate the phase-diagram in the closed system ($\Gamma = E = 0$), we add a symmetry-breaking to a simple tight binding chain

$$H = \sum_i (-1)^i s c_i^\dagger c_i + c_i^\dagger c_{i+1} + c_{i+1}^\dagger c_i \tag{8.5.7}$$

and investigate how this symmetry breaking would be generated by a nearest-neighbor interaction in self-consistent Hartree-Fock (compare Section 3.4.2). The retarded Green's function in momentum space reads

$$g^{\mathrm{ret}}_{k|k'}(\omega) = \frac{1}{\omega - \begin{pmatrix} -s & 2\cos(k) \\ 2\cos(k) & s \end{pmatrix} + i0}\delta_{k,k'},\ k = -\frac{\pi}{2}\ldots\frac{\pi}{2}, \quad (8.5.8)$$

where the matrix structure denotes the two sites in the unit cell. As shown in Figure 8.4, the staggered potential opens a gap at $k = \frac{\pi}{2}$ and is accompanied by corresponding van-Hove singularities at $\omega = \pm s$. Due to the fact, that the Bloch-Hamiltonian is diagonal for $k = \frac{\pi}{2}$ (which is the only momentum with states at energy $\omega = \pm s$) the *local* density of states on the odd (even sites) feature only one divergence at $\omega = -s$ ($\omega = s$) while the other one is suppressed. As this divergence drives the mean-field phase transition, we inspect the vicinity of $k = \frac{\pi}{2}$ more closely and write for the first site in the unit cell

$$\begin{aligned}\left(g^{\mathrm{ret}}_{k}(\omega)\right)_{1,1} &\approx \left[\omega - \begin{pmatrix} -s & 2\left(\frac{\pi}{2}-k\right) \\ 2\left(\frac{\pi}{2}-k\right) & s \end{pmatrix} + i0\right]^{-1}_{1,1} \\ &= \frac{\omega - s}{-s^2 - 4\tilde{k}^2 + \omega^2 + 0\omega i}\end{aligned} \quad (8.5.9)$$

with $\tilde{k} = k - \frac{\pi}{2}$. The change in occupation on the odd sites in the ground-state can therefore be obtained as the difference of the occupation at staggered potential $s$ and $0$

$$\begin{aligned}\delta n &\sim \int dk \int_{-\infty}^{0} d\omega\, \mathrm{Im}\left(\frac{s}{\omega^2 - 4\tilde{k}^2 - s^2 - i0}\right) \\ &\sim \int dk \frac{s}{\sqrt{4\tilde{k}^2 + s^2}} \sim -s\log(s) \text{ for } s \ll 1\end{aligned} \quad (8.5.10)$$

When the staggered potential is induced by a nearest-neighbor interaction the self-consistency equation reads:

$$\begin{aligned} s &= U\delta n \sim -Us\log(s) \\ &\Rightarrow s = \exp\left(-\frac{1}{U}\right)\end{aligned} \quad (8.5.11)$$

which indicates a continuous phase transition of infinite order with a critical interaction strength $U_c = 0$. While this simplified calculation demonstrates how MFT produces a phase transition, the results presented in Figure 8.7 are obtained solving the full mean field equations (see Section 3.4.2).

The phenomenology of this phase transition (in the thermal, closed case) is understood beyond MFT and is characterized by a Berezinskii-Kosterlitz-Thouless transition that occurs at $U_c = 2$ in 1D.

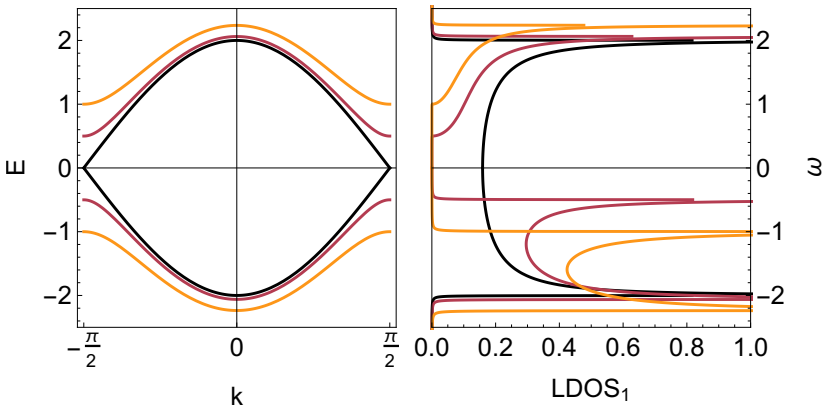


Figure 8.4: *Left panel*: Band structure of the Hamiltonian presented in Equation 8.5.7 for $s = 0, 0.5, 1$ (dark to light colors). *Right panel*: The corresponding local density of states on the odd sites, featuring Van-Hove singularities at the edges of the bands. The LDOS of the even sites is inverted. Each site features only one of the peaks at $\omega = \pm s$ due to the form of the eigenvectors at $k = \pm\pi/2$.

#### 8.5.1.5 *The Berezinskii-Kosterlitz-Thouless transition*

First discussed by Berezinskii [Ber71; Ber72], later developed further by Kosterlitz and Thouless [KT73; Kos74], the BKT transition describes a phase transition between a quasi-ordered and a disordered phase, originally in the classical XY-model in two dimensions. The low-temperature phase is reported to feature slowly decaying correlations ($\langle S(x) \cdot S(0)\rangle \sim x^{-\alpha T}$) [FS81] which corresponds to quasi-order. Beyond a critical temperature the order is destroyed and correlations decay exponentially. This destruction comes about in the form of unbinding of vortex anti-vortex pairs, which beyond a critical temperature proliferate.

The low-temperature, quasi ordered phase is not in violation of the Mermin-Wagner theorem because long-range correlations do indeed decay at long distances (at finite temperature), restoring the continuous rotational symmetry of the XY-model.

The transition is of infinite order with correlation diverging exponentially

$$\xi \sim \exp\left(\frac{\alpha}{\sqrt{T - T_C}}\right) \tag{8.5.12}$$

making this an *essential* phase transition.

A tight-binding chain with nearest neighbor interaction is a lattice regularization of the sine-Gordon model [PP99] and features a BKT transition at the critical interaction strength $U_c = 2$ [Gia06; Caz+11].

This phase-transition has previously been studied with an equilibrium second-order fRG approximation [Mar+18].

## 8.6 INTERPLAY OF INTERACTION, DRIVING AND HYBRIDIZATION

While the behavior in the cases $U = 0$ and $E = 0$, $\Gamma = 0$ are well understood, the interplay of the effects that dominate these regimes are widely unexplored. For the most part, we will focus on investigating the stability of the CDW phase against hybridization and driving. Therefore, we will first demonstrate, that we can converge the algorithm presented in the relevant parameters for the observable of interest (see Section 8.6.1). We than present our findings in equilibrium (Section 8.6.2), where we can also employ DMRG to provide a qualitative comparison. We then discuss the case of finite driving (Sections 8.6.3, 8.6.4 and 8.6.5).

Beyond discussing the vicinity of the phase transition, Section 8.6.6 discusses transport properties when Wannier-Stark localization becomes relevant.

Lastly, we present a generalization of the algorithm introduced above, that might yield more accurate results in the future (see Section 8.7).

### 8.6.1 *Convergence of the algorithm*

The algorithm presented is controlled by various numerical and physical parameters. It is therefore essential to demonstrate convergence. As the core of our discussion will revolve around the CDW phase transition, we use the susceptibility towards this phase as the relevant observable of interest. Similar to our mean-field analysis we therefore introduce a term that breaks the translational symmetry of the system $H_S^n = s(-1)^n c_n^\dagger c_n$ (a technique proposed in the context of the fRG by [Sal+04]) and observe the CDW response in form of the order-parameter and susceptibility

$$\begin{aligned} \mathrm{OP} &= \frac{n_{\mathrm{odd}} - n_{\mathrm{even}}}{2} \\ \chi &= \lim_{s \to 0} \mathrm{OP}/s. \end{aligned} \tag{8.6.1}$$

In the disordered phase, this susceptibility is expected to converge in the limit of small symmetry breaking terms. In the ordered phase it diverges for $s \to 0$ while the order parameter becomes independent of $S$.[6]

Figure 8.5 demonstrates that we can reach convergence in $M \to \infty$, $s \to 0$, and in the frequency discretization for this observable. All computation show results for the open system $\Gamma > 0$; while the left

6 Note that it is also common to define the susceptibility in the ordered phase as the deviation of the order-parameter from its $s \to 0$ value. This would yield a well-defined susceptibility in the ordered phase.

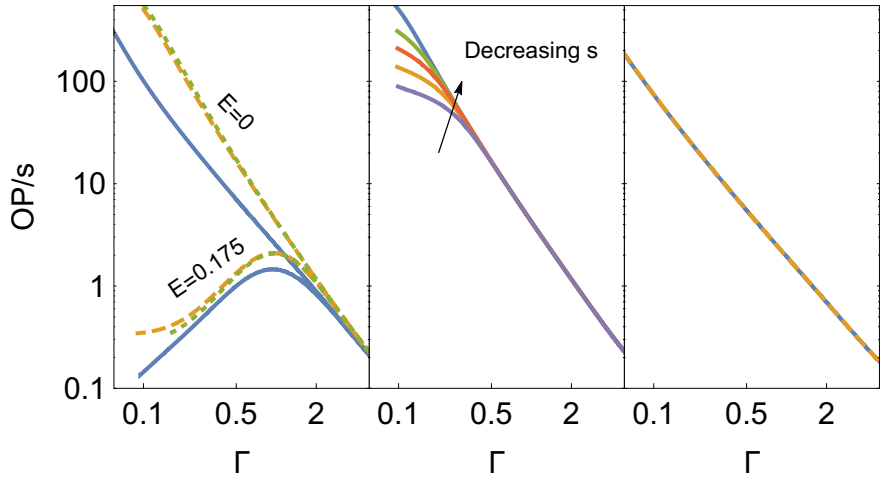


Figure 8.5: Convergence in the parameters of the algorithm. *Left panel*: To investigate the convergence in $M$ we set $U = 4.5$, use $N_\omega \approx 2200$ and $E = 0,\ 0.175$ as indicated while varying $M = 2, 4, 6$ (solid blue, dashed orange and dotted green line respectively). *Middle panel*: Fixed $E = 0$, $U = 4.5$, $M = 4$ while varying $S = 2.5 \cdot 10^{-3},\ 1.25 \cdot 10^{-3},\ 6.25 \cdot 10^{-4},\ 3.125 \cdot 10^{-4},\ 10^{-4}$. Apparently $OP/s$ converges to a finite susceptibility. *Right panel*: Comparison of the results at $E = 0$, $U = 3$ $M = 4$ with $N_\omega \approx 2200,\ 6600$ (solid and dashed lines respectively).

panel shows convergence in $M$ with and without electric field, the other two panels demonstrate convergence in the equilibrium case.

If not stated otherwise, the results presented from here on are converged in $s \to 0$ and the discretization and use $M = 4$.

### 8.6.2 *Equilibrium susceptibility with fRG and DMRG*

Let us first discuss the equilibrium case of the open system, where $E = 0$, $\Gamma > 0$. Numerically, this limit is at least as difficult for the algorithm presented, as the different energies decouple and the correlation functions have to be obtained self-consistently (compare Appendix D). We refrain from explicitly using the equilibrium properties of the Green's functions and thus the recovery of the fluctuation-dissipation theorem provides a non-trivial check of our approximations. The $\Gamma$ dependence of the susceptibility is shown in the left panel of Figure 8.6 for different strengths of the interaction. We find that the susceptibility converges in the limit $s \to 0$ for any $\Gamma > 0$, indicating the destruction of the CDW at any finite coupling. In the limit $\Gamma \to 0$ the susceptibility appears to diverge for large interactions while converging for smaller ones. This is compatible with a finite-interaction phase transition in the decoupled system.

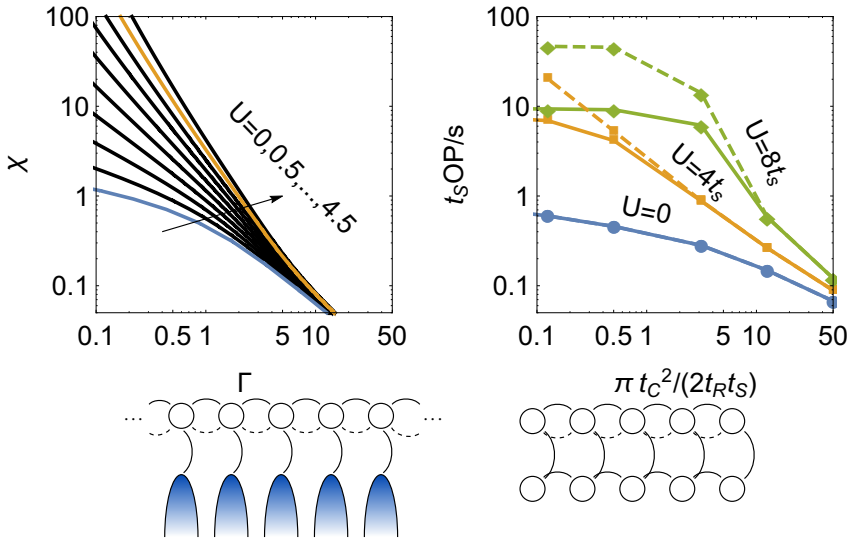


Figure 8.6: *Left panel*: Equilibrium ($E = 0$) results for the susceptibility in the limit $s \to 0$ for interactions $U = 0, 0.5, \ldots, 4.5$. The susceptibility remains finite for all interactions shown. Small interaction appear to converge, indicating a disordered phase while large interactions seem to diverge in the limit $\Gamma \to 0$, indicating a phase transition to an ordered phase. *Right panel*: Equilibrium DMRG[7] results for the model defined in Equation 8.6.2 at $s/t_S = 0.1$ (solid) and $s/t_S = 0.02$ (dashed). The blue and orange line in the left and right panel indicate corresponding interaction strengths and show qualitative agreement.

In the equilibrium limit we can also use DMRG[7] (compare Section 5.3) to qualitatively benchmark our algorithm. As even in equilibrium, the reservoirs, that make the full system effectively 2D, pose a problem to DMRG, we have to settle for a qualitative agreement of two similar models. Hence, in DMRG we analyze two coupled 1D chains (labeled suggestively S and R) where the interaction is restricted to one of the chains:

$$\begin{aligned} H_{\text{DMRG}} = & \sum_n t_S c^\dagger_{S,n} c_{S,n+1} + t_R c^\dagger_{R,n} c_{R,n+1} + \text{h.c.}. \\ & + \sum_n t_C c^\dagger_{S,n} c_{R,n} + \text{h.c.}. \\ & + \sum_n U \left( c^\dagger_{S,n} c_{S,n} - \frac{1}{2} \right) \left( c^\dagger_{S,n+1} c_{S,n+1} - \frac{1}{2} \right) \end{aligned} \tag{8.6.2}$$

The R-subsystem acts as reservoir to the other half of the system. If $t_S \ll t_R$ the reservoir's bandwidth is large compared to the one of the S-subsystem. The results of this calculation using $t_S/t_R = 0.5$ are shown in the right panel of Figure 8.6 and are in qualitative agreement to the fRG results. Consistent with our fRG results, DMRG shows a strong susceptibility but no clear sign of a finite-$\Gamma$ phase-transition. Quantitative agreement is, however, not expected as the

7 DMRG data was provided by C. Karrasch.

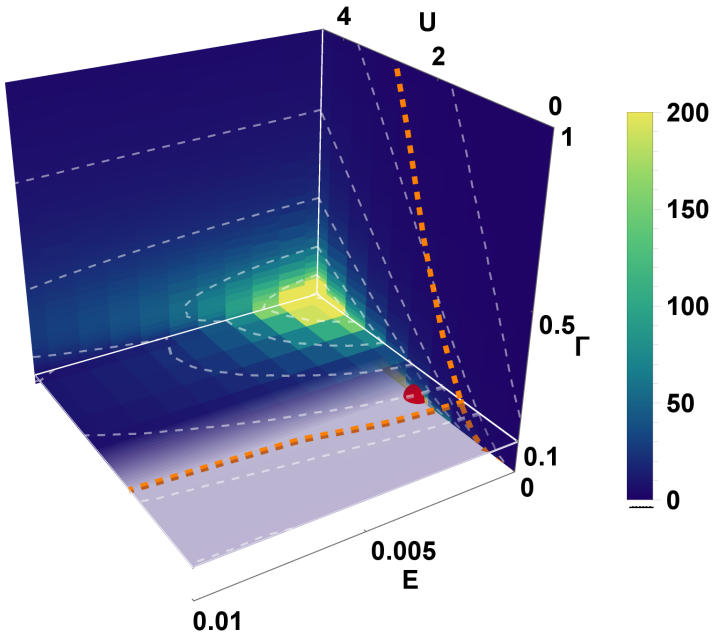


Figure 8.7: The colors show the susceptibility $\chi(U, \Gamma, E)$ as obtained with fRG. We find that the system is in a metallic phase at all finite couplings, while the strong susceptibility indicates a phase transition in the limit $E \to 0$, $\Gamma \to 0$ at a finite $U_c > 0$. The red sphere indicates the analytically known phase transition of the decoupled system to a CDW for $U > 2, \Gamma = 0, E = 0$. The dashed orange lines show the phase transition obtained by MFT for $E = 0$ and $\Gamma = 0.1$.

two models vastly differ in addition to the approximate nature of fRG.[8]

### 8.6.3 *Susceptibility out of equilibrium*

Out of equilibrium, the susceptibility becomes a function of the interaction $U$, coupling to the environment $\Gamma$ and electric field $E$ and is shown in Figure 8.7. The parameter space is visualized by providing slices at constant $U = 4.5$, $E = 0$ as well as $\Gamma = 0.1$. The latter is shown semi transparently to allow view on the position of the phase transition in the closed system ($\Gamma = 0$) that is known to take place at $U_c = 2$ (marked by a red sphere). As we already found in equilibrium, the susceptibility remains finite for all accessible parameters and convergence in $M \to \infty$ and $s \to 0$ can be reached. The addition of an electric field only diminishes the susceptibility and thus our data indicates a CDW only for $U > 2$, $\Gamma = 0$, $E = 0$. This is contrasted by the orange dashed lines that indicates the extent of the ordered

8 In our formalism, the model described by $H_{DMRG}$ features a single reservoir with $T = \mathbb{1}$.

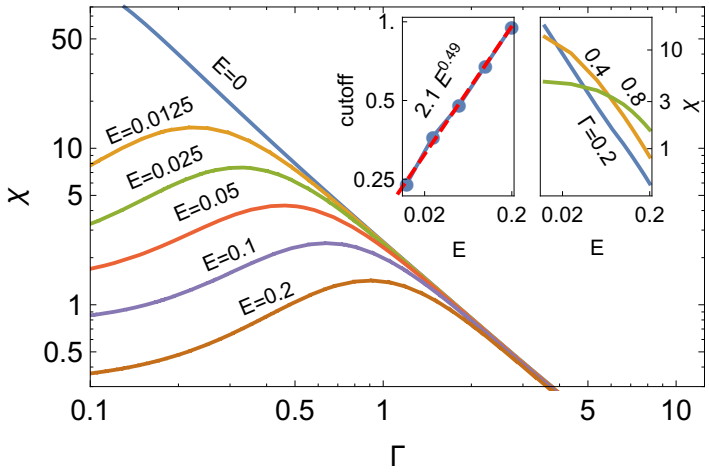


Figure 8.8: Analysis of CDW susceptibility to a symmetry-breaking with various electric fields as obtained with fRG at $U = 4$. *Main panel*: Any finite electric field destroys the ordering tendency of the system when lowering the coupling to the environment. *Left inset*: The cutoff provided to the susceptibility as a function of the electric field. A power-law fit (dashed line) indicates behavior consistent with $\sim \sqrt{E}$. *Right inset*: Similarly, the coupling to the environment also produces a cutoff to the divergence of $\chi(E)$ in the limit $E \to 0$.

phase as obtained by MFT, predicting order at large couplings and at any interaction for $\Gamma \to 0$. Even at finite driving, MFT predicts the existence of an ordered phase.

We will now analyze the effect of the electric field more quantitatively.

### 8.6.4 *Electric field as a cutoff*

To quantify the influence of the electric field, Figure 8.8 shows the CDW susceptibility at constant interactions $U = 4$ as a function of the hybridization $\Gamma$. In closed system, this interaction leads to spontaneous symmetry breaking. $U = 4$ is not small compared to any other scale and especially in the neighborhood of a phase transition the quality of the approximation strictly relies on the quality of the resummation.

We find that any electric field cuts off the ordering tendency of the system in the limit $\Gamma \to 0$. The cutoff of $\chi(\Gamma)$ appears to scale as $\sqrt{E}$. Vice versa, the hybridization $\Gamma$ can be understood to provide a cutoff to $\chi(E)$. Therefore, at finite electric field, even in the limit $\Gamma \to 0$, no order emerges within our approximation scheme.

### 8.6.5 *Transport close to the phase-transition*

To understand the interplay between order and the current induced by an electric field, Figure 8.9 analyzes the conductivity $\sigma = \frac{I}{E}$ at $U = 1$ (where the closed system is disordered) and $U = 4$ (where a CDW is expected). We limit our discussion to small electric fields ($E \ll \Gamma$), where the system is delocalized and the current is described by an Ohmic law (see inset of Figure 8.9). As we discussed in the non-interacting case (see Section 8.5.1) transport at $\Gamma \gg 1$ is governed by short-range processes resulting in a $I \sim \Gamma^{-2}$ scaling. When the free coherence length starts to span multiple site (i.e. $\Gamma \lessapprox 1$) the long range contributions to the current change the behavior to $I \sim \Gamma^{-1}$. In this regime, we find that close to the CDW phase (i.e. for $U > 2$) the current is strongly suppressed when the translational symmetry is broken by $s > 0$. This observation is formalized in terms of a current susceptibility $\chi_\sigma = \lim_{s\to 0} \sigma/s$ indicating a complete halt of transport for $\Gamma \to 0$, $U > U_c$, $E \to 0$. This can be interpreted as a strong additional resistance due to the proximity to a quantum phase transition. Consistent with our prior observations, this susceptibility is cut off by a finite electric field as the field prevents the formation of a CDW.

### 8.6.6 *Results for* $\Gamma \ll E$

When the coupling to the reservoirs becomes small compared to the electric field Wannier Stark localization becomes relevant. In a classical picture, a fermion is reflected many times by the electric field before it tunnels into one of the reservoirs; the typical distance traveled becomes independent of $\Gamma$ and is given by the Wannier-Stark localization length, as we discussed in Section 8.5.1.

For simplicity we will only discuss the system far from the phase-transition by only considering relatively large electric fields. In this regime, the susceptibility remains small and we can set $s = 0$. Furthermore, large electric fields ensure short correlation lengths and therefore allow for easier convergence in $M$.

Without interaction ($U = 0$) we correctly recover the linear relation $I \sim \Gamma/E$ for $\Gamma \to 0$ (see left panel of Figure 8.10). When the interaction is finite we find a finite current in the limit $\Gamma \to 0$, indicating that fermions are no longer confined by the Wannier-Stark localization. While we find a finite current for almost all interaction strengths (compare right panel of Figure 8.10), we observe that the direction of the current depends on the relative strength of the electric field and the interaction: when the scattering is dominated by the interaction (i.e. $U^2 \gg E$) the residual current at $\Gamma \to 0$ follows the electric field; if a fermion is expected to scatter from the electric field many times before interaction ($U^2 \ll E$) we find a current in the opposite direction.

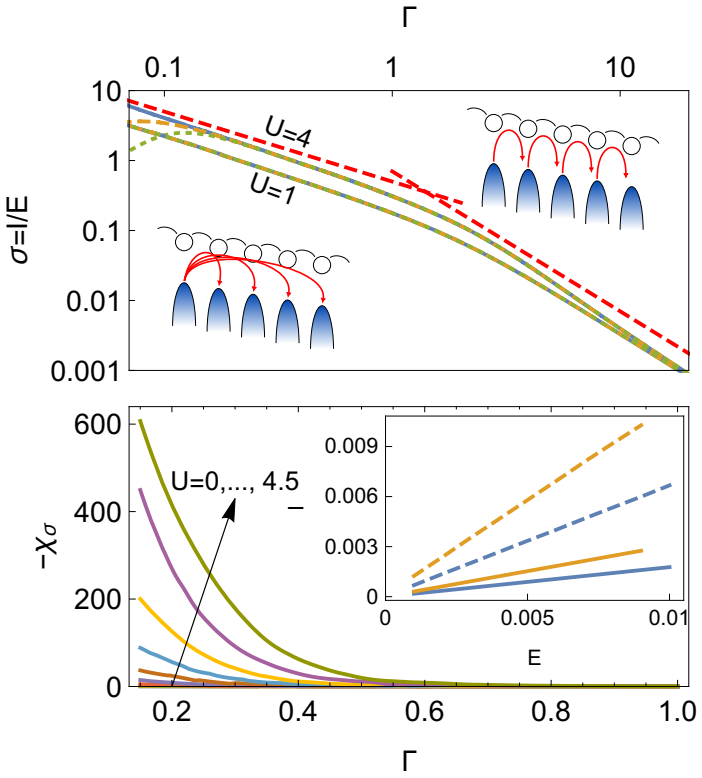


Figure 8.9: *Upper panel*: The conductivity $\sigma = I/E$ of the system at $E = 10^{-3}$ at $U = 1$ and $U = 4$. For large $\Gamma \gg 1$ the transport is dominated by short ranged processes leading to $\sigma \sim 1/\Gamma^2$ . For smaller $\Gamma \lessapprox 1$ the leading contribution to the particle transport is provided by long-range processes. These power-laws (compare Section 8.5.1) are indicated by the red dashed lines. We find, that for $U > U_c$ a small breaking of translational symmetry can diminish the current significantly in the limit $\Gamma \to 0$. To this end, the orange dashed and green dotted lines show the current with $s = 10^{-4}$ and $s = 2 \cdot 10^{-4}$ respectively for both interactions. *Lower panel*: To quantify this, we analyze the susceptibility of the current to symmetry-breaking $\lim_{s\to 0} \sigma/s$ at $E = 0.0125$. *Inset*: Without symmetry-breaking, the current appears to follow an Ohmic relation for $E \to 0$. This is demonstrated for $\Gamma = 0.3$ (orange) and $\Gamma = 1$ (blue) as well as $U = 1$ (solid) and $U = 4$ (dashed). The interaction dependent resistance is dominated by linear contributions.

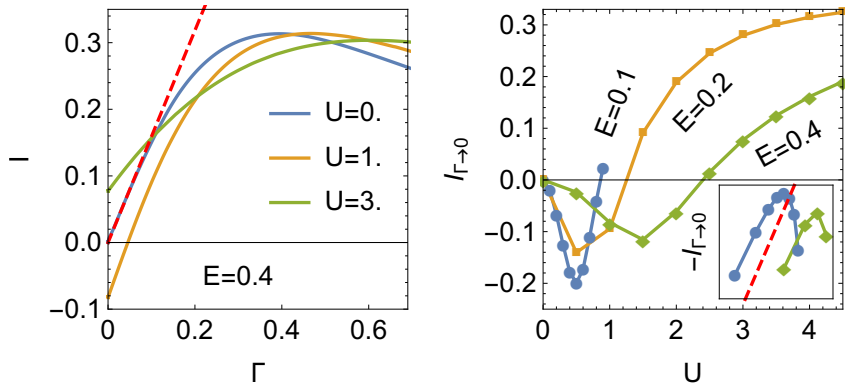


Figure 8.10: *Left panel*: The current as a function of the hybridization to the reservoirs at $E = 0.4$ and interactions $U = 0, 1, 3$. Localization prevents transport for $\Gamma \to 0$ without interaction and the current decreases linearly with $\Gamma$ (compare Equation 8.5.4). $U = 1, 3$ display residual current in that limit. Note that the *direction* of this current depends on $U$. *Right panel*: The current we find in the limit $\Gamma \to 0$ depending on the interaction at different field strengths. For interactions small compared to the field we find a negative current. *Inset*: A double logarithmic presentation of the small-$U$ behavior. The current increases $\sim U^2$ (indicated by the dashed line).

An analysis of the interaction dependence shows, that the effect is of order $\mathcal{O}\left(U^2\right)$ and therefore consistent with our approximation scheme (compare inset of the right panel of Figure 8.10). As the effect is limited to the parameter region where the electric field dominates the two particle interaction one finds a positive current in the limit $E \to 0$ at any finite $U$ (compare right panel of Figure 8.10). Hence this effect is beyond linear response and a true non-equilibrium phenomenon.

A simple analysis of the self-energy provides a thermodynamic interpretation: when the system is close to equilibrium the ratio of the components of the self-energy

$$\frac{\mathrm{Im}\left(\Sigma^{K}_{i,i}(\omega)\right)}{\mathrm{Im}\left(\Sigma^{ret}_{i,i}(\omega)\right)} \sim (1 - 2n(\omega)) \tag{8.6.3}$$

can be used as a proxy of the distribution function (see Section 3.3.5).[9] Our finding as presented in Figure 8.11 indicate, that the system experiences occupation inversion (i.e. a negative effective temperature) when the distribution *within* the bandwidth is considered. This generically results in transport in the opposite direction as in the thermal

9 We use this quantity to estimate the effective temperature as computing the effective distribution operator is numerically costly. If the self-energy was generated by a reservoir, this procedure would yield its distribution.

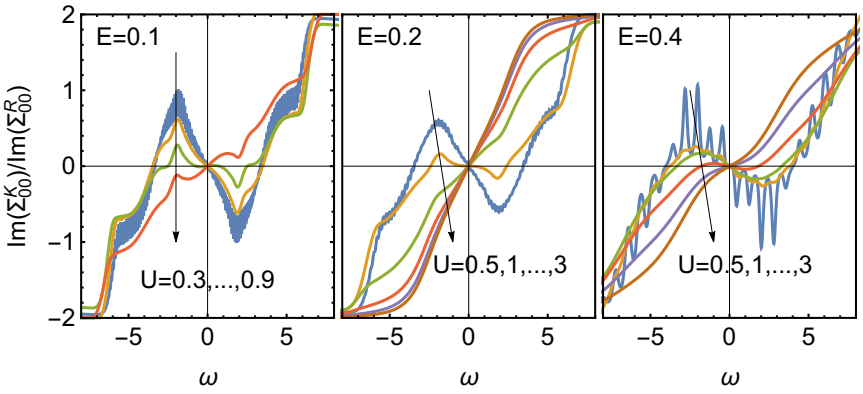


Figure 8.11: The ratio of the Keldysh- and retarded component of the self-energy can be used as an estimate of $2(1-2n(\omega))$. At low interactions we find a negative slope within the (local) bandwidth of the system, indicating an occupation inversion. Higher interactions show finite effective temperatures.

case (compare Section 8.5.1). As a simple example, consider two coupled reservoirs and employ Equation 8.5.1.

While negative temperature states have been produced by quenches in cold atomic gases [Bra+13], they emerge naturally as a stationary state in our approximation.

While these results are interesting they have to be considered with utmost caution. We observe the negative current only in the case, where the system is almost closed. Therefore, the dominant scattering terms in the weak-coupling limit are vastly different from those considered throughout the solution of the flow equations and it is therefore possible, that the self-energy computed with the truncated flow equations does not reflect the correct behavior. In Chapter 7, we already saw, that in this limit, the influence of the cutoff might spoil the results in a non-perturbative fashion. On the other hand, RG techniques are designed to resum such contributions and the scheme employed here goes beyond the perturbative treatment of the two-particle vertex discussed in Chapter 7.

## 8.7 OUTLOOK - EXTENDING THE FEEDBACK OF THE TWO-PARTICLE VERTEX

In Section 8.4.4, we spatially restricted the feedback for the two-particle vertex in to the second-order flow equation to the support of the bare interaction (see Equation 8.4.16 and approximation (4) in Section 8.4.6). While this approximation is justified perturbatively and it is possible, that the results regarding phase transitions depend on this restriction. To investigate this dependence, we generalized the implementation and abandon the simplification to the feedback

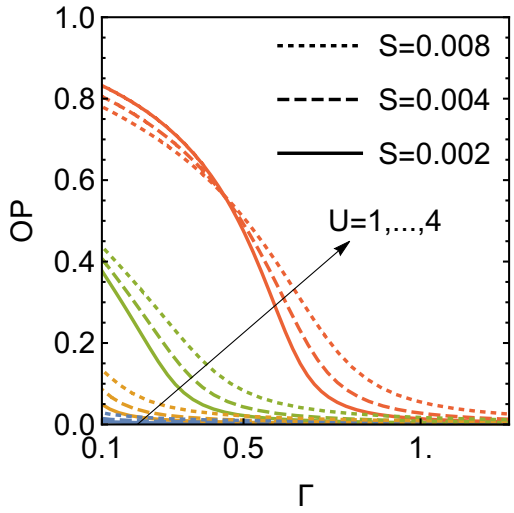


Figure 8.12: The order parameter $\frac{1}{2}|n_{even} - n_{odd}|$ in equilibrium ($E = 0$) as a function of coupling to the reservoirs with an initial symmetry breaking of $s = 0.008, 0.004, 0.002$ (dotted, dashed and solid respectively) using $M = 2$ with the feedback of the two-particle vertex truncated to the finite range $M = 2$. The color encode $U = 1, \ldots, 4$. We find, that in contrast to the algorithm previously discussed, the order parameter does not scale linear with $s$ but instead order spontaneous symmetry breaking sets in at finite coupling for larger $U$.

made in Equation 8.4.16. Approximations (1)-(3) summarized in Section 8.4.6 remain unchanged.

In this more general scheme the evaluation of all rhs of the second-order flow-equations takes $\mathcal{O}(M^3)$ operations, increasing the numerical cost significantly. Note that even for $M = 2$, this includes the feedback of more terms into the second-order flow-equation than the approximation scheme defined by Section 8.4.6, as e.g. $\gamma_{1,1|2,2}$ does generally not vanish, even though the bare two-particle vertex has no such contribution.

In contrast to our previous calculations, we find indications of spontaneous symmetry breaking in equilibrium ($E = 0$) at finite $\Gamma$ (compare Figure 8.12). The order parameter does not scale as $OP \sim s$ for $s \to 0$ (at constant $\Gamma$) but instead finite, $s$-independent order emerges at strong interactions.

As these results are preliminary and a careful analysis of the $M$-dependence is required, it is difficult to evaluate the implications of this finding at this moment and this is left as future work.

## 8.8 CONCLUSION

We have introduced a flexible method to study one-dimensional systems that are coupled to reservoirs (such as a substrate) and penetrated by an electric field. This method is right at the interface of non-equilibrium physics and emergent phenomena that are of paramount importance to condensed matter physics. In the process we demonstrated, how to iteratively obtain correlation functions in presence of a known, frequency dependent self-energy in such infinite systems.

As an example, we applied this method to an interacting tight-binding chain to investigate the interplay of the electric field with the (equilibrium) BKT transition. While we find some evidence, that any electric field destroys the ordered phase, we also observe that a more sophisticated scheme might yield different results. In the proximity of the phase transition, transport is highly sensitive to any breaking of translational invariance, which we interpret as a large, additional resistivity.

Furthermore, we observe that small interactions in the limit of small couplings to the environment delocalize the system, even at large fields, and allow for residual transport. Furthermore, we find a parameter regime where the electric field could induce occupation inversion. This leads to anomalous transport *against* the applied electric field. To decide, whether this is a genuine phenomenon or an indication of a localized-to-delocalized transition requires further analysis, and ideally a complementary numerical method is required.

While this work leaves open questions it can be seen as a starting point to investigate questions that are inaccessible to other methods. Furthermore, the algorithm to obtain local correlation functions of systems in an electric field can likely be transferred to other methods or physical scenarios; future work could include the extension of a similar technique to address periodically driven systems.

# 9 CONCLUSION

## 9.1 SUMMARY

Before we close, we will briefly summarize the methods developed in this thesis as well as the physical results obtained within each chapter.

### 9.1.1 *Methodological foundation*

In Chapters 2, 3 and 4 we presented a pedagogical introduction to the non-equilibrium Green's function formalism, perturbation theory and the functional renormalization group. Due to their importance for later chapters we discuss in detail how to obtain local correlation functions in larger systems. Moreover, we discuss under what conditions equilibrium reservoirs thermalize subsystems and how the fluctuation-dissipation theorem emerges in equilibrium. We furthermore put emphasis on the conservation of symmetries within diagrammatic approximations and the fRG.

As tight-binding chains take a central roll throughout this thesis, we also discuss efficient numeric algorithms to obtain their local correlation functions. This methodological introduction forms the basis for the developments presented in the following chapters.

### 9.1.2 *Transport in a quasiperiodic potential*

We have demonstrated, that transport in a quasiperiodic potential displays a much richer phenomenology than previously expected. In contrast to the case of quenched disorder, we demonstrate that breaking integrability does not immediately induce diffusion but instead yields superdiffusive transport on long time-scales. When increasing the two-particle interaction, we do not observe a finite region of diffusion but instead find a smooth transition from ballistic (at U=0), to superdiffusive, to subdiffusive transport. In quenched disorder subdiffusive transport is commonly explained by regions of unusually strong disorder. Our work, however, provides evidence that subdiffusive transport also appears in a quasiperiodic potential, where such regions are absent. We demonstrate this in linear response using DMRG as well as in the relaxation of a domain wall using fRG, indicating that the Griffiths picture is incomplete.

### 9.1.3 *Excited eigenstates using fRG*

We developed a set of novel techniques to obtain approximate single-particle correlation functions of arbitrary excited eigenstates in interacting systems. On the example of simple tight-binding chains, we demonstrated that an efficient implementation can be achieved. The complexity of three of the algorithms proposed scale linearly in the system size. This allows us to access long chains of up to $\mathcal{O}\left(10^5\right)$ sites.

First, we employ the analytically known ground-state properties of this system to evaluate the quality of these approximations. We then provide evidence, that the excitation energy of a generic pure state above the ground state can serve as an infrared cutoff to low-energy properties and itself results in the emergence of power law behavior. In contrast, we demonstrate that individual, highly excited states can result in characteristic features in the spectral function that greatly differ from a thermal expectation.

As an outlook, we presented a potential rout to go beyond the first-order approximation and introduce an algorithm to simulate quenches from an excited eigenstate.

### 9.1.4 *Steady state of large, open systems*

One of the crucial ingredients to transport in the presence of interaction is inelastic scattering, which is not included in an effective single-particle picture produced by a first order truncation within fRG. To overcome this limitation, we developed an algorithm that includes two-particle scattering on the level of perturbation theory for large systems of interacting particles. In the process, we also discuss how such an algorithm can be parallelized on a large number of independent CPUs without shared memory for a sparse two-particle interaction.

We then study transport in long chains with leads attached to the ends. We demonstrate, that we recover the fluctuation-dissipation theorem in equilibrium when the cutoff is chosen accordingly.

To drive the system out of equilibrium we apply a bias in form of different chemical potentials in the reservoirs. We argue that the appropriate choice of cutoff is a priori not clear and compare results for different possibilities. We find that physical observables out of equilibrium depend strongly on this choice. We associate this with artificial scattering introduced by the cutoff and demonstrate, that this affects the physical system non-perturbatively.

### 9.1.5 *Systems in an electric field*

We demonstrated, how to effectively employ the symmetries of a translationally invariant system in an electric field. This allows us to systematically investigate infinite systems in the presence of spatially extended correlations within a second-order fRG approximation.

We then apply this method to a tight-binding model with nearest neighbor interaction. In the absence of an environment and electric field the system is known to undergo a transition to a charge-density wave at large interaction.

In equilibrium, we provide evidence that our fRG approximation reproduces this transition in the closed limit but any finite coupling to the environment destroys the order. Out of equilibrium, we demonstrate that any electric field provides a cutoff to the ordering tendencies and therefore prevents ordering even in the weak coupling limit.

We then discuss the large electric fields at low coupling to the reservoirs, where Wannier-Stark localization becomes relevant. In that limit, we find that interactions delocalize the system and allow for transport. Furthermore, we identify a weakly interacting regime where the driving induces a state with current opposite to the electric field and the system appears to feature a negative effective temperature.

As an outlook, we presented an improved version of the approximation discussed before and provide preliminary evidence for symmetry breaking in the open system.

## 9.2 OUTLOOK

The schemes developed in this work are designed to be flexible and we believe that they will be useful to answer interesting questions beyond what we discussed in this work. The approximate nature of the methods used is bound to leave open questions for future investigation, some of which should be explored with complementary methods. Next, we identify some avenues to apply and extend this work beyond the problems discussed:

MOBILITY EDGES IN MANY-BODY LOCALIZED SYSTEMS The method we introduced in Chapter 6 can be applied to investigate mobility edges in many-body localized systems [LLA15; Li+15; Wei+19]. Especially the possibility of quenches from an excited eigenstate is promising, as it allows for direct access to transport properties.

However, many of the algorithms introduced in that chapter rely on an effective single-particle picture. In contrast, most of the phenomenology of many-body localized systems lies beyond a first-order treatment; therefore, taking into account higher-order contributions is imperative for a better understanding of this phase.

While in Chapter 6 we already provide an idea how to go beyond first order the details of such a method is left for future work.

PERIODIC DRIVING In the presence of periodic driving, the *Floquet theorem*, as the time-space analog of the Bloch theorem, leads to a decomposition into time-periodic Floquet modes [Shi65; GH98].

$$\begin{aligned} \Psi(t) &= e^{-i\epsilon_\alpha t}\phi_\alpha(t),\ \phi_\alpha(t+T) = \phi_\alpha(t) \\ \bar{H}(t) &= H(t) - i\partial_t \Rightarrow \bar{H}(t)\phi_\alpha(t) = \epsilon_\alpha\phi_\alpha(t). \end{aligned} \tag{9.2.1}$$

As Floquet modes at different energy are not independent

$$\bar{H}(t)\phi_\alpha(t)e^{in\Omega t} =: \bar{H}(t)\phi_{\alpha,n} = (\epsilon_\alpha + n\Omega)\phi_{\alpha,n} \tag{9.2.2}$$

we consequently restrict $\epsilon_\alpha$ to its unit cell and introduce the Floquet index $n$. The Floquet Hamiltonian in this basis reads

$$\bar{H}_{n,n'} = -n\Omega\delta_{n,n'} + H_{n'-n} \tag{9.2.3}$$

where $H_n$ denotes the Fourier components of the time-dependent Hamiltonian.

Driven systems are of great theoretical interest because of their uses in quantum control [Pre+08; GJo3; Lig+07] and the promise of novel phases of matter [Rec+13; Zha+17]. First-order fRG approximations have been successfully used to describe such systems in their synchronized state in presence of two-particle interactions [EMK16b; EMK16a; Ken18].

At finite driving, the Floquet Hamiltonian $\bar{H}$ has the same structure as the problem discussed in Chapter 8. We therefore believe the methods discussed in that chapter can also be employed to discuss finite, interacting systems in the presence of periodic driving in a second-order truncation scheme.

TWO-DIMENSIONAL MODELS In one dimension, methods like DMRG have lead to great theoretical progress. While some extensions of the DMRG idea exist to describe ground states of two-dimensional systems [Jor+08] any calculation at finite energy density quickly becomes impractical [Gol+16; CDC19]. In higher dimensions, correlations become less significant and satisfactory results can be obtained with the dynamical mean-field theory [Kot+06; Geo+96]. Correlated systems out of equilibrium in two dimensions, however have remained inaccessible to most methods.

While this work focuses on one-dimensional lattices, the functional renormalization group has no inherent dependence on the dimensionality and was successfully used to investigate competing instabilities in two dimensions [Met+12]. Some of the concepts discussed throughout this thesis can be readily transferred to two-dimensional models. The technique presented in Chapter 7 can be applied to finite patches

in an almost arbitrary spatial arrangement. As we have demonstrated in Chapter 8, symmetries of a system in an electric field allow for an effective dimensional reduction of the problem, making it a promising candidate to study effects of driving in an infinite cylinder .

Furthermore, we hope that some of the simplifications achieved in this work can be transferred to a real-time version of a second-order fRG. This would allow us to directly investigate quenches in the presence of spontaneous symmetry breaking [Sad+06] or the effects of many-body localization on transport in two dimensions [Cho+16].

# APPENDIX

# A

# TWO GREEN'S FUNCTION INTEGRALS

In Chapter 7, we discuss how to include the flow of the two-particle vertex on a perturbative level. To obtain an efficient algorithm, we rely on analytic expressions for all two-Green's-function integrals (see Section 7.3.3). In this appendix, we are going to discuss in more detail how to obtain these.

## A.1 PRIMITIVE INTEGRALS

Using Equations 7.3.13 and 7.3.17, the fermionic degrees of freedom can be largely decoupled from the frequency. As an example, Equation 7.3.18 shows how to decompose the retarded-Keldysh two-Green's function integral. The remaining frequency integrals are all of one of three types.

$$\begin{aligned} f_0(a,b) &= \int d\omega \frac{1}{\omega - a}\frac{1}{\omega - b} \\ f_1(a,b,\mu) &= \int d\omega \frac{1}{\omega - a}\frac{1}{\omega - b}\mathrm{sgn}(\omega - \mu) \\ f_2(a,b,\mu,\mu') &= \int d\omega \frac{1}{\omega - a}\frac{1}{\omega - b}\mathrm{sgn}(\omega - \mu)\mathrm{sgn}(\omega - \mu') \end{aligned} \tag{A.1.1}$$

An efficient notation of the results can be achieved using the indefinite integral

$$\begin{aligned} \eta(\omega,a,b) &= \int d\omega \frac{1}{\omega - a}\frac{1}{\omega - b} \\ &= \begin{cases} \frac{1}{a-b}\left(\ln(\omega - a) - \ln(\omega - b)\right) & \text{for } a \neq b \\ \frac{1}{a-\omega} & \text{for } a = b \end{cases} \end{aligned} \tag{A.1.2}$$

with the limiting behavior

$$\begin{aligned} &\eta(\infty,a,b) = 0, \\ &\eta(-\infty,a,b) = \begin{cases} -\left[\mathrm{sgn}(\mathrm{Im}\, a) - \mathrm{sgn}(\mathrm{Im}\, b)\right]\frac{i\pi}{a-b} & \text{for } a \neq b \\ 0 & \text{for } a = b. \end{cases} \end{aligned} \tag{A.1.3}$$

Here, we decide to place the branch cut (as is conventional) along the negative real axis. Finally, the three integrals needed read:

$$\begin{aligned} f_0(a,b) &= \eta(\infty,a,b) - \eta(-\infty,a,b) \\ &= \begin{cases} 0 & \operatorname{sgn}(\operatorname{Im} a) = \operatorname{sgn}(\operatorname{Im} b) \\ 2\pi i \frac{1}{a-b} & \operatorname{Im} a > 0,\ \operatorname{Im} b < 0 \\ -2\pi i \frac{1}{a-b} & \operatorname{Im} a < 0,\ \operatorname{Im} b > 0 \end{cases} \\ f_1(a,b,\mu) &= \eta(\infty,a,b) - \eta(\mu,a,b) - [\eta(\mu,a,b) - \eta(-\infty,a,b)] \\ &= -2\eta(\mu,a,b) - [\operatorname{sgn}(\operatorname{Im} a) - \operatorname{sgn}(\operatorname{Im} b)]\,\frac{i\pi}{a-b} \end{aligned} \tag{A.1.4}$$

$$\begin{aligned} &f_2(a,b,\mu,\mu') \\ &= \begin{cases} f_0(a,b) & \mu = \mu' \\ -2\eta(\mu',a,b) + 2\eta(\mu,a,b) & \mu < \mu' \\ + [\operatorname{sgn}(\operatorname{Im} a) - \operatorname{sgn}(\operatorname{Im} b)]\,\frac{i\pi}{a-b} & \end{cases} \end{aligned} \tag{A.1.5}$$

where for convenience we set $0/0 = 0$.

## A.2 TWO-GREEN'S-FUNCTION INTEGRALS

Now a full table of the two-Green's function integrals can be provided:

| | R | A | K |
|---|---|---|---|
| R | $0$ | $\pm Q_{q_1} \otimes Q^{\dagger}_{q_2} f_0(\pm\lambda_{q_1}, \lambda^*_{q_2} - \Omega)$ | $\pm Q_{q_1} \otimes Q_{q_2}\eta_k f_1(\pm\lambda_{q_1}, \lambda_{q_2} - \Omega, \mu_k)$<br>$\mp Q_{q_1} \otimes \eta_k Q^{\dagger}_{q_2} f_1(\pm\lambda_{q_1}, \lambda^*_{q_2} - \Omega, \mu_k)$ |
| A | | $0$ | $\pm Q^{\dagger}_{q_1} \otimes Q_{q_2}\eta_k f_1(\pm\lambda^*_{q_1}, \lambda_{q_2} - \Omega, \mu_k)$<br>$\mp Q^{\dagger}_{q_1} \otimes \eta_k Q^{\dagger}_{q_2} f_1(\pm\lambda^*_{q_1}, \lambda^*_{q_2} - \Omega, \mu_k)$ |
| K | | | $\pm Q_{q_1}\eta_{k_1} \otimes Q_{q_2}\eta_{k_2} f_2(\pm\lambda_{q_1}, \lambda_{q_2} - \Omega, \mu_{k_1}, \mu_{k_2})$<br>$\mp Q_{q_1}\eta_{k_1} \otimes \eta_{k_2} Q^{\dagger}_{q_2} f_2(\pm\lambda_{q_1}, \lambda^*_{q_2} - \Omega, \mu_{k_1}, \mu_{k_2})$<br>$\mp \eta_{k_1} Q^{\dagger}_{q_1} \otimes Q_{q_2}\eta_{k_2} f_2(\pm\lambda^*_{q_1}, \lambda_{q_2} - \Omega, \mu_{k_1}, \mu_{k_2})$<br>$\pm \eta_{k_1} Q^{\dagger}_{q_1} \otimes \eta_{k_2} Q^{\dagger}_{q_2} f_2(\pm\lambda^*_{q_1}, \lambda^*_{q_2} - \Omega, \mu_{k_1}, \mu_{k_2})$ |

Table A.1: $\int d\omega g^{\text{row}}(\pm\omega) g^{\text{col}}(\omega + \Omega)$. For readability, we omit the summations as well as the external indices. They are to be placed in analogy to Equation 7.3.18. The missing entries of the Table can be obtained by considering $\int d\omega g^{\text{row}}(\pm\omega) g^{\text{col}}(\omega + \Omega) = \int d\omega g^{\text{col}}(\pm\omega) g^{\text{row}}(\omega \mp \Omega)$.

# B

# THREE GREEN'S FUNCTION INTEGRALS

## B.1 DECOUPLING FREQUENCY DEPENDENCE

Similar to the case of two Green's functions we use Equations 7.3.13 and 7.3.17 to decouple the frequency dependence from the fermionic degrees of freedom. To this end, let us inspect the self-energy contribution in the x/p channel:

$$\Sigma^{x}_{1'|1}(\varphi) + \Sigma^{p}_{1'|1}(\varphi) = \frac{1}{8\pi^2} \sum \bar{v}_{1'4'|32} \bar{v}_{3'2'|14} \underbrace{\int d\Omega \int d\omega G_{3|3'}(\omega) G_{4|4'}(\omega + \Omega)\, G_{2|2'}(\Omega + \varphi)}_{T_{342|3'4'2'}} \tag{B.1.1}$$

From here, we proceed similar to the case of two Green's functions. Thus, we only give a rudimentary sketch of how to obtain these. Essentially, we have to integrate the results from Appendix A one more time. To that end, we will continue to employ the definition of $\eta$ from that section.

## B.2 ADDITIONALLY NEEDED PRIMITIVE INTEGRAL

Just using the tabulated version of this integral is however misleading. The following expression is a correct indefinite integral:

$$\begin{aligned} g_0(\omega, a, b, c) &= \int d\omega \ln(\omega - a) \frac{1}{\omega - b} \frac{1}{\omega - c} \\ &= \frac{1}{b - c} \left\{ \ln(x - a) \left[ \ln\left( \frac{x - b}{a - b} \right) - \ln\left( \frac{x - c}{a - c} \right) \right] \right. \\ &\quad \left. + \mathrm{Li}_2\left( \frac{a - x}{a - b} \right) - \mathrm{Li}_2\left( \frac{a - x}{a - c} \right) \right\} \end{aligned} \tag{B.2.1}$$

For $a, b, c \in \mathbb{C}$ this primitive integral is, however, not continuous. Hence, the fundamental theorem of calculus does not apply (compare Figure B.1):

$$g_0(\omega_2, a, b, c) - g_0(\omega_1, a, b, c) \neq \int_{\omega_1}^{\omega_2} d\omega \ln(\omega - a) \frac{1}{\omega - b} \frac{1}{\omega - c}$$

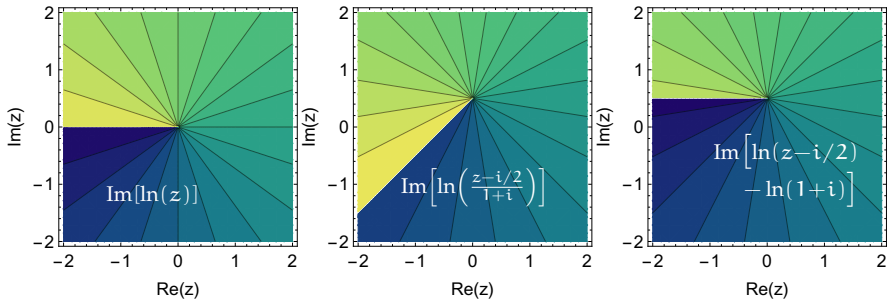


Figure B.1: *Left panel:* This panel shows the imaginary part of the logarithm in the complex plane. It has a branching point at $z = 0$ and the usual convention is to position the branch cut along the negative real axis. *Middle panel:* When linearly transforming $z$ the branching point can be shifted and rotated. This can lead to a discontinuous function on the real axis even though the branching point has a finite imaginary part. *Right panel:* The difference between the function shown in the center panel to the one shown here is piecewise constant. This constant, however, moves the branch cut parallel to the real axis making the function continuous there.

This can be fixed by adding piecewise constant functions to get a continuous primitive integral. We fix the free constant remaining by defining

$$\lim_{\Omega\to-\infty} g(\Omega, a, b, c) = 0$$
$$\Rightarrow g(\Omega, a, b, c) = \int_{-\infty}^{\Omega} d\omega \ln(\omega - a)\frac{1}{\omega - b}\frac{1}{\omega - c}$$

Let us fix the two summands of Equation B.2.1 individually. For the product of two logarithms with $a, b, c \in \mathbb{C}$ we find

$$\ln\left(\frac{x+a}{b}\right)\ln(x+c)$$
$$-2\pi i \ln(x_0+c)\mathrm{sgn}(\mathrm{Im}(a))\theta(x-x_0)\theta(-\mathrm{Re}(\frac{a+x_0}{b}))$$

with $x_0 = -\mathrm{Im}(ab^*)/\mathrm{Im}(b*)$ is continuous on the real axis. The second summand of this expression is piecewise constant and makes the whole function continuous (if not differentiable). Similarly

$$\mathrm{Li}_2\left(\frac{x+a}{b}\right) + \theta(x-x_0)\theta(\mathrm{Re}(\frac{a+x_0}{b})-1)\mathrm{sgn}(\mathrm{Im}(a))2\pi i \ln\left(\frac{x_0+a}{b}\right)$$

is continuous and only differs from the dilogarithm by a piecewise constant function. Putting these together we end up with a unique, continuous definition of a function $g$ that differs from $g_0$ only by a piecewise constant function.

### B.2.1 *Decomposed three-Green's function integrals*

With the shorthand

$$S(a,b) = \operatorname{sgn}(\operatorname{Im} a) - \operatorname{sgn}(\operatorname{Im} b)$$

we set out to obtain the three types of integrals appearing when evaluating Equation B.1.1.

NO SIGNS

$$\begin{aligned}&\int_{-\infty}^{\infty} dx' \int_{-\infty}^{\infty} dx \frac{1}{x-a}\frac{1}{x \pm x' - b}\frac{1}{x'-c}\\ &= \mp i\pi S(a,b)\eta(-\infty, \mp a \pm b, c)\end{aligned}$$

ONE SIGNS A single sign can always be transformed to appear in the $x'$ component.

$$\begin{aligned}&\int_{-\infty}^{\infty} dx' \int_{-\infty}^{\infty} dx \frac{1}{x-a}\frac{1}{x \pm x' - b}\frac{1}{x'-c}\operatorname{sgn}(x'-\mu')\\ &= \mp i\pi S(a,b)\left[2\eta(\mu', \mp a \pm b, c) - \eta(-\infty, \mp a \pm b, c)\right]\end{aligned}$$

TWO SIGNS Two signs can be shifted such that they are in $x$ and $x'$ respectively.

$$\begin{aligned}&\int_{-\infty}^{\infty} dx' \int_{-\infty}^{\infty} dx \frac{1}{x-a}\frac{1}{x \pm x' - b}\frac{1}{x'-c}\operatorname{sgn}(x-\mu)\operatorname{sgn}(x'-\mu')\\ &= \pm\left[-i\pi S(a,b) - 2\ln(\mu - a)\right]\left[\eta(-\infty, \mp a \pm b, c) - 2\eta(\mu', \mp a \pm b, c)\right]\\ &\quad 2[g(\infty, -\mu + b, -a + b, \pm c) + g(-\infty, -\mu + b, -a + b, \pm c)\\ &\quad - 2g(\mu', -\mu + b, -a + b, \pm c)]\end{aligned}$$

THREE SIGNS

$$\begin{aligned}&\int_{-\infty}^{\infty} dx' \int_{-\infty}^{\infty} dx \frac{1}{x-a}\frac{1}{x \pm x' - b}\frac{1}{x'-c}\\ &\qquad \operatorname{sgn}(x-\mu)\operatorname{sgn}(x'-\mu')\operatorname{sgn}(x \pm x' - \tilde{\mu})\\ &= \int_{-\infty}^{\infty} dx'\left[-\eta(-\infty, a, \mp x' + b)\right]\frac{1}{x'-c}\operatorname{sgn}(x'-\mu')\\ &+ \int_{-\infty}^{\infty} dx'\left[-2\operatorname{sgn}(\mu - \tilde{\mu}(x'))(\eta(\mu, a, \mp x' + b))\right]\frac{1}{x'-c}\operatorname{sgn}(x'-\mu')\\ &+ \int_{-\infty}^{\infty} dx'\left[+2\operatorname{sgn}(\mu - \tilde{\mu}(x'))(\eta(\tilde{\mu}(x'), a, \mp x' + b))\right]\frac{1}{x'-c}\operatorname{sgn}(x'-\mu')\\ &= T_1 + T_2 + T_3\end{aligned}$$

The first term is already known:

$$\begin{aligned}T_1 &= \int_{-\infty}^{\infty} dx'\left[-\eta(-\infty, a, \mp x' + b)\right]\frac{1}{x'-c}\operatorname{sgn}(x'-\mu')\\ &= \mp i\pi S(a,b)\left[2\eta(\mu', \mp a \pm b, c) - \eta(-\infty, \mp a \pm b, c)\right]\end{aligned}$$

For the second term

$$\begin{aligned}
T_2 &= \int_{-\infty}^{\infty} dx' \big[-2\mathrm{sgn}(\mu - \tilde{\mu}(x'))(\eta(\mu, a, \mp x' + b))\big] \frac{1}{x' - c} \mathrm{sgn}(x' - \mu') \\
&= -2 \int_{-\infty}^{\infty} dx' \frac{1}{a \pm x' - b} \big[\ln(\mu - a) - \ln\big(\mu \pm x' - b\big)\big] \\
&\quad \frac{1}{x' - c} \mathrm{sgn}(x' - \mu') \mathrm{sgn}(\mu \pm x' - \bar{\mu})
\end{aligned}$$

we concentrate on the $+$ case, the $-$ case follows analogously.

$$\begin{aligned}
T_2^+ &= -2 \int_{-\infty}^{\infty} dx' \frac{1}{a + x' - b} \big[\ln(\mu - a) - \ln\big(\mu + x' - b\big)\big] \\
&\qquad \frac{1}{x' - c} \mathrm{sgn}(x' - \mu') \mathrm{sgn}(\mu + x' - \bar{\mu}) \\
&= -2 \ln(\mu - a) \Big[ -\eta(-\infty, b - a, c) \\
&\qquad - 2\mathrm{sgn}(\bar{\mu} - \mu - \mu') \left\{ \eta(\bar{\mu} - \mu, b - a, c) - \eta(\mu', b - a, c) \right\} \Big] \\
&\qquad + 2 \big[ g(\infty, b - \mu, b - a, c) - g(-\infty, b - \mu, b - a, c) \\
&\qquad - 2\mathrm{sgn}(\bar{\mu} - \mu - \mu') \big\{ g(\bar{\mu} - \mu, b - \mu, b - a, c) \\
&\qquad - g(\mu', b - \mu, b - a, c) \big\} \big]
\end{aligned}$$

and finally the third part analogously

$$\begin{aligned}
&T_3^+ \\
&= \int_{-\infty}^{\infty} dx' \big[+2\mathrm{sgn}(\mu - \tilde{\mu}(x'))(\eta(\tilde{\mu}(x'), a, \mp x' + b))\big] \frac{1}{x' - c} \mathrm{sgn}(x' - \mu') \\
&= -2 \ln(\bar{\mu} - b) \Big[ -\eta(-\infty, a - b, -c) \\
&\qquad - 2\mathrm{sgn}(\mu + \mu' - \bar{\mu}) \left\{ \eta(\mu - \bar{\mu}, a - b, -c) - \eta(-\mu', a - b, -c) \right\} \Big] \\
&\quad + 2 \big[ g(\infty, a - \bar{\mu}, a - b, -c) - g(-\infty, a - \bar{\mu}, a - b, -c) \\
&\quad - 2\mathrm{sgn}(\mu - \bar{\mu} + \mu') \big\{ g(\mu - \bar{\mu}, a - \bar{\mu}, a - b, -c) \\
&\qquad - g(-\mu', a - \bar{\mu}, a - b, -c) \big\}.
\end{aligned}$$

Using these integrals, a table analogous to Table A.1 can be compiled. As we already found there, special care has to be take if any of the $a, b, c, \mu\mu', \bar{\mu}$ coincide. When implemented, these can be used to obtain the second-order perturbation theory self-energy numerically efficiently.

# C

# HOW TO CONVOLVE

## C.1 DEFINITION

We define the convolution of the functions $f, g \in \mathbb{C}^{\mathbb{R}}$ as

$$(f * g)(y) = \int_{-\infty}^{\infty} dx f(x) g(y - x) \tag{C.1.1}$$

To naively evaluate this using some discretization is expected to scale as $\mathcal{O}\left(N^2\right)$ where $N$ is the number of points in the grid. In certain cases, this can be done more efficiently, as we will discuss in this appendix.

## C.2 EQUIDISTANT GRIDS

For equidistant grids, we can rewrite the convolution in terms of discrete Fourier transforms, which will allow us to perform significantly faster computations.

### C.2.1 *Discretization*

We employ an equidistant grid with $N \in 2\mathbb{N} + 1$ points to obtain an approximation of $f$ and $g$ in the form of piecewise constant functions (compare left panel of Figure C.1):

$$f(x) = \begin{cases} 0 & & x & < & -\frac{N}{2} w \\ f_i & \left(i - \frac{1}{2}\right) w & \leqslant & x & < & \left(i + \frac{1}{2}\right) w \\ 0 & \frac{N}{2} w & \leqslant & x & & \end{cases} \tag{C.2.1}$$

with a vector $(f_i)_{i=-\frac{N-1}{2} \dots \frac{N-1}{2}}$ the convolution reduces to a convolution of vectors:

$$(f * g)(iw) = \int_{-\infty}^{\infty} dx f(x) g(y - x) = w \sum_k f_k g_{i-k}$$

with the summation bounded appropriately. The summation runs over $\mathcal{O}(N)$ elements, so to obtain the convolution on the entire orginial grid (with $\mathcal{O}(N)$ points) takes $\mathcal{O}\left(N^2\right)$ operations. This can be improved by the use of a Fourier transform.

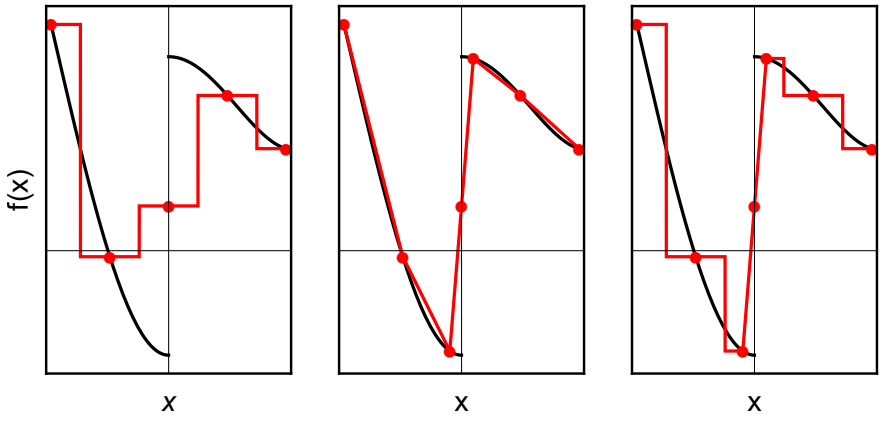


Figure C.1: Pictorial representation of the three different discretizations discussed in this appendix. From left to right we show a piecewise constant approximation on an equidistant grid (discussed in Section C.2), a piecewise linear approximation on an arbitrary grid (see Section C.3) and a piecewise constant approximation with piecewise linear refinements (see Section C.4).

### C.2.2 *Fourier transform*

Using the discrete Fourier transform[1]

$$\begin{aligned} \bar{f}_k &= \frac{1}{\sqrt{N}} \sum_l e^{ilk\frac{2\pi}{N}} f_l \\ f_l &= \frac{1}{\sqrt{N}} \sum_k e^{-ilk\frac{2\pi}{N}} \bar{f}_k \end{aligned} \tag{C.2.2}$$

one rewrites the discrete convolution as

$$\begin{aligned} w \sum_j f_j g_{n-j} &= \frac{w}{N} \sum_{k_1,k_2} \sum_j e^{-ijk_1\frac{2\pi}{N}} \bar{f}_{k_1} e^{-i(n-j)k_2\frac{2\pi}{N}} \bar{g}_{k_2} \\ &= w \sum_k e^{-ink\frac{2\pi}{N}} \bar{f}_k \bar{g}_k. \end{aligned} \tag{C.2.3}$$

which is the back-transform of the product of $\bar{f}_k \bar{g}_k$.

By employing the *fast Fourier transform* (FFT) the discrete Fourier transform can be computed in $\mathcal{O}(N \log(N))$ operations,[2] allowing us to obtain *all* components of the convolution on the same grid in $\mathcal{O}(N \log(N))$ operations.

While this algorithm is very efficient, it is specifically designed for equidistant grids. For our application, however, where vastly different energy scales are to be considered, one is forced to use an overly dense grid, which diminishes the advantage of this method.

1 Note that the library used (FFTW [Fri99]) omits the prefactor

2 In our implementation of the algorithm we employ the FFTW library [Fri99], which provides a FFT implementation for discrete Fourier transforms. To obtain optimal performance, it is beneficial to chose a grid size with small prime factors; as our grid contains an odd number of points we chose a power of 3.

## C.3 ARBITRARY GRIDS

The alternative is an entirely arbitrary grid. As the computations are not much harder, we will assume that the functions convolved are approximated piecewise linearly. On a given grid defined by $\{x_1, \ldots, x_N\}$ with $x_1 < \cdots < x_N$ we assume (compare center panel of Figure C.1)

$$h(x) = \begin{cases} 0 & & & x & < & x_1 \\ a_i^h x + b_i^h & x_i & \leqslant & x & < & x_{i+1} \\ 0 & x_N & \leqslant & x & & \end{cases} \tag{C.3.1}$$

for $h = f, g$ and with $a_i x_{i+1} + b_i = a_{i+1} x_{i+1} + b_{i+1}$ $\forall i$. Then the convolution of the two functions can be written as

$$\begin{aligned} (f * g)(x_i) &= \int_{-\infty}^{\infty} dx f(x) g(x_i - x) \\ &= \sum_{k=1}^{N} \sum_{k'} \int dx \left(a_k^f x - b_k^f\right) \left(a_{k'}^g (x_i - x) - b_{k'}^g\right). \end{aligned} \tag{C.3.2}$$

As the grid is not equidistant, it can happen, that $g(y - x)$ is not linear within an interval of linear $f(x)$. In that case, that segment has to be subdivided into smaller intervals until both functions are linear. This is represented by a sum over $k'$, where we refrain from giving the bounds explicitly; in practice they are easily obtained in $\log(N)$ operations. Using the indefinite integral

$$\int_{-\infty}^{\infty} dx \, (ax - b)(a'x - b') = \frac{1}{3} a a' x^3 + \frac{1}{2} \left(ab' + ba'\right) x^2 + bb' x + c \tag{C.3.3}$$

the convolution can easily be evaluated.

Note that for an efficient algorithm it is of crucial importance, that the grid of $x_i$ is sorted and appropriate algorithms to identify the correct $k'$ are used. Doing this will yield an algorithm of $\mathcal{O}\left(N^2 \log N\right)$.

While this algorithm allows for grids that take the vastly different energy scales of the problem into account, it is (compared with the case of equidistant grids) slow and is the bottleneck of such an implementation.

## C.4 MIXED GRIDS

Assume functions $f$, $g$ are known on a grid $G$ containing $\mathcal{O}(N)$ equidistant points but also $\mathcal{O}(k)$ additional points at arbitrary position.

$$G = \left\{ -\frac{N-1}{2} w, \ldots, \frac{N-1}{2} w \right\} \cup \{x_1, \ldots, x_k\} \tag{C.4.1}$$

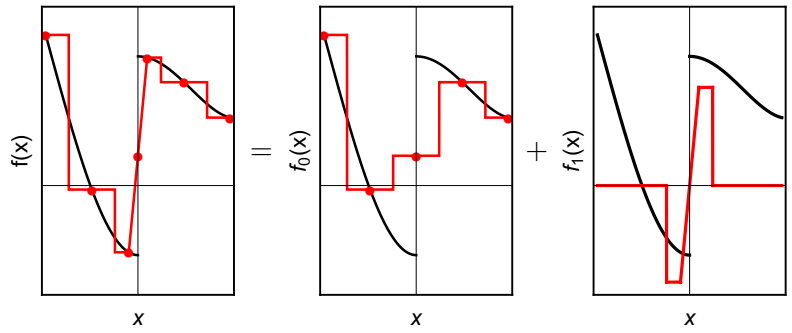


Figure C.2: Pictorial representation of the decomposition proposed in Equation C.4.2. We obtain a approximation on a refined equidistant grid as a decomposition into a piecewise constant function $f_0$ and a series of piecewise linear functions (here only $f_1$) with support only within one segment of the equidistant grid. We have the freedom to chose $\int dx f_1(x) = 0$.

We then define a approximate for of $f$ by decomposing it into a series of functions

$$f(x) \approx \tilde{f}_0(x) + \sum_{i=1}^{N^f} f_i(x) \tag{C.4.2}$$

with particular properties: $\tilde{f}_0(x)$ is the piecewise constant approximation of $f$ on the equidistant subgrid that we discussed in Section C.2. Next, we group together all points outside the equidistant that share the same nearest member of the equidistant grid. The number of these groups is called $N^f$ and we note $N^f \leqslant k$. For each of these groups, we define a piecewise constant function $f_i$, $i \in \underline{N^f}$ such that

1. $f_i$ is linear on all segments of $G \cup \left(\mathbb{Z} + \frac{1}{2}\right) w$
2. $\exists! n \in \{-N, -N+1, \ldots, N\} \ni f_i(x) = 0 \ \forall |x - nw| > \frac{w}{2}$
3. $\int dx f_i(x) = 0 \ \forall i > 0$
4. $\tilde{f}_0(x) + \sum_{i=1}^{N^f} f_i(x) - f(x)$ is constant on all points within each interval of width $w$ centered around a point of the equidistant grid.

The piecewise constant difference is acquired due to requirement (3) and can be absorbed into the piecewise constant function $\tilde{f}_0(x)$. The function including these constants will be referred to as $f_0(x)$. Such a decomposition is illustrated in Figure C.2.

Using the linearity of the operation, a convolution of two functions approximated in such a way can always be decomposed as:

$$(f * g)(y) = (f_0 * g_0)(y) + \sum_i (f_i * g_0)(y) + \sum_j (f_0 * g_j)(y) + \sum_{i,j} (f_i * g_j)(y)$$

We now evaluate this decomposition on the grid and have to distinguish between two cases:

FOR ALL $y$ IN THE EQUIDISTANT GRID the first term can be computed as outlined in Sec. C.2 in $\mathcal{O}(N \log(N))$. Due to out choice $\int dx f_i(x) = 0 = \int dx g_i(x)$, the support of these functions and the fact, that $f_0$ and $g_0$ are piecewise constant the second and third term vanish. The last term can be explicitly computed in $\mathcal{O}\left(k^2 \log(N)\right)$ operations, as $f_i$ and $g_i$ only contain a finite number of points.

FOR EACH $y$ OUTSIDE THE EQUIDISTANT GRID the first term can be explicitly computed in $\mathcal{O}(N)$ operations. The second and third term in this case also result in finite contributions and contribute $\mathcal{O}(k \log(N))$ operations. Most addends of the last term vanish and its contribution to the complexity is sub-leading.

As there are $k$ points outside the equidistant grid and we assume $k \gg N$, evaluating the convolution on all the additional points is of complexity $\mathcal{O}(kN)$.

# D

# GREEN'S FUNCTIONS IN AN ELECTRIC FIELD

In this appendix, we discuss how to obtain the necessary local correlation functions to solve the flow equations discussed in Chapter 8.

As we restricted the number of independent components of the vertex functions in Chapter 8, we only need to obtain a finite number of (frequency dependent) components of the Green's functions and single-scale propagators to compute the rhs of the flow equations.

How to compute these is, however, not clear. In this appendix, we will introduce algorithms to compute all $G_{i,j}$, $S_{i,j}$ for $i,j \in \underline{N}$ with a given $N \in \mathbb{N}$ in the presence of a given self-energy with

$$\begin{aligned} \Sigma_{1'|1} &= 0 \qquad \forall\, |1-1'| \geqslant M \\ \Sigma_{1'|1}(\omega) &= \Sigma_{1'+L|1+L}(\omega + LE) \end{aligned} \tag{D.0.1}$$

and

$$\begin{aligned} h_{1'|1} &= 0 \qquad \forall\, |1-1'| \geqslant M \\ h_{1'|1} &= h_{1'+L|1+L} - LE \end{aligned} \tag{D.0.2}$$

as needed for the approximated flow equations discussed in Chapter 8.

## D.1 SOME NOTATION

Omitting the frequency dependence of the self-energy[1] for an easier notation, $H + \Sigma^{\text{ret}}$ can be decomposed as

$$H + \Sigma^{\text{ret}} = \left(\begin{array}{cc|c|cc} & L & 0 & 0 & 0 \\ & & T_{LS} & 0 & 0 \\ \hline 0 & T_{SL} & S & T_{SR} & 0 \\ \hline 0 & 0 & T_{RS} & & \\ 0 & 0 & 0 & \multicolumn{2}{c}{R} \end{array}\right)$$

with finite matrices $T_{\bullet\bullet}$, $S \in \mathbb{C}^{N\times N}$ and $N \geqslant M$. Note that in general $T_{LS} \neq T_{SL}^{\dagger}$. For simplicity we assume $L|N$.

As we have to distinguish various Green's functions, we will introduce some notation. To indicate a block of the full Green's function we employ a vertical bar:

$$G\big|_{SS}(\omega) = G\big|_{S}(\omega) = \big(G_{i,j}(\omega)\big)_{i,j\in S} \tag{D.1.1}$$

1 Note that the self-energy is $\omega$-local due to energy conservation, which is essential for our procedure.

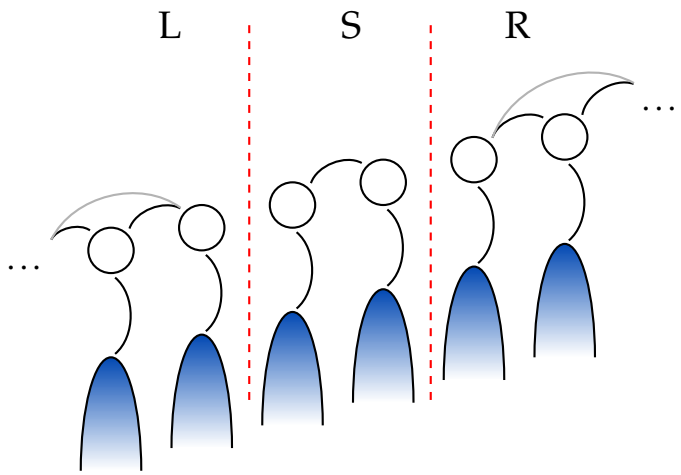


Figure D.1: Pictorial representation of the separation of the system in its three parts. Once the Green's functions for all individual parts are known, the Green's function on subsystem S of the coupled system can be computed.

Instead of considering the infinite matrices in the case of subsystem L and R we only consider the $N \times N$ matrices closest to the system S. The symmetry of the system is therefore expressed as

$$G\big|_{LL}(\omega - NE) = G\big|_{SS}(\omega) = G\big|_{RR}(\omega + NE) \tag{D.1.2}$$

As we will follow the steps employed in Section 2.8.1, we will consider the effects of the couplings consecutively, making a notation for the Green's functions in their absence necessary. To that end $G_{T_{SL}=0}$ denotes the Green's function obtained in a system where $T_{SL} = 0 = T_{LS}$ (similarly for the right subsystem). Therefore, we also note the symmetry

$$G_{T_{SL}=0}\big|_{LL}(\omega - NE) = G_{T_{SR}=0}\big|_{SS}(\omega). \tag{D.1.3}$$

To denote the absence of both couplings, we write

$$G_0(\omega) := G_{T_{SL}=0=T_{SR}}(\omega). \tag{D.1.4}$$

## D.2 RETARDED GREEN'S FUNCTION

First, we will demonstrate, how to obtain $G^{ret}\big|_{SS}$. To this end, we proceed in complete analogy to Section 2.8.1. We therefore discuss the cases of the decouples S-part of the system and the two semi-infinite chains separately and then discuss how to combine these to obtain the Green's function of the full system. The decoupled ($T_{\bullet\bullet} = 0$) $G_0^{ret}\big|_{SS}$ is easily obtained

$$G_0^{ret}\big|_{SS} = \frac{1}{\omega - S + i0}. \tag{D.2.1}$$

With that we find for the semi-infinite chain ($T_{SR} = 0$):

$$\begin{aligned} G^{ret}_{T_{SR}=0}\big|_{SS}(\omega) =& \frac{1}{G^{ret}_0\big|_{SS}{}^{-1}(\omega) - T_{SL} G^{ret}_0\big|_{LL}(\omega) T_{LS}} \\ =& \frac{1}{G^{ret}_0\big|_{SS}{}^{-1}(\omega) - T_{SL} G^{ret}_{T_{SR}=0}\Big|_{SS}(\omega + NE) T_{LS}} \end{aligned} \tag{D.2.2}$$

and similarly for $T_{SL} = 0$. In the second step, we used the inherent symmetry of the system.

Without an electric field, this equation is local in the frequencies and has to be solved self-consistently. At finite electric field, however, this equation couples Green's functions at different energies. If the discretization of the frequencies is fine enough to interpolate Green's functions at intermediate frequencies, this can be used to solve the equation iteratively: the starting point is formed by the boundary condition $\lim_{\omega\to\pm\infty} G(\omega) = 0$, from there we proceed using the above equation to obtain the Green's function at smaller frequencies.[2]

Once we know the exact Green's functions of the three parts that constitute the whole system (compare Figure D.1) we can immediately write down the solution for the infinite system:

$$\begin{aligned} G^{ret}|_{SS}(\omega) =& \frac{1}{G^{ret}_0|^{-1}_{SS}(\omega) - T_{SL} G^{ret}_0|_{LL}(\omega) T_{LS} - T_{SR} G^{ret}_0|_{RR}(\omega) T_{RS}} \\ =& \Big[ G^{ret}_0|^{-1}_{SS}(\omega) - T_{SL} G^{ret}_{T_{SR}=0}|_{SS}(\omega + NE) T_{LS} \\ & \qquad - T_{SR} G^{ret}_{T_{SL}=0}|_{SS}(\omega - NE) T_{RS} \Big]^{-1} \end{aligned} \tag{D.2.3}$$

## D.3 KELDYSH GREEN'S FUNCTION

For the Keldysh component we proceed similarly. In the semi-infinite chain ($T_{SR} = 0$) we use the Dyson equation (compare Equation 2.5.39, corresponding diagrams can be found in Figure D.2):

$$\begin{aligned} & G^{K}_{T_{SR}=0}|_{SS}(\omega) \\ =& \sum_{\alpha,\beta\in\{L,S\}} G^{ret}_{T_{SR}=0}\big|_{S\alpha}(\omega) \Sigma^{K}\big|_{\alpha\beta} G^{adv}_{T_{SR}=0}\Big|_{\beta S}(\omega) \\ =& G^{ret}|_{T_{SR}=0}|_{SS}(\omega) \Sigma^{K}|_{SS}(\omega) G^{adv}|_{T_{SR}=0}|_{SS}(\omega) \\ &+ G^{ret}|_{T_{SR}=0}|_{SS}(\omega) \Sigma^{K}|_{SL}(\omega) G^{adv}_0|_{LL}(\omega) T_{LS} G^{adv}|_{T_{SR}=0}|_{SS}(\omega) \\ &+ G^{ret}_{T_{SR}=0}|_{SS}(\omega) T_{SL} G^{ret}_0|_{LL}(\omega) \Sigma^{K}|_{LS}(\omega) G^{adv}_{T_{SR}=0}|_{SS}(\omega) \\ &+ G^{ret}_{T_{SR}=0}|_{SS}(\omega) T_{SL} G^{K}_{T_{SR}=0}|_{SS}(\omega + NE) T_{LS} G^{adv}|_{T_{SR}=0}|_{SS}(\omega). \end{aligned} \tag{D.3.1}$$

2 If the electric field is smaller than the spacing of the frequency grid, a self-consistency loop is still required.

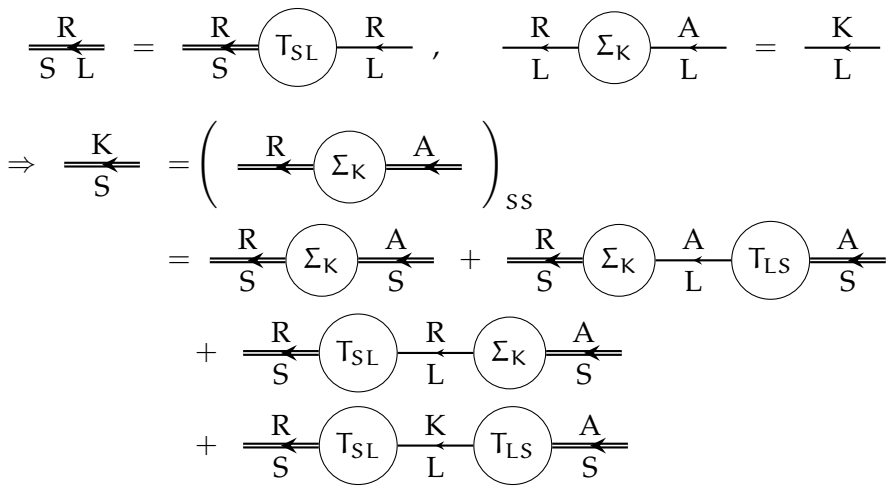


Figure D.2: Diagrammatic representation of Equation D.3.1 for the semi-infinite chain with $T_{SR} = 0$. Single lines represent the decoupled correlators with ($T_{SL} = 0$) while the full lines include this coupling. The letters above the line indicate the RKA-basis while the ones below indicate the domain of *both* single-particle indices of the Green's function.

where in the last line we employed

$$G_0^{ret}|_{LL}(\omega)\Sigma^K|_{LL}(\omega)G_0^{adv}|_{LL}(\omega) = G^K_{T_{SR}=0}|_{SS}(\omega + NE). \quad \text{(D.3.2)}$$

Similar to our findings for the retarded component, this forms a self-consistency equation in the absence of an electric field ($E = 0$). A finite field couples frequencies of distance $E$, allowing us to iteratively solve the equation on a fine enough grid using the initial condition $G^K(\omega) \to 0$ for $\omega \to \pm\infty$.

Combining the results for the two semi-infinite chains we finally find for the Keldysh component of the entire chain:

$$\begin{aligned}
&G^K|_{SS}(\omega) \\
&\quad = G^{ret}\big|_{SS}(\omega)\Big[\Sigma^K|_{SS}(\omega) \\
&\qquad + \Sigma^K|_{SL}(\omega)G_0^{adv}|_{LL}(\omega)T_{LS} + \Sigma^K|_{SR}(\omega)G_0^{adv}|_{RR}(\omega)T_{RS} \\
&\qquad + T_{SL}G_0^{ret}|_{LL}(\omega)\Sigma^K|_{LS}(\omega) + T_{SR}G_0^{ret}|_{RR}(\omega)\Sigma^K|_{RS}(\omega) \\
&\qquad + T_{SL}G^K_{T_{SR}=0}|_{SS}(\omega - EN)T_{LS} + T_{SR}G^K_{T_{SL}=0}|_{SS}(\omega + EN)T_{RS} \\
&\quad \Big]G^{adv}|_{SS}(\omega).
\end{aligned} \quad \text{(D.3.3)}$$

which can be computed immediately once the problems for the semi-infinite chains is solved.

Using these iterations we can obtain all Green's functions necessary to compute the flow equations efficiently in an infinite system.

A similar algorithm could also allow for an efficient computation of correlation functions in a Floquet system.

## D.4 SINGLE-SCALE PROPAGATORS

To obtain the single scale propagators, it is easiest to use the notion

$$S(\omega) = \partial_\Lambda^* G(\omega). \tag{D.4.1}$$

Where $\partial_\Lambda^*$ indicates the derivative with respect to the $\Lambda$-dependence that is directly induced by the cutoff (in contrast to the implicit dependence acquired through the flow equations). For simplicity, we assume that the cutoff is described in terms of a self-energy and therefore included in $T, \Sigma^K$ (see Section 4.2.6). The self-energy will therefore generally include an *explicit* and an *implicit* cutoff dependence.

To compute the single-scale propagators, we make use of the fact that in the cutoff we employ

$$\partial_\Lambda^* \Sigma^\eta_{ab} = 0 \; \forall a \neq b, \; \eta \in \{\text{ret, adv, K}\}$$

so

$$\begin{aligned} \partial_\Lambda^* T_{S\alpha} &= \partial_\Lambda^* T_{\alpha S} = 0 \qquad \alpha = L, R \\ \partial_\Lambda^* \Sigma^K_{S\alpha} &= \partial_\Lambda^* \Sigma^K_{\alpha S} = 0 \qquad \alpha = L, R. \end{aligned} \tag{D.4.2}$$

This restriction reduces the number of terms but a generalization to a more involved cutoff scheme is straightforward.

### D.4.1 *Retarded single-scale propagator*

Using this and Equation D.2.2 we find in the semi-infinite chain:

$$\begin{aligned} S^{ret}_{T_{SR}=0|SS}(\omega) &= \left(\partial_\Lambda^* G^{ret}_{T_{SR}=0}(\omega)\right)\Big|_{SS} \\ &= -\, G^{ret}_{T_{SR}=0}\big|_{SS}(\omega) \Big\{ \partial_\Lambda^* \left[ G_0^{ret}\Big|_{SS}(\omega) \right]^{-1} \\ &\quad - T_{SL} S^{ret}_{T_{SR}=0|SS}(\omega + EN) T_{LS} \Big\} \, G^{ret}_{T_{SR}=0}\big|_{SS}(\omega) \end{aligned} \tag{D.4.3}$$

where the value of $\partial_\Lambda^* \left[ G_0^{ret}\Big|_{SS}(\omega) \right]^{-1}$ depends on the specific cutoff used. Yet again, this provides either a self-consistency equation (at $E = 0$) or can be evaluated iteratively (for $E \neq 0$).

After the retarded single-scale propagator for semi-infinite systems is computed the single-scale propagator of an infinite chain can be obtained as

$$\begin{aligned} S^{\mathrm{ret}}\big|_{SS}(\omega) = &- G^{\mathrm{ret}}\big|_{SS}(\omega)\Big\{\partial^*_\Lambda\left[G_0^{\mathrm{ret}}\Big|_{SS}(\omega)\right]^{-1} \\ &- T_{SL}S^{\mathrm{ret}}_{T_{SR}=0}|_{SS}(\omega+EN)T_{LS} \\ &- T_{SR}S^{\mathrm{ret}}_{T_{SL}=0}|_{SS}(\omega-EN)T_{RS} \\ &\Big\} G^{\mathrm{ret}}_{T_{SR}=0}\big|_{SS}(\omega). \end{aligned} \tag{D.4.4}$$

### D.4.2 *Keldysh single-scale propagator*

Similarly one uses Equation D.3.3 to obtain the Keldysh component of the single-scale propagator:

$$\begin{aligned} &S^K|_{SS}(\omega) \\ =&S^{\mathrm{ret}}|_{SS}(\omega)\Big[\dots\Big]G^{\mathrm{adv}}|_{SS}(\omega) + G^{\mathrm{ret}}|_{SS}(\omega)\Big[\dots\Big]S^{\mathrm{adv}}|_{SS}(\omega) \\ &+ G^{\mathrm{ret}}||_{SS}(\omega)\big(\partial^*_\Lambda\Sigma^K|_{SS}(\omega) + \Sigma^K|_{SL}(\omega)S_0^{\mathrm{adv}}|_{LL}(\omega)T_{LS} \\ &+ \Sigma^K|_{SR}(\omega)S_0^{\mathrm{adv}}|_{RR}(\omega)T_{RS} + T_{SL}S_0^{\mathrm{ret}}|_{LL}(\omega)\Sigma^K|_{LS}(\omega) \\ &+ T_{SR}S_0^{\mathrm{ret}}|_{RR}(\omega)\Sigma^K|_{RS}(\omega) + T_{SL}S^K_{T_{SR}=0}|_{SS}(\omega+EN)T_{LS} \\ &+ T_{SR}S^K_{T_{SL}=0}|_{SS}(\omega-EN)T_{RS}\big)G^{\mathrm{adv}}|_{SS}(\omega). \end{aligned}$$

The brackets $\Big[\dots\Big]$ denote the corresponding brackets from Equation D.3.3. Depending on the cutoff $\Sigma^K$ might include an explicit $\Lambda$ dependence. One example is the $T = 0$ reservoir cutoff.

While these equations are cumbersome, they allow us to numerically efficiently obtain the full Green's function and single-scale propagators of an *infinite* system and are crucial to the algorithm presented in Chapter 8.

# BIBLIOGRAPHY


[Aga+15] K. Agarwal, S. Gopalakrishnan, M. Knap, M. Müller, and E. Demler. "Anomalous Diffusion and Griffiths Effects Near the Many-Body Localization Transition." In: *Physical Review Letters* 114.16 (2015). DOI: 10.1103/physrevlett.114.160401.

[Aga+17] K. Agarwal, E. Altman, E. Demler, S. Gopalakrishnan, D. A. Huse, and M. Knap. "Rare-region effects and dynamics near the many-body localization transition." In: *Annalen der Physik* 529.7 (2017), p. 1600326. DOI: 10.1002/andp.201600326.

[Alt10] A. Altland. *Condensed Matter Field Theory*. Cambridge University Press, 2010. ISBN: 0521769752.

[AV15] E. Altman and R. Vosk. "Universal Dynamics and Renormalization in Many-Body-Localized Systems." In: *Annual Review of Condensed Matter Physics* 6.1 (2015), pp. 383–409. DOI: 10.1146/annurev-conmatphys-031214-014701.

[Ama+12] A. Amaricci, C. Weber, M. Capone, and G. Kotliar. "Approach to a stationary state in a driven Hubbard model coupled to a thermostat." In: *Physical Review B* 86.8 (2012). DOI: 10.1103/physrevb.86.085110.

[And+04] S. Andergassen, T. Enss, V. Meden, W. Metzner, U. Schollwöck, and K. Schönhammer. "Functional renormalization group for Luttinger liquids with impurities." In: *Physical Review B* 70.7 (2004). DOI: 10.1103/physrevb.70.075102.

[And06] S. Andergassen. "Functional Renormalization-Group Analysis of Luttinger Liquids with Impurities." PhD thesis. University of Stuttgart, 2006.

[And+99] E. Anderson et al. *LAPACK Users' Guide*. Third. Philadelphia, PA: Society for Industrial and Applied Mathematics, 1999. ISBN: 0-89871-447-8 (paperback).

[And58] P. W. Anderson. "Absence of Diffusion in Certain Random Lattices." In: *Physical Review* 109.5 (1958), pp. 1492–1505. DOI: 10.1103/physrev.109.1492.

[And61] P. W. Anderson. "Localized Magnetic States in Metals." In: *Physical Review* 124.1 (1961), pp. 41–53. DOI: 10.1103/physrev.124.41.

[Aok+14] H. Aoki, N. Tsuji, M. Eckstein, M. Kollar, T. Oka, and P. Werner. "Nonequilibrium dynamical mean-field theory and its applications." In: *Reviews of Modern Physics* 86.2 (2014), pp. 779–837. DOI: 10.1103/revmodphys.86.779.

[Ash76] N. W. Ashcroft. *Solid State Physics*. Cengage Learning, 1976. ISBN: 0030839939.

[Ata+13] Y. Y. Atas, E. Bogomolny, O. Giraud, and G. Roux. "Distribution of the Ratio of Consecutive Level Spacings in Random Matrix Ensembles." In: *Physical Review Letters* 110.8 (2013). DOI: 10.1103/physrevlett.110.084101.

[Aul+04] C. Aulbach, A. Wobst, G.-L. Ingold, P. Hänggi, and I. Varga. "Phase-space visualization of a metal–insulator transition." In: *New Journal of Physics* 6 (2004), pp. 70–70. DOI: 10.1088/1367-2630/6/1/070.

[BPM12] J. H. Bardarson, F. Pollmann, and J. E. Moore. "Unbounded Growth of Entanglement in Models of Many-Body Localization." In: *Physical Review Letters* 109.1 (2012). DOI: 10.1103/physrevlett.109.017202.

[Bar13] T. Barthel. "Precise evaluation of thermal response functions by optimized density matrix renormalization group schemes." In: *New Journal of Physics* 15.7 (2013), p. 073010. DOI: 10.1088/1367-2630/15/7/073010.

[BAA06] D. Basko, I. Aleiner, and B. Altshuler. "Metal–insulator transition in a weakly interacting many-electron system with localized single-particle states." In: *Annals of Physics* 321.5 (2006), pp. 1126–1205. DOI: 10.1016/j.aop.2005.11.014.

[BHD14] F. Bauer, J. Heyder, and J. von Delft. "Functional renormalization group approach for inhomogeneous interacting Fermi systems." In: *Phys. Rev. B* 89.4 (2014), p. 045128. DOI: 10.1103/PhysRevB.89.045128.

[Ber+17] S. Bera, T. Martynec, H. Schomerus, F. Heidrich-Meisner, and J. H. Bardarson. "One-particle density matrix characterization of many-body localization." In: *Annalen der Physik* 529.7 (2017), p. 1600356. DOI: 10.1002/andp.201600356.

[Ber71] V. L. Berezinsky. "Destruction of long range order in one-dimensional and two-dimensional systems having a continuous symmetry group. I. Classical systems." In: *Sov. Phys. JETP* 32 (1971), pp. 493–500.

[Ber72] V. L. Berezinsky. "Destruction of Long-range Order in One-dimensional and Two-dimensional Systems Possessing a Continuous Symmetry Group. II. Quantum Systems." In: *Sov. Phys. JETP* 34.3 (1972), p. 610.

[BBW04] J. Berges, S. Borsányi, and C. Wetterich. "Prethermalization." In: *Physical Review Letters* 93.14 (2004). DOI: 10.1103/physrevlett.93.142002.

[BJW99] J. Berges, D.-U. Jungnickel, and C. Wetterich. "Two flavor chiral phase transition from nonperturbative flow equations." In: *Physical Review D* 59.3 (1999). DOI: 10.1103/physrevd.59.034010.

[BTW02] J. Berges, N. Tetradis, and C. Wetterich. "Non-perturbative renormalization flow in quantum field theory and statistical physics." In: *Physics Reports* 363.4-6 (2002), pp. 223–386. DOI: 10.1016/s0370-1573(01)00098-9.

[BDZ08] I. Bloch, J. Dalibard, and W. Zwerger. "Many-body physics with ultracold gases." In: *Rev. Mod. Phys.* 80.3 (2008), pp. 885–964. ISSN: 00346861. DOI: 10.1103/RevModPhys.80.885.

[Boo15] Boost. *Boost C++ Libraries*. http://www.boost.org/. 2015.

[BF28] M. Born and V. Fock. "Beweis des adiabatensatzes." In: *Zeitschrift für Physik A Hadrons and Nuclei* 51.3 (1928), pp. 165–180.

[Bra+13] S. Braun, J. P. Ronzheimer, M. Schreiber, S. S. Hodgman, T. Rom, I. Bloch, and U. Schneider. "Negative Absolute Temperature for Motional Degrees of Freedom." In: *Science* 339.6115 (2013), pp. 52–55. DOI: 10.1126/science.1227831.

[Bru04] H. Bruus. *Many-Body Quantum Theory in Condensed Matter Physics: An Introduction (Oxford Graduate Texts)*. Oxford University Press, 2004. ISBN: 0198566336.

[BP87] U. Busch and K. A. Penson. "Tight-binding electrons on open chains: Density distribution and correlations." In: *Physical Review B* 36.17 (1987), pp. 9271–9274. DOI: 10.1103/physrevb.36.9271.

[Büt86] M. Büttiker. "Four-Terminal Phase-Coherent Conductance." In: *Physical Review Letters* 57.14 (1986), pp. 1761–1764. DOI: 10.1103/physrevlett.57.1761.

[Caz+11] M. A. Cazalilla, R. Citro, T. Giamarchi, E. Orignac, and M. Rigol. "One dimensional bosons: From condensed matter systems to ultracold gases." In: *Reviews of Modern Physics* 83.4 (2011), pp. 1405–1466. DOI: 10.1103/revmodphys.83.1405.

[Chi+06] G. D. Chiara, S. Montangero, P. Calabrese, and R. Fazio. "Entanglement entropy dynamics of Heisenberg chains." In: *Journal of Statistical Mechanics: Theory and Experiment* 2006.03 (2006), P03001–P03001. DOI: 10.1088/1742-5468/2006/03/p03001.

[Chi+10] C. Chin, R. Grimm, P. Julienne, and E. Tiesinga. "Feshbach resonances in ultracold gases." In: *Reviews of Modern Physics* 82.2 (2010), pp. 1225–1286. DOI: 10.1103/revmodphys.82.1225.

[Cho+16] J. y. Choi, S. Hild, J. Zeiher, P. Schauss, A. Rubio-Abadal, T. Yefsah, V. Khemani, D. A. Huse, I. Bloch, and C. Gross. "Exploring the many-body localization transition in two dimensions." In: *Science* 352.6293 (2016), pp. 1547–1552. DOI: 10.1126/science.aaf8834.

[Cho+17] S. Choi et al. "Observation of discrete time-crystalline order in a disordered dipolar many-body system." In: *Nature* 543.7644 (2017), pp. 221–225. DOI: 10.1038/nature21426.

[Cho+85] K.-C. Chou, Z.-B. Su, B.-L. Hao, and L. Yu. "Equilibrium and nonequilibrium formalisms made unified." In: *Physics Reports* 118.1-2 (1985), pp. 1–131. DOI: 10.1016/0370-1573(85)90136-x.

[CR13] E. S. Coakley and V. Rokhlin. "A fast divide-and-conquer algorithm for computing the spectra of real symmetric tridiagonal matrices." In: *Appl. Comput. Harmon. Anal.* 34.3 (2013), pp. 379–414. ISSN: 10635203. DOI: 10.1016/j.acha.2012.06.003.

[CDC19] P. Czarnik, J. Dziarmaga, and P. Corboz. "Time evolution of an infinite projected entangled pair state: An efficient algorithm." In: *Physical Review B* 99.3 (2019). DOI: 10.1103/physrevb.99.035115.

[DR14] L. D'Alessio and M. Rigol. "Long-time Behavior of Isolated Periodically Driven Interacting Lattice Systems." In: *Physical Review X* 4.4 (2014). DOI: 10.1103/physrevx.4.041048.

[D'A+16] L. D'Alessio, Y. Kafri, A. Polkovnikov, and M. Rigol. "From quantum chaos and eigenstate thermalization to statistical mechanics and thermodynamics." In: *Advances in Physics* 65.3 (2016), pp. 239–362. DOI: 10.1080/00018732.2016.1198134.

[Deu91] J. M. Deutsch. "Quantum statistical mechanics in a closed system." In: *Physical Review A* 43.4 (1991), p. 2046. DOI: 10.1103/PhysRevA.43.2046.

[Deu18] J. M. Deutsch. "Eigenstate thermalization hypothesis." In: *Reports on Progress in Physics* 81.8 (2018), p. 082001. DOI: 10.1088/1361-6633/aac9f1.

[DP04] I. S. Dhillon and B. N. Parlett. "Orthogonal Eigenvectors and Relative Gaps." In: *SIAM J. Matrix Anal. Appl.* 25.3 (2004), pp. 858–899. ISSN: 0895-4798. DOI: 10.1137/S0895479800370111.

[ECP10] J. Eisert, M. Cramer, and M. B. Plenio. "Colloquium: Area laws for the entanglement entropy." In: *Reviews of Modern Physics* 82.1 (2010), pp. 277–306. DOI: 10.1103/revmodphys.82.277.

[EMK16a] A. Eissing, V. Meden, and D. Kennes. "Renormalization in Periodically Driven Quantum Dots." In: *Physical Review Letters* 116.2 (2016). DOI: 10.1103/physrevlett.116.026801.

[EMK16b] A. K. Eissing, V. Meden, and D. M. Kennes. "Functional renormalization group in Floquet space." In: *Physical Review B* 94.24 (2016). DOI: 10.1103/physrevb.94.245116.

[Ens+05] T. Enss, V. Meden, S. Andergassen, X. Barnabé-Thériault, W. Metzner, and K. Schönhammer. "Impurity and correlation effects on transport in one-dimensional quantum wires." In: *Phys. Rev. B* 71.15 (2005), p. 155401. ISSN: 1098-0121. DOI: 10.1103/PhysRevB.71.155401.

[Fra17] F. Franchini. *An Introduction to Integrable Techniques for One-Dimensional Quantum Systems*. Springer International Publishing, 2017. DOI: 10.1007/978-3-319-48487-7.

[Fre08] J. K. Freericks. "Quenching Bloch oscillations in a strongly correlated material: Nonequilibrium dynamical mean-field theory." In: *Physical Review B* 77.7 (2008). DOI: 10.1103/physrevb.77.075109.

[FTZ06] J. K. Freericks, V. M. Turkowski, and V. Zlatić. "Nonequilibrium Dynamical Mean-Field Theory." In: *Physical Review Letters* 97.26 (2006). DOI: 10.1103/physrevlett.97.266408.

[Fri+15] M. Friesdorf, A. H. Werner, W. Brown, V. B. Scholz, and J. Eisert. "Many-body localization implies that eigenvectors are matrix-product states." In: *Phys. Rev. Lett.* 114.17 (2015), p. 170505. ISSN: 10797114. DOI: 10.1103/PhysRevLett.114.170505.

[Fri99] M. Frigo. "A fast Fourier transform compiler." In: *Proceedings of the ACM SIGPLAN 1999 conference on Programming language design and implementation - PLDI '99*. ACM Press, 1999. DOI: 10.1145/301618.301661.

[FS81] J. Fröhlich and T. Spencer. "The Kosterlitz-Thouless transition in two-dimensional abelian spin systems and the Coulomb gas." In: *Comm. Math. Phys.* 81.4 (1981), pp. 527–602.

[Gal09] M. Galassi. *GNU Scientific Library Reference Manual (3rd Ed.)* Network Theory Ltd., 2009. ISBN: 0954612078.

[Geo+96] A. Georges, G. Kotliar, W. Krauth, and M. J. Rozenberg. "Dynamical mean-field theory of strongly correlated fermion systems and the limit of infinite dimensions." In: *Reviews of Modern Physics* 68.1 (1996), pp. 13–125. DOI: 10.1103/revmodphys.68.13.

[GPM07] R. Gezzi, T. Pruschke, and V. Meden. "Functional renormalization group for nonequilibrium quantum many-body problems." In: *Physical Review B* 75.4 (2007). DOI: 10.1103/physrevb.75.045324.

[Gia03] T. Giamarchi. *Quantum Physics in One Dimension*. International Series of Monographs on Physics. Clarendon Press, 2003. ISBN: 9780198525004.

[Gia06] T. Giamarchi. "Strong Correlations in Low Dimensional Systems." In: *AIP Conference Proceedings*. AIP, 2006. DOI: 10.1063/1.2222267.

[Gol+10] S. Goldstein, J. L. Lebowitz, R. Tumulka, and N. Zanghì. "Long-time behavior of macroscopic quantum systems." In: *The European Physical Journal H* 35.2 (2010), pp. 173–200. DOI: 10.1140/epjh/e2010-00007-7.

[Gol+16] V. M.L.D. P. Goli, S. Prodhan, S. Mazumdar, and S. Ramasesha. "Correlated electronic properties of some graphene nanoribbons: A DMRG study." In: *Physical Review B* 94.3 (2016). DOI: 10.1103/physrevb.94.035139.

[Gop+15] S. Gopalakrishnan, M. Müller, V. Khemani, M. Knap, E. Demler, and D. A. Huse. "Low-frequency conductivity in many-body localized systems." In: *Physical Review B* 92.10 (2015). DOI: 10.1103/physrevb.92.104202.

[Gop+16] S. Gopalakrishnan, K. Agarwal, E. A. Demler, D. A. Huse, and M. Knap. "Griffiths effects and slow dynamics in nearly many-body localized systems." In: *Physical Review B* 93.13 (2016). DOI: 10.1103/physrevb.93.134206.

[GMP05] I. V. Gornyi, A. D. Mirlin, and D. G. Polyakov. "Interacting electrons in disordered wires: Anderson localization and low-T transport." In: *Phys. Rev. Lett.* 95.20 (2005), p. 206603. ISSN: 00319007. DOI: 10.1103/PhysRevLett.95.206603.

[Gri69] R. B. Griffiths. "Nonanalytic Behavior Above the Critical Point in a Random Ising Ferromagnet." In: *Physical Review Letters* 23.1 (1969), pp. 17–19. DOI: 10.1103/physrevlett.23.17.

[GH98] M. Grifoni and P. Hänggi. "Driven quantum tunneling." In: *Physics Reports* 304.5-6 (1998), pp. 229–354. DOI: 10.1016/s0370-1573(98)00022-2.

[Gri+12] M. Gring, M. Kuhnert, T. Langen, T. Kitagawa, B. Rauer, M. Schreitl, I. Mazets, D. A. Smith, E. Demler, and J. Schmiedmayer. "Relaxation and Prethermalization in an Isolated Quantum System." In: *Science* 337.6100 (2012), pp. 1318–1322. DOI: 10.1126/science.1224953.

[GB17] C. Gross and I. Bloch. "Quantum simulations with ultracold atoms in optical lattices." In: *Science* 357.6355 (2017), pp. 995–1001. DOI: 10.1126/science.aal3837.

[GJ+10] G. Guennebaud, B. Jacob, et al. *Eigen v3*. http://eigen.tuxfamily.org/. 2010.

[GJ03] S. Guérin and H. R. Jauslin. "Control of Quantum Dynamics by Laser Pulses: Adiabatic Floquet Theory." In: *Advances in Chemical Physics*. John Wiley & Sons, Inc., 2003, pp. 147–267. DOI: 10.1002/0471428027.ch3.

[HHZ84] A. Hamiltonian, B Horvatic, and V Zlatic. "Magnetic field effects for the asymmetric." In: 30.11 (1984).

[Han13] J. E. Han. "Solution of electric-field-driven tight-binding lattice coupled to fermion reservoirs." In: *Phys. Rev. B* 87 (8 2013), p. 085119. DOI: 10.1103/PhysRevB.87.085119.

[HJ08] H Haug and A Jauho. *Quantum Kinetics in Transport and Optics of Semiconductors*. Springer Berlin Heidelberg, 2008. DOI: 10.1007/978-3-540-73564-9.

[HHMP16] J. Hauschild, F. Heidrich-Meisner, and F. Pollmann. "Domain-wall melting as a probe of many-body localization." In: *Physical Review B* 94.16 (2016). DOI: 10.1103/physrevb.94.161109.

[Hey18] M. Heyl. "Dynamical quantum phase transitions: a review." In: *Reports on Progress in Physics* 81.5 (2018), p. 054001. DOI: 10.1088/1361-6633/aaaf9a.

[Hof76] D. R. Hofstadter. "Energy levels and wave functions of Bloch electrons in rational and irrational magnetic fields." In: *Physical Review B* 14.6 (1976), pp. 2239–2249. DOI: 10.1103/physrevb.14.2239.

[HKK97] D. W. Hone, R. Ketzmerick, and W. Kohn. "Time-dependent Floquet theory and absence of an adiabatic limit." In: *Physical Review A* 56.5 (1997), pp. 4045–4054. DOI: 10.1103/physreva.56.4045.

[HS01] C. Honerkamp and M. Salmhofer. "Temperature-flow renormalization group and the competition between superconductivity and ferromagnetism." In: *Physical Review B* 64.18 (2001). DOI: 10.1103/physrevb.64.184516.

[HNO14] D. A. Huse, R. Nandkishore, and V. Oganesyan. "Phenomenology of fully many-body-localized systems." In: *Physical Review B* 90.17 (2014). DOI: 10.1103/physrevb.90.174202.

[IN17] E. Ilievski and J. D. Nardis. "Microscopic Origin of Ideal Conductivity in Integrable Quantum Models." In: *Physical Review Letters* 119.2 (2017). DOI: 10.1103/physrevlett.119.020602.

[IG09] A. Imambekov and L. I. Glazman. "Universal Theory of Nonlinear Luttinger Liquids." In: *Science* 323.5911 (2009), pp. 228–231. DOI: 10.1126/science.1165403.

[ISG12] A. Imambekov, T. L. Schmidt, and L. I. Glazman. "One-dimensional quantum liquids: Beyond the Luttinger liquid paradigm." In: *Reviews of Modern Physics* 84.3 (2012), pp. 1253–1306. DOI: 10.1103/revmodphys.84.1253.

[Imb16a] J. Z. Imbrie. "Diagonalization and Many-Body Localization for a Disordered Quantum Spin Chain." In: *Physical Review Letters* 117.2 (2016). DOI: 10.1103/physrevlett.117.027201.

[Imb16b] J. Z. Imbrie. "On Many-Body Localization for Quantum Spin Chains." In: *Journal of Statistical Physics* 163.5 (2016), pp. 998–1048. DOI: 10.1007/s10955-016-1508-x.

[IRS17] J. Z. Imbrie, V. Ros, and A. Scardicchio. "Local integrals of motion in many-body localized systems." In: *Annalen der Physik* 529.7 (2017), p. 1600278. DOI: 10.1002/andp.201600278.

[Isi25] E. Ising. "Beitrag zur Theorie des Ferromagnetismus." In: *Zeitschrift für Physik* 31.1 (1925), pp. 253–258. ISSN: 0044-3328. DOI: 10.1007/BF02980577.

[Jak15] S. G. Jakobs. "Functional RG for nonequilibrium transport through mesoscopic systems." 2015.

[JMS07] S. G. Jakobs, V. Meden, and H. Schoeller. "Nonequilibrium functional renormalization group for interacting quantum systems." In: *Phys. Rev. Lett.* 99.15 (2007), p. 150603. ISSN: 00319007. DOI: 10.1103/PhysRevLett.99.150603.

[JPS10a] S. G. Jakobs, M. Pletyukhov, and H. Schoeller. "Nonequilibrium functional renormalization group with frequency-dependent vertex function: A study of the single-impurity Anderson model." In: *Physical Review B* 81.19 (2010). DOI: 10.1103/physrevb.81.195109.

[JPS10b] S. G. Jakobs, M. Pletyukhov, and H. Schoeller. "Properties of multi-particle Green's and vertex functions within Keldysh formalism." In: *Journal of Physics A: Mathematical and Theoretical* 43.10 (2010), p. 103001. DOI: 10.1088/1751-8113/43/10/103001.

[Jak+07] S. G. Jakobs, V. Meden, H. Schoeller, and T. Enss. "Temperature-induced phase averaging in one-dimensional mesoscopic systems." In: *Phys. Rev. B* 75.3 (2007), p. 035126. ISSN: 10980121. DOI: 10.1103/PhysRevB.75.035126.

[Jak09] S. Jakobs. "Functional renormalization group studies of quantum transport through mesoscopic systems." PhD thesis. RWTH Aachen University, 2009.

[Jit99] S. Y. Jitomirskaya. "Metal-Insulator Transition for the Almost Mathieu Operator." In: *The Annals of Mathematics* 150.3 (1999), p. 1159. DOI: 10.2307/121066.

[Jor+08] J. Jordan, R. Orús, G. Vidal, F. Verstraete, and J. I. Cirac. "Classical Simulation of Infinite-Size Quantum Lattice Systems in Two Spatial Dimensions." In: *Physical Review Letters* 101.25 (2008). DOI: 10.1103/physrevlett.101.250602.

[JHR06] P. Jung, R. W. Helmes, and A. Rosch. "Transport in Almost Integrable Models: Perturbed Heisenberg Chains." In: *Physical Review Letters* 96.6 (2006). DOI: 10.1103/physrevlett.96.067202.

[Kam11] A. Kamenev. *Field theory of non-equilibrium systems*. Cambridge New York: Cambridge University Press, 2011. ISBN: 9780521760829.

[KL09] A. Kamenev and A. Levchenko. "Keldysh technique and non-linear σ-model: basic principles and applications." In: *Advances in Physics* 58.3 (2009), pp. 197–319. DOI: 10.1080/00018730902850504.

[KBM12] C. Karrasch, J. H. Bardarson, and J. E. Moore. "Finite-Temperature Dynamical Density Matrix Renormalization Group and the Drude Weight of Spin-1/2Chains." In: *Physical Review Letters* 108.22 (2012). DOI: 10.1103/physrevlett.108.227206.

[KEM06] C. Karrasch, T. Enss, and V. Meden. "Functional renormalization group approach to transport through correlated quantum dots." In: *Physical Review B* 73.23 (2006). DOI: 10.1103/physrevb.73.235337.

[KKHM15] C. Karrasch, D. M. Kennes, and F. Heidrich-Meisner. "Spin and thermal conductivity of quantum spin chains and ladders." In: *Physical Review B* 91.11 (2015). DOI: 10.1103/physrevb.91.115130.

[Kar+08] C Karrasch, R Hedden, R Peters, T. Pruschke, K Schönhammer, and V Meden. "A finite-frequency functional renormalization group approach to the single impurity Anderson model." In: *Journal of Physics: Condensed Matter* 20.34 (2008), p. 345205. DOI: 10.1088/0953-8984/20/34/345205.

[Kar+10] C. Karrasch, S. Andergassen, M. Pletyukhov, D. Schuricht, L. Borda, V. Meden, and H. Schoeller. "Non-equilibrium current and relaxation dynamics of a charge-fluctuating quantum dot." In: *EPL (Europhysics Lett.)* 90.3 (2010), p. 30003. ISSN: 0295-5075. DOI: 10.1209/0295-5075/90/30003.

[Kar10] C. Karrasch. "The Functional Renormalization Group for Zero-Dimensional Quantum Systems in and out of Equilibrium." doctoralthesis. RWTH Aachen, 2010.

[Kat04] A. A. Katanin. "Fulfillment of Ward identities in the functional renormalization group approach." In: *Physical Review B* 70.11 (2004). DOI: 10.1103/physrevb.70.115109.

[Kel+65] L. V. Keldysh et al. "Diagram technique for nonequilibrium processes." In: *Sov. Phys. JETP* 20.4 (1965), pp. 1018–1026.

[KSK92] G. Keller, M Salmhofer, and C Kopper. "Perturbative renormalization and effective Langrangians in Φ 4 4." In: *Helvetica Physica Acta* 65.1 (1992), pp. 32–52.

[Ken18] D. M. Kennes. *Transport through Periodically Driven Correlated Quantum Wires*. 2018.

[KK16a] D. M. Kennes and C. Karrasch. "Entanglement scaling of excited states in large one-dimensional many-body localized systems." In: *Phys. Rev. B* 93.24 (2016), p. 245129. ISSN: 24699969. DOI: 10.1103/PhysRevB.93.245129.

[KM13] D. M. Kennes and V. Meden. "Luttinger liquid properties of the steady state after a quantum quench." In: *Phys. Rev. B* 88.16 (2013), p. 165131. ISSN: 10980121. DOI: 10.1103/PhysRevB.88.165131.

[KMV14] D. M. Kennes, V Meden, and R Vasseur. "Universal quench dynamics of interacting quantum impurity systems." In: *Physical Review B* 90.11 (2014), p. 115101. DOI: 10.1103/PhysRevB.90.115101.

[Ken+12] D. M. Kennes, S. G. Jakobs, C. Karrasch, and V. Meden. "Renormalization group approach to time-dependent transport through correlated quantum dots." In: *Phys. Rev. B* 85.8 (2012), p. 085113. ISSN: 10980121. DOI: 10.1103/PhysRevB.85.085113.

[KKM14] D. Kennes, C. Klöckner, and V. Meden. "Spectral Properties of One-Dimensional Fermi Systems after an Interaction Quench." In: *Physical Review Letters* 113.11 (2014). DOI: 10.1103/physrevlett.113.116401.

[KK16b] D. Kennes and C. Karrasch. "Extending the range of real time density matrix renormalization group simulations." In: *Computer Physics Communications* 200 (2016), pp. 37–43. DOI: 10.1016/j.cpc.2015.10.019.

[Ken+17] D. M. Kennes, E. Y. Wilner, D. R. Reichman, and A. J. Millis. "Transient superconductivity from electronic squeezing of optically pumped phonons." In: *Nat. Phys.* 13.5 (2017), pp. 479–483. ISSN: 1745-2473. DOI: 10.1038/nphys4024.

[KPS16] V. Khemani, F. Pollmann, and S. L. Sondhi. "Obtaining highly-excited eigenstates of many-body localized Hamiltonians by the density matrix renormalization group." In: *Phys. Rev. Lett.* 116.24 (2016), p. 247204. DOI: 10.1103/PhysRevLett.116.247204.

[KSF01] H. Kleinert and V. Schulte-Frohlinde. *Critical Properties of* phi *4-theories*. World Scientific, 2001.

[KKK18] C. Klöckner, D. M. Kennes, and C. Karrasch. "Exploring excited eigenstates of many-body systems using the functional renormalization group." In: *Physical Review B* 97.19 (2018). DOI: 10.1103/physrevb.97.195121.

[KBS10] P. Kopietz, L. Bartosch, and F. Schütz. *Introduction to the Functional Renormalization Group*. Lecture Notes in Physics. Springer-Verlag Berlin Heidelberg, 2010. ISBN: 978-3-642-05094-7. DOI: 10.1007/978-3-642-05094-7.

[Kos74] J. M. Kosterlitz. "The critical properties of the two-dimensional xy model." In: *Journal of Physics C: Solid State Physics* 7.6 (1974), pp. 1046–1060. DOI: 10.1088/0022-3719/7/6/005.

[KT73] J. M. Kosterlitz and D. J. Thouless. "Ordering, metastability and phase transitions in two-dimensional systems." In: *Journal of Physics C: Solid State Physics* 6.7 (1973), pp. 1181–1203. DOI: 10.1088/0022-3719/6/7/010.

[Kot+06] G. Kotliar, S. Y. Savrasov, K. Haule, V. S. Oudovenko, O. Parcollet, and C. A. Marianetti. "Electronic structure calculations with dynamical mean-field theory." In: *Reviews of Modern Physics* 78.3 (2006), pp. 865–951. DOI: 10.1103/revmodphys.78.865.

[KM93] B Kramer and A MacKinnon. "Localization: theory and experiment." In: *Reports on Progress in Physics* 56.12 (1993), pp. 1469–1564. DOI: 10.1088/0034-4885/56/12/001.

[Kub57] R. Kubo. "Statistical-Mechanical Theory of Irreversible Processes. I. General Theory and Simple Applications to Magnetic and Conduction Problems." In: *Journal of the Physical Society of Japan* 12.6 (1957), pp. 570–586. DOI: 10.1143/jpsj.12.570.

[Lan57] R. Landauer. "Spatial Variation of Currents and Fields Due to Localized Scatterers in Metallic Conduction." In: *IBM Journal of Research and Development* 1.3 (1957), pp. 223–231. DOI: 10.1147/rd.13.0223.

[LGS15] T. Langen, R. Geiger, and J. Schmiedmayer. "Ultracold Atoms Out of Equilibrium." In: *Annual Review of Condensed Matter Physics* 6.1 (2015), pp. 201–217. DOI: 10.1146/annurev-conmatphys-031214-014548.

[LDM14a] A. Lazarides, A. Das, and R. Moessner. "Equilibrium states of generic quantum systems subject to periodic driving." In: *Physical Review E* 90.1 (2014). DOI: 10.1103/physreve.90.012110.

[LDM14b] A. Lazarides, A. Das, and R. Moessner. "Periodic Thermodynamics of Isolated Quantum Systems." In: *Physical Review Letters* 112.15 (2014). DOI: 10.1103/physrevlett.112.150401.

[LAG04] I. V. Lerner, B. L. Altshuler, and Y. Gefen, eds. *Fundamental Problems of Mesoscopic Physics*. Springer Netherlands, 2004. DOI: 10.1007/1-4020-2193-3.

[LCR15] Y. B. Lev, G. Cohen, and D. R. Reichman. "Absence of Diffusion in an Interacting System of Spinless Fermions on a One-Dimensional Disordered Lattice." In: *Physical Review Letters* 114.10 (2015). DOI: 10.1103/physrevlett.114.100601.

[LR14] Y. B. Lev and D. R. Reichman. "Dynamics of many-body localization." In: *Physical Review B* 89.22 (2014). DOI: 10.1103/physrevb.89.220201.

[Lev+17] Y. B. Lev, D. M. Kennes, C. Klöckner, D. R. Reichman, and C. Karrasch. "Transport in quasiperiodic interacting systems: From superdiffusion to subdiffusion." In: *EPL (Europhysics Letters)* 119.3 (2017), p. 37003. DOI: 10.1209/0295-5075/119/37003.

[LM16] F. Levkovich-Maslyuk. "The Bethe ansatz." In: *Journal of Physics A: Mathematical and Theoretical* 49.32 (2016), p. 323004. DOI: 10.1088/1751-8113/49/32/323004.

[Lew+07] M. Lewenstein, A. Sanpera, V. Ahufinger, B. Damski, A. Sen(De), and U. Sen. "Ultracold atomic gases in optical lattices: mimicking condensed matter physics and beyond." In: *Advances in Physics* 56.2 (2007), pp. 243–379. DOI: 10.1080/00018730701223200.

[Li+15] X. Li, S. Ganeshan, J. Pixley, and S. D. Sarma. "Many-Body Localization and Quantum Nonergodicity in a Model with a Single-Particle Mobility Edge." In: *Physical Review Letters* 115.18 (2015). DOI: 10.1103/physrevlett.115.186601.

[Lie+18] V. Lienhard, S. de Léséleuc, D. Barredo, T. Lahaye, A. Browaeys, M. Schuler, L.-P. Henry, and A. M. Läuchli. "Observing the Space- and Time-Dependent Growth of Correlations in Dynamically Tuned Synthetic Ising Models with Antiferromagnetic Interactions." In: *Physical Review X* 8.2 (2018). DOI: 10.1103/physrevx.8.021070.

[Lig+07] H. Lignier, C. Sias, D. Ciampini, Y. Singh, A. Zenesini, O. Morsch, and E. Arimondo. "Dynamical Control of Matter-Wave Tunneling in Periodic Potentials." In: *Physical Review Letters* 99.22 (2007). DOI: 10.1103/physrevlett.99.220403.

[LS16] S. P. Lim and D. N. Sheng. "Many-body localization and transition by density matrix renormalization group and exact diagonalization studies." In: *Phys. Rev. B* 94.4 (2016), p. 045111. ISSN: 1550235X. DOI: 10.1103/PhysRevB.94.045111.

[Lue+17] H. P. Lueschen, P. Bordia, S. Scherg, F. Alet, E. Altman, U. Schneider, and I. Bloch. "Observation of Slow Dynamics near the Many-Body Localization Transition in One-Dimensional Quasiperiodic Systems." In: *Physical Review Letters* 119.26 (2017). DOI: 10.1103/physrevlett.119.260401.

[LLA15] D. J. Luitz, N. Laflorencie, and F. Alet. "Many-body localization edge in the random-field Heisenberg chain." In: *Physical Review B* 91.8 (2015), p. 081103. DOI: 10.1103/PhysRevB.91.081103.

[LL17] D. J. Luitz and Y. B. Lev. "The ergodic side of the many-body localization transition." In: *Annalen der Physik* 529.7 (2017), p. 1600350. DOI: 10.1002/andp.201600350.

[MA16] N. H. March and G. G. N. Angilella. *Exactly Solvable Models in Many-Body Theory*. World Scientific, 2016. DOI: 10.1142/10048.

[Mar+18] L. Markhof, B. Sbierski, V. Meden, and C. Karrasch. "Detecting phases in one-dimensional many-fermion systems with the functional renormalization group." In: *Physical Review B* 97.23 (2018). DOI: 10.1103/physrevb.97.235126.

[Mat55] T. Matsubara. "A New Approach to Quantum-Statistical Mechanics." In: *Progress of Theoretical Physics* 14.4 (1955), pp. 351–378. DOI: 10.1143/ptp.14.351.

[Med+02a] V. Meden, W. Metzner, U. Schollwöck, and K. Schönhammer. "A Single Impurity in a Luttinger Liquid: How It "Cuts" the Chain." In: *Journal of Low Temperature Physics* 126.3/4 (2002), pp. 1147–1163. DOI: 10.1023/a:1013823514926.

[Med+02b] V. Meden, W. Metzner, U. Schollwöck, and K. Schönhammer. "Scaling behavior of impurities in mesoscopic luttinger liquids." In: *Phys. Rev. B* 65.4 (2002), pp. 453181–453184. ISSN: 01631829. DOI: 10.1103/PhysRevB.65.045318.

[MW92] Y. Meir and N. S. Wingreen. "Landauer formula for the current through an interacting electron region." In: *Phys. Rev. Lett.* 68.16 (1992), pp. 2512–2515. ISSN: 00319007. DOI: 10.1103/PhysRevLett.68.2512.

[MB93] E. E. Mendez and G. Bastard. "Wannier-Stark Ladders and Bloch Oscillations in Superlattices." In: *Physics Today* 46.6 (1993), pp. 34–42. DOI: 10.1063/1.881353.

[Met+12] W. Metzner, M. Salmhofer, C. Honerkamp, V. Meden, and K. Schönhammer. "Functional renormalization group approach to correlated fermion systems." In: *Reviews of Modern Physics* 84.1 (2012), pp. 299–352. DOI: 10.1103/revmodphys.84.299.

[Mit18] A. Mitra. "Quantum Quench Dynamics." In: *Annual Review of Condensed Matter Physics* 9.1 (2018), pp. 245–259. DOI: 10.1146/annurev-conmatphys-031016-025451.

[Mit+16] M. Mitrano et al. “Possible light-induced superconductivity in K3C60 at high temperature.” In: *Nature* 530.7591 (2016), pp. 461–464. DOI: 10.1038/nature16522.

[Modo9] M. Modugno. “Exponential localization in one-dimensional quasi-periodic optical lattices.” In: *New Journal of Physics* 11.3 (2009), p. 033023. DOI: 10.1088/1367-2630/11/3/033023.

[Mor94] T. R. Morris. “The exact renormalization group and approximate solutions.” In: *International Journal of Modern Physics A* 09.14 (1994), pp. 2411–2449. DOI: 10.1142/s0217751x94000972.

[Mou+17] S. Moudgalya, S. Rachel, B. A. Bernevig, and N. Regnault. “Exact Excited States of Non-Integrable Models.” In: (2017).

[NER16] P. Naldesi, E. Ercolessi, and T. Roscilde. “Detecting a many-body mobility edge with quantum quenches.” In: *SciPost Physics* 1.1 (2016). DOI: 10.21468/scipostphys.1.1.010.

[NH15] R. Nandkishore and D. A. Huse. “Many-body localization and thermalization in quantum statistical mechanics.” In: *Annu. Rev. Condens. Matter Phys.* 6.1 (2015), pp. 15–38. DOI: 10.1146/annurev-conmatphys-031214-014726.

[NO88] J. Negele and H. Orland. *Quantum many-particle systems*. Frontiers in physics. Addison-Wesley Pub. Co., 1988. ISBN: 9780201125931.

[Neu29] J. v. Neumann. “Beweis des Ergodensatzes und desH-Theorems in der neuen Mechanik.” In: *Zeitschrift für Physik* 57.1-2 (1929), pp. 30–70. DOI: 10.1007/bf01339852.

[Ney+17] B. Neyenhuis, J. Zhang, P. W. Hess, J. Smith, A. C. Lee, P. Richerme, Z.-X. Gong, A. V. Gorshkov, and C. Monroe. “Observation of prethermalization in long-range interacting spin chains.” In: *Science Advances* 3.8 (2017), e1700672. DOI: 10.1126/sciadv.1700672.

[Ngh+16] H. T. M. Nghiem, D. M. Kennes, C. Klöckner, V. Meden, and T. A. Costi. “Ohmic two-state system from the perspective of the interacting resonant level model: Thermodynamics and transient dynamics.” In: *Physical Review B* 93.16 (2016). DOI: 10.1103/physrevb.93.165130.

[OH07] V. Oganesyan and D. A. Huse. “Localization of interacting fermions at high temperature.” In: *Physical Review B* 75.15 (2007). DOI: 10.1103/physrevb.75.155111.

[PP99] S. Pallua and P. Prester. "XXZ spin chain in a transverse field as a regularization of the sine-Gordon model." In: *Physical Review D* 59.12 (1999). DOI: 10.1103/physrevd.59.125006.

[PL86] T. J. Park and J. C. Light. "Unitary quantum time evolution by iterative Lanczos reduction." In: *The Journal of Chemical Physics* 85.10 (1986), pp. 5870–5876. DOI: 10.1063/1.451548.

[Pei33] R. Peierls. "Zur Theorie des Diamagnetismus von Leitungselektronen." In: *Zeitschrift für Physik* 80.11 (1933), pp. 763–791. ISSN: 0044-3328. DOI: 10.1007/BF01342591.

[Pol84] J. Polchinski. "Renormalization and effective lagrangians." In: *Nuclear Physics B* 231.2 (1984), pp. 269–295. DOI: 10.1016/0550-3213(84)90287-6.

[Polo3] J. Polonyi. "Lectures on the functional renormalization group method." In: *Open Physics* 1.1 (2003), pp. 1–71. DOI: 10.2478/bf02475552.

[Pon+15] P. Ponte, Z. Papić, F. Huveneers, and D. A. Abanin. "Many-Body Localization in Periodically Driven Systems." In: *Physical Review Letters* 114.14 (2015). DOI: 10.1103/physrevlett.114.140401.

[Pre+08] D. Press, T. D. Ladd, B. Zhang, and Y. Yamamoto. "Complete quantum control of a single quantum dot spin using ultrafast optical pulses." In: *Nature* 456.7219 (2008), pp. 218–221. DOI: 10.1038/nature07530.

[Pro11] T. Prosen. "Open XXZ Spin Chain: Nonequilibrium Steady State and a Strict Bound on Ballistic Transport." In: *Physical Review Letters* 106.21 (2011). DOI: 10.1103/physrevlett.106.217206.

[Ramo4] J. Rammer. *Quantum Transport Theory*. Frontiers in Physics. Avalon Publishing, 2004. ISBN: 9780813346229.

[RS86] J. Rammer and H. Smith. "Quantum field-theoretical methods in transport theory of metals." In: *Reviews of Modern Physics* 58.2 (1986), pp. 323–359. DOI: 10.1103/revmodphys.58.323.

[Ramo7] J. Rammer. *Quantum field theory of non-equilibrium states*. Cambridge University Press, 2007.

[Rec+13] M. C. Rechtsman, J. M. Zeuner, Y. Plotnik, Y. Lumer, D. Podolsky, F. Dreisow, S. Nolte, M. Segev, and A. Szameit. "Photonic Floquet topological insulators." In: *Nature* 496.7444 (2013), pp. 196–200. DOI: 10.1038/nature12066.

[RJM14] J. F. Rentrop, S. G. Jakobs, and V. Meden. "Nonequilibrium transport through a Josephson quantum dot." In: *Physical Review B* 89.23 (2014). DOI: 10.1103/physrevb.89.235110.

[Reu98] M. Reuter. "Nonperturbative evolution equation for quantum gravity." In: *Physical Review D* 57.2 (1998), pp. 971–985. DOI: 10.1103/physrevd.57.971.

[RTT11] J. Reuther, R. Thomale, and S. Trebst. "Finite-temperature phase diagram of the Heisenberg-Kitaev model." In: *Physical Review B* 84.10 (2011). DOI: 10.1103/physrevb.84.100406.

[RMS15] V. Ros, M. Müller, and A. Scardicchio. "Integrals of motion in the many-body localized phase." In: *Nuclear Physics B* 891 (2015), pp. 420–465. DOI: 10.1016/j.nuclphysb.2014.12.014.

[Sad+06] L. E. Sadler, J. M. Higbie, S. R. Leslie, M. Vengalattore, and D. M. Stamper-Kurn. "Spontaneous symmetry breaking in a quenched ferromagnetic spinor Bose–Einstein condensate." In: *Nature* 443.7109 (2006), pp. 312–315. DOI: 10.1038/nature05094.

[SH01] M. Salmhofer and C. Honerkamp. "Fermionic Renormalization Group Flows: Technique and Theory." In: *Progress of Theoretical Physics* 105.1 (2001), pp. 1–35. DOI: 10.1143/ptp.105.1.

[Sal+04] M. Salmhofer, C. Honerkamp, W. Metzner, and O. Lauscher. "Renormalization Group Flows into Phases with Broken Symmetry." In: *Progress of Theoretical Physics* 112.6 (2004), pp. 943–970. DOI: 10.1143/ptp.112.943.

[Sal99] M. Salmhofer. *Renormalization*. Springer Berlin Heidelberg, 1999. DOI: 10.1007/978-3-662-03873-4.

[Sam98] K. V. Samokhin. "Lifetime of excitations in a clean Luttinger liquid." In: *Journal of Physics: Condensed Matter* 10.31 (1998), pp. L533–L538. DOI: 10.1088/0953-8984/10/31/002.

[SPL10] L. Sanchez-Palencia and M. Lewenstein. "Disordered quantum gases under control." In: *Nature Physics* 6.2 (2010), pp. 87–95. DOI: 10.1038/nphys1507.

[SK17] B. Sbierski and C. Karrasch. "Second-order functional renormalization group approach to one-dimensional systems in real and momentum space." In: *Physical Review B* 96.23 (2017). DOI: 10.1103/physrevb.96.235122.

[SK18] M. Schmitt and S. Kehrein. "Irreversible dynamics in quantum many-body systems." In: *Physical Review B* 98.18 (2018). DOI: 10.1103/physrevb.98.180301.

[Sch11] U. Schollwöck. "The density-matrix renormalization group in the age of matrix product states." In: *Annals of Physics* 326.1 (2011), pp. 96–192. DOI: 10.1016/j.aop.2010.09.012.

[Sch+15a] M. Schreiber, S. S. Hodgman, P. Bordia, H. P. Lüschen, M. H. Fischer, R. Vosk, E. Altman, U. Schneider, and I. Bloch. "Observation of many-body localization of interacting fermions in a quasirandom optical lattice." In: *Science* 349.6250 (2015), pp. 842–845. DOI: 10.1126/science.aaa7432.

[Sch+15b] M. Schreiber, S. S. Hodgman, P. Bordia, H. P. Lüschen, M. H. Fischer, R. Vosk, E. Altman, U. Schneider, and I. Bloch. "Observation of many-body localization of interacting fermions in a quasi-random optical lattice." In: 2 (2015). ISSN: 0036-8075. DOI: 10.1126/science.aaa7432.

[SW66] J. R. Schrieffer and P. A. Wolff. "Relation between the Anderson and Kondo Hamiltonians." In: *Physical Review* 149.2 (1966), pp. 491–492. DOI: 10.1103/physrev.149.491.

[Shi65] J. H. Shirley. "Solution of the Schrödinger Equation with a Hamiltonian Periodic in Time." In: *Physical Review* 138.4B (1965), B979–B987. DOI: 10.1103/physrev.138.b979.

[SBD16] L. M. Sieberer, M Buchhold, and S Diehl. "Keldysh field theory for driven open quantum systems." In: *Reports on Progress in Physics* 79.9 (2016), p. 096001. DOI: 10.1088/0034-4885/79/9/096001.

[Sir12] J. Sirker. "The Luttinger liquid and integrable models." In: (2012). DOI: 10.1142/S0217979212440092.

[Sre99] M. Srednicki. "The approach to thermal equilibrium in quantized chaotic systems." In: *Journal of Physics A: Mathematical and General* 32.7 (1999), pp. 1163–1175. DOI: 10.1088/0305-4470/32/7/007.

[Ste+14] R. Steinigeweg, F. Heidrich-Meisner, J. Gemmer, K. Michielsen, and H. D. Raedt. "Scaling of diffusion constants in the spin-12XX ladder." In: *Physical Review B* 90.9 (2014). DOI: 10.1103/physrevb.90.094417.

[SB11] R. Steinigeweg and W. Brenig. "Spin Transport in the XXZ Chain at Finite Temperature and Momentum." In: *Physical Review Letters* 107.25 (2011). DOI: 10.1103/physrevlett.107.250602.

[TOA08] N. Tsuji, T. Oka, and H. Aoki. "Correlated electron systems periodically driven out of equilibrium: Floquet+DMFT formalism." In: 78.23 (2008). DOI: 10.1103/physrevb.78.235124.

[TOA09] N. Tsuji, T. Oka, and H. Aoki. "Nonequilibrium Steady State of Photoexcited Correlated Electrons in the Presence of Dissipation." In: *Physical Review Letters* 103.4 (2009). DOI: 10.1103/physrevlett.103.047403.

[Usm94] R. A. Usmani. "Inversion of a tridiagonal jacobi matrix." In: *Linear Algebra Appl.* 212 (1994), pp. 413–414.

[Wan60] G. H. Wannier. "Wave Functions and Effective Hamiltonian for Bloch Electrons in an Electric Field." In: *Phys. Rev.* 117 (2 1960), pp. 432–439. DOI: 10.1103/PhysRev.117.432.

[Was+93] C. Waschke, H. G. Roskos, R. Schwedler, K. Leo, H. Kurz, and K. Köhler. "Coherent submillimeter-wave emission from Bloch oscillations in a semiconductor superlattice." In: *Phys. Rev. Lett.* 70 (21 1993), pp. 3319–3322. DOI: 10.1103/PhysRevLett.70.3319.

[WH73] F. J. Wegner and A. Houghton. "Renormalization Group Equation for Critical Phenomena." In: *Physical Review A* 8.1 (1973), pp. 401–412. DOI: 10.1103/physreva.8.401.

[Wei+19] X. Wei, C. Cheng, G. Xianlong, and R. Mondaini. "Investigating many-body mobility edges in isolated quantum systems." In: *Physical Review B* 99.16 (2019). DOI: 10.1103/physrevb.99.165137.

[Wet93] C. Wetterich. "Exact evolution equation for the effective potential." In: *Physics Letters B* 301.1 (1993), pp. 90–94. DOI: 10.1016/0370-2693(93)90726-x.

[Whi92] S. R. White. "Density matrix formulation for quantum renormalization groups." In: *Physical Review Letters* 69.19 (1992), pp. 2863–2866. DOI: 10.1103/physrevlett.69.2863.

[Wic50] G. C. Wick. "The Evaluation of the Collision Matrix." In: *Physical Review* 80.2 (1950), pp. 268–272. DOI: 10.1103/physrev.80.268.

[Wil12] F. Wilczek. "Quantum Time Crystals." In: *Physical Review Letters* 109.16 (2012). DOI: 10.1103/physrevlett.109.160401.

[Yan+18] H. Yang, A. Liang, C. Chen, C. Zhang, N. B. M. Schroeter, and Y. Chen. "Visualizing electronic structures of quantum materials by angle-resolved photoemission spectroscopy." In: *Nature Reviews Materials* 3.9 (2018), pp. 341–353. DOI: 10.1038/s41578-018-0047-2.

[YPC17] X. Yu, D. Pekker, and B. K. Clark. "Finding Matrix Product State Representations of Highly Excited Eigenstates of Many-Body Localized Hamiltonians." In: *Phys. Rev. Lett.* 118.1 (2017), p. 017201. ISSN: 10797114. DOI: 10.1103/PhysRevLett.118.017201.

[Zen34] C. Zener. "A Theory of the Electrical Breakdown of Solid Dielectrics." In: *Proceedings of the Royal Society A: Mathematical, Physical and Engineering Sciences* 145.855 (1934), pp. 523–529. DOI: 10.1098/rspa.1934.0116.

[Zha+17] J. Zhang et al. "Observation of a discrete time crystal." In: *Nature* 543.7644 (2017), pp. 217–220. DOI: 10.1038/nature21413.

[Žni11] M. Žnidarič. "Spin Transport in a One-Dimensional Anisotropic Heisenberg Model." In: *Physical Review Letters* 106.22 (2011). DOI: 10.1103/physrevlett.106.220601.

[ŽPP08] M. Žnidarič, T. Prosen, and P. Prelovšek. "Many-body localization in the Heisenberg XXZ magnet in a random field." In: *Physical Review B* 77.6 (2008). DOI: 10.1103/physrevb.77.064426.

[Zot04] X. Zotos. "High Temperature Thermal Conductivity of Two-Leg Spin-1/2Ladders." In: *Physical Review Letters* 92.6 (2004). DOI: 10.1103/physrevlett.92.067202.

[ZP96] X. Zotos and P. Prelovšek. "Evidence for ideal insulating or conducting state in a one-dimensional integrable system." In: *Physical Review B* 53.3 (1996), pp. 983–986. DOI: 10.1103/physrevb.53.983.

## PUBLICATIONS

Some excerpts and figures have appeared previously in the following publications:


[KKK18] C. Klöckner, D. M. Kennes, and C. Karrasch. "Exploring excited eigenstates of many-body systems using the functional renormalization group." In: *Physical Review B* 97.19 (2018). DOI: 10.1103/physrevb.97.195121.

[Lev+17] Y. B. Lev, D. M. Kennes, C. Klöckner, D. R. Reichman, and C. Karrasch. "Transport in quasiperiodic interacting systems: From superdiffusion to subdiffusion." In: *EPL (Europhysics Letters)* 119.3 (2017), p. 37003. DOI: 10.1209/0295-5075/119/37003.


## OTHER PUBLICATIONS:


[KKM14] D. Kennes, C. Klöckner, and V. Meden. "Spectral Properties of One-Dimensional Fermi Systems after an Interaction Quench." In: *Physical Review Letters* 113.11 (2014). DOI: 10.1103/physrevlett.113.116401.

[Ngh+16] H. T. M. Nghiem, D. M. Kennes, C. Klöckner, V. Meden, and T. A. Costi. "Ohmic two-state system from the perspective of the interacting resonant level model: Thermodynamics and transient dynamics." In: *Physical Review B* 93.16 (2016). DOI: 10.1103/physrevb.93.165130.

# ACKNOWLEDGEMENTS

First and foremost I would like to thank my advisor, Christoph Karrasch, for the opportunity to work with him and giving me the freedom and time to explore my interests. I want to thank him especially for his guidance, forthright communication, patience and trust.

I am grateful to Felix von Oppen, who agreed to co-referee this thesis. His light-hearted attitude contributed to the positive atmosphere of the Dahlem Center.

In particular I would like to express my gratitude to Björn Sbierski and Dante Kennes, whose support went far beyond mere scientific discussions. Their advice and companionship was remarkable and formative.

Furthermore, I want to thank all the colleagues who made my time at this institute a truly memorable experience. Among those, Sergio Acero stands out - having not only shared an office but also adventures and laughter. Over the years, too many to name them all have contributed to make the Dahlem Center a second home to me: Thomas Kiendl, Laura Baez, Max Geier, Elina Locane, Jonas Sonnenschein, Kevin Madsen, Andi Bauer, Markus Kesselring, Alex Nietner, Jakob Steiner, Flore Kunst, Eddie Seabrook and so many more.

I am grateful to my family for encouraging me to follow my passion, for their advice and support. They made this work possible.

Finally, I want to thank Charlotte, who has been by my side throughout this time. It is hard to overstate her role in providing encouragement, keeping me motivated and making me smile.

# CURRICULUM VITAE

For reasons of data protection, the curriculum vitae is not published in the online version.